HIGH ANGLE OF ATTACK MANEUVERING
AND STABILIZATION CONTROL OF AIRCRAFT

A THESIS SUBMITTED TO
THE GRADUATE SCHOOL OF NATURAL AND APPLIED SCIENCES
OF
MIDDLE EAST TECHNICAL UNIVERSITY

BY

ÖZGÜR ATEŞOĞLU

IN PARTIAL FULFILLMENT OF THE REQUIREMENTS
FOR
THE DEGREE OF DOCTOR OF PHILOSOPHY
IN
MECHANICAL ENGINEERING

JULY 2007

Approval of the Thesis

"HIGH ANGLE OF ATTACK MANEUVERING AND STABILIZATION CONTROL OF AIRCRAFT"

Submitted by **ÖZGÜR ATEŞOĞLU** in partial fulfillment of the requirements for the degree of **Doctor of Philosophy in Mechanical Engineering** by,

Prof. Dr. Canan ÖZGEN
Dean, Graduate School of **Natural and Applied Sciences** ____________________________

Prof. Dr. S. Kemal İDER
Head of Department, **Mechanical Engineering** ____________________________

Prof. Dr. M. Kemal ÖZGÖREN
Supervisor, **Mechanical Engineering Dept., METU** ____________________________

Examining Committee Members:

Prof. Dr. Bülent E. PLATİN (*)
Mechanical Engineering Dept., METU ____________________________

Prof. Dr. M. Kemal ÖZGÖREN (**)
Mechanical Engineering Dept., METU ____________________________

Prof. Dr. M. Kemal LEBLEBİCİOĞLU
Electrical and Electronics Engineering Dept., METU ____________________________

Prof. Dr. Tuna BALKAN
Mechanical Engineering Dept., METU ____________________________

Asst. Prof. Dr. Yakup ÖZKAZANÇ
Electrical and Electronics Engineering Dept., HÜ ____________________________

Date: ____________________________

(*) Head of Examining Committee

(**) Supervisor

I hereby declare that all information in this document has been obtained and presented in accordance with academic rules and ethical conduct. I also declare that, as required by these rules and conduct, I have fully cited and referenced all material and results that are not original to this work.

Name, Last Name : Özgür ATEŞOĞLU

Signature :

ABSTRACT

HIGH ANGLE OF ATTACK MANEUVERING AND STABILIZATION CONTROL OF AIRCRAFT

ATEŞOĞLU, Özgür
Ph. D., Department of Mechanical Engineering
Supervisor: Prof. Dr. M. Kemal ÖZGÖREN

July 2007, 281 pages

In this study, the implementation of modern control techniques, that can be used both for the stable recovery of the aircraft from the undesired high angle of attack flight state (stall) and the agile maneuvering of the aircraft in various air combat or defense missions, are performed. In order to accomplish this task, the *thrust vectoring control* (TVC) actuation is blended with the conventional aerodynamic controls. The controller design is based on the *nonlinear dynamic inversion* (NDI) control methodologies and the stability and robustness analyses are done by using *robust performance* (RP) analysis techniques. The control architecture is designed to serve both for the recovery from the undesired stall condition (*the stabilization controller*) and to perform desired agile maneuvering (*the attitude controller*). The detailed modeling of the aircraft dynamics, aerodynamics, engines and thrust vectoring paddles, as well as the flight environment of the aircraft and the on-board sensors is performed. Within the

control loop the human pilot model is included and the design of a fly-by-wire controller is also investigated. The performance of the designed stabilization and attitude controllers are simulated using the custom built 6 DoF aircraft flight simulation tool. As for the stabilization controller, a forced deep-stall flight condition is generated and the aircraft is recovered to stable and pilot controllable flight regimes from that undesired flight state. The performance of the attitude controller is investigated under various high angle of attack agile maneuvering conditions. Finally, the performances of the proposed controller schemes are discussed and the conclusions are made.

Keywords: High Alpha Maneuvering, Thrust Vectoring Control (TVC), Nonlinear Inverse Dynamics (NID), Robust Performance (RP) Analysis, Human Pilot.

ÖZ

UÇAKLARIN YÜKSEK HÜCUM AÇISINDA MANEVRA VE STABİLİZASYON DENETİMİ

ATEŞOĞLU, Özgür
Doktora, Makina Mühendisliği Bölümü
Tez Yöneticisi: Prof. Dr. M. Kemal ÖZGÖREN

Temmuz 2007, 281 sayfa

Bu çalışmada, uçakların yüksek hücum açılarında denetimi için modern yöntemler kullanılarak denetleyici tasarımları gerçekleştirilmiştir. Denetleyiciler hem stabilizasyon hem de yönelim denetiminde kullanılabilecek yapıda tasarlanmıştır. Tasarlanan denetleyiciler, uçakları istenmeden karşılaşılan ve oldukça tehlikeli olabilecek yüksek hücum açılarındaki uçuşlardan kurtarmak ve pilot tarafından kolaylıkla denetlenebilecek kararlı uçuş durumlarına getirmekte kullanılabildiği gibi, aynı zamanda, savaş ve savunma uçuşlarında yüksek hücum açılarında gerçekleştirilen çevik manevraların denetiminde de kullanılabilmektedir. Denetim *itki vektörü denetimi* (İVD) yöntemi ile geleneksel aerodinamik kontrol eyleticileri harmanlanarak gerçekleştirilmiştir. Denetim tasarımında *doğrusal olmayan evrik dinamik* (DOED) yöntemi kullanılmış ve *dayanıklılık* analizleri yapılmıştır. Hava aracının dinamiği, aerodinamiği, motoru, itki yönlendirme pedalları, uçuş ortamı ve üzerindeki algılayıcılar detaylı olarak modellenmiş ve 6 serbestlik dereceli bir hava aracı uçuş benzetimi sentezlenmiştir. Bu modellere pilot modeli de eklenmiş ve denetim yapılarının pilot modeli ile birlikte dayanıklılık analizleri yapılmıştır. Stabilizasyon denetimi için hava aracı bilerek istenmeyen bir yüksek hücum açısında uçuş durumuna itilmiş ve buradan denetim yardımı ile kurtarılarak kararlı ve kolay denetlenebilir uçuş rejimlerine çekilmiştir. Yönelim denetiminin başarımı ise yüksek hücum açılarında yapılan farklı çevik manevra benzetimleri ile gösterilmiştir. Gerçekleştirilen benzetimlerin sonuçları incelenmiş ve tasarlanan denetim yapılarının başarımları yorumlanmıştır.

Anahtar Kelimeler: Yüksek Hücum Açılarında Manevralar, İtki Vektörü Denetimi (İVD), Doğrusal Olmayan Evrik Dinamik (DOED), Dayanıklılık Başarım Analizi, Pilot Modeli.

In the Name of My Beloved Father

ACKNOWLEDGMENTS

Above all, I wish to express my sincere gratitude to my supervisor, Prof. Dr. M. Kemal ÖZGÖREN for his guidance, helpful suggestions, encouragements, valuable interaction and feedbacks throughout the study.

I would also like to thank to my Thesis Supervising Committee members, Prof. Dr. Bülent E. PLATİN and Prof. Dr. M. Kemal LEBLEBİCİOĞLU for their constructive comments and guidance throughout my study. Furthermore, I would like to thank to my thesis jury committee members Prof. Dr. Tuna BALKAN and Asst. Prof. Dr. Yakup ÖZKAZANÇ for their contributions.

I would like to thank to my colleague Dr. Volkan NALBANTOĞLU for his prompt comments and feedbacks, and also, my manager and colleagues and friends from Aselsan MGEO for their help and friendship.

In addition, I am indebted to my family to form a part of my vision of life and teach me to do the things at my best rate. Also, I am thankful to my father, and his happy memory, to teach the strong, straight and joyful side of life from the mathematics point of view.

Finally, my sincere gratitude is dedicated to the cosmological *Prime Mover* for giving me the inspiration to begin and the desire to conclude this thesis work.

TABLE OF CONTENTS

LIST OF TABLES

TABLES

LIST OF FIGURES

FIGURES

LIST OF SYMBOLS

$\vec{a}_{b/o}$	:	Translational acceleration vector of the aircraft
a^+, a_n, a^-	:	Upper, nominal and lower limits of parameter a
$AoACont$	:	Angular to linear velocity controller switch
b^+, b_n, b^-	:	Upper, nominal and lower limits of parameter b
b_i	:	General symbol for bias values of sensors
$\hat{C}^{(o,b)}$	:	Rotation matrix from earth fixed to body fixed reference frame
$\hat{C}^{(b,w)}$	:	Rotation matrix from body fixed to wind reference frame
$\hat{C}^{(o,w)}$	:	Rotation matrix from earth fixed to wind reference frame
C_i	:	General symbol for aerodynamic force and moment coefficients
$C_{n\beta}, C_{l\beta}$	:	Sensitivities of the yaw and roll moments to β
$C_{n\beta dyn}$	:	Dynamic sensitivity of yaw moment to side slip angle
$C_{n\beta dynT}$	:	Trigger value of $C_{n\beta dyn}$ to start high AoA stabilization
$\hat{D}, \hat{Q}, \hat{G}$	:	Scaling matrices for upper and lower bound μ calculation
d_m	:	Gust length

d_{dz}	:	Lateral distance between the aircraft and the fixed ground target
$\overline{e}_i$	:	General symbol for vector components of error signals
$\vec{F}_L, \vec{F}_R$	:	Thrust force vectors of the left and right engines
$\vec{F}_a, \vec{M}_a$	:	Aerodynamic force and moment vectors
$\overline{F}_{com}^{(b)}$	:	Array of computed force components
$\hat{F}_l$	:	The lower LFT of a system
$\hat{F}_u$	:	The upper LFT of a system
f_{nT}	:	Natural frequency of the paddle actuator dynamics
$\hat{G}_1(s)$	:	Controller transfer matrix for the 1st set of cascaded differential equations
$\hat{G}_2(s)$	:	Controller transfer matrix for the 2nd set of cascaded differential equations
$G_n(s), G_d(s)$	:	Pilot time delay and neuro-motor lag transfer functions
$\hat{G}_{nom}^{sta}(s)$	:	Nominal transfer matrix for uncertainty calculation of the stabilization controller
$\hat{G}_{nom}^{att}(s)$	:	Nominal transfer matrix for uncertainty calculation of the attitude controller
$\hat{G}_{des}^{sta}(s)$	:	Desired matching model transfer matrix for stabilization controller
$\hat{G}_{des}^{att}(s)$	:	Desired matching model transfer matrix for attitude controller
$\vec{g}$	:	Earth gravity field vector
$\overline{H}_e^{(b)}$	:	Engine angular momentum vector components
h	:	Altitude of the aircraft

h_0	:	Trim altitude of the aircraft
$\hat{J}$	:	Inertia matrix of the aircraft
J_e	:	Directional inertia component of the aircraft engine
J_x, J_y, J_z	:	Primary inertial components of the aircraft along *x*, *y*, *z* directions of the body fixed frame
$\hat{K}_{pi}, \hat{K}_{ii}, \hat{K}_d$	:	Generalized expression for controller matrix gains
k_p, k_i, k_{fq}, k_{rq}	:	Controller gains for desired dynamics assignment
$k_{\alpha\beta}, k_{\beta\alpha}$	:	Cross-coupling coefficients of flow angles α, β
$LCDP$	:	Lateral control departure parameter
$LCDP_T$	:	Trigger value of $LCDP$ to start high AoA stabilization
L_u, L_v, L_w	:	Turbulence scale lengths
M	:	Mach number
$\hat{M}$	:	Interconnection structure
$\hat{M}_{11}$	:	Left upper corner block of $\hat{M}$
m	:	Mass of the aircraft
$\lvert m_g \rvert_{max}$	:	Maximum gust amplitude
$\overline{M}_{com}^{(b)}$	:	Array of computed moment components
$\overline{M}_e^{(b)}$	:	Array of moment components created by engine angular momentum
$M_\alpha, M_q, M_{\delta_e}$	:	Pitching moment dimensional aerodynamic derivatives
n_i	:	General symbol for noise signals on sensors
$\overline{n}$	:	Disturbance signals vector
p_0	:	Nominal value of a generalized parameter p

P_a, P_c	:	Actual and commanded power levels of the engine
p, q, r	:	Angular velocity components of the aircraft
p_0, q_0, r_0	:	Trim angular velocity components of the aircraft
$\dot{p}_e, \dot{q}_e, \dot{r}_e$	:	Angular acceleration components of the aircraft originating from the engine angular momentum
$\mathrm{TAttack}_{in}$	:	Fixed ground target attack trigger
Q_d	:	Dynamic pressure
R_{dz}	:	Fixed ground target defense zone circular radius
$\hat{R}_k(\theta)$	:	Rotation matrix of angle θ about the k^{th} axis
$\vec{r}_{be_L}$, $\vec{r}_{be_R}$	:	Position vectors of the engine nozzle exits with respect to the mass center
$\vec{r}_{b/o}$	:	Position vector of the aircraft
$s_{1,2}$	:	Complex conjugate pole pairs
$\vec{v}_{b/o}$	:	Translational velocity vector of the aircraft
v_s	:	Speed of sound
T_L, T_R	:	Total thrust created by the aircraft engines
T_{L0}, T_{R0}	:	Trim total thrust created by the aircraft engines
$T_{mil}, T_{idle}, T_{\max}$	:	Military, idle and maximum thrust levels
T_i	:	General symbol for time constants of the sensor dynamics
t_f	:	Desired amount of time in which the desired final values are reached
$\vec{u}_1, \vec{u}_2, \vec{u}_3$	:	Unit vectors along the body frame axes
u, v, w	:	Translational velocity components of the aircraft in the

		body fixed frame
$\overline{u}_c$	:	Commanded control deflections vector
V_T	:	Total velocity of the aircraft
V_{T0}	:	Trim total velocity of the aircraft
V_w	:	Wind velocity
$\hat{W}_a, \hat{W}_u, \hat{W}_y$	:	Uncertainty weighting transfer matrices
$W_{ni}(s)$	:	General expression of shaping filters of the measurement noises in the robustness analysis
$W_{di}(s)$	:	General expression of shaping filters of the disturbance noises in the robustness analysis
$\hat{W}_p^{sta}(s), \hat{W}_p^{att}(s)$	:	Performance weight transfer matrices for stabilization and attitude controllers
w_i	:	General symbol for white Gaussian noise signals affecting the sensors
$\overline{x}(t)$	:	Aircraft states vector
$\overline{x}_1(t)$	:	States vector for the 1^{st} set of cascaded differential equations
$\overline{x}_2(t)$	:	States vector for the 2^{nd} set of cascaded differential equations
x, y, z	:	Position components of the aircraft
x_t, y_t, z_t	:	Position components of the target
α, β	:	Angle of attack and side slip angle
α_0, β_0	:	Trim angle of attack and side slip angle
$\vec{\alpha}_{b/o}$	:	Angular acceleration vector of the aircraft

$\hat{\Delta}_a, \hat{\Delta}_u, \hat{\Delta}_y$	:	Uncertainty matrices
$\Delta\hat{G}^{sta}(s)$	:	Additive uncertainty transfer matrix for the stabilization controller
$\Delta\hat{G}^{att}(s)$	:	Additive uncertainty transfer matrix for the attitude controller
$\delta_{L1}, \delta_{L2}, \delta_{L3}$	:	Left engine thrust-vectoring paddle deflections
$\delta_{R1}, \delta_{R2}, \delta_{R3}$	:	Right engine thrust-vectoring paddle deflections
$\delta_a, \delta_e, \delta_r$	:	Aileron, elevator, and rudder deflections
$\delta_{a0}, \delta_{e0}, \delta_{r0}$	:	Trim aileron, elevator, and rudder deflections
$\delta_{Lth}, \delta_{Rth}$	:	Left and right engine throttle deflections
δ_p, δ_y	:	Effective pitch and yaw angles of the thrust deviation
δ_{icom}	:	General symbol for the computed aerodynamic surface and throttle deflections
$\gamma_x, \gamma_y, \gamma_z$	:	Velocity vector orientation angles
γ_{zt}, γ_{yt}	:	Flight path angles of the target
$\gamma_{ztd}, \gamma_{ytd}$	:	Desired flight path angles of the target
Ω	:	Spatial frequency of turbulence field
$\vec{\omega}_{b/o}$	:	Angular velocity vector of the aircraft expressed at body axis coordinates
$\vec{\omega}_{w/o}$	:	Angular velocity vector of the aircraft expressed at wind axis coordinates
ω_e	:	Angular velocity of aircraft engine
$\omega_{ni}, \zeta_i, \omega'_{ni}$	:	Control parameters of the desired closed loop dynamics

$\sigma_u, \sigma_v, \sigma_w$	:	Turbulence intensities
$\overline{\sigma}_{sta}$	:	Random noise signals vector for stabilization controller
$\overline{\sigma}_{att}$	:	Random noise signals vector for attitude controller
$\overline{\sigma}(\hat{\Delta})$	:	Largest singular value of $\hat{\Delta}$
μ	:	Structured singular value
μ_{peak}	:	Peak of upper bound of μ value
τ_{eng}	:	Time constant of the aircraft engine
τ_d, τ_n	:	Pilot time delay and neuro-motor lag time constants
ψ, θ, ϕ	:	Euler angles describing the attitude of the aircraft
ψ_L, ψ_R	:	Azimuth deviation of the total thrust of the left and right engines
ψ_w	:	Direction of wind
θ_L, θ_R	:	Elevation deviation of the total thrust of the left and right engines
ρ	:	Air density

$\cdot$	:	First Time Derivative
$\cdot\cdot$	:	Second Time Derivative
$\rightarrow$	:	Vector
$-$	:	Column
^	:	Matrix
~	:	Skew-Symmetric Matrix

LIST OF ABBREVIATIONS

AoA	:	Angle of Attack
HCA	:	Heading Crossing Angle
BFM	:	Basic Fighter Maneuvers
EFM	:	Enhanced Fighter Maneuverability
ACT	:	Air Combat Tactics
SAM	:	Surface to Air Missile
HARV	:	High Angle of Attack Research Vehicle
MATV	:	Multi-axis Thrust Vectoring
PST	:	Post Stall Technology
CAP	:	Control Anticipation Parameter
TVC	:	Thrust Vector Control
NID	:	Nonlinear Inverse Dynamics
NDI	:	Nonlinear Dynamic Inversion
ND	:	Nonlinear Dynamics
HUD	:	Head-up Display
FQ	:	Flying Quality
RQ	:	Ride Quality
LQG	:	Linear Quadratic Gaussian
LQR	:	Linear Quadratic Regulators
RMS	:	Root Mean Square

MIMO	:	Multi Input Multi Output
LFT	:	Linear Fractional Transformations
RP	:	Robust Performance
RS	:	Robust Stability
NP	:	Nominal Performance
TM	:	Transfer Matrix
TF	:	Transfer Function
IMU	:	Inertial Measurement Unit
INS	:	Inertial Navigation System
AHRS	:	Attitude and Heading Reference System
LCDP	:	Lateral Control Departure Parameter
IBW	:	Integrated Bihrle Weissmann Chart
NPR	:	Nozzle Pressure Ratio
IEEE	:	The Institute of Electrical and Electronics Engineers
AIAA	:	The American Institute of Aeronautics and Astronautics
NASA	:	National Aeronautics and Space Administration
WGS84	:	World Geodetic System 1984
ICAO	:	International Civil Aviation Organization
RLG	:	Ring Laser Gyroscope
FOG	:	Fiber Optic Gyroscope
MEMS	:	Micro-Electro Mechanic Systems
PIO	:	Pilot Induced Oscillations
SCAS	:	Stability and Control Augmentation System
GPS	:	Global Positioning System

CFD	:	Computational Fluid Dynamics
A/P	:	Autopilot
A/C	:	Aircraft
H/P	:	Human Pilot
LOS	:	Line of Sight
STOL	:	Short Take-off and Landing
VSTOL	:	Very Short Take-off and Landing

CHAPTER 1

INTRODUCTION

In this chapter, the basis of the study will be introduced. First, the scope of the study will be summarized. The information on controlling a general aircraft will be given and the basic conventional and fighter aircraft maneuvers will be explained. Then, the fundamentals of air combat maneuvers including the basic air combat maneuvers and air combat tactics will be discussed. Eventually, an introduction on the aerodynamic properties of high angle of attack flight, which is directly related to complicated flight maneuvers, will be given. Then, a summary of the related literature on high angle of attack maneuvering control will be given. In that section, the dynamic inverse controller design including 2-time scale method, assignment of the desired dynamics, the basic issues on dynamic inversion and stability and robustness analysis will be explained. Finally, at the last section of the chapter, the outline of the thesis study will be summarized.

1.1. The Scope of the Study

The scope of the study is to implement modern control techniques that can be used both for the stable recovery of the aircraft from the undesired high angle of attack flight, i.e. *stall*, and the agile maneuvering of the aircraft in various air combat or defense scenarios. In order to achieve the desired task, the *thrust vectoring control* (TVC) actuators and *nonlinear dynamic inversion* (NDI) control methodologies are used in conjunction with *robust performance* (RP) analysis techniques.

1.2. Controlling the Aircraft

The flight, regardless of the aircraft used or the route flown, is essentially based on the basic maneuvers. In visual flight, the attitude of the aircraft is controlled with relation to the natural horizon by using certain reference points on the aircraft. Also, in instrument flight, the attitude of the aircraft is controlled by reference to the flight instruments. Thus, a proper interpretation of the flight instruments will give essentially the same information that the outside references do in visual flight.

The attitude of the aircraft is the relationship of its longitudinal and lateral axes with respect to the Earth's horizon. The pilot's goal is to safely control the aircraft's trajectory relative to the ground. The primary technique that the pilots are taught to accomplish this goal is called *attitude flying* (using the aircraft's attitude to control the trajectory). In this method the pilot uses the aircraft's pitch, bank and power to control the trajectory [1], [2].

The aircraft performance is achieved by controlling the attitude and the power of the aircraft. This is known as the *control and performance* method of attitude flying and can be applied to any basic maneuver.

The aircraft instruments help the pilot to control the attitude and the power of the aircraft as desired. The flight instruments are generally categorized in three different groups; *control*, *performance* and *navigation* instruments.

The control instruments display the immediate attitude and power indications and are calibrated to permit attitude and power adjustments in definite amounts. Here, the term power is used for the more technically correct terms; the *thrust* and *drag* relationship. Control is determined by the references to the attitude and power indicators. The measurement of power can vary with aircraft and include tachometers, engine pressure ratio, manifold pressure or fuel flow indicators. The performance instruments indicate the aircraft's actual performance by the altimeter, airspeed or mach indicator, the vertical velocity indicator, the heading indicator, the angle of attack indicator and the turn and slip indicator. The navigation instruments indicate the position of the aircraft in relation to a selected navigation facility or fix. This group of instruments include various types of course indicators, range indicators, glide slope indicators and bearing pointers.

The attitude control of an aircraft is based on maintaining a constant attitude, knowing when and how much to change the attitude and smoothly changing the attitude a definite amount. It is accomplished by the proper use of the attitude references that provide immediate and direct indication of any change in aircraft pitch or bank attitude. The power control of an aircraft results from the ability to smoothly establish or maintain desired airspeeds in coordination with attitude changes. The power changes are made by throttle adjustments and reference to the power indicators. The power indicators are not affected by the factors such as turbulence or improper trim. Thus, in most aircraft, little attention is required to ensure the power setting remains constant. The control, power and navigation instruments panel of a fighter aircraft can be seen in the following figure.

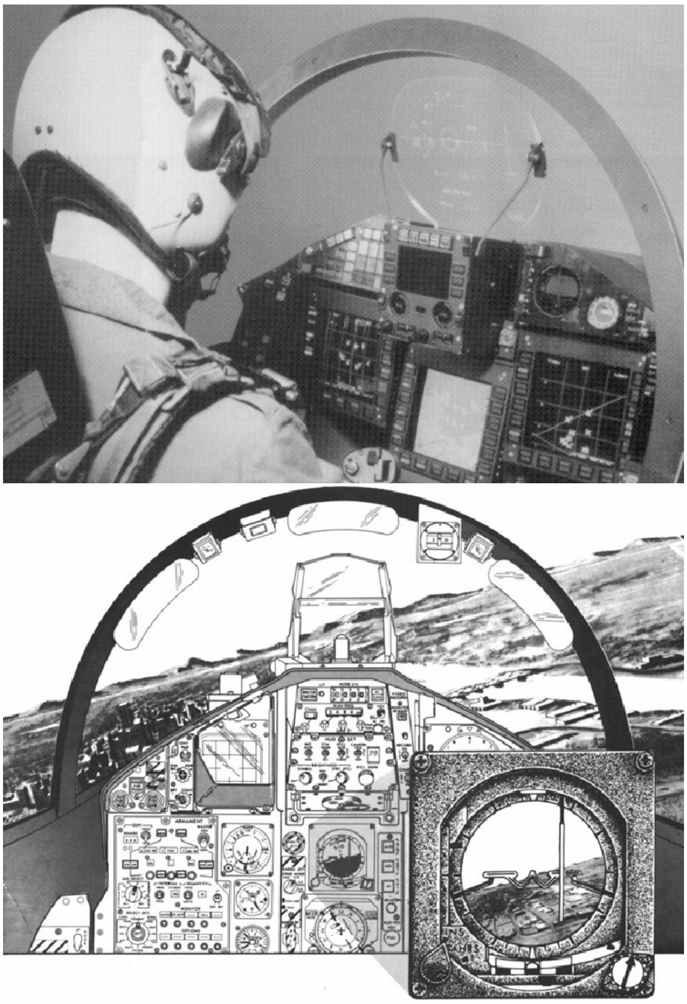

Figure 1. The Flight Instruments Panel of a Fighter Aircraft

1.2.1. Basic Flight Maneuvers

The basic flight maneuvers for an aircraft include the *straight and level flight*, the *straight climbs and descents* and the *turns*.

In straight and level flight the pitch attitude, i.e. the angle between the longitudinal axis of the aircraft and the actual horizon, varies with airspeed. At a constant airspeed there is only one specific pitch attitude for straight and level flight. The instruments used for pitch attitude control of the aircraft are the attitude indicator, the altimeter, the vertical speed indicator and the airspeed indicator. At slow cruise speeds the level flight pitch attitude is *nose-high* and at fast cruise speeds the level flight pitch attitude is *nose-low*.

The bank attitude of an aircraft is the angle between the lateral axis of the aircraft and the natural horizon. To maintain a straight and level flight path the wings of the aircraft should be kept level with the horizon. Any deviation from the straight flight resulting from a bank error should be corrected by coordinated *aileron* and *rudder* actuation. The instruments used for bank attitude control of the aircraft are the attitude indicator, the heading indicator and the turn coordinator.

The power control produces the thrust which overcomes the forces originating from the gravity, drag and inertia of the aircraft. Power control should be related to its consecutive effect on altitude and airspeed. Because, any change in power settings results in a change in the airspeed or the altitude of the aircraft. At any given airspeed the power settings determine whether the aircraft is in a level flight, climb or descent. If the power is increased in straight and level flight and the pitch attitude is held constant the aircraft will eventually climb. On the contrary, if the power is decreased while holding the pitch attitude constant the aircraft will eventually descend. The relationship between altitude and airspeed determines the need for a change in pitch or power. If the altitude is higher than desired and the airspeed is low, or vice versa, a change in pitch alone may return the aircraft to the desired altitude and airspeed. If both airspeed and altitude are high or low then a change in both pitch and power is necessary to return to the desired airspeed and altitude. For changes in airspeed in straight and level flight pitch, bank and power must be coordinated in order to maintain constant altitude and heading.

For a given power setting and load condition there is only one attitude that will give the most efficient rate of climb. Details of the technique for entering a climb vary according to the airspeed on entry and the type of climb (constant airspeed or constant rate) desired. To enter a constant airspeed climb from cruising airspeed the aircraft is brought to a proper nose-high indication. Thus, the pitch attitude of the aircraft will change. Here the pitch and power corrections should be closely coordinated. For example, if the vertical speed is correct but the airspeed is low extra power should be added. A descent can be made at various airspeeds and attitudes by reducing the power, adding drag and lowering the nose of the aircraft to a predetermined attitude. Then, the airspeed will be stabilized at a constant value.

The turns are generally classified as *standard-rate* and *steep* turns. To enter a *standard-rate level turn*, coordinated aileron and rudder controls should be applied in the desired direction of turn. On the start of the roll maneuver, attitude indicator is used to establish the approximate angle of bank and the turn coordinator is checked for a standard-rate turn indication. The bank angle is maintained for this rate of turn using the turn coordinator's miniature aircraft as the primary bank reference and the attitude indicator as the supporting bank instrument. Also, the altimeter, vertical speed indicator, and attitude indicator for the necessary pitch adjustments are checked since the vertical lift component decreases with an increase in bank. If constant airspeed is to be maintained, the airspeed indicator becomes primary for power, and, the throttle should be adjusted as drag increases.

Any turn with a rate greater than a standard-turn rate can be considered as a steep turn. Entering a steep turn is done similar to a shallower turn. However, since the vertical lift component is quickly decreasing, the pitch control is usually the main and difficult aspect of this maneuver. The pitch attitude should immediately be noted and corrected with a pitch increase carefully watching altimeter, the vertical speed indicator and the airspeed needles. If the rate of the bank change is high the lift decrease will be fast accordingly. In order to execute climbing and descending turns the techniques used in straight climbs and descents are combined with the turn techniques. The aerodynamic factors affecting the lift and power control should be considered in determining power, bank and pitch attitude settings.

1.2.2. Basic Flight Maneuvers for Fighters

In the previous section the conventional maneuvers to fly an aircraft are introduced. In this chapter, the basic fighter aircraft maneuvers will be discussed.

The *vertical S* series of maneuvers are the proficiency maneuvers designed to improve a pilot's crosscheck of flight instruments and aircraft control. There are four basic types called A, B, C, and D.

The *vertical S-A maneuver* is a continuous series of rate climbs and descents flown on a constant heading. The altitude flown between changes of vertical direction and the rate of vertical velocity used must be compatible with aircraft performance. The maneuver is excellent if flown at final approach airspeed with precisely controlling the glide path. The transition from descent to climb can be used to simulate the missed approach. However, sufficient altitude for “cleaning-up” the aircraft and establishing the climb portion of the maneuver should be allowed.

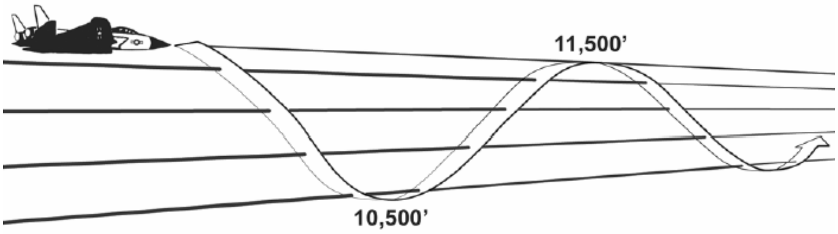

Figure 2. The Vertical S-A Maneuver

The *vertical S-B maneuver* is the same as the vertical S-A except that a constant angle of bank is maintained during the climb and descent. The angle of bank used should be compatible with aircraft performance (usually that is required for a normal turn). The turn is established simultaneously with the initial climb or descent. The angle of bank is maintained constant throughout the maneuver.

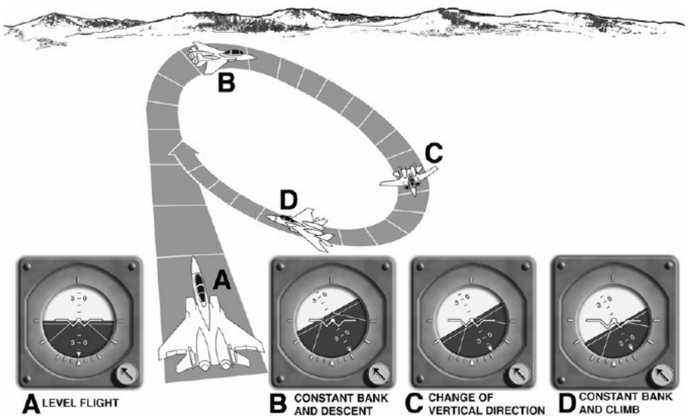

Figure 3. The Vertical S-B Maneuver

The *vertical S-C maneuver* is the same as vertical S-B except that the direction of turn is reversed at the beginning of each descent. The vertical S-C maneuver is entered in the same manner as the vertical S-B. The *vertical S-D maneuver* is the same as the vertical S-C except that the direction of turn is reversed simultaneously with each change of vertical direction. The vertical S-D maneuver is entered in the same manner as the vertical S-B or S-C. Any of the vertical S maneuvers may be initiated with a climb or descent. The maneuvers are generally practiced at approach speeds and low altitudes or at cruise speeds and higher altitudes.

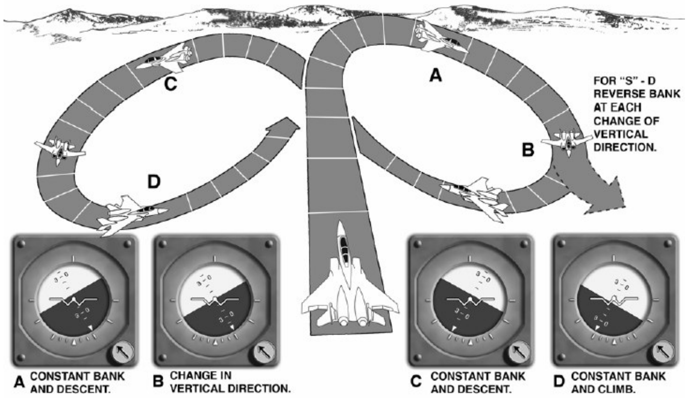

Figure 4. The Vertical S-C, S-D Maneuvers

There are also basic maneuvers called as *confidence maneuvers*. Confidence maneuvers are basic aerobatic maneuvers designed to gain confidence in the use of the attitude indicator in extreme pitch and bank attitudes. In addition, mastering these maneuvers will be helpful when recovering from unusual attitudes.

The *wingover maneuver* is a confidence maneuver that begins from straight and level flight. After obtaining the desired airspeed the climbing turn is started in the left or right direction until reaching 60° of bank. Meanwhile, the nose of the aircraft starts getting down and the bank of the aircraft is increased up to 90°. Then, angle the bank angle is decreased backwards to 60°. Keeping the constant turn rate the aircraft is recovered to wings level attitude. The rate of roll during the recovery should be the same as the rate of roll used during the entry. Throughout the maneuver the pitch and bank attitudes of the aircraft are controlled by reference to the attitude indicator.

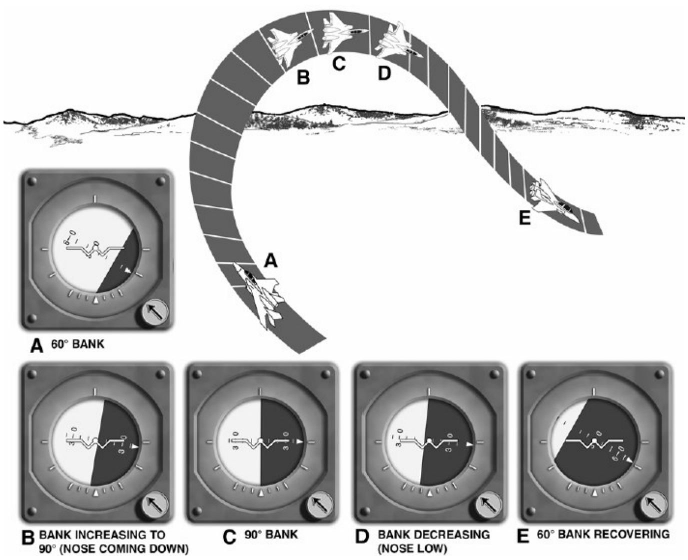

Figure 5. The Wingover Maneuver

The *aileron roll maneuver* is a confidence maneuver that begins from the straight and level flight after obtaining the desired airspeed. The pitch attitude is smoothly increased from the wings level attitude to 15° or 25°. Then, a roll maneuver is started in the left or right direction and the rate of roll is adjusted such that, when inverted, the wings will be level. Afterwards, the roll maneuver is continued and a nose-low, wings level attitude is recovered. The entire maneuver should be accomplished by reference to the attitude indicator.

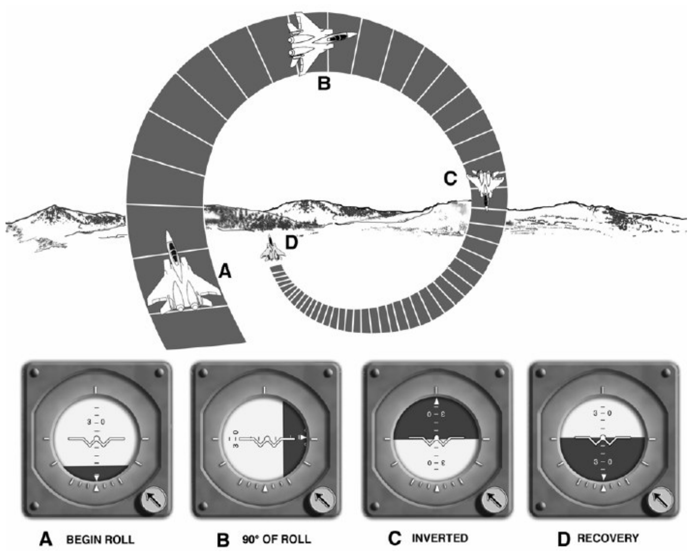

Figure 6. The Aileron Roll Maneuver

1.3. The Fundamentals of Air Combat Maneuvers

The fundamentals of air combat maneuvers depend on some basic definitions [3]. The positional geometry is defined by *angle off, range* and *aspect angle*. They describe the relative positions and the advantage or disadvantage of one aircraft versus another.

Angle off is the difference between the aircraft and the opponent measured in degrees. If the aircraft and the opponent are heading in the same direction then angle off is 0°. Angle off is also known as heading crossing angle (HCA). Range is the distance between the aircraft and the opponent. This can be displayed in feet or miles. Most modern military aircraft heads up display (HUD) systems read in nautical miles or tenths of miles unless the range is less than one mile from the target. Afterwards, the display will read in feet. Some European aircraft use the SI system in a similar fashion. Aspect angle is the number of degrees, measured from the tail of opponent to the aircraft. It indicates the relative angular position with respect to the opponent's tail. The aspect angle can remain the same regardless of the angle off. Aspect angle is determined from the tail of the opposing aircraft. If the aircraft is are on the right side of the opponent it means the right aspect, or, if the aircraft is on the left side it means the left aspect. The aspect angle is very important in assisting in determining the position of the aircraft with respect to the opponent. By using the aspect angle and range the lateral displacement or the *turning room* available can be determined.

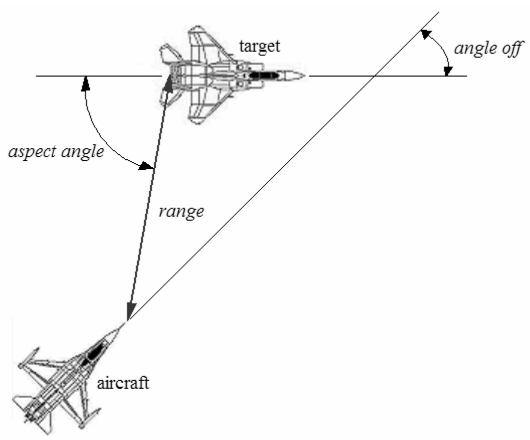

Figure 7. The Definitions of the Angle Off, Range and Aspect Angle

The attack geometry describes the aircraft's flight path to its target. If the aircraft is pointing behind the target, then the aircraft is in *lag pursuit*. If the aircraft's nose is on the target, then the aircraft is in *pure pursuit*. And if the nose of the aircraft is pointing in front of the target, then it is called *lead pursuit*.

Lag pursuit is primarily used for approaching the target. It can also be used when the opponent pulls out of plane; that is, when the opponent pulls out of the same plane of flight or motion as the attacking aircraft. In a lag pursuit, it is very important to be able to pull the aircraft's nose out of lag to shoot guns or a missile. If the target at least matches the similar turn rate of the aircraft, it can be able to keep the follower aircraft in lag and prevent it from getting a shot. In pure pursuit the aircraft's nose is kept on the target and the aircraft flies straight to it. The pure pursuit is used whenever the aircraft is ready to shoot the target. It is especially used for missile shots. The lead pursuit is the short-cut to the target. It is helpful to close on the target and get into weapons parameters. This is also the most commonly used pursuit for gun shots. The lead pursuit should not be established earlier than gaining much higher turn rate than the opponent, that the target can be over-shot.

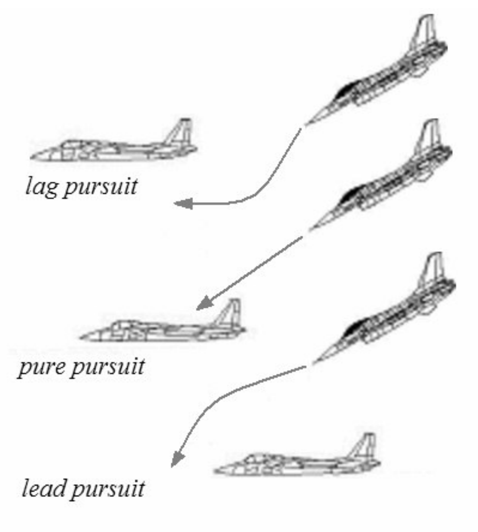

Figure 8. The Lag, Pure and Lead Pursuit

It is very important to determine the pursuit course. There are two positions that the opponent can be in, *in-plane* or *out-of-plane*.

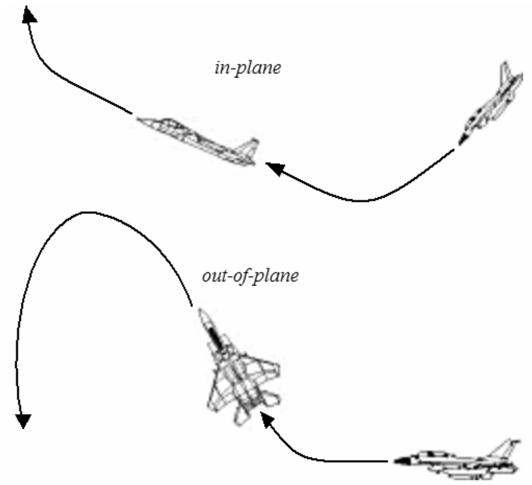

Figure 9. The In-plane and Out-of-plane Positions

In-plane is the position where the attacker and the defender are both in the same plane of motion. If the opponent is in-plane with the aircraft, the HUD *velocity vector* will determine the pursuit course. The figure below shows an example of a *flight path marker* in a HUD displaying the velocity vector.

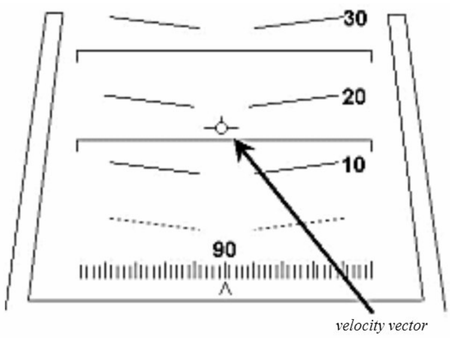

Figure 10. The Flight Path Marker in HUD

The velocity vector is the travel direction of the aircraft and it is indicated by the flight path marker on the HUD. If the defender and attacker are not in the same plane of motion, then it is called the out-of-plane position. To determine the pursuit course during the out-of-plane maneuvers the *lift vector* is used. The lift vector is a vector pointing out of the top of the aircraft. The lift vector is positioned by rolling the aircraft so that the lift vector points in the desired direction of travel and the nose of the aircraft will track towards the lift vector.

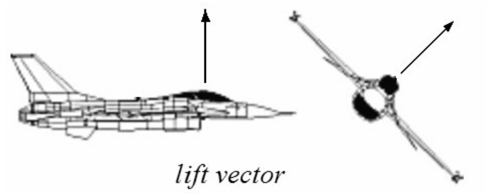

Figure 11. The Lift Vector

The *weapons envelope* is the area in which a particular weapon is effective. It takes into account the weapons maximum and minimum ranges, weapons capabilities, aspect angle, speed, angle off, the relative headings. The following figure is an example of a weapons envelope when the target is flying straight and level.

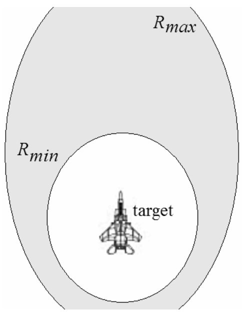

Figure 12. The Weapons Envelope of an All Aspect Missile

Here, R_{max} is the maximum effective range and R_{min} is the minimum effective range of a particular weapon. The effective operating range to the front of the opponent is much larger than the rear area. Obviously, if the aircraft is shooting the target head-on, it is moving towards the aircraft as the weapon moves towards it. However, a rear aspect shot forces the weapon to *chase down* the target. If the missile is release too soon, it will burn out the motor before even coming close to the target.

The shape of the weapons envelope will change as the target starts to maneuver and pull g's. The weapons envelope will deform and may grow in one area while almost completely disappearing in another. The target will eventually attempt to put the less effective portion of the weapons envelope towards the attack aircraft. Most missiles will generally have similar weapons envelopes but the R_{min} and R_{max} values will differ.

1.3.1. Basic Air Combat (Fighter) Maneuvers

In order to define the air combat maneuvers of fighter aircraft, generally the phrase *Basic Fighter Maneuvers* (*BFM*) is used. BFM is known as the art of exchanging energy for the aircraft position. Here, the word energy is used as a synonym for the fighter speed and altitude. The goals of offensive maneuvering are to remain behind an adversary and to get in a position to shoot the weapons. In defensive maneuvering the aircraft turns and move the opponent out of position for shot the defensive aircraft. In head-on maneuvering the aircraft gets behind the opponent from a neutral position. During these maneuvers there is a huge amount of energy is expended. Pulling g's and turning cause all aircraft to slow down or lose altitude (or both). Here, the geometry of the flight and the specific maneuvers needed to be successful in air-to-air combat are described.

The offensive BFM must be performed when the opponent turns towards the offensive aircraft and creates aspect, angle-off, and range problems. In the next coming parts the methods for going through the basic BFM steps (observe, predict, maneuver and react) are discussed.

Offensive BFM is necessary since an opponent will turn his jet at high g's. To solve the BFM problems created by this turn the offensive aircraft should execute a turn with the objective of flying to the *elbow*. The key to offensive BFM is knowing when and how to execute this turn. If the offensive aircraft is behind the opponent the first action is to decide to execute a shot. If shooting is not possible (since the opponent will most probably execute a hard turn towards the offensive aircraft) flying to the elbow is necessary. In the *elbow turn* whenever the turn direction of the opponent is observed a prediction of its movement should be made and a turn in the same direction should be started. For example, if the opponent moves to the right (seen in the head up display (HUD) or threat indicator) then the offensive aircraft should turn right.

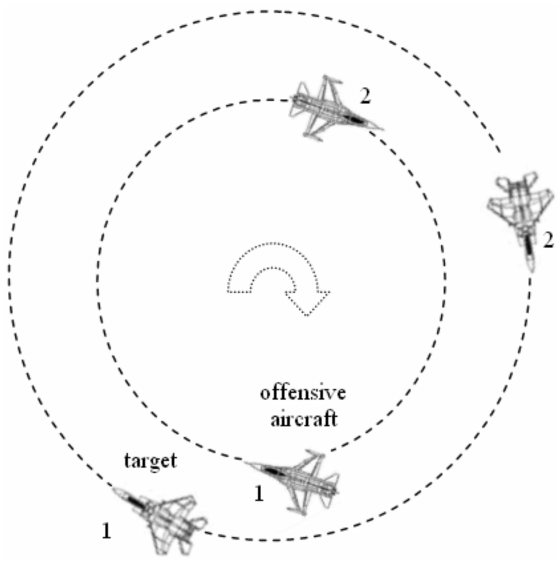

Figure 13. The Offensive BFM, Flying to the Elbow

During the elbow turn, it should be continuously noted that, if the opponent keeps turning at its present rate, will it be possible to point its nose to the offensive aircraft? In order to avoid this situation the offensive aircraft should fly inside the opponent's turn circle. If the offensive aircraft is outside the opponent’s turn circle, then it can always point its nose towards the offensive aircraft and force a head-on pass. In order to get to the elbow of the opponent both the attitude and speed of the offensive aircraft should be adjusted throughout the whole maneuver. This means that the pilot should not only move the stick but also the throttle.

In the defensive BFM, the geometry of the fight is very simple and the maneuvers are equally straightforward. However, they are executed under pressure and at very high g’s. Thus, the defensive maneuvers require patience, stamina and optimism.

It is very important to create BFM problems for the opponent and perform a steep defensive turn. In defensive maneuvers it is useful to engage the countermeasures like chaff, flares and etc. When the opponent is on the backwards of the defensive aircraft, the defensive maneuver turn direction is important. If the opponent is on the right-back side, the defensive aircraft should turn right and visa versa. The turn should be executed approximately at 80° or 90° roll angle at maximum possible g’s.

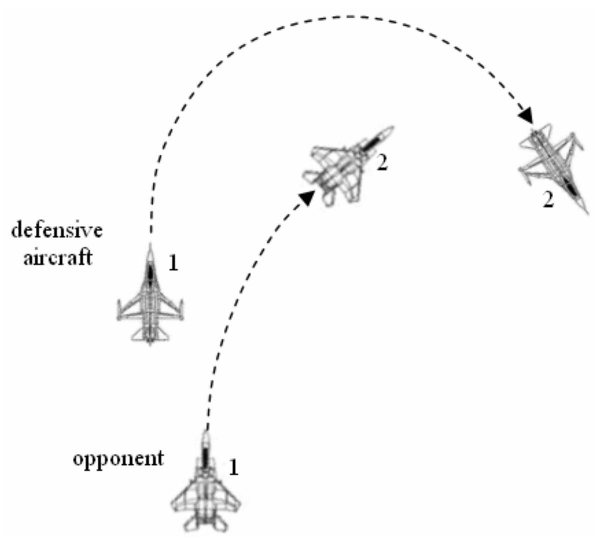

Figure 14. The Defensive BFM

The head-on BFM is flown after a head-on pass to the opponent. At this stage it is possible to keep going away from the opponent or turn and make offensive maneuvers. Head-on BFM is very easy to execute, but, somehow difficult to convert it into an offensive one. It should always be watched to take the right time to execute a hard turn towards the opponent in the vertical and horizontal planes of motion.

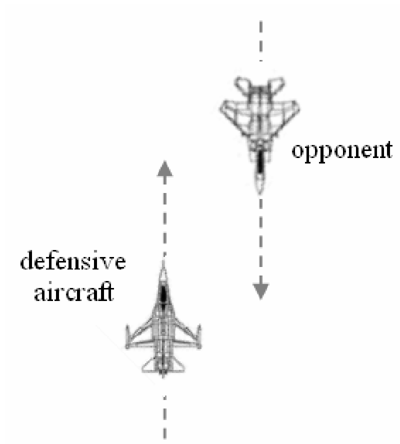

Figure 15. The Head-on BFM

1.3.2. Basic Air Combat Tactics

Air combat tactics (ACT) are used when more than two aircraft engage. All ACT is built on BFM tactics; the bottom-line in ACT is always to use the best one-vs.-one tactics first before considering the other aircraft in the fight. For example, if an attack decision is made best one-vs.-one offensive BFM should be implemented regardless of how many other opponents are in the area. The crucial part here is to make the decision to engage and decide how long to stay in a turning fight. The offensive BFM may require only a few degrees turn to possess the opponent. The ACT is an extension of a single ship BFM involving tactical decision.

One-versus-many: Single ship combat against multiple enemy aircraft is one of the most challenging air-to-air engagements a fighter pilot will ever face. One-versus-many tactics are difficult to execute but straightforward conceptually.

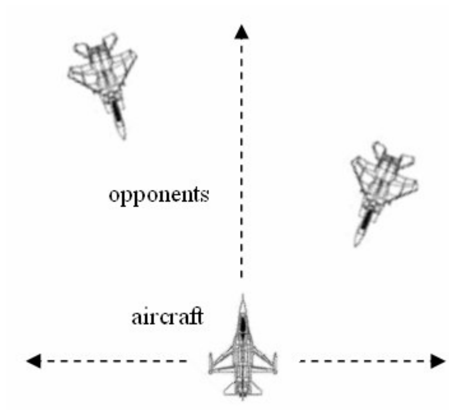

Figure 16. One-vs.-many Engagement

If the opponent aircraft are all out in front of the offensive aircraft, then the offensive one is in one-vs.-many situation. Keeping the opponents out in front is the difficult part. It is important to shoot as soon as possible at the nearest opponent and then maneuver to stay in control of the fight. If the offensive aircraft shoot a missile at the nearest opponent and hit it, then the opponents change their mind from attack to survive immediately. If the shot is missed, then the maneuvering is even more critical because the opponents are more eager to fight. A rule of thumb for maintaining control of the fight is to keep the opponents on one side of the offensive aircraft. This makes it much easier to keep the opponents in sight and makes it harder to make squeezing maneuvers. In addition, it is also necessary to keep all of the opponents either above or below in altitude to make it easier to keep track of them. If there are more than two opponents in a fight and the first shoot is missed before they all see the offensive aircraft, the only solution is to separate from the fight. This is done in a way such that the offensive aircraft passes the opponents as close as possible at 180° heading crossing angle at the maximum possible speed.

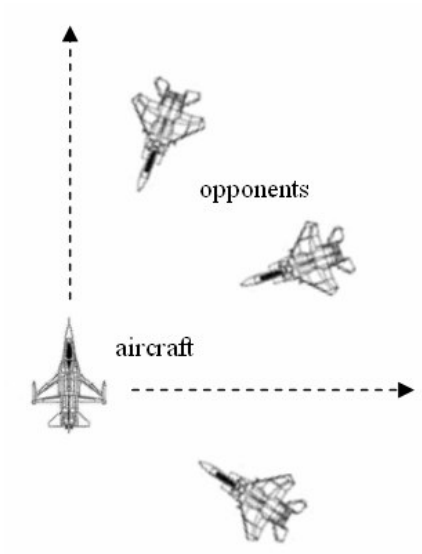

Figure 17. One-vs.-many Separation

A rule-of-thumb is that if the offensive aircraft is single (without the wingmen) and there are more than two opponents, then it should never turn more than 90° to get a shot and let the airspeed reach below 400 knots. After 90° of turn (or when 400 knots airspeed is being reached), the decision for separating from the fight should be made. Separating from fights is a critical fighter pilot's skill.

Two-versus-many: Two-vs.-many fights are conceptually very similar to one-vs.-many engagements. The difference is that the wingman can give several additional options than a single ship. The presence of a wingman does not mean abandoning the principles of one-vs.-many air combat. The wingman could be blown up or engaged by a surface to air missile (SAM), thus, always fighting with the best one-vs.-one BFM and following the rules for one-vs.-many is crucial. The biggest advantage of having a wingman is to stay in a turning fight longer than one-vs.-many to achieve a shot.

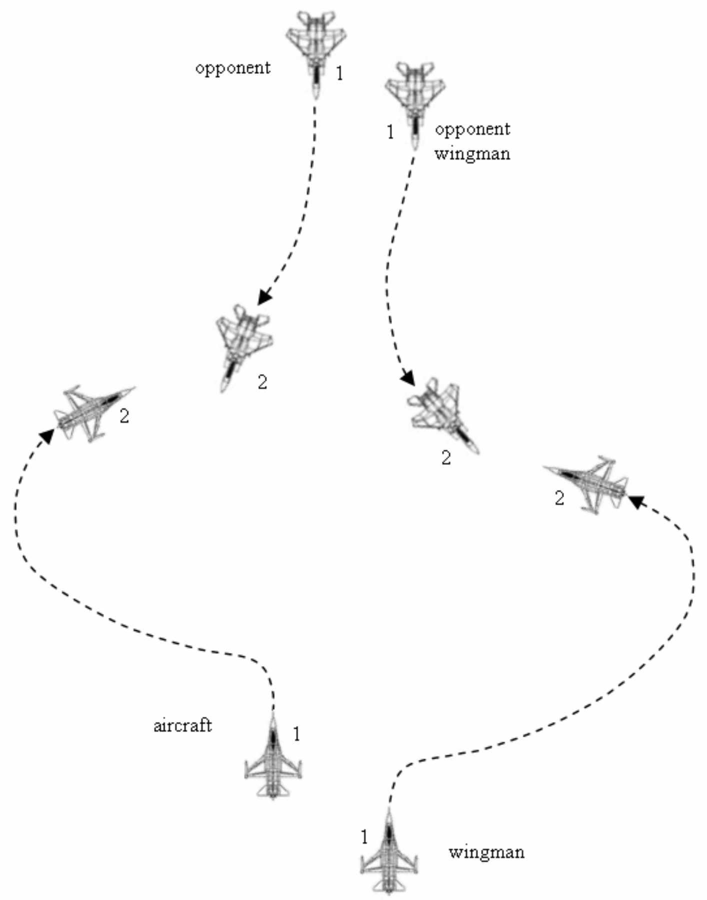

Figure 18. Two-vs.-many Engagement

1.4. High Angle of Attack Aerodynamics

Most of the basic maneuvers of air-superiority fighters are executed at high angle of attack values. This is generally necessary to perform successful maneuvers. Hence, in this section high angle of attack aerodynamics will be discussed in brief.

High angle of attack aerodynamics is inherently associated with separated flows and nonlinear aerodynamics [4]. One of the key aspects is the interaction of components, and in particular, the vortex flows. Studies on high angle of attack aerodynamics are heavily dependent on wind tunnel testing and connected with flight simulation to ensure good handling qualities. This means that large amounts of data should be acquired to construct the mathematical aerodynamic model. The detailed tutorials and surveys on high angle of attack aerodynamics can be found in references [5] and [6].

Typical high angle of attack concerns for general aviation aircraft are the prevention or recovery from spins. To improve the spin resistance the drooped outer panel (NASA LaRC) or the interrupted leading edge (NASA Ames) and placing the vertical tail where it can encounter the effective flow during a spin are proposed. Also, placing a ventral strake ahead of the rudder not only adds side area, but also produces a vortex at sideslip that helps maintaining the entire surface effectiveness.

The transport aircraft also encounter high angle of attack flight regime. Here, the primary high angle of attack problem is the suppression and control of pitch-up and avoidance of deep stall. The case study of the DC-9 development provides an excellent overview of the issues with the T-tail configuration and the stall issues in general.

High angle of attack aerodynamics is mostly more important for fighters. Resistance to departure from controlled flight, ability to control the aircraft at high angle of attack air combat maneuvers and allowance for unlimited angle of attack range is the major concerns that a super-maneuverable fighter should have. There are certain requirements for fighters that they should be able to perform *velocity vector rolls*, perform the so called *Cobra* and *Herbst maneuver* and do *nose pointing maneuver* to allow missile lock-on and fire. Most fighter concepts, *F-18 HARV*, *X-31*, *X-29*, *F16 MATV* gave great importance on thrust vectoring to enhance the controls. Super-maneuverability and aircraft agility still are of current interest. This requires the use of dynamic measures to assess the performance.

From Figure 19 to Figure 22, the typical examples of aerodynamic coefficients; C_L and C_m, $C_{n\beta}$ and $C_{l\beta}$, as a function of angle of attack, for different fighter aircraft are shown. It is important to figure out that after a certain value of angle of attack the parameters decreases gradually and changes their signs. That causes weak spin resistances, roll reversals and departures.

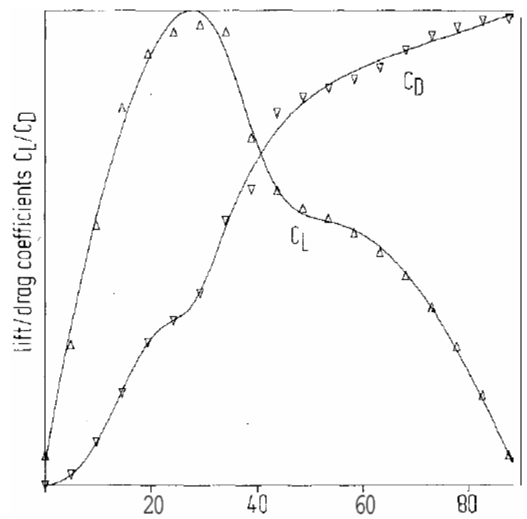

Figure 19. Lift and Drag Coefficients for a High Alpha Fighter Aircraft [7]

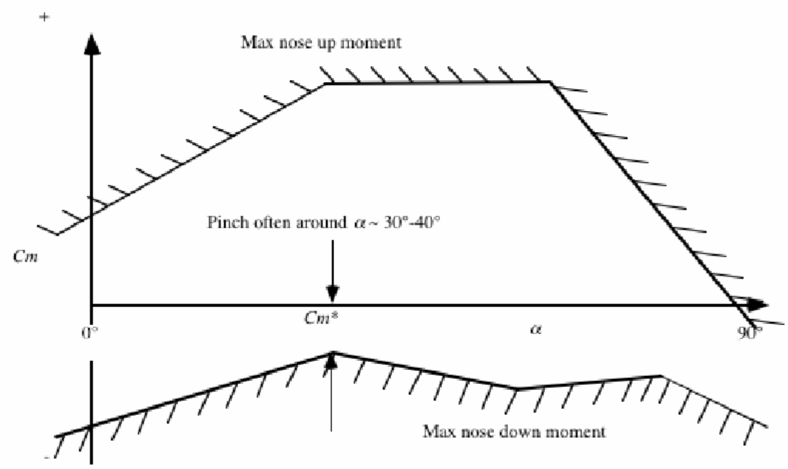

Figure 20. Typical Example of Pitching Moment Assessment Chart [4]

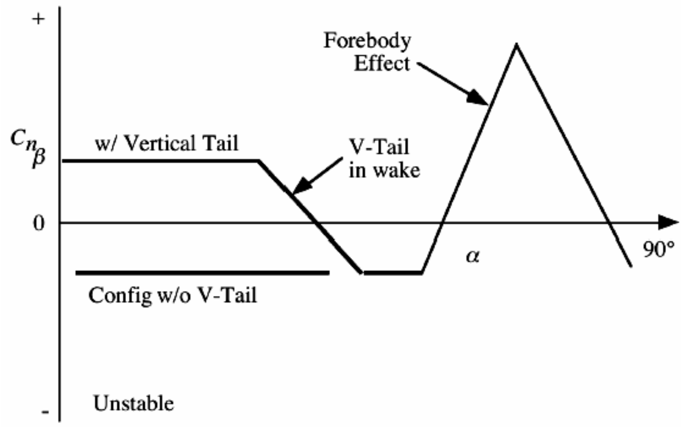

Figure 21. Generic Directional Aerodynamic Characteristics [4]

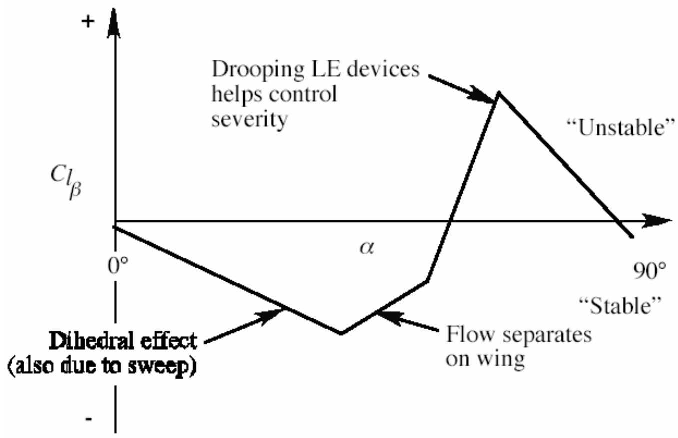

Figure 22. Generic Lateral Aerodynamic Characteristics [4]

Controllability of flight at high angle of attack can encounter several different types of problems. They are generally categorized as *departure*, *wing drop*, *wing rock* and *nose slice*. Departure occurs when the airplane departs from the controlled flight. It may develop into a spin. Wing drop is caused by asymmetric wing stall. It is considered as a roll-type problem. As for the wing rock case the aerodynamic rate-damping moments become negative and the wing starts to oscillate in roll. This is associated with an interaction of the separated flow above the wing, typically the leading edge vortices that are above the wing. Nose slice is the case when the aerodynamic yaw moments exceed the control authority of the rudder. Hence, the airplane will tend to exceed the acceptable sideslip angle and depart through a yawing motion. It is considered as a yaw-type problem. These basic aerodynamic characteristics are often used to try to assess how susceptible the aircraft to departure. In reality, the dynamic aerodynamic characteristics are also important to predict the resistance of the aircraft to departure.

In the literature some static derivative based dynamic criteria are available to provide guidance. The reference [8] provided a summary of directional data for numerous aircraft and the description of the departure problem related to the piston fighters to high speed jet fighters.

The spin is another important issue. Basically, it depends on the mechanical inertial properties of the aircraft. For example, if the difference $I_x - I_y$ (the rotational inertia components of the aircraft in the body forward and sideward direction) is positive the plane is said to be wing heavy. Or, if it is negative the plane is said to be fuselage heavy (typically modern supersonic fighters). If an aircraft is wing heavy in order to recover from a spin the ailerons should be applied against the spin and the elevator should be retracted downwards. If the aircraft is fuselage heavy only the ailerons should be applied with the spin [9].

On the other hand, the control effectiveness tends to diminish as the angle of attack increases. This is especially true for the ability to generate the yawing moment. The following figure shows the reduction in control forces with angle of attack for *F-16* wind tunnel test [10]. The thrust vectoring can also play an important role in providing control power at high angles of attack. This also means that the thrust must be provided so as to create a moment arm.

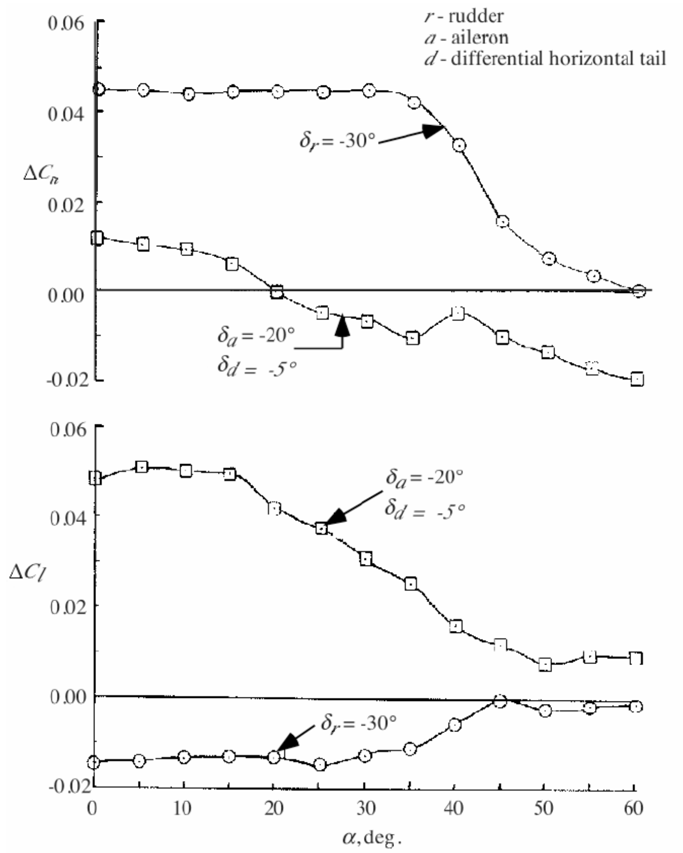

Figure 23. Loss of Control Effectiveness as AoA Increases for F-16 [4]

1.5. High Angle of Attack Maneuvering Control

The fighter aircraft before 70's exhibited poor stability characteristics at high angles of attack. The maneuvering was often limited by the air-flow departure boundaries, and stall and spin accidents were a major cause of loss of aircraft and pilots [11]. With the emergence of close combat scenarios, it became very important to make certain critical maneuvers rapidly such as evasion, pursuit, and nose pointing to obtain the first opportunity of firing the weapons. Thus, the demand for increased agility and maneuvering led to the necessity of high angle of attack flight. This created the need for the development of the *short take-off and landing* (*STOL*), *very short take-off and landing* (*VSTOL*), agile and super-maneuverable aircraft such as the *Harrier AV-8*, *Yakovlev Yak-141*, *Sukhoi Su-27*, *Sukhoi Su-37*, *F-35B* and *F-22*. These aircraft are shown (from left to right) in the following figure.

Figure 24. Examples of Super-maneuverable Aircraft

On the other hand, the demand for increased agility and maneuvering also led to the development of research programs such as the *X-31A Enhanced Fighter Maneuverability* [12], [13]. *F-16 Multi-Axis Thrust-vectoring* [14], *X-29A vortex flight control system* [15] and *NASA High-Alpha Technology Program* [16].

Figure 25. X-31 VECTOR

Figure 26. F-16 Multi-Axis Thrust-vectoring (MATV)

Figure 27. NASA High-Alpha Research Program Vehicle (HARV)

The conventional aerodynamic control system requirements are typically specified for low angle of attack conditions. Requirements for high angles of attack are posed only for emergency avoidance from uncontrollable flight. However, the latter requirements are hard to meet because the effectiveness of the aerodynamic control surfaces happens to degrade rapidly at high angles of attack.

The control system configurations for fighter aircraft are primarily based on the criterion of achieving the desired translational and angular accelerations especially for rapid maneuvering tasks. The maneuvering requirements in turn depend primarily on the sizes of the aerodynamic control effectors to provide the necessary control forces and moments for the desired accelerations. This suggests unfeasibly large control effectors in the high-α maneuverability case. Therefore, there is an increasing demand for alternative control effectors such as TVC paddles and also for advanced stabilization and control methodologies.

The fighter aircraft are required to perform controlled maneuvers well beyond traditional aircraft limits, such as pitch up to a high angle of attack, rapid point to shoot, and other close combat maneuvers. To perform these fast multi-axis motions, most tactical aircraft need the use of innovative technologies such as TVC. The best aircraft for these extreme flight conditions should combine several disciplines successfully in its design phase, e.g. nonlinear flight mechanics, unsteady aerodynamics, flexible structural modeling, advanced control theory and realistic simulation studies.

There is a great technological interest in the area of super-maneuverability. It induces demands on more sophisticated flight control systems with capabilities such as increased usable lift, thrust-vectoring and insensitivity to unsteady aerodynamic effects.

The idea of super maneuverability is introduced by Dr. W.B. Herbst in 1980. He defined super-maneuverability as the capability to execute maneuvers with controlled sideslip at angles of attack well beyond those for maximum lift, i.e. the capability of post-stall maneuvering. Post-stall maneuvering is flying at very high angles of attack up to 70° or even 90° for short periods of time. Thus, fighters make drastic changes in direction within extremely short distances and times. A super-maneuverable fighter aircraft can turn faster than a conventional aircraft and dissipate less energy in the process. It can have the adversary aircraft in the field of view of its weapon system earlier than the conventionally controlled aircraft. To make post-stall maneuvering the aircraft has to be controllable at very high angles of attack. At high angles of attack the aerodynamic control surfaces lose their effectiveness, the airspeed often becomes quite low, and the vortices in the wake of the stalled wing have a drastic adverse effect on the vertical and horizontal tail surfaces. Therefore, the aerodynamic control surfaces such as rudders and elevators should be accompanied by other controlling techniques such as vectoring the engine thrust.

Currently, some modern fighter aircraft are capable of performing transient maneuvers involving high angular velocities at extreme angles of attack. Typical examples for such maneuvers are the so-called Cobra and Herbst (J-Turn) maneuvers. The advances on high angle of attack control effectors such as thrust-vectoring, side jets and passive and active aerodynamic control surfaces with different shapes provide greater capability to have an effectively enlarged maneuvering envelope for air combat.

During rapid high angle of attack maneuvers unsteady aerodynamics effects, which have a crucial impact on the aircraft flight dynamics including stability and control, are extremely important. Since, the aircraft is operating in highly nonlinear flow regimes with substantial angular rates the prediction of departures from stall safe flight and related complex dynamics should receive increased attention. Several studies exist on this area including development of guidelines for preliminary design [17], improved testing techniques [18], improved analysis techniques (e.g. prediction of falling leaf motions) [19] and simulation-based predictive capabilities [20].

As explained before, a critical tactical measure in an air combat is the target aspect angle. If the target aspect angle is 0°, then the target aircraft is pointed directly at the attacker. If the target aspect angle is 180°, then the attacker is on target's tail. Tactical advantage in close air combat can be measured as the difference between the target aspect angle and the attack aircraft's aspect angle. The most desirable condition for the attacker is to point directly at the target while the target is pointed directly away from the attacker.

An important technological aspect of many modern fighter aircraft is the use of *post-stall technology* (PST). It refers to systems such as the thrust vectoring and advanced flight controls that enable the pilot to fly at extremely high angles of attack, well beyond the normal stall limits of the conventional aircraft. Using PST flight modes pilots have developed an entirely new class of combat maneuvers that include the Cobra and Herbst maneuvers explained before.

In the Cobra maneuver the aircraft makes a very quick pitch-up maneuver from horizontal position to past vertical (even 120° sometimes). The airspeed of the aircraft slows dramatically as the plane continues its horizontal travel. The pilot then uses the thrust vectoring to help pitch the aircraft's nose down and recover the normal flight angles. This allows the aircraft to rapidly strip airspeed causing a pursuing fighter to overshoot.

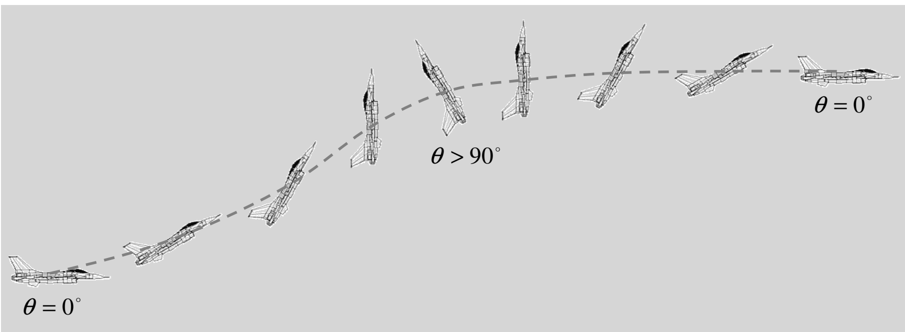

Figure 28. The Cobra Maneuver

The Herbst maneuver is one of the well known PST maneuvers. In that maneuver the aircraft quickly reverses direction through a combination of high angle of attack and rolling. It is named after W.B. Herbst who is one of the original developers of PST.

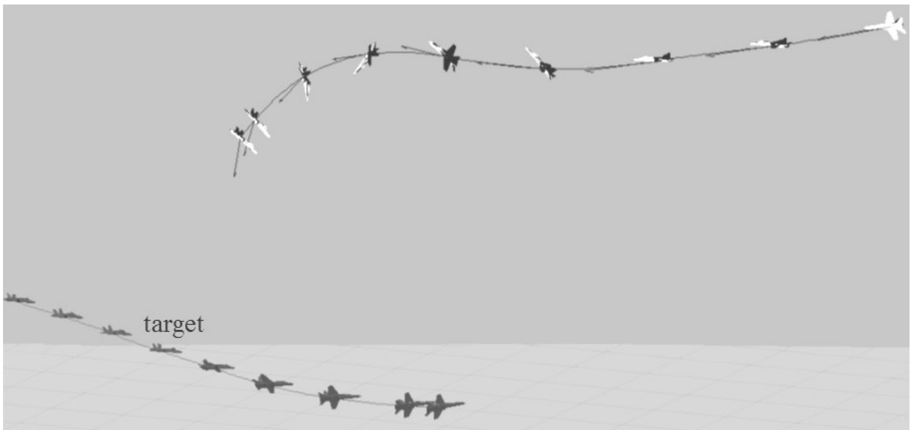

Figure 29. The Herbst (J-Turn) Maneuver

The *helicopter gun attack* or the *offensive spiral* maneuver is another PST maneuver. The following figure shows a flight reconstruction of that maneuvers where the offensive aircraft acquired the target at the end of a high alpha reversal and continued to track the target at approximately 50° angle of attack. The offensive aircraft stays essentially at the center of the loaded turn being flown by the target. Although the offensive aircraft began the maneuver with an altitude advantage the aircraft is actually below the target by the end of the maneuver. This maneuver illustrates the significant energy loss associated with sustained high angle of attack maneuvering.

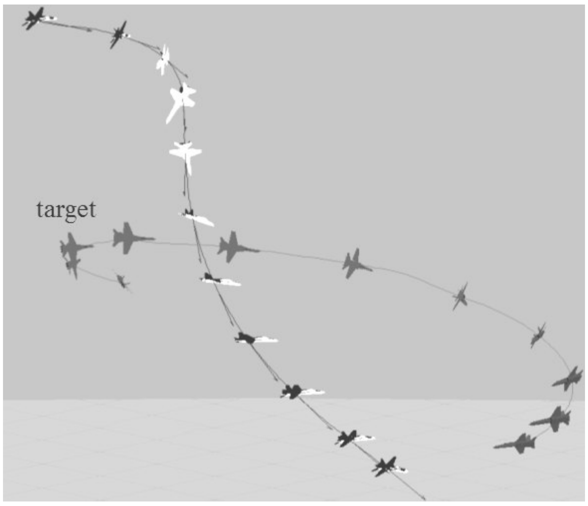

Figure 30. The Offensive Spiral Maneuver

High angle of attack flight maneuvers primarily address the significance of high confidence prediction of aircraft dynamics together with modeling and simulation as well as reliable advanced control effectors driven by sophisticated control algorithms to compensate for the loss of airframe stability.

The first step in any aircraft control law design is to determine the required forces and moments that can be realized given the limitations of the control effectors. This can be done conveniently by using the nonlinear dynamic inversion (NDI) approach [21], [22], [23]. This approach depends primarily on the direct manipulation of the equations of motion to generate control laws yielding desired responses for the achievement of the desired maneuver. The controlled outputs are generally taken as the angular body rates but the angle of attack and the side slip angle are also carefully monitored.

NDI is a widely used nonlinear control method, popular in mechanical system design, robotics and vehicle control. Different names are being used for this method such as computed torque or force method, feedback linearization, etc. However, they all mean the same mathematical approach. The theoretical background on this approach is extensively investigated in different control system design books [24].

NDI is also used extensively in designing flight control systems [25], [26], [27], [28]. This controller design technique uses the information about the nonlinear dynamics of the aircraft. The resulting nonlinear controller is valid for the whole flight envelope and therefore there is no need to apply any gain scheduling technique. Other important features of this design technique can be stated as the decoupling of the longitudinal dynamics from the lateral dynamics even at a high-α flight [29], the consequent facility of independent assignment of closed-loop dynamics for each output channel [30] and the simplicity in designing the controllers for the decoupled output channels.

The central idea of dynamic inversion is based on linearizing the dynamics by using appropriate nonlinear terms in the feedback inputs to the system. This approach algebraically transforms a nonlinear system dynamics into a linear one so that linear control techniques can be applied. This is different from the conventional linearization based on the Jacobian approach. In feedback linearization, an exact state transformation is considered, which is based on transforming the original system model into an equivalent model of a simpler linear form.

The nonlinear dynamic inversion is actually a special case of the *model following technique* [31]. Similar to other model following controllers, an NDI controller requires exact knowledge of the system dynamics to achieve a satisfactory performance. Therefore, robustness has a significant role during the design process. In the presence of parameter uncertainty and/or un-modeled dynamics, the robustness of the system may not be guaranteed. The un-modeled dynamics is very important, because the exact model of the system is never available in practice. Moreover, the sensitivity to modeling errors may be particularly severe when the linearizing transformation happens to be poorly conditioned.

1.5.1. Dynamic Inverse Controller Design

In this section dynamic inversion (DI) approach will be explained with an application to a simple aircraft control problem. A dynamic inversion controller can be designed in many different ways. First of all, depending on the nature of the plant to be controlled, the controller might be in either linear or nonlinear form. Also, a DI controller is not limited to a first order inversion; it can take on higher order forms as well. First, a brief outline of the dynamic inversion process is given to review the concept. Eventually, the dynamic inversion design process and different forms of desired dynamics are introduced.

In general, the aircraft dynamics are expressed by

$$\dot{\bar{x}} = \bar{f}(\bar{x}) + \hat{B}(\bar{x})\bar{u} \tag{1.1}$$

$$\bar{y} = \bar{h}(\bar{x}) \tag{1.2}$$

Here, $\bar{x} \in \Re^n$ is the state vector, $\bar{u} \in \Re^m$ is the control vector, $\bar{y} \in \Re^m$ is the output vector, m < n, $\bar{f}(\bar{x})$, $\hat{B}(\bar{x})$, and $\bar{h}(\bar{x})$ are nonlinear state-dependent functions.

If we assume $\hat{B}(\bar{x})$ is invertible for all values of $\bar{x}$, the control law is obtained by subtracting $\bar{f}(\bar{x})$ from $\dot{\bar{x}}$ and then multiplying by $\hat{B}^{-1}(\bar{x})$:

$$\bar{u} = \hat{B}^{-1}(\bar{x})(\dot{\bar{x}} - \bar{f}(\bar{x})) \tag{1.3}$$

The next step is to command the aircraft to specified states. Instead of specifying the desired states directly, we specify the rate of the desired states $\dot{\bar{x}}$. By swapping $\dot{\bar{x}}$ in the previous equation to $\dot{\bar{x}}_c$ (commanded state values), we get the final form of a dynamic inversion control law:

$$\bar{u}_c = \hat{B}^{-1}(\bar{x})(\dot{\bar{x}}_c - \bar{f}(\bar{x})) \tag{1.4}$$

The following figure shows the block diagram representation of the DI process.

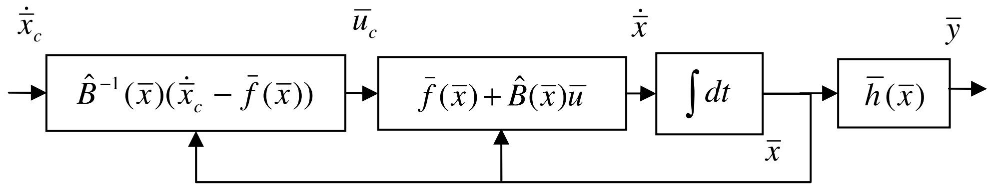

Figure 31. The DI Process

Even though the basic dynamic inversion process is simple there are some points to be emphasized. First, we assume that $\hat{B}(\bar{x})$ is invertible for all values of $\bar{x}$. However, this assumption is not always true. For example, $\hat{B}(\bar{x})$ is not generally invertible if there are more states than there are controls. Furthermore, even if $\hat{B}(\bar{x})$ is invertible (but small), the control inputs ($\bar{u}_c$) may become large and this growth can lead to actuator saturation. The dynamics of the actuators in the feed-forward loop and the dynamics of the sensors and the sensor noise in the feedback loop are neglected during this controller development process.

Dynamic inversion is also essentially a special case of model-following. Similar to other model-following controllers the DI controller requires exact knowledge of the model dynamics to achieve a good performance. Therefore, robustness issues play a significant role during the design process and this issue is discussed in detail in Chapter 4. In order to overcome these difficulties a DI controller is generally used as an inner loop controller in combination with an outer loop controller designed using robust control design techniques. The closed loop transfer function for a desired control variable being inverted is found according to the following block diagram. Here, it is observed that the desired dynamics operate on the error between the commanded states and their feedback term. [32].

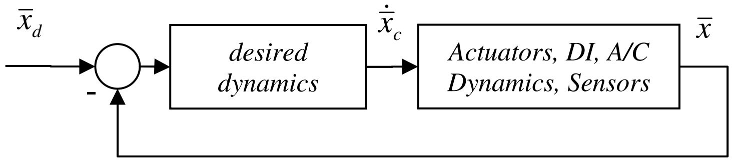

Figure 32. Block Diagram to Calculate the Closed-loop Transfer Function

1.5.1.1. 2-Time Scale Method

In order to by-pass a singularity problem in the inversion of an ineffective control matrix $\hat{B}(\bar{x})$ a 2-time scale method was developed and found to be quite successful in solving such a problem [43]. This approach is especially useful when inverting the motion variables, such as angle of attack, side slip angle, roll, pitch and yaw angles. In the aircraft control literature, since the control effectiveness on the dynamics of these variables is quite low, they are counted for the slow dynamics variables. On the other hand, the control effectiveness on the body angular rate components (p, q, r) is high, therefore, they are considered as the fast dynamics variables. The 2-time scale method formulates a set of two separate and cascaded differential equations:

$$\dot{\bar{x}}_1 = \bar{f}_1(\bar{x}_1) + \hat{B}_1(\bar{x}_1)\bar{x}_2 \tag{1.5}$$

$$\dot{\bar{x}}_2 = \bar{f}_2(\bar{x}_1, \bar{x}_2) + \hat{B}_2(\bar{x}_1, \bar{x}_2)\bar{u} \tag{1.6}$$

In this approach, first, the commanded value of the time rate of change of $\bar{x}_1$ ($\dot{\bar{x}}_{1c}$) is calculated. This is shown in *s*-domain as:

$$s\bar{X}_{1c}(s) = \hat{G}_1(s)\left[\bar{X}_{1d}(s) - \bar{X}_1(s)\right] \tag{1.7}$$

Here, $\bar{X}_{1c}(s)$, $\bar{X}_{1d}(s)$ and $\bar{X}_1(s)$ are the Laplace transforms of the signals $\bar{x}_{1c}(t)$, $\bar{x}_{1d}(t)$ and $\bar{x}_1(t)$ respectively. Then, $\dot{\bar{x}}_{1c}$ is used to calculate the commanded value of $\bar{x}_2$ ($\bar{x}_{2c}$):

$$\bar{x}_{2c} = \hat{B}_1^{-1}(\bar{x}_1)\left[\dot{\bar{x}}_{1c} - \bar{f}_1(\bar{x}_1)\right] \tag{1.8}$$

Afterwards, the commanded value of the time rate of change of $\bar{x}_2$ ($\dot{\bar{x}}_{2c}$) is calculated. This is shown in *s*-domain as:

$$s\bar{X}_{2c}(s) = \hat{G}_2(s)\left[\bar{X}_{2d}(s) - \bar{X}_2(s)\right] \tag{1.9}$$

Here, $\bar{X}_{2c}(s)$, $\bar{X}_{2d}(s)$ and $\bar{X}_2(s)$ are the Laplace transforms of the signals $\bar{x}_{2c}(t)$, $\bar{x}_{2d}(t)$ and $\bar{x}_2(t)$ respectively. Consequently, $\dot{\bar{x}}_{2c}$ is used to calculate the commanded control deflections ($\bar{u}_c$) which then serve as the input to the inherent dynamics.

$$\bar{u}_c = \hat{B}_2^{-1}(\bar{x}_1, \bar{x}_2)\left[\dot{\bar{x}}_{2c} - \bar{f}_2(\bar{x}_1, \bar{x}_2)\right] \tag{1.10}$$

Here, $\hat{G}_1(s)$ and $\hat{G}_2(s)$ are the controller transfer matrices for the first and second set of differential equations.

1.5.1.2. Simplified Longitudinal Controller Example for an Aircraft

A simplified form of the linear equation for an aircraft's pitch axis is defined by the pitching moment equation [33]:

$$\dot{q} = M_{\alpha}\alpha + M_{q}q + M_{\delta_e}\delta_e \tag{1.11}$$

Here, $M_{\alpha}, M_{q}, M_{\delta_e}$ are the dimensional stability derivatives which define the linear pitching motion characteristics of an aircraft. Also, q is the pitch rate, α is the angle of attack and δ_e is the elevator deflection of the aircraft.

Since M_{δ_e} is a constant for a linear time invariant system the inverse of the control distribution function is always obtained as a constant: $1/M_{\delta_e}$. Now, we need to invert this equation for the elevator deflection angle. This mapping is giving in the following equation:

$$\delta_{ec} = (1/M_{\delta_e})\left[\dot{q}_c - (M_{\alpha}\alpha + M_{q}q)\right] \tag{1.12}$$

Here, α and q are the aircraft longitudinal states which are measured by using the onboard sensors.

In this linear model for the longitudinal motion of the aircraft the nonlinearities and higher order terms in the actual aircraft dynamics are neglected. Therefore, this simple DI controller cannot completely cancel out the real aircraft dynamics and potentially will show degraded controller performance.

Similarly, because of the actuator dynamics $\delta_{ec} \neq \delta_e$ and this is also neglected during this simplification of the control law development. This error is most noticeable when the control surface position and rate exceed their limits which occurs often if the value of M_{δ_e} is too small (in this case δ_{ec} is unbounded). Also, α and q will have some noise and bias due to the sensor processing. This is also neglected in the control law development and will potentially degrade the controller performance as well.

In order to calculate δ_{ec}, $\dot{q}_c$ should be calculated first. Here, it should be noted that $\dot{q}_c$ represents the fast dynamics. Thus, it can be calculated from $sQ_c(s) = G_q(s)[Q_c(s) - Q(s)]$. Here, $Q_c(s)$ and $Q(s)$ are the Laplace transforms of the signals $q_c(t)$ and $q(t)$. Also, $q_c = \dot{\theta}_c$ and it represents the slow dynamics. Consequently, it is calculated from $Q_c(s) = s\theta_c(s) = G_\theta(s)[\theta_d(s) - \theta(s)]$. Here, $\theta_c(s)$ and $\theta(s)$ are the Laplace transforms of the signals $\theta_c(t)$ and $\theta(t)$. The block diagram representation for the 2-time scale simplified longitudinal controller for an aircraft is shown in the following diagram.

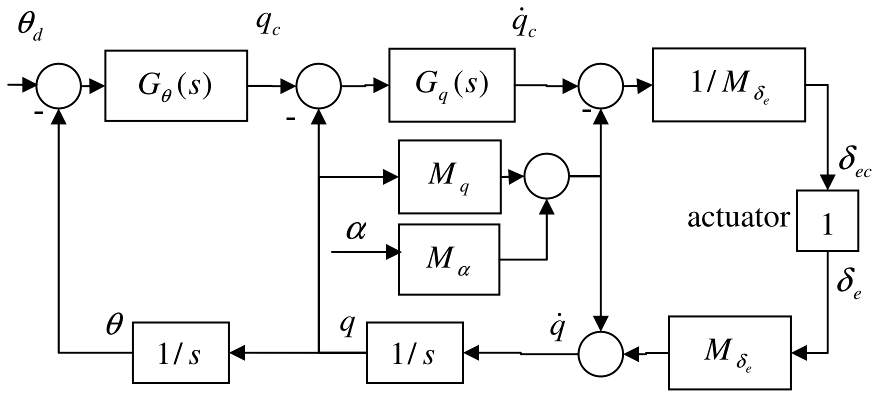

Figure 33. 2-time Scale Simplified Longitudinal Controller for an Aircraft

Here, $G_q(s)$ and $G_\theta(s)$ are the controller transfer functions for $\dot{\theta}$ and $\dot{q}$ dynamics. They are generated from the *desired dynamics* assignment which will be explained in the following section.

1.5.1.3. The Assignment of the Desired Dynamics

The DI control requires the acceleration terms. For example, as equation (1.12) shows, the desired value of pitch angular acceleration ($\dot{q}_c$) is required. However, applications normally utilize either displacements or rates as command states to control the system. The desired dynamics block acts as a mapping function between the rate commands and the desired acceleration terms, which are the required form for the DI equations. The structure of the desired dynamics block is shown in the flow chart depicted in the following figure.

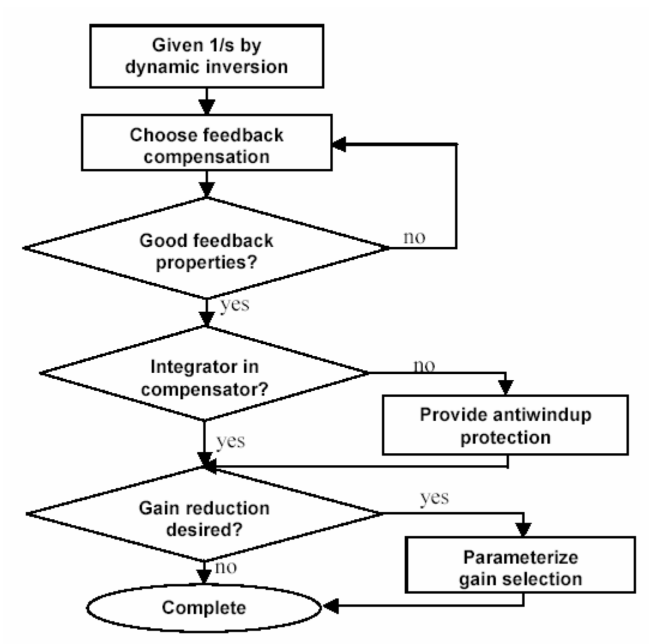

Figure 34. Desired Dynamics Development for Dynamic Inversion [43]

The different forms of the desired dynamics consist of: *Proportional* (*P*) dynamics [34], *Proportional Integral* (*PI*) dynamics [32], *Flying Quality* (*FQ*) dynamics [35], *Ride Quality* (*RQ*) dynamics.

The simplest way of desired dynamics implementation is the proportional or first order case. In this case the desired dynamics are expressed as $\dot{x}_c = k_p(x_d - x)$. Here, k_p sets the bandwidth of the response. The bandwidth must be selected to satisfy time-scale separation assumptions without exciting structural modes or becoming subject to rate limiting of the control actuators. The constant k_p amplifies the error between the control variable command and its feedback term. The closed loop transfer function for the proportional form of desired dynamics places a single pole at $s = -k_p$:

$$\frac{x(s)}{x_d(s)} = \frac{k_p}{s + k_p} \tag{1.13}$$

The desired dynamics block is not limited to a first-order component. If the desired dynamics block does not create satisfactory handling qualities using a set of first order equations, then, a higher order system is used. A commonly-used higher order block is PI. This form is particularly popular in DI literature using fighter aircraft examples [26], [32].

In this case, the desired dynamics is expressed as $\dot{x}_c = k_p(x_d - x) + k_i \int^t (x_d - x) d\tau$. Here, k_p and k_i set the bandwidth and damping properties of the response. The PI form of the desired dynamics places complex conjugate pole pairs at $s_{1,2} = -\omega_{nd}\xi_d \pm j\omega_{nd}(1-\xi_d^2)^{1/2}$, where, $k_p = 2\xi_d\omega_{nd}$ and $k_i = \omega_{nd}^2$ for the desired damping ξ_d and natural frequency ω_{nd}. Thus, the closed loop transfer function for the PI form is:

$$\frac{x(s)}{x_d(s)} = \frac{k_p s + k_i}{s^2 + k_p s + k_i} \tag{1.14}$$

The desired dynamics can also be specified in terms of flying quality levels. The Mil-STD-1797A [35] contains the flying quality specifications for different vehicle classes and mission types. Based on this information the proper time domain characteristics corresponding to a desired flying quality level (damping ratio, natural frequency and time constant) can be selected. These characteristics can be used to determine the proper values for the gains and pole locations. The flying qualities desired dynamics is represented by

$$\dot{x}_c(s) = \frac{k_{fq}(s+a)}{s^2+bs+c}\left[x_d(s) - x(s)\right] \tag{1.15}$$

where $b = 2\xi_d \omega_{nd}$ and $c = \omega_{nd}^2 - k_{fq}$ for the desired damping ξ_d and natural frequency ω_{nd}. Both the gain, k_{fq}, and zero location, *a*, are real constant values. Thus, the closed loop transfer function for the flying quality form is:

$$\frac{x(s)}{x_d(s)} = \frac{k_{fq}(s+a)}{s^3+bs^2+(c+k_{fq})s+k_{fq}a} \tag{1.16}$$

The ride qualities forms of desired dynamics that can also be used in dynamic inversion are given as:

$$\dot{x}_c(s) = \frac{k_{rq}}{s+b}\left[x_d(s) - x(s)\right] \tag{1.17}$$

Also, the closed loop transfer function for this set of desired dynamics is:

$$\frac{x(s)}{x_d(s)} = \frac{k_{rq}}{s^2+bs+k_{rq}} \tag{1.18}$$

The above transfer function places complex conjugate pole pairs at $s_{1,2} = -0.5b \pm j0.5(b^2 - 4k_{rq})^{1/2}$.

For highly augmented airplanes the Control Anticipation Parameter (CAP) replaces the longitudinal short period requirements such as damping ratio and natural frequency [35]. The desired longitudinal dynamics are instead designed by selecting a desired damping ratio (ξ_{sp}) and CAP value ($CAP = \omega_{nd}^2 / n_\alpha$). Here, n_α is the specific load factor and ω_{nd} is the desired natural frequency. Once CAP and ξ_{sp} are selected to satisfy a desired flying quality level, then, the desired short period natural frequency can be calculated. The gain and pole locations for the open loop desired dynamics are then assigned from ω_{nd} and ξ_{sp}.

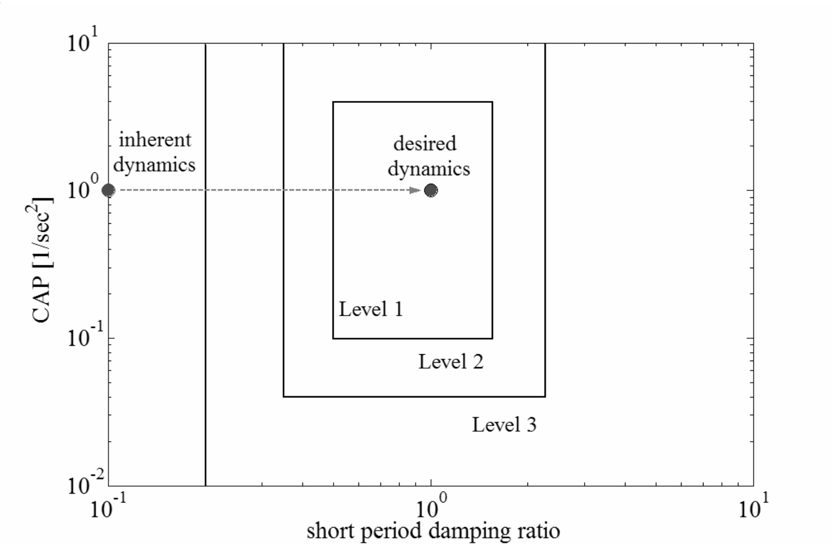

Figure 35. CAP Requirements for the Highly Augmented Vehicles

1.5.1.4. The Basic Issues of Dynamic Inversion

The procedure for the main steps in DI controller design is shown in the following figure.

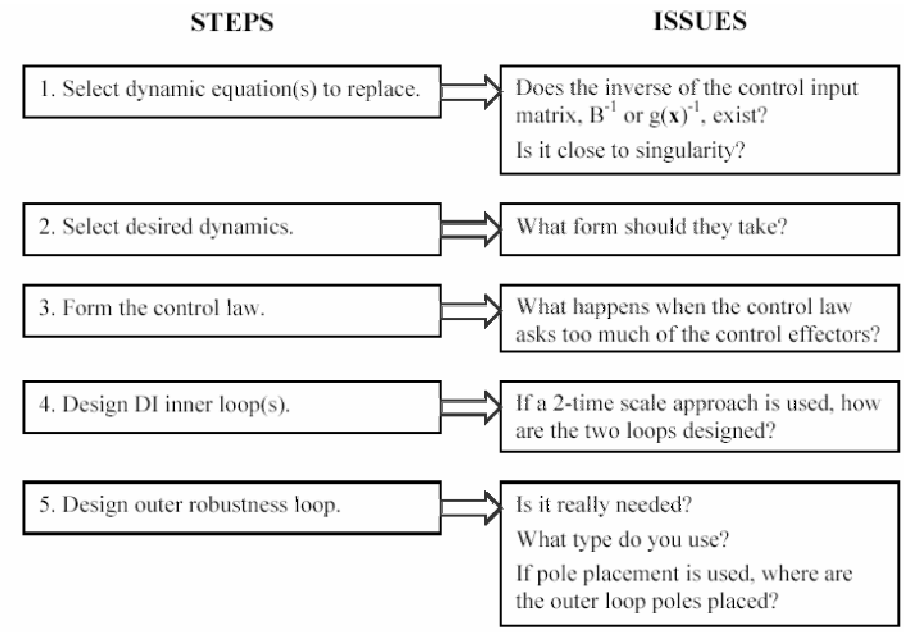

Figure 36. Basic Steps in the DI Controller Design [43]

In addition to the basic steps, some possible solutions or options when using the DI design methodology are summarized in the below paragraphs.

If the inverse of the control input matrix does not exist a 2-time scale method can be used. Also, feedback linearization with higher order is a possibility. There are no limitations on the form the desired dynamics may take. However, some of the common forms found in the literature include proportional, proportional integral and flying qualities.

If redundant control effectors are available a control allocation scheme can be designed in an effort to keep the required control deflections within the constraints of the actuator. Adjustment or replacement of the desired dynamics may also help in reducing the control response.

A robust outer loop is required because dynamic inversion alone does not guarantee robustness. The most popular robust outer loop design methodology for dynamic inversion controllers is *structured singular value* (μ) *synthesis*. Also *linear quadratic regulators* (LQR) have been shown to be effective and are another possibility for robust outer loop design of DI controllers.

1.5.2. Stability and Robustness Analysis

In this section the stability and robustness analysis are described for the DI controller. Also, some definitions on the tools and methodologies used to analyze the stability and robustness of a system will be given. The most commonly used methodology employed to analyze the robustness and performance of linear systems is based on the *structured singular value* (μ) of the system, and, this analysis technique is called as μ-analysis.

The performance specifications are weighted transfer functions that describe magnitude and frequency content of control inputs, exogenous inputs, sensor noise, tracking errors, actuator activity and flying qualities. A family of models consisting of a nominal model plus structured perturbation models is used, with magnitude bounds and frequency content specified using weighted transfer functions. All of this is wrapped into a single standard interconnection structure which is then operated upon by the algorithm.

A control system is robust if it is insensitive to the differences between the actual system and the model of the system which is used to design the DI controller. These differences are generally referred to as the model-plant mismatch or simply the model uncertainty. In order to analyze the controlled system one should quantify the stability and performance characteristics of the system. Hence, the uncertainties on the model should be identified and a mathematical representation of these uncertainties should be set. Then on, the robust stability (RS) of the system should be checked whether the system subjected to uncertainties still remains stable. Finally, the robust performance (RP) is checked whether the desired performance specifications are met under the effect of the uncertainties describing the "worst-case" plant.

The source of the uncertainty in the plant can be the model parameters which are known approximately. The change of the model parameters is due to nonlinearities or operating conditions and the imperfections of the measurement devices. Also, there are cases in which a very detailed model is known, but the controller is designed on a lower order model to ease the controller design work. Another origin of an uncertainty can be the real time realization of the controller. Although the controller is perfectly synthesized, due to implementation capabilities the final controller may differ from the nominal one. These entire model uncertainties can be grouped in two main classes; *parametric* and *unmodelled dynamics* uncertainty.

In the parametric uncertainty the structure of the model and the order of the model are known, however, some of the parameters of the model are uncertain. As for the unmodelled dynamics uncertainty, because of the missing dynamics, the model itself is actually erroneous. The reason for the missing dynamics to exist is generally the wish to omit the nonlinear part of the dynamics or lack of understanding the physical process. There are also cases that the system may contain parametric and unmodelled dynamics uncertainties together. This is defined as the *lumped* uncertainty.

Considering the controller design for flight dynamics, during the linearization process, generally, higher order terms in the aircraft equations of motion are ignored. Also, other uncertainties arise due to aero-elasticity, control surface variations and the air vehicle flexibility. Usually, the plant model is a good system representation term at low to mid frequency inputs. However, the uncertainties become larger with high frequency inputs. Instead of attempting to include all modeling uncertainties they are treated as additives to the plant inputs.

Before defining the basis of robust stability and performance analysis main introductory issues on signals and systems are visited. In the time domain the finite dimensional systems can be represented as sets of ordinary differential equations and signals as functions of time. In case of linear systems, the Laplace transform of both the signals and the systems lead to representation of them as functions of complex variable s. The signals and systems can be classified into spaces based on their properties. The robust control theory mostly deals with the following norms. The H_2 norm of a signal $x(t)$ is defined as

$$\|x(t)\|_2 = \left(\int_{-\infty}^{\infty} |x(t)|^2 \, dt \right)^{1/2} \tag{1.19}$$

On the other hand, the H_∞ norm of a system is the *supremum* of the largest *singular value* of the transfer matrix of the system evaluated on the $j\omega$ axis.

$$\|G\|_\infty = \sup_\omega \bar{\sigma}(G(j\omega)) \tag{1.20}$$

The set of systems which are analytic on the right half plane with a finite H_∞ norm is called the H_∞ space. Thus, H_∞ is defined as the space of stable and proper transfer functions (the transfer functions with a number of zeros less than or equal to the number of poles). Also, minimizing the H_∞ norm, which is actually the objective in RS and RP, corresponds to the minimization of the peak value in the Bode magnitude plot of the transfer function in the SISO or the singular value ($\bar{\sigma}$) plot in the MIMO cases.

Measuring the performance of a system in terms of the H_∞ norm rather than the H_2 norm brings certain advantages in dealing with the uncertainties in the system [36]. By comparison the H_2 norm minimizes the root mean square (RMS) values of the regulated variables when the disturbances are unknown; however, the H_∞ norm minimizes the RMS values of the regulated variables and the disturbances which are at unit intensity.

Define two linear time invariant systems as $\hat{M}$ and $\hat{\Delta}$. The H_∞ norm of these systems satisfies the sub-multiplicative property (which cannot be satisfied by the H_2 norm):

$$\left\|\hat{M}\hat{\Delta}\right\|_{\infty} \leq \left\|\hat{M}\right\|_{\infty}\left\|\hat{\Delta}\right\|_{\infty} \tag{1.21}$$

The small gain theorem [36] states that a feedback loop consisting of some stable subsystems is stable if the loop-gain is less than unity. Using the sub-multiplicative property and the small gain theorem together one can state that a plant $\hat{M}$ is robustly stable to the perturbations $\hat{\Delta}$ that are "pulled-out" from the inherent dynamics of the system. Minimizing the H_{∞} norm of the system $\hat{M}$ means increasing the robustness of the system to the uncertainties defined in the block $\hat{\Delta}$. Returning back to H_2 norm the uncertainties, here, can only be modeled as stochastic processes. However, the H_{∞} norm can deal with the uncertainties modeled as the elements of a bounded set.

The representation of the uncertain model perturbations, in the H_{∞} framework, is done by defining them in a block diagonal matrix:

$$\hat{\Delta} = \mathrm{diag}(\Delta_i) \tag{1.22}$$

Here, each Δ_i represents a specific source of uncertainty. The plant $\hat{M}$ is defined to be composed of the controller $\hat{K}$ and the generalized plant $\hat{P}$. Dealing with $\hat{P}$ and $\hat{K}$ separately is used for robust controller synthesis. Whenever, the controller is already synthesized and the aim is the RP analysis $\hat{M}$ and $\hat{\Delta}$ structure is used. Such structures are called as the *Linear Fractional Transformations* (LFT).

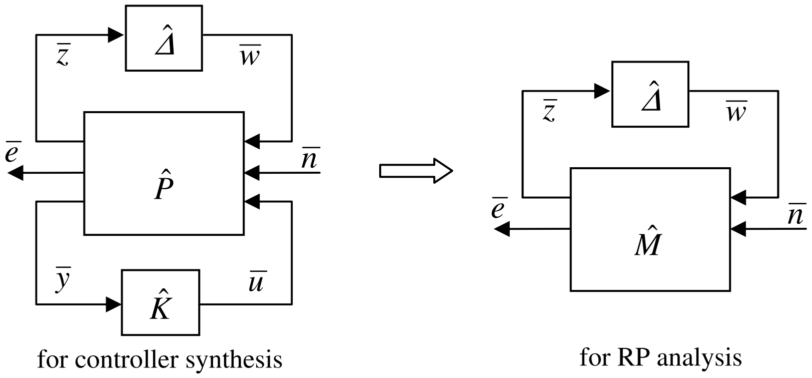

Figure 37. The LFT Block Diagrams

Here, $\bar{n}$ is the noise or disturbance and $\bar{e}$ is the error which is desired to be minimized. The errors can be the errors between the desired command values and the outputs of the system, as well as, the errors between the outputs of the system and the outputs of the desired model plant subjected to the same inputs as the controlled plant. Also, $\bar{w}$ and $\bar{z}$ are the signals between the uncertainties and the system $\hat{P}$ or $\hat{M}$.

In the LFT formulation (for the H_∞ synthesis and analysis framework) $\hat{M}$ is related to $\hat{P}$ and $\hat{K}$ by a lower LFT representation $\hat{F}_l(\hat{P},\hat{K})$ [37]:

$$\hat{M} = \hat{F}_l(\hat{P},\hat{K}) \stackrel{\Delta}{=} \hat{P}_{11} + \hat{P}_{12}\hat{K}(\hat{I} - \hat{P}_{22}\hat{K})^{-1}\hat{P}_{21} \tag{1.23}$$

Also, the uncertain closed loop transfer matrix from $\bar{w}$ to $\bar{z}$ is related to $\hat{M}$ and $\hat{\Delta}$ by an upper LFT representation $\hat{F}_u(\hat{M},\hat{\Delta})$:

$$\hat{F}_u(\hat{M},\hat{\Delta}) \stackrel{\Delta}{=} \hat{M}_{22} + \hat{M}_{21}\hat{K}(\hat{I} - \hat{M}_{11}\hat{\Delta})^{-1}\hat{M}_{12} \tag{1.24}$$

Here, the diagonal and off-diagonal entries are defined as

$$\hat{P} = \begin{bmatrix} \hat{P}_{11} & \hat{P}_{12} \\ \hat{P}_{21} & \hat{P}_{22} \end{bmatrix}, \ \hat{M} = \begin{bmatrix} \hat{M}_{11} & \hat{M}_{12} \\ \hat{M}_{21} & \hat{M}_{22} \end{bmatrix} \qquad (1.25)$$

For the robust stability (RS) it is enough to construct the analysis only by considering the transfer matrix from the output to the input of the perturbations ($\hat{M}_{11}$) together with $\hat{\Delta}$:

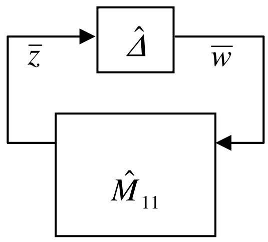

for RS analysis

Figure 38. $\hat{M}_{11}$ and $\hat{\Delta}$ Structure for RS Analysis

As a H_∞ framework design criterion each individual perturbation Δ_i (in $\hat{\Delta}$) is assumed to be stable and normalized [37]:

$$\bar{\sigma}(\Delta_i(j\omega)) \le 1 \quad \forall\omega \qquad (1.26)$$

Also, the individual perturbations (Δ_i's) shall satisfy $|\Delta_i(j\omega)| \le 1 \quad \forall\omega$ condition if they are complex valued, and, satisfy $-1 \le \Delta_i \le 1$ if they are real valued.

Thus, for $\hat{\Delta} = \mathrm{diag}(\Delta_i)$ the following statement can be written using the property that the maximum singular value of a block diagonal matrix is equal to the largest of the maximum singular values of the individual blocks:

$$\bar{\sigma}(\Delta_i(j\omega)) \leq 1 \quad \forall\omega, \forall i \;\; \Leftrightarrow \left\|\hat{\Delta}\right\|_\infty \leq 1 \tag{1.27}$$

Here, note that, $\hat{\Delta}$ is built from components which are themselves uncertain with norm bounded perturbations. This results in the structure of the uncertainty block $\hat{\Delta}$.

As mentioned before the modeling uncertainties in the H_∞ framework can be described as parametric and unmodelled dynamics uncertainties. In the parametric uncertainty case the parameters of the system are assumed to lie in a set given as

$$p \in \{p_0 + w\delta,\ \delta \in [-k, k]\} \tag{1.28}$$

Here, p_0 is the nominal value of the parameter. δ is allowed to take any value in the $[-k, k]$ interval and w is the scaling factor related to the problem. In general, k is scaled to be 1.

The un-modeled dynamics uncertainties are unstructured uncertainties and a full complex perturbation matrix $\hat{\Delta}$ is used here. The common forms of these types of uncertainties are *additive*, *multiplicative input* and *multiplicative output* uncertainties.

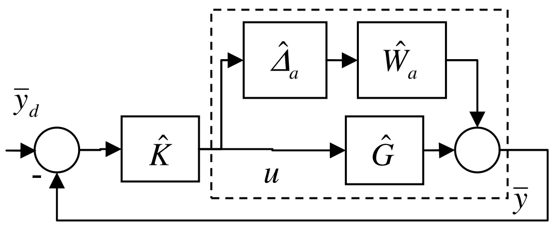

Figure 39. The Additive Uncertainty

This type of uncertainty is parameterized with two elements $\hat{W}_a$ and $\hat{\Delta}_a$. Here, $\hat{W}_a$ is a weighting transfer function (assumed to be known) and reflects the amount of uncertainty in a model with respect to the frequency. The other parameter $\hat{\Delta}_a$ is a stable (norm bounded) unknown transfer function.

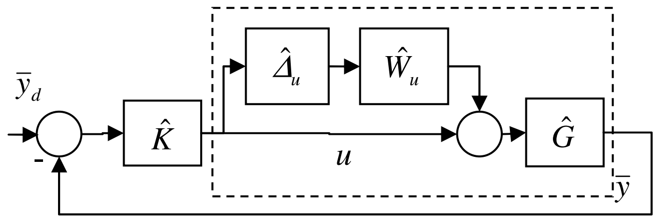

Figure 40. The Multiplicative Input Uncertainty

Similar to the additive uncertainty, this type of uncertainty is parameterized with two elements $\hat{W}_u$ and $\hat{\Delta}_u$. Where, $\hat{W}_u$ is a weighting transfer function and $\hat{\Delta}_u$ is a norm bounded transfer function.

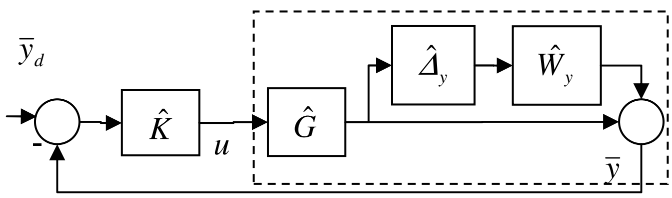

Figure 41. The Multiplicative Output Uncertainty

Similar to the previous cases multiplicative input uncertainty is parameterized with two elements $\hat{W}_y$ and $\hat{\Delta}_y$. Where, $\hat{W}_y$ is a weighting transfer function and $\hat{\Delta}_y$ is a norm bounded transfer function.

In the H_∞ framework the weights are the only design parameters that the designer should specify. Constant weights are used for scaling inputs and outputs. The transfer function weights are used to shape the various measures of performance in the frequency domain. The weights are also used to satisfy the rank conditions.

Proper selection of the weights depends a great deal on the understanding of the modeling process and the physics of the problem. The necessary conditions for a solution are stabilization and detection ability of the system, various rank requirements on the system matrices and that the transfer function between exogenous system inputs and the outputs is nonzero at high frequencies. This last condition is frequently violated since the transfer function is strictly proper (it has more poles than zeros).

The parametric uncertainty can be defined with the following introductory example. Suppose a linear system which is described by

$$\begin{aligned} \dot{x} &= ax + bu \\ y &= x \end{aligned} \tag{1.29}$$

Now we assume that the value of a varies between $a^- = a_n - \Delta a$ and $a^+ = a_n + \Delta a$. Here, a_n is the nominal value of a. This relation can also be written as:

$$a = a_n + \Delta a \delta_a \tag{1.30}$$

$$-1 \leq \delta_a \leq 1 \tag{1.31}$$

Similarly, assume that the value of b varies between $b^- = b_n - \Delta b$ and $b^+ = b_n + \Delta b$. Here, b_n is the nominal value of b. This relation can also be written as:

$$b = b_n + \Delta b \delta_b \tag{1.32}$$

$$-1 \leq \delta_b \leq 1 \tag{1.33}$$

Thus, the following linear system is obtained:

$$\begin{aligned} \dot{x} &= a_n x + b_n u + \Delta a \delta_a x + \Delta b \delta_b u \\ y &= x \end{aligned} \tag{1.34}$$

Now, introducing new input and output variables to the system as $z_a = x$, $z_b = u$ and $w_a = \delta_a z_a$, $w_b = \delta_b z_b$, following state space representation is obtained:

$$\begin{bmatrix} \dot{x} \\ y \\ z_a \\ z_b \end{bmatrix} = \begin{bmatrix} a_n & b_n & \Delta_a & \Delta_b \\ 1 & 0 & 0 & 0 \\ 1 & 0 & 0 & 0 \\ 0 & 1 & 0 & 0 \end{bmatrix} \begin{bmatrix} x \\ u \\ w_a \\ w_b \end{bmatrix} \tag{1.35}$$

Here, both the uncertainties on the parameters a and b are considered. Using this methodology the uncertainties of the parameters of the system are "pulled-out" from the system and defined as a 2×2 diagonal matrix, i.e. structured, with normalized uncertainty terms:

$$\hat{\Delta} = \begin{bmatrix} \delta_a & 0 \\ 0 & \delta_b \end{bmatrix} \tag{1.36}$$

The LFT structure of the system with the defined structured uncertainty block ($\hat{\Delta}$) is shown in the following block diagram.

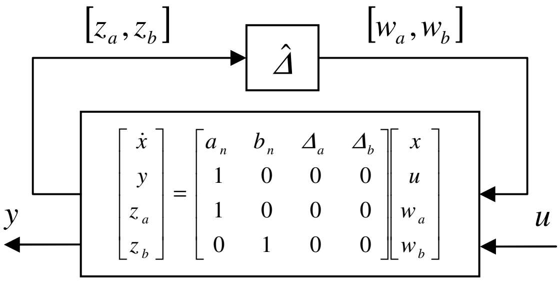

Figure 42. The LFT Block Diagram for Uncertainty in a and b

The definitions of stability and performance in the H_∞ framework are very important and they should be defined precisely. In terms of previously mentioned $\hat{M}$ and $\hat{\Delta}$ structure the requirement for stability and performance can be summarized as follows; if $\hat{M}$ is internally stable then *nominal stability* (NS) is satisfied by definition. In addition to NS the closed-loop system should satisfy the performance requirement. This is called as the *nominal performance* (NP). It is achieved if and only if $\|M_{22}\|_\infty < 1$. Also, recall the upper LFT definition $\hat{F}_u(\hat{M},\hat{\Delta})$. The controller ($\hat{K}$) must stabilize all plants defined by that uncertainty description $\hat{F}_u(\hat{M},\hat{\Delta})$. This is called as RS. It is satisfied if the LFT $\hat{F}_u(\hat{M},\hat{\Delta})$ is stable for all $\hat{\Delta}$ with $\|\hat{\Delta}\|_\infty \le 1$ if and only if $\|M_{11}\|_\infty < 1$ [38].

The entire performance specifications must be satisfied by the closed-loop system for all plants defined by the uncertainty description. This is done by determining the "largeness" of the transfer function from exogenous inputs $\overline{w}$ to outputs $\overline{z}$ for all plants in the uncertainty set. This is called as RP. It is satisfied if and only if $\|\hat{F}_u(\hat{M},\hat{\Delta})\|_\infty < 1$ for all $\hat{\Delta}$ with $\|\hat{\Delta}\|_\infty \le 1$ [37], [38].

In the H_∞ analysis and synthesis framework the structure of the uncertainty is not taken into account. That is, H_∞ deals with the uncertainty without knowing any information on the structure of it, and, treats the uncertainty as if it is a full block. However, in general, a system is built from components which are themselves uncertain with norm bounded perturbations. This results in the structure of the uncertainty block ($\hat{\Delta}$). Using the previously given norm bounds for robust stability ($\|M_{11}\|_\infty < 1$) and nominal performance ($\|M_{22}\|_\infty < 1$) will induce too much conservatism on the realistic problems with structured uncertainties. In order to reduce this conservatism the *structured singular value* (μ) is introduced [37], [39], [40].

The structured singular value is a function which provides a generalization of the singular value and the spectral radius of the system. The definition of μ is as follows; find the smallest structured $\hat{\Delta}$ (measured in terms of $\overline{\sigma}(\hat{\Delta})$) which makes $\det(\hat{I} - \hat{M}\hat{\Delta}) = 0$, and this means that $\mu(\hat{M}) = 1/\overline{\sigma}(\hat{\Delta})$. Or mathematically:

$$\mu(\hat{M}) \overset{\Delta}{=} \left(\min\left\{\overline{\sigma}(\hat{\Delta}) \mid \det(\hat{I} - \hat{M}\hat{\Delta}) = 0 \text{ for structured } \hat{\Delta}\right\}\right)^{-1} \tag{1.37}$$

It is obvious that $\mu(\hat{M})$ not only depends on $\hat{M}$ but also on the allowed structure of $\hat{\Delta}$. This is defined by the notation $\mu_\Delta(\hat{M})$. Here, if there does not exist any $\hat{\Delta}$ making $\hat{I} - \hat{M}\hat{\Delta}$ singular, then, $\mu_\Delta(\hat{M})$ is taken to be zero. An exact solution for μ does not exist, but a solution via upper and lower bounds on μ can be approximated. The method of approximation depends on the structure of the $\hat{\Delta}$ block. In the solution of upper and lower bounds of μ depending on the complex or real valuedness of the elements of $\hat{\Delta}$ two or three scaling matrices ($\hat{Q}$ and $\hat{D}$ or $\hat{Q}$, $\hat{D}$ and $\hat{G}$) are used.

Normally, the upper bound of μ is used since they are "safer" than the lower bound values. The upper bound is defined as:

$$\mu_{\Delta}(\hat{M}) \leq \inf_{\hat{D}\in \underline{D}} \overline{\sigma}(\hat{D}\hat{M}\hat{D}^{-1}) \tag{1.38}$$

Here, $\hat{D}$ is the aforementioned scaling matrix described in the following figure to geometrically illustrate the effect of *D-scales*.

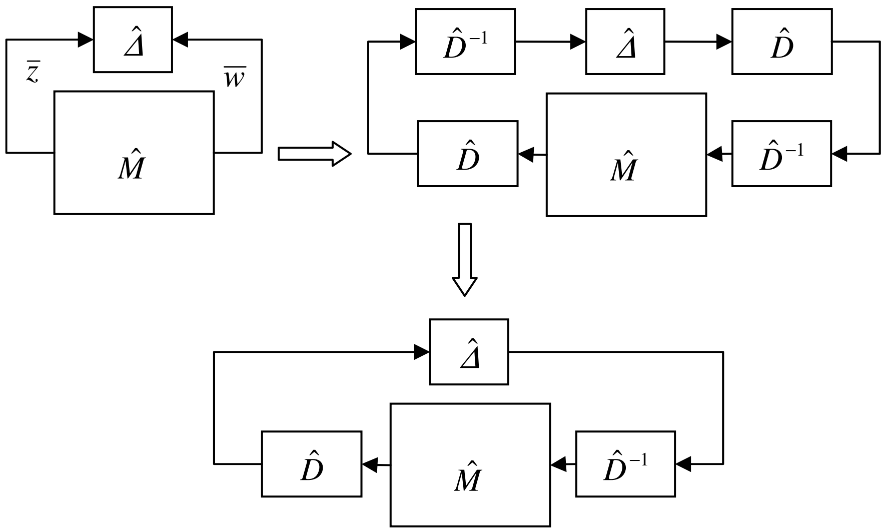

Figure 43. The Effect of D-scales

The solution method for the upper bounds of μ (depending on the complex or real valuedness of the elements of $\hat{\Delta}$) is explained in detail in the references [37], [39], [41] and [42].

Recall that RP means that the performance objective is satisfied for all possible plants in the uncertainty set including the "worst case" plant. In the H_∞ framework, for multi input multi output (MIMO) systems, the RP condition is identical to a RS condition with an additional perturbation block. Here, the additional perturbation block is the fictitious uncertainty block ($\hat{\Delta}_P$) representing the H_∞ performance specification.

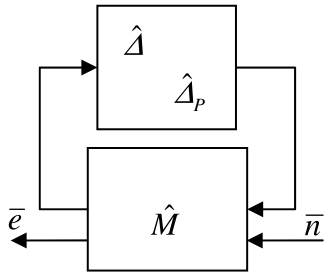

Figure 44. The LFT Block Diagram for RP with RS and NP

The steps needed to test the RP using μ-analysis is summarized in the sequel. Rearrange the uncertain system into $\hat{M}\hat{\Delta}$ structure where the block diagonal perturbations satisfy $\left\|\hat{\Delta}\right\|_\infty \le 1, \forall\omega$. Let the performance requirement for RP is defined as $\left\|\hat{F}_u(\hat{M},\hat{\Delta})\right\|_\infty \le 1$ for the defined perturbations. Hence,

$$\text{NP} \Leftrightarrow \mu_{\Delta P} = \bar{\sigma}(\hat{M}_{22}) < 1, \forall\omega \tag{1.39}$$

$$\text{RS} \Leftrightarrow \mu_{\Delta}(\hat{M}_{11}) < 1, \forall\omega \tag{1.40}$$

$$\text{RP} \Leftrightarrow \mu_{\Delta RP}(\hat{M}) < 1, \forall\omega,\ \hat{\Delta}_{RP} = \begin{bmatrix} \hat{\Delta} & \hat{0} \\ \hat{0} & \hat{\Delta}_P \end{bmatrix} \tag{1.41}$$

Here, $\hat{\Delta}$ is a block diagonal matrix where its detailed structure depends on the defined uncertainty and $\hat{\Delta}_P$ is always a full complex matrix.

Eventually, calculate the frequency response of $\hat{M}$ to conduct a test across all frequencies. Then on calculate the upper and lower bounds for $\mu_{\Delta RP}$ and evaluate the peak value of the upper bound (μ_{peak}). Whether $\mu_{peak} < 1$ the system ($\hat{M}\hat{\Delta}$) satisfies NP, RS and RP.

1.6. Outline of the Thesis

In this section, the outline of the Ph.D. study will be given. The thesis is composed of the following chapters:

1. Introduction,
2. Modeling the Aircraft,
3. Nonlinear Inverse Dynamics Controller Design,
4. Robust Performance Analysis,
5. Stabilization at High Angle of Attack,
6. High Angle of Attack Maneuvers
7. Discussion and Conclusion.

In the first chapter, an introduction to the study was done and the scope of the study is summarized. Controlling a general aircraft and the basic conventional and fighter aircraft maneuvers are explained. Then, the fundamentals of air combat maneuvers and air combat tactics are discussed. Eventually, an introduction on the aerodynamic properties of high angle of attack flight is given. Then, the related literature on high angle of attack maneuvering control is introduced. Also, the dynamic inverse controller, assignment of the desired dynamics, the basic issues on dynamic inversion and stability and robustness analysis are explained.

In Chapter 2, modeling the aircraft dynamics is discussed. Then, the nonlinear aerodynamics of the aircraft and the related stall indication parameters are presented. Next, the models for the aircraft engines and thrust-vectoring paddles are investigated. Afterwards, flight environment of the aircraft, the turbulence and discrete gust effects are discussed. Eventually, the models of Inertial Navigation System (INS), Inertial Measurement Unit (IMU) and the Angle of Attack (AoA) and side slip sensors are presented. This chapter is concluded with the human pilot model.

In Chapter 3, the general aspects of the nonlinear inverse dynamics controller design strategy are discussed. Then, the nonlinear inverse dynamics controller design for the aircraft is presented. The controller design based on the thrust vectoring controls will be investigated. Eventually, the stabilization and the attitude controllers are presented. Then, the controller design based on blending the aerodynamic and thrust vectoring controls is discussed.

In Chapter 4, the general aspects of the trim analysis and linearization of the nonlinear dynamics of the aircraft is discussed. Then, the modeling of the uncertainties and the disturbances on the aircraft are presented. Eventually, the robust performance analysis of the controller loops with and without the pilot model is constituted. At the end of this chapter, the performance of the designed stabilization and attitude controllers are analyzed.

In Chapter 5, the performance of the designed stabilization controller is investigated. A pull-up maneuver to bring the aircraft manually into stall is introduced and the stall indication trigger to activate the stabilization controller is discussed. Eventually, the trim angle of attack calculation and the trim angle of attack control is constituted. Then, two stabilization control cases are analyzed with simulations.

In Chapter 6, the performance of the designed attitude controller is investigated. For that purpose, the Cobra maneuver is analyzed by using the aerodynamic controls only and TVC only. Then, the Herbst maneuver is introduced and analyzed similarly. Eventually, different attitude control maneuvers such as velocity vector roll, fixed ground target attack, tail chase acquisition and target aircraft pointing maneuvers are introduced and analyzed by simulations.

In Chapter 7, the entire study is discussed and the conclusions are made. The contributions and innovations of the study are summarized and some recommendations on the possible future work are given.

CHAPTER 2

MODELING THE AIRCRAFT

In this chapter, first, modeling the aircraft kinematics and dynamics will be discussed. The effect of engine angular momentum on the aircraft dynamics will also be included in the derivations. Then, the nonlinear aerodynamics of the aircraft and the related stall indication parameters will be presented. Next, the models for the aircraft engines and thrust-vectoring paddles will be investigated. Afterwards, flight environment of the aircraft, the turbulence and discrete gust effects will be discussed. Eventually, the models of the onboard sensors such as Inertial Navigation System (INS), Inertial Measurement Unit (IMU) and the Angle of Attack (AoA) and side slip sensors will be presented. Finally, the chapter will be concluded with the human pilot model.

2.1. Modeling The Aircraft Dynamics

In the process of dynamic modeling, the aircraft is assumed to be rigid with practically constant mass and density and symmetric about its x-z plane. The un-deflected thrust force of each engine is assumed to act parallel to the longitudinal body axis. However, it can be deviated as desired by using the thrust-vectoring paddles.

Dynamic modeling of the aircraft is started by defining two reference frames: the earth fixed reference frame (assumed to be inertial) and the body fixed reference frame attached to the mass center of the aircraft. The two control forces (i.e. the forces obtained by thrust deviations) in the TVC phase are denoted by $\vec{F}_L$ and $\vec{F}_R$, which are applied at arbitrary directions at different locations. These locations are defined with respect to the origin of the body fixed reference frame by the position vectors $\vec{r}_{be_L}$ and $\vec{r}_{be_R}$. Note that the aerodynamic forces and moments are treated as disturbances in this phase. The position of the aircraft with respect to the earth fixed reference frame is defined by the vector $\vec{r}_{ob}$. Fig. 1 shows the mentioned reference frames, actuation forces with their locations, and the aerodynamic forces and moments on the aircraft.

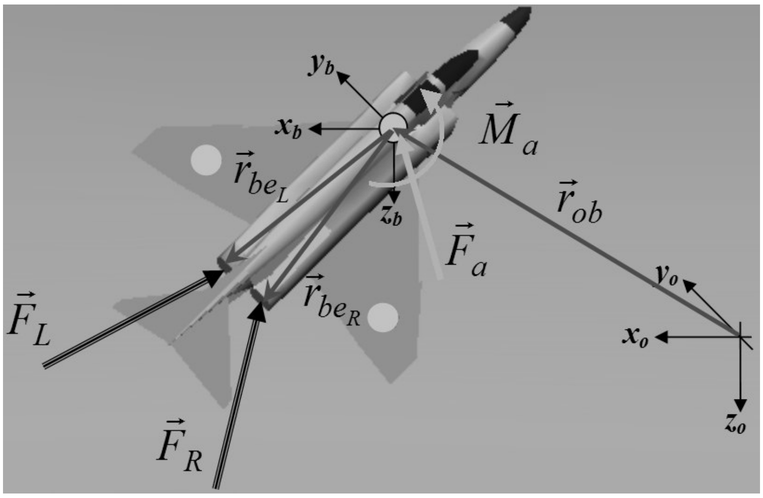

Figure 45. The Forces and Moments on the Aircraft

The rotational transformation between the earth fixed reference frame and the body fixed reference frame is defined by three successive rotations. These three rotations are defined by the Euler angles ψ, θ, and ϕ. $\hat{C}^{(o,b)}$ is the rotation matrix from the earth fixed reference frame to the body fixed reference frame. The angular velocity of the aircraft with respect to the earth fixed reference frame, i.e. $\vec{\omega}_{b/o}$, can be expressed in the body fixed frame as follows, where s and c are used to denote the sine and cosine functions for sake of brevity.

$$\overline{\omega}_{b/o}^{(b)} = (\dot{\phi} - \dot{\psi} s\theta)\overline{u}_1 + (\dot{\theta} c\phi + \dot{\psi} c\theta s\phi)\overline{u}_2 + (\dot{\psi} c\theta c\phi - \dot{\theta} s\phi)\overline{u}_3 \tag{2.1}$$

If the angular velocity components in the body fixed reference frame are denoted as p, q and r, then $\overline{\omega}_{b/o}^{(b)}$ can also be written as

$$\overline{\omega}_{b/o}^{(b)} = \begin{bmatrix} p \\ q \\ r \end{bmatrix} = \begin{bmatrix} 1 & 0 & -s\theta \\ 0 & c\phi & c\theta s\phi \\ 0 & -s\phi & c\theta c\phi \end{bmatrix} \begin{bmatrix} \dot{\phi} \\ \dot{\theta} \\ \dot{\psi} \end{bmatrix} \tag{2.2}$$

The angular acceleration of the aircraft with respect to the earth fixed reference frame, i.e. $\vec{\alpha}_{b/o}$, is the time derivative of $\overline{\omega}_{b/o}^{(b)}$ and can be expressed in the body fixed frame as

$$\overline{\alpha}_{b/o}^{(b)} = \begin{bmatrix} 1 & 0 & -s\theta \\ 0 & c\phi & c\theta s\phi \\ 0 & -s\phi & c\theta c\phi \end{bmatrix} \begin{bmatrix} \ddot{\phi} \\ \ddot{\theta} \\ \ddot{\psi} \end{bmatrix} + \begin{bmatrix} 0 & 0 & -\dot{\theta} c\theta \\ 0 & -\dot{\phi} s\phi & -\dot{\theta} s\theta s\phi + \dot{\phi} c\theta c\phi \\ 0 & -\dot{\phi} c\phi & -\dot{\theta} s\theta c\phi - \dot{\phi} c\theta s\phi \end{bmatrix} \begin{bmatrix} \dot{\phi} \\ \dot{\theta} \\ \dot{\psi} \end{bmatrix} \tag{2.3}$$

The translational acceleration $\vec{a}_{b/o}$ of the aircraft with respect to the earth fixed reference frame can be found by differentiating its translational velocity vector, which is expressed in the body fixed frame as $\vec{v}_{b/o} = u\vec{u}_1^{(b)} + v\vec{u}_2^{(b)} + w\vec{u}_3^{(b)}$. Hence, $\overline{a}_{b/o}^{(b)} = \dot{\overline{v}}_{b/o}^{(b)} + \tilde{\omega}_{b/o}^{(b)}\overline{v}_{b/o}^{(b)}$, and in detailed form it can be written as

$$\overline{a}_{b/o}^{(b)} = \begin{bmatrix} \dot{u} \\ \dot{v} \\ \dot{w} \end{bmatrix} + \begin{bmatrix} 0 & -r & q \\ r & 0 & -p \\ -q & p & 0 \end{bmatrix} \begin{bmatrix} u \\ v \\ w \end{bmatrix} \tag{2.4}$$

Since, the total velocity V_T, the angle of attack α and the side slip angle β can be measured directly on the aircraft and have direct relationship to piloting, it is preferable to write the translational equations in terms of the wind frame variables. For this purpose, let $\overline{v}_{b/o}^{(w)} = V_T \overline{u}_1$ so that $\overline{v}_{b/o}^{(b)} = V_T \hat{C}^{(b,w)} \overline{u}_1$. Then, differentiating $\overline{v}_{b/o}^{(b)}$, the acceleration of the aircraft with respect to earth fixed reference frame can be found as follows with its expression in the body fixed frame:

$$\overline{a}_{b/o}^{(b)} = \dot{V}_T \hat{C}^{(b,w)} \overline{u}_1 + V_T \dot{\hat{C}}^{(b,w)} \overline{u}_1 + V_T \tilde{\omega}_{b/o}^{(b)} \hat{C}^{(b,w)} \overline{u}_1 \tag{2.5}$$

Hence, using the equations (2.4) and (2.5), the relation between the wind frame variables and the body frame variables of the translational acceleration can be found. Here, $\hat{C}^{(b,w)} = \hat{R}_2(-\alpha)\hat{R}_3(\beta)$ and its elements are shown in the following equation:

$$\hat{C}^{(b,w)} = \begin{bmatrix} c\alpha c\beta & -c\alpha s\beta & -s\alpha \\ s\beta & c\beta & 0 \\ s\alpha c\beta & -s\alpha s\beta & c\alpha \end{bmatrix} \tag{2.6}$$

Thus, equations (2.4), (2.5) and (2.6) lead to

$$\begin{bmatrix} \dot{u} \\ \dot{v} \\ \dot{w} \end{bmatrix} = \begin{bmatrix} c\alpha c\beta & -V_T s\alpha c\beta & -V_T c\alpha s\beta \\ s\beta & 0 & V_T c\beta \\ s\alpha c\beta & V_T c\alpha c\beta & -V_T s\alpha s\beta \end{bmatrix} \begin{bmatrix} \dot{V}_T \\ \dot{\alpha} \\ \dot{\beta} \end{bmatrix} \tag{2.7}$$

The six nonlinear rigid-body equations of motion are derived using the Newton-Euler equations. In these equations, the mass of the aircraft is denoted with

m, the inertia tensor of the aircraft is expressed by the matrix $\hat{J} = \hat{J}^{(b)}$ in the body fixed frame, the earth gravity field vector is denoted with $\vec{g}$, and the aerodynamic force and moment vectors created on the aircraft during its flight are denoted with $\vec{F}_a$ and $\vec{M}_a$. $\vec{F}_L$ and $\vec{F}_R$ are the thrust force vectors of the two engines with magnitudes T_L and T_R. Their azimuth and elevation angles with respect to the body fixed reference system are denoted by the pairs { ψ_L, ψ_R } and { θ_L, θ_R }. The force equation can be written in the body fixed frame as

$$m\bar{a}_{b/o}^{(b)} = m\dot{\bar{v}}_{b/o}^{(b)} + m\tilde{\omega}_{b/o}^{(b)}\bar{v}_{b/o}^{(b)} = \bar{F}_L^{(b)} + \bar{F}_R^{(b)} + mg\hat{C}^{(b,o)}\bar{u}_3 + \bar{F}_a^{(b)} \tag{2.8}$$

Here, $\bar{F}_L^{(b)} = T_L\hat{R}_3(\psi_L)\hat{R}_2(\theta_L)\bar{u}_1$ and $\bar{F}_R^{(b)} = T_R\hat{R}_3(\psi_R)\hat{R}_2(\theta_R)\bar{u}_1$. Similarly, the moment equation can be written in the body fixed frame as

$$\hat{J}\bar{\alpha}_{b/o}^{(b)} = -\tilde{\omega}_{b/o}^{(b)}\hat{J}\bar{\omega}_{b/o}^{(b)} + \tilde{r}_{be_L}^{(b)}\bar{F}_L^{(b)} + \tilde{r}_{be_R}^{(b)}\bar{F}_R^{(b)} + \bar{M}_a^{(b)} \tag{2.9}$$

Finally, the Newton-Euler equations describing the rigid body motion of the aircraft can be combined into a single augmented matrix equation as

$$\begin{bmatrix} [\dot{u} \quad \dot{v} \quad \dot{w}]^{\mathrm{T}} \\ [\dot{p} \quad \dot{q} \quad \dot{r}]^{\mathrm{T}} \end{bmatrix} = \bar{F} + \hat{G}\begin{bmatrix} \bar{F}_L^{(b)} \\ \bar{F}_R^{(b)} \end{bmatrix} + \hat{H}\begin{bmatrix} \bar{F}_a^{(b)} \\ \bar{M}_a^{(b)} \end{bmatrix} \tag{2.10}$$

Here, the matrices $\bar{F}$, $\hat{G}$, and $\hat{H}$ are used for short hand notation. They are defined as shown below:

$$\bar{F} = \begin{bmatrix} -\tilde{\omega}_{b/o}^{(b)}\bar{v}_{b/o}^{(b)} + g\hat{C}^{(b,o)}\bar{u}_3 \\ -\hat{J}^{-1}\tilde{\omega}_{b/o}^{(b)}\hat{J}\bar{\omega}_{b/o}^{(b)} \end{bmatrix}, \hat{G} = \begin{bmatrix} \hat{I}/m & \hat{I}/m \\ \hat{J}^{-1}\tilde{r}_{be_L}^{(b)} & \hat{J}^{-1}\tilde{r}_{be_R}^{(b)} \end{bmatrix}, \hat{H} = \begin{bmatrix} \hat{I}/m & 0 \\ 0 & \hat{J}^{-1} \end{bmatrix}$$

2.1.1. Modeling the Effect of Engine Angular Momentum

In this section the additional effect of the angular momentum arising from the rotary parts of the engine spinning at high velocities will be included in the Newton-Euler equations.

$$\begin{bmatrix} [\dot{u} \quad \dot{v} \quad \dot{w}]^{\mathrm{T}} \\ [\dot{p} \quad \dot{q} \quad \dot{r}]^{\mathrm{T}} \end{bmatrix} = \hat{F} + \hat{G}\begin{bmatrix} \overline{F}_1^{(b)} \\ \overline{F}_2^{(b)} \end{bmatrix} + \hat{H}\begin{bmatrix} \overline{F}_a^{(b)} \\ \overline{M}_a^{(b)} \end{bmatrix} + \begin{bmatrix} \overline{0} \\ [\dot{p}_e \, \dot{q}_e \, \dot{r}_e]^{\mathrm{T}} \end{bmatrix} \tag{2.11}$$

Here, $[\dot{p}_e \, \dot{q}_e \, \dot{r}_e]^{\mathrm{T}} = \hat{J}^{-1}\overline{M}_e^{(b)}$, and, $\overline{M}_e^{(b)}$ is the moment vector at the body fixed reference frame arising from the engine angular momentum $\overline{H}_e^{(b)}$ and shown as

$$\overline{M}_e^{(b)} = \dot{\overline{H}}_e^{(b)} + \tilde{\omega}_{b/o}^{(b)}\overline{H}_e^{(b)} \tag{2.12}$$

Assuming $\overline{H}_e^{(b)} = [\, J_e\omega_e \quad 0 \quad 0]^{\mathrm{T}}$ and ω_e is constant, i.e. $\overline{H}_e^{(b)}$ has the component only in the forward direction of the aircraft body and it is constant. Then, $\overline{M}_e^{(b)}$ is

$$\overline{M}_e^{(b)} = \begin{bmatrix} 0 & -r & q \\ r & 0 & -p \\ -q & p & 0 \end{bmatrix}\begin{bmatrix} J_e\omega_e \\ 0 \\ 0 \end{bmatrix} = \begin{bmatrix} 0 \\ rJ_e\omega_e \\ -qJ_e\omega_e \end{bmatrix} \tag{2.13}$$

The angular acceleration at the body fixed reference frame originating from the engine angular momentum can be expressed as

$$\begin{bmatrix} \dot{p}_e \\ \dot{q}_e \\ \dot{r}_e \end{bmatrix} = \hat{J}^{-1} \begin{bmatrix} 0 \\ rJ_e\omega_e \\ -qJ_e\omega_e \end{bmatrix} = \begin{bmatrix} -J_{xz}/(-J_xJ_z + J_{xz}^2)(qJ_e\omega_e) \\ (-1/J_y)(rJ_e\omega_e) \\ -J_x/(-J_xJ_z + J_{xz}^2)(qJ_e\omega_e) \end{bmatrix} \tag{2.14}$$

The engine on the aircraft under study has a maximum spin velocity of 7,460 rpm at the full power. Assuming 80% of the full power during the maneuvers and moment of inertia for the rotating machinery of the engine is equal to 0.86 kg.m^2, H_e is found to be 538.95 kg.m^2/sec. This value is very high when compared to the angular momentum value of single engine F-16 aircraft which is equal to 216.93 kg.m^2/sec. This is actually caused by the heavier rotating machinery of the two engines of the aircraft under study.

If we examine the effect of the rotating machinery on the maneuvers, we simply see a coupling between the maneuvers at the longitudinal and lateral planes of motion. This is further investigated with the following turn maneuver example. Assume that the aircraft makes a $\dot{\psi} = 3^\circ/\sec$ coordinated turn maneuver at 0.8 Mach in the lateral plane without gaining or loosing any altitude. Thus, the roll angle of the aircraft making such a maneuver without any side slip is found from the following formula [33]:

$$\phi = \tan^{-1}(\frac{V_T\dot{\psi}}{g}) = 55.44^\circ \tag{2.15}$$

Using the kinematic relation between the angular velocities, the yaw rate component of the aircraft at the body fixed reference frame (r) without any pitch angle and pitch angle rate of the aircraft can be found as

$$\begin{aligned} r &= -\dot{\theta}\sin(\phi) + \dot{\psi}\cos(\theta)\cos(\phi) \\ &= (3/180\pi)\cos(55.44/180\pi) = 0.03\, rad/\sec \end{aligned} \tag{2.16}$$

Since J_y = 165,667 kg.m^2 for the aircraft under study, $\dot{q}_e = (\text{-}1/J_y)(rJ_e\omega_e) =$ (-9.76)10^{-5} rad/sec^2. The aircraft is making a $\dot{\psi} = 3^\circ/\sec$ coordinated turn maneuver, thus, it takes 1 min to make a full heading reversal. Assuming $\dot{q}_e$ remains constant throughout the whole turn, $\Delta q_e = (60)(\text{-}9.76)10^{-5}$ = (-5.86)10^{-3} rad/sec maximum pitch rate is induced at the end of the maneuver.

Thus 19.51% of the desired yawing maneuver is induced at the longitudinal plane causing the undesired pitching maneuver. In other words the pilot should have approximately 20% more workload to suppress the undesired pitch maneuver at the end of the full heading reversal maneuver. From the controller design point of view the cross coupled motion arising from the engine angular momentum is treated as a disturbance on the controlled system and it will be suppressed by the designed controller.

2.2. Modeling The Aircraft Aerodynamics

2.2.1. High Angle of Attack and Stall Indication Parameters

High angle of attack aerodynamics is inherently associated with separated flows and nonlinear aerodynamics. Studies on high angle of attack aerodynamics are heavily dependent on wind tunnel and flight testing. The data generated from these tests are used to construct an aerodynamic model of the aircraft. Such a model is important in that it should represent the major design concerns for a super-maneuverable fighter aircraft. The important design concerns are (i) ability to control the aircraft at high angle of attack maneuvering, (ii) flight without departure when the pilot is in the loop, and (iii) allowance for nearly unlimited angle of attack range.

The studies on unsteady aerodynamics indicated two important parameters of stall phenomena. They are $C_{n\beta dyn}$ and *LCDP* (lateral control departure parameter). $C_{n\beta dyn}$ is known as a convenient stall predictor, but it only indicates an approximate tendency to stall. Since it does not contain any aerodynamic terms related to the control surfaces, it is an open loop parameter. $C_{n\beta dyn}$ is a combination of the lateral and directional moment affectivities as a function of the angle of attack and the inertia ratio in the x-z plane of the aircraft. For a safe and stall free region, it should have a positive value. As for *LCDP*, it seems to be a better predictor to indicate the tendency to stall. This is because it is not an open loop parameter, since it contains aerodynamic terms related to the ailerons in addition to the lateral and directional moment affectivities. For a safe and stall free region, *LCDP* should also have a positive value. Negative values imply roll reversal. The expressions for these stall prediction parameters are given as

$$C_{n\beta dyn} = C_{n\beta}\cos(\alpha) - (J_z / J_x)C_{l\beta}\sin(\alpha) \tag{2.17}$$

$$LCDP = C_{n\beta} - C_{l\beta}(C_{n\delta_a} / C_{l\delta_a}) \tag{2.18}$$

Here, $C_{n\beta}$ and $C_{l\beta}$ are the sensitivities of the yaw and roll moments to the side slip angle respectively and J_z and J_x are the inertia components of the aircraft along the z and x directions of the body fixed frame.

Bihrle and Weissmann proposed a chart that indicates the regions in which the aircraft will encounter spin, roll reversal, and departure from controlled flight [4]. This chart looks as shown in Figure 46. On this chart, region A implies a high resistance to both departure and spin. Region B implies a considerable resistance to spin but it also implies occurrence of roll reversals that induce departure and post-stall gyrations. Region C implies a weak tendency for spin and occurrence of strong roll reversals inducing departures. Different from region C, the spin tendency is also strong in region D. Region E implies a weak tendency for spin and a moderate tendency for departure. Region F implies resistance to both departure and spin but it is weaker than region A. It also implies that roll reversals do not occur. Finally, region U is characterized by high directional instability.

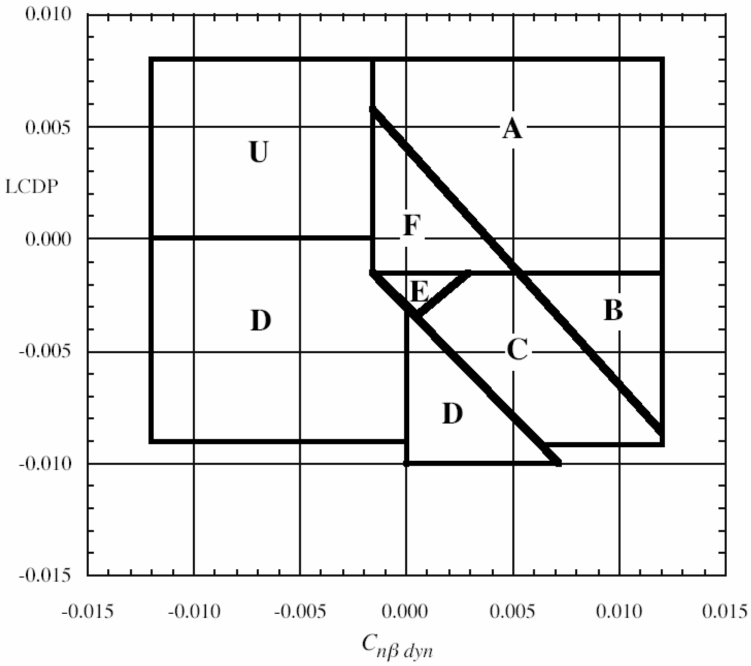

Figure 46. Regions of the Integrated Bihrle and Weissmann Chart [4]

2.2.2. Nonlinear Modeling of the Aircraft Aerodynamics

The modeled aircraft, considered in this study, is a two-seat all-weather fighter-bomber aircraft and fitted with a low-mounted swept wing with wingtip dihedral. The tail section consists of an all-moving horizontal stabilator placed in a cathedral configuration and a single vertical tail. The trailing edge of the main wing contains the control surfaces acting as ailerons and flaps. The trailing edge of the vertical tail has a rudder control surface. Thrust is provided by two afterburning jet engines mounted on the left and right sides of the rear part of the fuselage.

The simulation model built for this study is aerodynamically controlled with the elevator, aileron, and rudder actions. The deflections of these aerodynamic control surfaces are denoted by δ_e, δ_a, and δ_r, respectively. The left and right engine thrusts are controlled by using the engine throttle deflections denoted by δ_{Lth} and δ_{Rth}. The aerodynamic data, which is used in the simulation model, is gathered assuming that the ground effect is absent, the landing gears are retracted, and there are no external stores. Aerodynamics is modeled in terms of polynomial functions that involve the control surface deflections, the angle of attack, the sideslip angle and the angular velocity components in the body fixed reference frame. Polynomial fits for each of the non-dimensional aerodynamic force and moment coefficients ($C_x, C_y, C_z, C_l, C_m, C_n$) are valid over an angle of attack range of $-15^\circ \leq \alpha \leq 55^\circ$. Aerodynamic coefficients are referenced to an assumed center of gravity location originated from the technical documentary of the aircraft. The yaw and pitch moment coefficients C_n and C_m include a correction for the center of gravity position. This is considered to account for the effect of changing center of gravity position due to fuel consumption during the flight. The control surface deflections are assumed to be limited as follows: $-21^\circ \leq \delta_e \leq 7^\circ$, $-16^\circ \leq \delta_a \leq 16^\circ$, and $-30^\circ \leq \delta_r \leq 30^\circ$. Any limitation on the side slip angle is not mentioned in the model [55]. The modeled aircraft is seen in Figure 47.

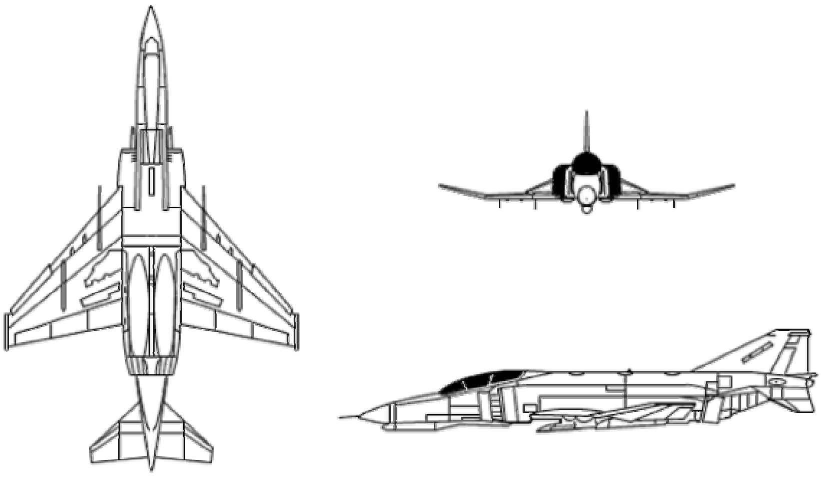

Figure 47. Three Views of the Modeled Aircraft

The non-dimensional aerodynamic force and moment coefficients for the aircraft model vary nonlinearly with the angles α and β, the angular velocity components p, q, r, and the control surface deflections δ_e, δ_a, and δ_r. The coefficients are computed as shown in equations (2.19) and (2.20) for the region $-15^\circ \leq \alpha \leq 15^\circ$, as shown in equations (2.21) and (2.22) for the region $15^\circ < \alpha < 30^\circ$ and as shown in equations (2.23) and (2.24) for the region $30^\circ \leq \alpha \leq 55^\circ$. For $\alpha > 55^\circ$ the same aerodynamic coefficient equations as those for $30^\circ \leq \alpha \leq 55^\circ$ are used [55].

For $\alpha \leq 15°$

$$C_X = -0.0434 + 2.39\times10^{-3}\alpha + 2.53\times10^{-5}\beta^2 - 1.07\times10^{-6}\alpha\beta^2 + 9.5\times10^{-4}\delta_e$$
$$-8.5\times10^{-7}\delta_e\beta^2 + \left(\frac{180q\overline{c}}{\pi 2V_t}\right)\left(8.73\times10^{-3} + 0.001\alpha - 1.75\times10^{-4}\alpha^2\right)$$
$$C_Y = -0.012\beta + 1.55\times10^{-3}\delta_r - 8\times10^{-6}\delta_r\alpha$$
$$+\left(\frac{180b}{\pi 2V_t}\right)\left(2.25\times10^{-3}p + 0.0117r - 3.67\times10^{-4}r\alpha + 1.75\times10^{-4}r\delta_e\right) \quad (2.19)$$
$$C_Z = -0.131 - 0.0538\alpha - 4.76\times10^{-3}\delta_e - 3.3\times10^{-5}\delta_e\alpha - 7.5\times10^{-5}\delta_a{}^2$$
$$+\left(\frac{180q\overline{c}}{\pi 2V_t}\right)(-0.111 + 5.17\times10^{-3}\alpha - 1.1\times10^{-3}\alpha^2)$$

$$C_l = -5.98\times10^{-4}\beta - 2.83\times10^{-4}\alpha\beta + 1.51\times10^{-5}\alpha^2\beta$$
$$-\delta_a(6.1\times10^{-4} + 2.5\times10^{-5}\alpha - 2.6\times10^{-6}\alpha^2)$$
$$-\delta_r(-2.3\times10^{-4} + 4.5\times10^{-6}\alpha)$$
$$+\left(\frac{180b}{\pi 2V_t}\right)(-4.12\times10^{-3}p - 5.24\times10^{-4}p\alpha + 4.36\times10^{-5}p\alpha^2$$
$$+4.36\times10^{-4}r + 1.05\times10^{-4}r\alpha + 5.24\times10^{-5}r\delta_e) \quad (2.20)$$
$$C_m = -6.61\times10^{-3} - 2.67\times10^{-3}\alpha - 6.48\times10^{-5}\beta^2$$
$$-2.65\times10^{-6}\alpha\beta^2 - 6.54\times10^{-3}\delta_e - 8.49\times10^{-5}\delta_e\alpha$$
$$+3.74\times10^{-6}\delta_e\beta^2 - 3.5\times10^{-5}\delta_a{}^2$$
$$+\left(\frac{180q\overline{c}}{\pi 2V_t}\right)(-0.0473 - 1.57\times10^{-3}\alpha) + \left(x_{c.g.,ref} - x_{c.g.}\right)C_Z$$

$$
\begin{aligned}
C_n &= 2.28\times10^{-3}\beta + 1.79\times10^{-6}\beta^3 + 1.4\times10^{-5}\delta_a \\
&\quad +7.0\times10^{-6}\delta_a\alpha - 9.0\times10^{-4}\delta_r + 4.0\times10^{-6}\delta_r\alpha \\
&\quad + \left(\frac{180b}{\pi 2V_t}\right)\Big(-6.63\times10^{-5}p - 1.92\times10^{-5}p\alpha + 5.06\times10^{-6}p\alpha^2 \\
&\qquad -6.06\times10^{-3}r - 8.73\times10^{-5}r\delta_e + 8.7\times10^{-6}r\delta_e\alpha\Big) \\
&\quad -\left(\frac{\overline{c}}{b}\right)\left(x_{c.g.,ref} - x_{c.g.}\right)C_Y
\end{aligned}
$$

<u>For $15^\circ < \alpha \leq 30^\circ$</u>

$$
\begin{aligned}
C_X &= 0.141 - 0.0154\alpha + 2.96\times10^{-4}\alpha^2 - 3.72\times10^{-4}\beta^2 \\
&\quad + 4.14\times10^{-5}\alpha\beta^2 - 9.12\times10^{-7}\alpha^2\beta^2 + 1.82\times10^{-3}\delta_e \\
&\quad -7.3\times10^{-5}\delta_e\alpha + \left(\frac{180q\overline{c}}{\pi 2V_t}\right)(-0.0602 + 2.04\times10^{-3}\alpha) \\
C_Y &= -2.08\times10^{-2}\beta + 6.07\times10^{-4}\alpha\beta + 2.37\times10^{-6}\beta^3 \\
&\quad -3.64\times10^{-7}\alpha\beta^3 + 2.3\times10^{-3}\delta_r - 5.9\times10^{-5}\delta_r\alpha \\
&\quad + \left(\frac{180b}{\pi 2V_t}\right)(-1.62\times10^{-3}p + 3.32\times10^{-4}p\alpha \\
&\quad + 0.0311r - 1.4\times10^{-3}r\alpha + 1.75\times10^{-4}r\delta_e) \\
C_Z &= -0.608 - 0.022\alpha - 6.77\times10^{-3}\delta_e + 9.7\times10^{-5}\delta_e\alpha - 7.5\times10^{-5}{\delta_a}^2 \\
&\quad + \left(\frac{180q\overline{c}}{\pi 2V_t}\right)(1.136 - 0.1418\alpha + 3.11\times10^{-3}\alpha^2)
\end{aligned}
\tag{2.21}
$$

$$
\begin{aligned}
C_l = \; & -1.29\times10^{-2}\beta + 1.04\times10^{-3}\alpha\beta - 2.02\times10^{-5}\alpha^2\beta \\
& +1.36\times10^{-5}\beta^3 - 1.13\times10^{-6}\alpha\beta^3 + 2.01\times10^{-8}\alpha^2\beta^3 \\
& -\delta_a(7.74\times10^{-4} - 1.9\times10^{-5}\alpha) - \delta_r(-2.0\times10^{-4} + 5.0\times10^{-6}\alpha) \\
& +\left(\frac{180b}{\pi 2V_t}\right)(2.78\times10^{-3}p - 2.79\times10^{-4}p\alpha - 6.81\times10^{-3}r \\
& +6.46\times10^{-4}r\alpha + 5.24\times10^{-5}r\delta_e) \\
C_m = \; & 0.0549 - 6.08\times10^{-3}\alpha - 1.69\times10^{-4}\beta^2 + 5.64\times10^{-7}\alpha\beta^2 \\
& -8.14\times10^{-3}\delta_e + 1.1\times10^{-4}\delta_e\alpha - 3.5\times10^{-5}{\delta_a}^2 \\
& +\left(\frac{180q\bar{c}}{\pi 2V_t}\right)(-0.0951 + 1.4\times10^{-3}\alpha) + \left(x_{c.g.,ref} - x_{c.g.}\right)C_Z \\
C_n = \; & 1.02\times10^{-2}\beta - 5.12\times10^{-4}\alpha\beta - 5.27\times10^{-6}\beta^3 \\
& +3.79\times10^{-7}\alpha\beta^3 + 9.1\times10^{-5}\delta_a + 3.0\times10^{-6}\delta_a\alpha \\
& -1.37\times10^{-3}\delta_r + 3.8\times10^{-5}\delta_r\alpha \\
& +\left(\frac{180b}{\pi 2V_t}\right)(0.0236p - 2.5\times10^{-3}p\alpha + 6.25\times10^{-5}p\alpha^2 \\
& +6.2\times10^{-4}r - 4.89\times10^{-4}r\alpha - 8.73\times10^{-5}r\delta_e + 8.7\times10^{-6}r\delta_e\alpha) \\
& -\left(\frac{\bar{c}}{b}\right)\left(x_{c.g.,ref} - x_{c.g.}\right)C_Y
\end{aligned}
\tag{2.22}
$$

For $\alpha > 30°$

$$\begin{aligned}
C_X &= -0.0326 - 2.16\times10^{-3}\alpha + 4.89\times10^{-5}\alpha^2 - 1.24\times10^{-4}\beta^2 \\
&\quad + 1.076\times10^{-5}\alpha\beta^2 - 1.54\times10^{-7}\alpha^2\beta^2 + 7.5\times10^{-4}\delta_e \\
&\quad - 3.9\times10^{-5}\delta_e\alpha + \left(\frac{180q\overline{c}}{\pi 2V_t}\right)(-0.026 + 8.73\times10^{-4}\alpha) \\
C_Y &= -2.095\times10^{-3}\beta - 6.36\times10^{-5}\alpha\beta - 2.15\times10^{-5}\beta^3 \\
&\quad + 5.42\times10^{-7}\alpha\beta^3 + 1.4\times10^{-3}\delta_r - 2.6\times10^{-5}\delta_r\alpha \\
&\quad + \left(\frac{180b}{\pi 2V_t}\right)(0.196p - 9.27\times10^{-3}p\alpha + 1.01\times10^{-4}p\alpha^2 \\
&\quad + 0.0326r - 2.55\times10^{-3}r\alpha + 3.26\times10^{-5}r\alpha^2 + 1.75\times10^{-4}r\delta_e) \\
C_Z &= -0.891 - 0.01146\alpha + 6.2\times10^{-3}\delta_e - 5.4\times10^{-3}\delta_e\alpha \\
&\quad + 6.2\times10^{-6}\delta_e\alpha^2 - 7.5\times10^{-5}\delta_a{}^2 \\
&\quad + \left(\frac{180q\overline{c}}{\pi 2V_t}\right)(0.589 - 0.0494\alpha + 6.11\times10^{-4}\alpha^2)
\end{aligned} \tag{2.23}$$

$$\begin{aligned}
C_l &= 1.18\times10^{-2}\beta - 5.29\times10^{-4}\alpha\beta + 4.88\times10^{-6}\alpha^2\beta \\
&\quad - 2.2\times10^{-5}\beta^3 + 9.05\times10^{-7}\alpha\beta^3 - 9.08\times10^{-9}\alpha^2\beta^3 \\
&\quad - 5.0\times10^{-5}\delta_a - \delta_r(-9.0\times10^{-5} + 1.8\times10^{-6}\alpha) \\
&\quad + \left(\frac{180b}{\pi 2V_t}\right)(-0.0428p + 1.82\times10^{-3}p\alpha - 1.94\times10^{-5}p\alpha^2 \\
&\quad + 0.073r - 3.02\times10^{-3}r\alpha + 3.14\times10^{-5}r\alpha^2 + 5.24\times10^{-5}r\delta_e) \\
C_m &= 7.3\times10^{-3} - 5.5\times10^{-3}\alpha - 7.93\times10^{-3}\delta_e + 8.23\times10^{-5}\delta_e\alpha \\
&\quad - 3.5\times10^{-5}\delta_a{}^2 + \left(\frac{180q\overline{c}}{\pi 2V_t}\right)(0.16 - 0.0101\alpha + 1.05\times10^{-4}\alpha^2) \\
&\quad + \left(x_{c.g.,ref} - x_{c.g.}\right)C_Z
\end{aligned} \tag{2.24}$$

$$
\begin{aligned}
C_n = & -9.23\times10^{-3}\beta + 1.52\times10^{-4}\alpha\beta + 1.62\times10^{-5}\beta^3 \\
& -3.46\times10^{-7}\alpha\beta^3 + 1.5\times10^{-4}\delta_a - 6.8\times10^{-4}\delta_r \\
& +1.2\times10^{-5}\delta_r\alpha - \delta_e\,(1.67\times10^{-4}\beta - 5.56\times10^{-6}\alpha\beta \\
& -3.81\times10^{-7}\beta^3 + 1.27\times10^{-8}\alpha\beta^3) \\
& +\left(\frac{180b}{\pi 2V_t}\right)(0.0385p - 1.73\times10^{-3}p\alpha + 1.92\times10^{-5}p\alpha^2 \\
& -0.0202r + 3.67\times10^{-4}r\alpha + 2.58\times10^{-3}r\delta_e \\
& -1.31\times10^{-4}r\delta_e\alpha + 1.69\times10^{-6}r\delta_e\alpha^2) - \left(\frac{\overline{c}}{b}\right)\left(x_{c.g.,ref} - x_{c.g.}\right)C_Y
\end{aligned}
$$

These coefficients are presented graphically in the following figures.

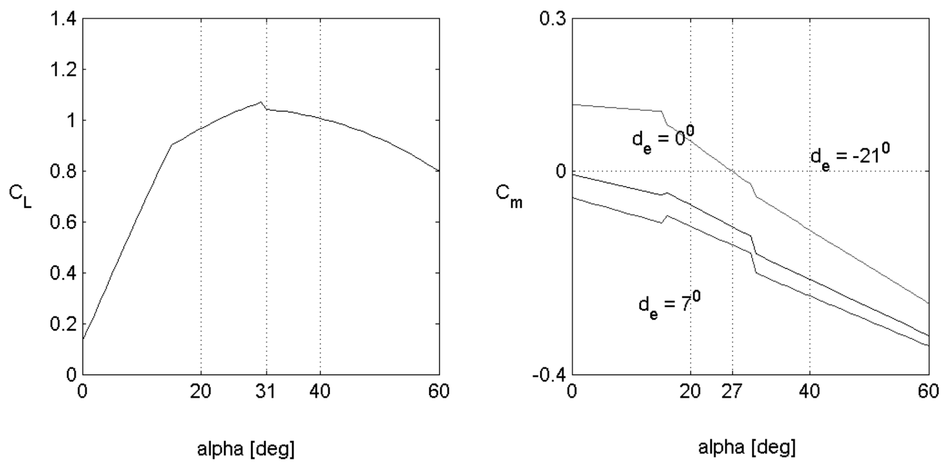

Figure 48. Longitudinal Plane Parameters

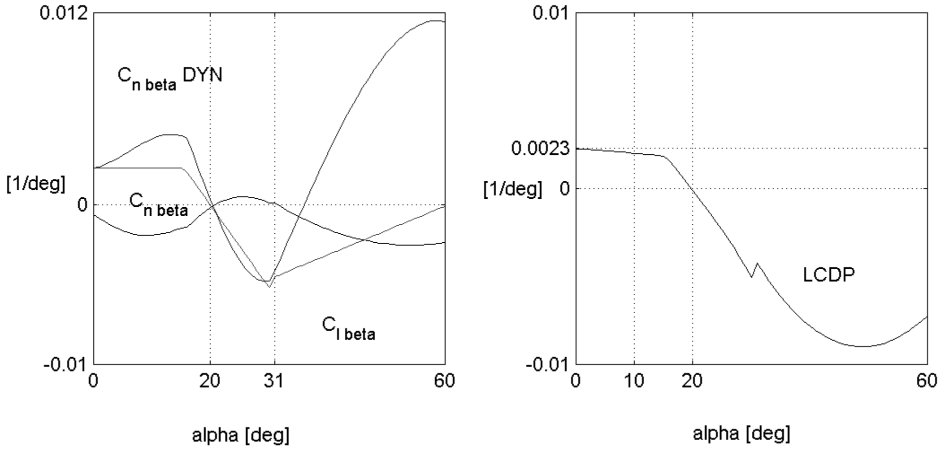

Figure 49. Lateral-Directional Plane Parameters

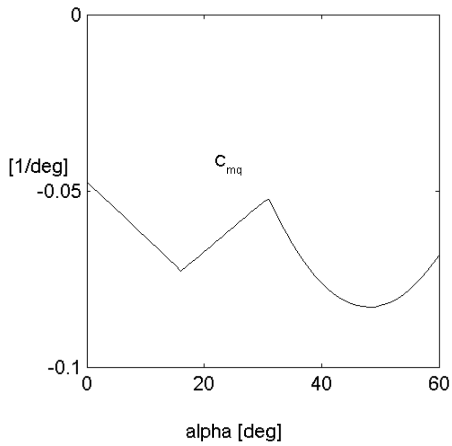

Figure 50. Longitudinal Plane Dynamic Derivative

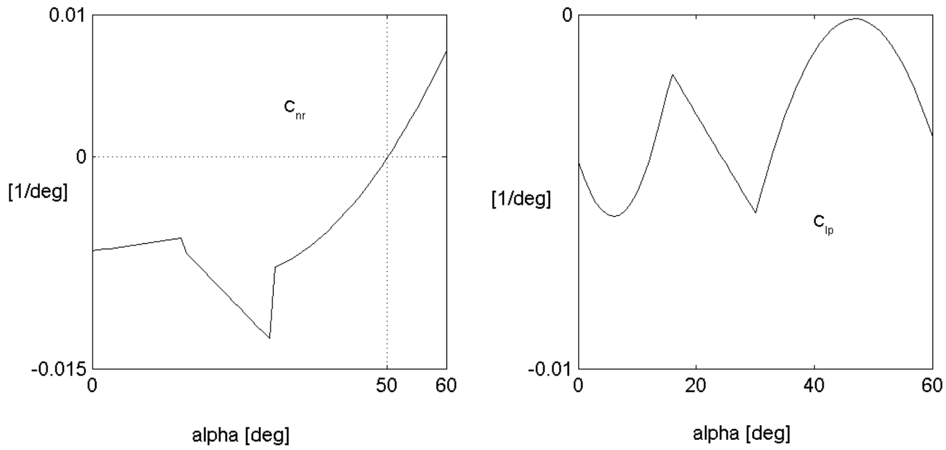

Figure 51. Lateral-Directional Plane Dynamic Derivatives

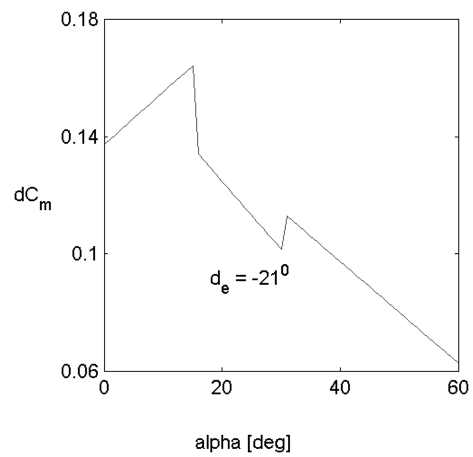

Figure 52. Longitudinal Plane Control Effectiveness Parameter

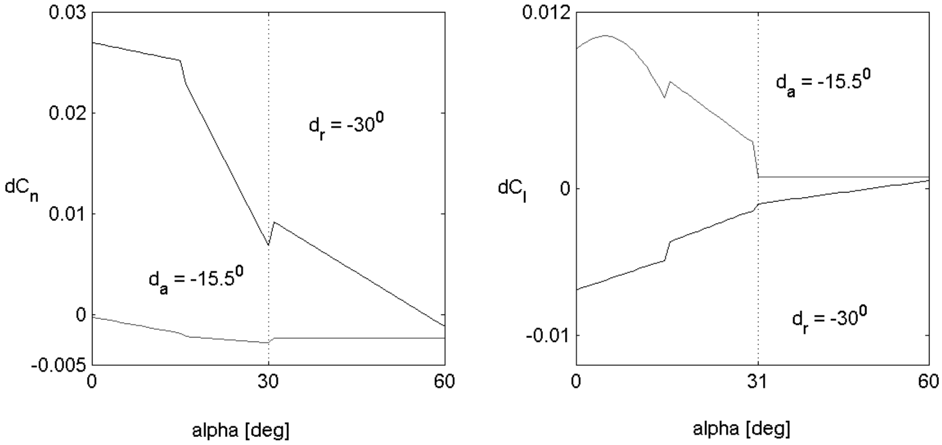

Figure 53. Lateral-Directional Plane Control Effectiveness Parameters

Studies on the aerodynamic coefficients have shown that the lift coefficient decreases after $\alpha = 31^\circ$. As another point, although the elevator is kept at -21° to produce positive pitching moment, the pitching moment changes sign after $\alpha = 27^\circ$. However, unfortunately $C_{n\beta dyn}$ and *LCDP* have negative values even after a not so large α such as $\alpha = 20^\circ$. The dynamic derivatives are not strongly affected at high angle of attack regions.

Using the aerodynamic coefficient functions, the stall analysis of the aircraft is made and the stall indication parameters are presented as shown in Figure 54. As Figure 54 is examined, it is seen that region A, i.e. the safest region, is encountered for $-15^\circ \le \alpha \le 17^\circ$. As the angle of attack increases further, weak spin resistance, roll reversals and departures can be seen. After $\alpha = 22^\circ$ roll reversals and departures become more effective and the control effectiveness parameters gradually decrease. This study reveals that $\alpha = 22^\circ$ is the critical angle of attack value after which the stall tendency starts to show up.

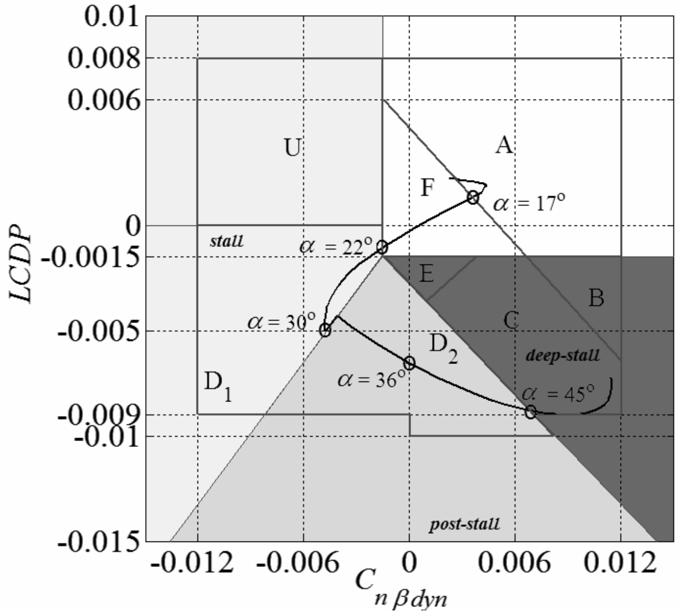

Figure 54. Integrated Bihrle-Weissmann Chart for the Aircraft

2.3. Modeling The Aircraft Engines

Each engine of the aircraft is modeled as a first order dynamic system with the following response equation to a commanded power demand:

$$\dot{P}_a = (1/\tau_{eng})(P_c - P_a) \tag{2.25}$$

Here P_a [%] is the actual power output and P_c [%] is the commanded power demand. P_c is computed as a function of the throttle position as described below and the engine time constant τ_{eng} [sec] is scheduled as also described below in order to achieve a satisfactory engine dynamics. The thrust force T [N] of each engine is typically determined as a function of the actual power, the altitude, and the Mach number for idle, military, and maximum power settings.

As mentioned above, the commanded power is computed as a function of the throttle position δ_{th} ($0 \le \delta_{th} \le 1$) as follows [10]:

$$P_c(\delta_{th}) = \begin{cases} (64.94)\delta_{th} & \text{if } \delta_{th} \le 0.77 \\ (217.38)\delta_{th} - 117.38 & \text{if } \delta_{th} > 0.77 \end{cases} \tag{2.26}$$

As for the engine time constant τ_{eng}, it is scheduled as a function of P_c as follows:

$$1/\tau_{eng} = \begin{cases} 5 & \text{if } P_c \ge 50 \text{ and } P_a \ge 50 \\ (1/\tau_{eng})^* & \text{if } P_c \ge 50 \text{ and } P_a < 50 \\ 5 & \text{if } P_c < 50 \text{ and } P_a \ge 50 \\ (1/\tau_{eng})^* & \text{if } P_c < 50 \text{ and } P_a < 50 \end{cases} \tag{2.27}$$

Where

$$(1/\tau_{eng})^* = \begin{cases} 1 & \text{if } (P_c - P_a) \le 25 \\ 0.1 & \text{if } (P_c - P_a) \ge 50 \\ 1.9 - 0.036(P_c - P_a) & \text{if } 25 < (P_c - P_a) < 50 \end{cases} \tag{2.28}$$

Finally, the resultant total thrust (T_{tot}) can be estimated using the following approximate formula, which involves the idle, military, and maximum thrust values as well as the actual power of the engine:

$$T_{\text{tot}} = \begin{cases} T_{\text{idle}}(M,h) + (T_{\text{mil}}(M,h) - T_{\text{idle}}(M,h))(\frac{P_a}{50}) & \text{if } P_a < 50 \\ T_{\text{mil}}(M,h) + (T_{\text{max}}(M,h) - T_{\text{mil}}(M,h))(\frac{P_a - 50}{50}) & \text{if } P_a \ge 50 \end{cases} \tag{2.29}$$

2.4. Modeling the Flight Environment of the Aircraft

The air density ρ [kg/m^3] and the speed of sound v_s [m/sec] are calculated using the ICAO model of the standard atmosphere [57]. According to this model, $\rho = \rho_0(1-0.00002256h^{4.256})$ and $v_s = (\gamma RT)^{1/2}$. Here, γ =1.4, R is the specific gas constant, ρ_0 is the air density at the sea level, and T [K] is the ambient temperature of the surrounding air. It is expressed as $T = T_0(1-0.00002256h)$, where T_0 is the ambient temperature at the sea level and h [m] is the altitude. The Mach number is expressed as $M = V_T / v_s$ and the dynamic pressure is expressed as $Q_d = (1/2)\rho V_T^2$ where V_T is the speed of the aircraft.

The curvature of the earth is ignored and the earth fixed reference frame is assumed to be inertial. It is also assumed that the gravity field is uniform, i.e. g is constant.

The position of the aircraft (the position of the aircraft center of gravity relative to the earth axes) is found by integrating the velocity components in the earth fixed reference frame as shown in equation (2.31). These components are calculated by using the velocity components in the body fixed reference frame. This is shown in equation (2.30).

$$\begin{bmatrix} \dot{x}(t) \\ \dot{y}(t) \\ \dot{z}(t) \end{bmatrix} = \hat{C}^{(o,b)}(t) \begin{bmatrix} u(t) \\ v(t) \\ w(t) \end{bmatrix} - \begin{bmatrix} V_w(t)\cos(\psi_v(t)) \\ V_w(t)\sin(\psi_v(t)) \\ \dot{z}_w(t) \end{bmatrix} \tag{2.30}$$

Here, $V_w(t)$ and $\psi_v(t)$ are the wind speed and direction expressed in the earth fixed reference frame. $\dot{z}_w(t)$ is the possible component of wind in the vertical axis of the earth fixed reference frame.

$$\begin{bmatrix} x(t) \\ y(t) \\ z(t) \end{bmatrix} = \begin{bmatrix} \int_0^t \dot{x}(t')dt' \\ \int_0^t \dot{y}(t')dt' \\ \int_0^t \dot{z}(t')dt' \end{bmatrix} \tag{2.31}$$

2.5. Modeling the Thrust-Vectoring Paddles

Thrust-vectoring applications encountered in some research and development programs focused on vectoring either in the pitch plane to improve the pitch control performance or in the yaw plane to improve the yaw control performance. There are also typical research aircrafts integrated with thrust-vectoring both in the pitch and yaw planes. These aircrafts are *X-31A* and *NASA F-18 HARV*. Both aircrafts are fitted with a thrust-vectoring system that employs three post-exit vanes radially displaced about their axisymmetric nozzles.

The geometry of the TVCS hardware uses three vanes mounted around each engine of the F-18 airplane. Vanes replace the standard divergent section of the nozzle and external flaps. The convergent section of the nozzle remains on the aircraft. The characterization data of an axisymmetric nozzle with post-exit exhaust vanes were provided by testing ground-based models of the F-18 HARV with the TVCS installed. These tests characterized the aerodynamic interaction effects on a full-configuration and supplied further examination on aerodynamic interaction effects caused by vectoring the exhaust plume.

Figure 55 shows the vane configuration for one engine. The upper-vane centerline is 5° outboard of the vertical plane. The outboard-vane centerline is 118° counterclockwise from the upper-vane centerline. The outboard-vane centerline to the lower-vane centerline measurement is 103.5° counterclockwise. The lower-vane centerline to the upper-vane centerline measurement is 138.5° counterclockwise. The upper vane was larger than the outer or lower vanes because of the uneven radial spacing caused by structural considerations. The exhaust-plume side of each vane is concave with each vane forming part of a spherical surface of 36 in radius axially and laterally.

The total amount of turning of the jet exhaust plume, or jet-turning angle, is defined as the root mean square of the equivalent thrust-vector deflection angle in pitch and yaw as measured by the resultant force. This is shown in Figure 56. The axial thrust loss for the deflected flow is defined as the loss in the thrust of the axial force when compared to the un-deflected thrust. The normalized axial thrust is the absolute value of the axial force divided by the absolute value of the un-deflected thrust.

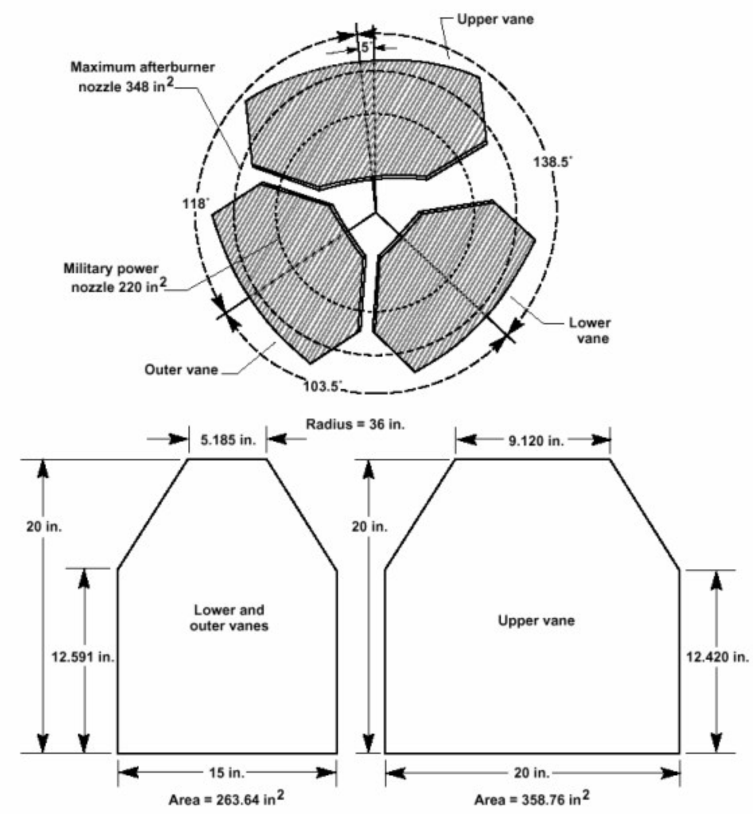

Figure 55. Vane Configuration for One Engine of HARV [56]

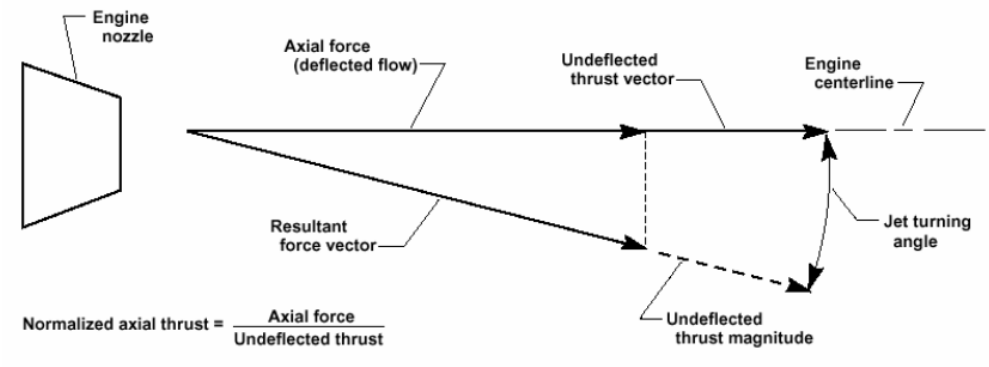

Figure 56. Jet Turning Angle and Axial Thrust Loss [56]

The thrust vectoring characterization tests on HARV lead to the results presented below [56]. The jet turning angle as a function of upper vane deflection and varying nozzle pressure ratio (NPR), i.e. the ratio of the air pressure at the outlet of the nozzle to the ambient pressure, with the military-power nozzle are shown at Figure 57. This figure also shows the axial thrust loss when the paddles are actuated and the thrust is deviated.

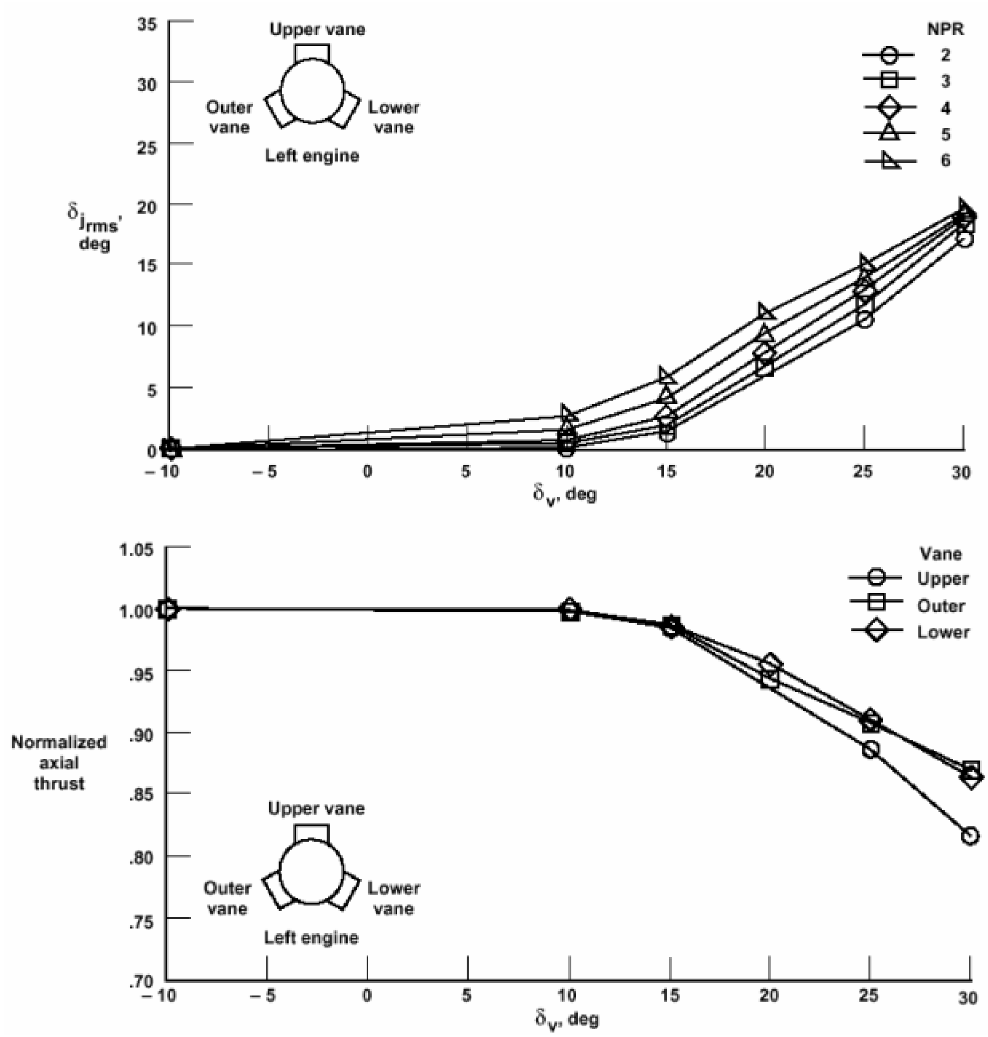

Figure 57. Consecutive Thrust Deviation and Axial Thrust Loss [56]

For longitudinal and lateral planes of motion maximum jet turning angle envelope in pitch and yaw where at least one vane is deflected 30° is shown in Figure 58. Maximum afterburner nozzle and varying nozzle pressure ratios are included and retracted vane interference near corners are also shown. As noted, the envelope contours are not affected by different values of NPR. The idle, military and maximum power settings of the engine all result in similar but smaller envelopes.

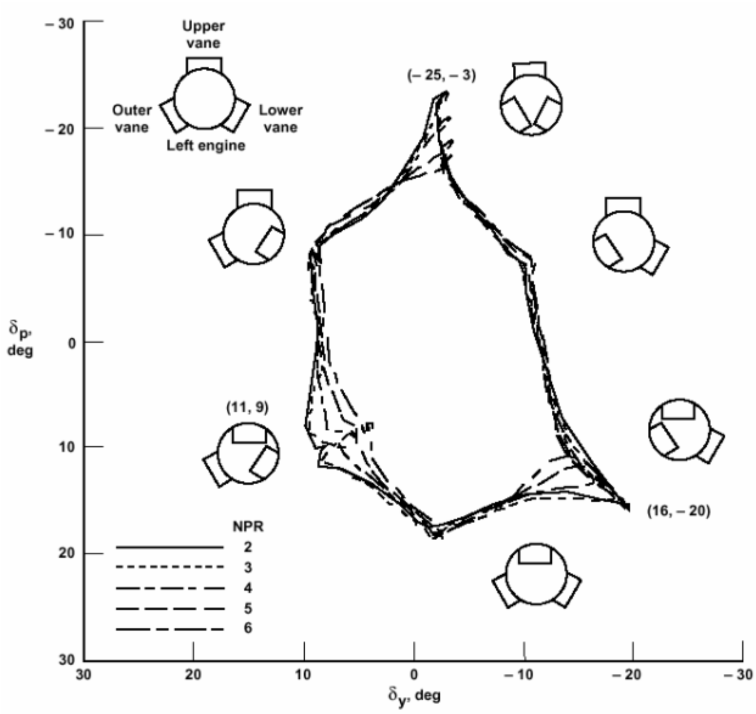

Figure 58. Maximum Jet Turning Angle Envelope for Pitch and Yaw [56]

The fighter-bomber aircraft considered in this study does not originally have the capability of thrust-vectoring. Therefore, it is assumed that it is also virtually fitted with a similar thrust-vectoring system as those that are used for the X-31A and NASA F-18 HARV aircrafts.

Throughout this study, a jet turning envelope similar to that of the HARV aircraft is generated for the modeling purposes. In that generic envelope different nozzle pressure ratios and engine power settings are neglected.

The virtually fitted thrust-vectoring system has three thrust-vectoring paddles on each of the right and left engines. Therefore, thrusts of the right and left engines can be deviated individually. A hexagonal shaped envelope is generated to define the transformation between the thrust-vectoring paddle deflections and the resultant thrust deviation angles. All of the three paddles of an engine are assumed to deflect 30° at most. The generated envelope is shown in Figure 59.

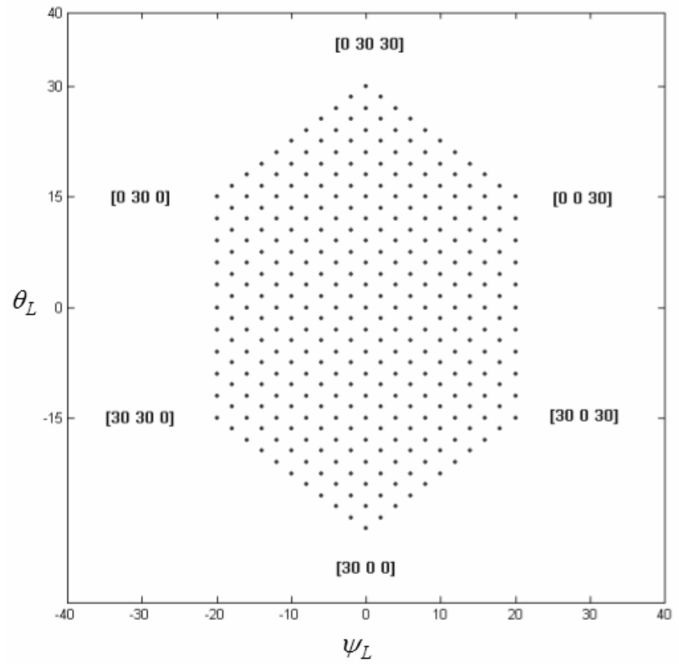

Figure 59. Maximum Jet Turning Envelope for the Modeled Aircraft [58]

Since the envelope is hexagonal shaped, maximum deflections of the three paddles lead to different maximum values of lateral and longitudinal thrust deviations which are 30° for pitch and 20° for yaw respectively. On the other hand, if the resultant pitch deflections are in between 15° and 30°, maximum yaw deflections should be less than 20°. The left engine equations defining the transformation between the thrust-vectoring paddle deflections and the resultant thrust deviation angles are shown through equations (2.32) to (2.35).

$$\begin{bmatrix} \theta_L \\ \psi_L \end{bmatrix} = \begin{bmatrix} -(30/30) & (1/2)(30/30) & (1/2)(30/30) \\ 0 & (20/30) & -(20/30) \end{bmatrix} \begin{bmatrix} \delta_{L1} \\ \delta_{L2} \\ \delta_{L3} \end{bmatrix} \tag{2.32}$$

$$\begin{bmatrix} \theta_L \\ \psi_L \end{bmatrix} = \begin{bmatrix} 1/2 & 1/2 \\ 2/3 & -2/3 \end{bmatrix} \begin{bmatrix} \delta_{L2} \\ \delta_{L3} \end{bmatrix} - \begin{bmatrix} \delta_{L1} \\ 0 \end{bmatrix} \tag{2.33}$$

$$\begin{bmatrix} \delta_{L2} \\ \delta_{L3} \end{bmatrix} = \begin{bmatrix} 1/2 & 1/2 \\ 2/3 & -2/3 \end{bmatrix}^{-1} \left\{ \begin{bmatrix} \theta_L \\ \psi_L \end{bmatrix} + \begin{bmatrix} \delta_{L1} \\ 0 \end{bmatrix} \right\} \tag{2.34}$$

$$\begin{bmatrix} \delta_{L2} - \delta_{L1} \\ \delta_{L3} - \delta_{L1} \end{bmatrix} = \begin{bmatrix} \theta_L + (3/4)\psi_L \\ \theta_L - (3/4)\psi_L \end{bmatrix} \tag{2.35}$$

From (2.35) it is seen that δ_{L1}, δ_{L2} and δ_{L3} cannot be solved independently. Only the differences $\delta_{L2} - \delta_{L1}$ and $\delta_{L3} - \delta_{L1}$ can be solved. The proposed solution method is as follows: $\delta_{L2} - \delta_{L1}$ and $\delta_{L3} - \delta_{L1}$ are found by assigning a proper value to δ_{L1}. This value is assigned as described below:

$$\begin{array}{ll} \text{if } (\delta_{L2} < 0^\circ) \text{ and } (\delta_{L3} > 0^\circ) \text{ then} & \delta_{L1} = |\delta_{L2}| \\ \text{if } (\delta_{L3} < 0^\circ) \text{ and } (\delta_{L2} > 0^\circ) \text{ then} & \delta_{L1} = |\delta_{L3}| \\ \text{if } (\delta_{L3} < 0^\circ) \text{ and } (\delta_{L2} < 0^\circ) \text{ then} & \delta_{L1} = \max(|\delta_{L2}|, |\delta_{L3}|) \end{array} \tag{2.36}$$

It can be seen in Figure 59 that $\psi_{L\max}$ decreases with increasing θ_L in the range between 15° and 30°. Thus, all of the three paddle deflections will be positive and limited in the range between and 0° and 30°. This is implemented as shown below:

$$|\psi_{L\max}| = \begin{cases} 20^\circ & \text{if} \quad |\theta_L| < 15^\circ \\ 20^\circ(1 - (|\theta_L| - 15^\circ)/15^\circ) & \text{if} \quad 15^\circ \le |\theta_L| \le 30^\circ \end{cases} \tag{2.37}$$

As for the mechanization the three thrust-vectoring paddles are actuated independently and the actuation dynamics is modeled simply as follows:

$$\begin{bmatrix} \dot{\delta}_{L1} \\ \dot{\delta}_{L2} \\ \dot{\delta}_{L3} \end{bmatrix} = (2\pi f_{nT}) \left\{ \begin{bmatrix} \delta_{L1com} \\ \delta_{L2com} \\ \delta_{L3com} \end{bmatrix} - \begin{bmatrix} \delta_{L1} \\ \delta_{L2} \\ \delta_{L3} \end{bmatrix} \right\} \tag{2.38}$$

Here the commanded (com) values are determined by the preceding equations and $f_{nT} = 30\,\mathrm{Hz}$.

2.6. Turbulence and Discrete Gust Model

2.6.1. Dryden Wind Turbulence Model

Dryden spectral representation is implemented to add turbulence by passing band-limited white noise through appropriate forming filters. The mathematical representation is from the military specification MIL-F-8785C [44]. Turbulence can be considered as a stochastic process defined by velocity spectra. For an aircraft flying at a speed V through a "frozen" turbulence field with a spatial frequency of Ω radians per meter, the circular frequency ω is calculated by multiplying V_T by Ω. The appropriate component spectra for the Dryden models of turbulence in the longitudinal, lateral and vertical directions are shown here.

$$\Phi_u(\omega) = \frac{2\sigma_u^2 L_u}{\pi V} \cdot \frac{1}{1 + (L_u \frac{\omega}{V})^2}, \quad \Phi_{p_g}(\omega) = \frac{\sigma_w^2}{V L_w} \cdot \frac{0.8\left(\frac{\pi L_w}{4b}\right)^{\frac{1}{3}}}{1 + \left(\frac{4b}{\pi}\frac{\omega}{V}\right)} \tag{2.39}$$

$$\Phi_v(\omega) = \frac{\sigma_v^2 L_v}{\pi V} \cdot \frac{1 + 3(L_v \frac{\omega}{V})^2}{[1 + (L_v \frac{\omega}{V})^2]^2}, \quad \Phi_r(\omega) = \frac{\left(\frac{\omega}{V}\right)^2}{1 + \left(\frac{3b}{\pi}\frac{\omega}{V}\right)^2} \cdot \Phi_v(\omega) \tag{2.40}$$

$$\Phi_w(\omega) = \frac{\sigma_w^2 L_w}{\pi V} \cdot \frac{1 + 3(L_w \frac{\omega}{V})^2}{[1 + (L_w \frac{\omega}{V})^2]^2}, \qquad \Phi_q(\omega) = \frac{\left(\frac{\omega}{V}\right)^2}{1 + \left(\frac{4b}{\pi}\frac{\omega}{V}\right)^2} \cdot \Phi_w(\omega) \tag{2.41}$$

Here, *b* is the aircraft wingspan, L_u, L_v, L_w are the turbulence scale lengths, and σ_u, σ_v, σ_w are the turbulence intensities. To generate a signal with the correct characteristics a unit variance band-limited white noise signal is passed through appropriate forming filters that are derived by taking the spectral square roots of the spectrum equations. The resulting transfer functions for the longitudinal, lateral and vertical directions are shown here.

$$H_u(s) = \sigma_u \sqrt{\frac{2L_u}{\pi V}} \frac{1}{1 + \frac{L_u}{V}s},$$

$$H_p(s) = \sigma_w \sqrt{\frac{0.8}{V}} \frac{(\pi/(4b))^{1/6}}{L_w^{1/3}\left(1 + \left(\frac{4b}{\pi}\right)s\right)} \tag{2.42}$$

$$H_v(s) = \sigma_v \sqrt{\frac{L_v}{\pi V}} \frac{1}{(1 + \frac{L_v}{V}s)^2},$$

$$H_r(s) = \frac{s/V}{\left(1 + \left(\frac{3b}{\pi V}\right)s\right)} \cdot H_v(s) \tag{2.43}$$

$$H_w(s) = \sigma_w \sqrt{\frac{L_w}{\pi V}} \frac{1}{(1 + \frac{L_w}{V}s)^2}, \tag{2.44}$$

$$H_q(s) = \frac{s/V}{\left(1+\left(\frac{4b}{\pi V}\right)s\right)} \cdot H_w(s)$$

For medium to high altitudes the turbulence scale lengths and intensities are based on the assumption that the turbulence is isotropic. In military specification (MIL-F-8785C) the scale lengths are as given as $L_u = L_v = L_w = 530$ m.

The turbulence intensities are determined from a lookup table that gives the turbulence intensity as a function of altitude and the probability of the turbulence intensities being exceeded.

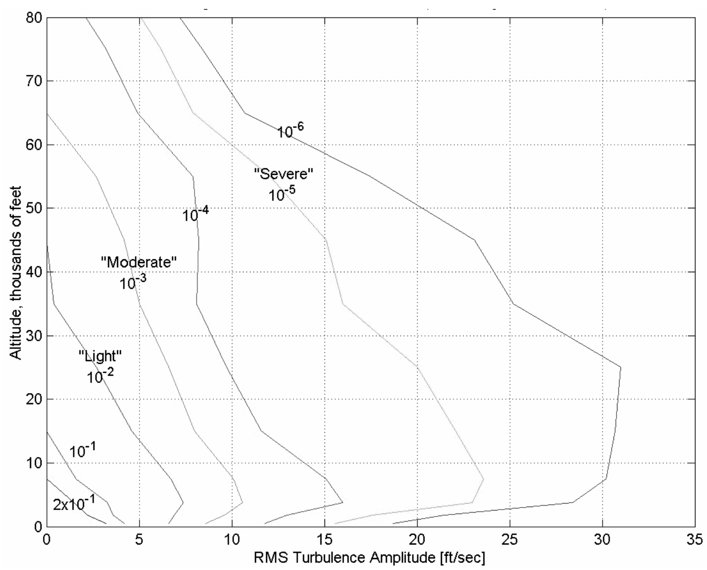

Figure 60. Medium and High Altitude Turbulence Intensities [44]

2.6.2. Discrete Rate Gust Model

A wind gust of the standard "1-cosine" shape is implemented using the military specification (MIL-F-8785C). The gust is applied to each axis individually or to all three axes at once. The gust amplitude (the increase in rotation rate generated by the gust), the gust length (length, in meters, over which the gust builds up) and the gust start time should be specified. The following figure shows the shape of the gust with a start time of zero. The parameters that govern the gust shape are indicated on the diagram.

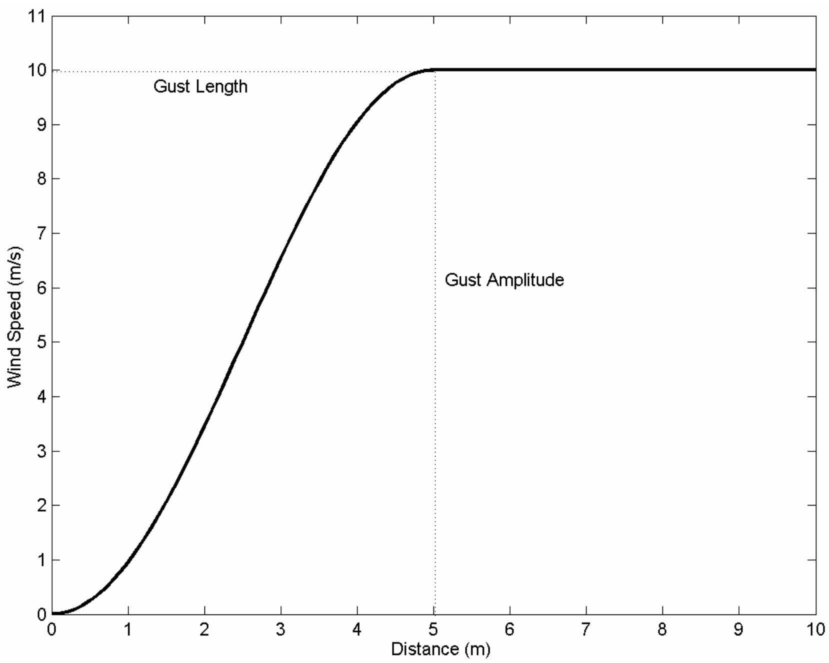

Figure 61. 1 – Cosine Gust Model

The discrete gust can be used to assess aircraft response to large rotation rate disturbances. The mathematical representation of the discrete gust is;

$$m_g = \begin{cases} 0 & x < 0 \\ \dfrac{|m_g|_{\max}}{2}(1-\cos(\dfrac{\pi x}{d_m})) & 0 \le x \le d_m \\ |m_g|_{\max} & x > d_m \end{cases} \quad (2.45)$$

Where, $\left|m_g\right|_{\max}$ is the maximum gust amplitude, d_m is the gust length, x is the distance traveled and m_g is the resultant incremental rotation rate caused by gust in the body axis frame.

2.7. Modeling the Sensors

In this section the modeling of the sensors necessary for the feedback variables in the control loops are presented. The modeled sensors are; the INS, the IMU, the AoA and the sideslip sensors.

The INS has the accelerometers (for the changes in velocity in the inertial frame) and the gyroscopes (for the changes in attitude with respect to the inertial frame). The accelerometers measure how the vehicle is moving in space. In order to measure the motion in three directions (up and down, left and right and forward and back) there are three accelerometers mounted orthogonally at each axis. The gyroscopes measure how the vehicle is rotating in space. In general, there are three sensors for each of the three axes (pitch, yaw and roll). A computer continually calculates the vehicle's current position. This is done by integrating the sensed amount of acceleration over time to find the current velocity. Transforming the calculated velocity to the inertial frame using the attitude (calculated from the gyroscope measurements) then integrating the velocity to figure the current position. The INSs are now usually combined with other systems such as; GPS (used to correct for long term drift in position), a barometric system (for altitude correction), a magnetic compass (for attitude correction) or an odometer (used to correct for long term drift in velocity) to compensate and correct the accumulated errors of the inertial system.

There are different types of INS systems as gimbaled and gyro-stabilized platforms, fluidic suspended gyro-stabilized platforms and strapdown systems. Although the former two systems are used in the past due to the advances in the field of lightweight digital computers the gimbaled systems are eliminated. In the strapdown systems the sensors are simply strapped to the vehicle which is reducing the cost, removing the need for lots of calibrations and increases the reliability by eliminating some of the moving parts.

The IMUs are normally one sensor component of the INSs. Other systems such as GPS (used to correct for long term drift in position), a barometric system (for altitude correction), a magnetic compass (for attitude correction) or an odometer (used to correct for long term drift in velocity) compensate for the limitations of an IMU. The sole property of an IMU is to detect the current acceleration and rate of change in attitude. The IMU (sensor) generally contains 3 accelerometers and 3 gyroscopes that are placed in such a way that their measuring axes are orthogonal to each other.

Both the gyroscopes and the accelerometers are very sensitive to temperature changes. Their error characteristics can be changed with the changing temperature. Thus, within the IMUs temperature sensors are included to act as additional sensors to calibrate the raw data of the gyroscopes (and accelerometers). There are also IMUs with the box designed such that the inside temperature is controlled and kept constant to achieve superior accuracy. Moreover, the walls of the box are made of materials that minimize electromagnetic interference.

IMUs are the typical sources of the accumulated errors. INSs use the measurements of the IMUs and continually add measured changes to the current velocity, position and attitude. This leads to the accumulated errors (drifts) between the calculated and actual values. As discussed before the inertial systems are combined with some other systems to correct for long term drifts.

The IMUs are, in general, produced from force feedback, pendulous rebalanced or vibrating beam type accelerometers and Ring Laser Gyroscopes (RLG), Fiber Optical Gyroscopes (FOG) and Micro-Electro Mechanic Systems (MEMS) gyroscopes. All of these sensors are produced from different materials and processed with different techniques that result in different error characteristics.

The errors sources on IMUs have both deterministic and stochastic nature. The well-known errors on these sensors are the bias errors, the instability of the bias, the scale factor and the misalignment errors. Most important of these errors are the bias and the bias instability. Others are also important; however, a valuable amount of calibration work is done to get rid of these errors in the laboratories before the products are released. Thus, they are not included in the modeling.

As mentioned before the outputs of the gyroscopes are the body angular velocities. Hence, a gyroscope triad in an IMU measures $\bar{\omega}_{b/o}^{(b)} = [p\ q\ r]^{\mathrm{T}}$ with errors. The measurements of the gyroscope triad (p_m, q_m, r_m) can be expressed as

$$\begin{bmatrix} p_m \\ q_m \\ r_m \end{bmatrix} = \begin{bmatrix} p \\ q \\ r \end{bmatrix} + \begin{bmatrix} b_p \\ b_q \\ b_r \end{bmatrix} + \begin{bmatrix} n_p \\ n_q \\ n_r \end{bmatrix} \tag{2.46}$$

Here, b_p, b_q, b_r are the constant biases and n_p, n_q, n_r are the stochastic bias instability signals on the roll, pitch and yaw gyroscopes. The b_p, b_q, b_r terms indicate the constant offset values on the rate measurements and n_p, n_q, n_r are the noise signals with random nature. In the next coming paragraphs the modeling of n_p, n_q, n_r signals is discussed.

In many instances the use of white Gaussian noise maybe enough to describe the noise signals. However, for some applications it would be desirable to be able to generate empirical autocorrelation or power spectral density data and then develop a mathematical model that would produce an output with similar characteristics. If observed data were in samples from a “random walk” motion or stationary Gaussian process with a known rational power spectral density, then a linear time invariant system, i.e. a shaping filter, driven by stationary white Gaussian noise provides such a model [45]. Furthermore, if only the first and second order statistics of a stationary process are known (which is often the case) then a Gaussian process with the same first and second order statistics can always be generated via a shaping filter. Suppose a system is defined as

$$\dot{\hat{x}}(t) = \hat{F}(t)\hat{x}(t) + \hat{G}(t)n(t)$$
$$z(t) = \hat{H}(t)\hat{x}(t) \tag{2.47}$$

Here, $n(t)$ is non-white and time-correlated Gaussian noise that is generated by the following linear shaping filter

$$\dot{\hat{x}}_f(t) = \hat{F}_f(t)\hat{x}_f(t) + \hat{G}_f(t)w(t)$$
$$n(t) = \hat{H}_f(t)\hat{x}_f(t) \tag{2.48}$$

The subscript f denotes the filter and $w(t)$ is a white Gaussian noise process. The filter output $n(t)$ is used to drive the system as shown in Figure 62.

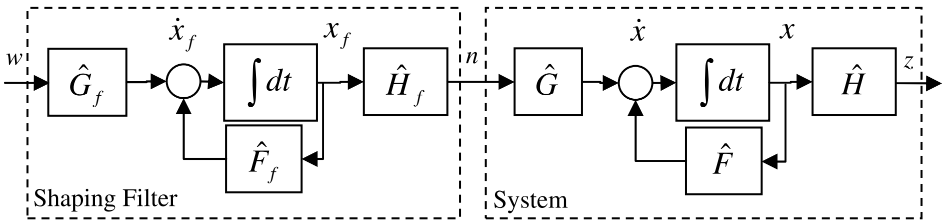

Figure 62. Shaping Filter and System

Hence the overall system can be defined as an augmented system driven by a white Gaussian noise:

$$\begin{bmatrix} \dot{\hat{x}}(t) \\ \dot{\hat{x}}_f(t) \end{bmatrix} = \begin{bmatrix} \hat{F}(t) & \hat{G}(t)\hat{H}_f(t) \\ \hat{0} & \hat{F}_f(t) \end{bmatrix} \begin{bmatrix} \hat{x}(t) \\ \hat{x}_f(t) \end{bmatrix} + \begin{bmatrix} \hat{0} \\ \hat{G}_f(t) \end{bmatrix} w(t)$$
$$z(t) = \begin{bmatrix} \hat{H}(t) \\ \hat{0} \end{bmatrix}^{\mathrm{T}} \begin{bmatrix} \hat{x}(t) \\ \hat{x}_f(t) \end{bmatrix} \tag{2.49}$$

There are certain shaping filter configurations useful enough for process modeling. The very first one is the "white Gaussian noise" itself. It has a mean m_0 and an auto-correlation $E\{w(t)w(t+\tau)\} = (P_0 + m_0^2)\delta(t) = X_0(\tau)$. The second one is the "constant bias" model. It is the output of an integrator without an input and with an initial condition modeled as a Gaussian random variable $x(t_0)$ with specified mean m_0 and variance P_0. The defining relationship is $\dot{x}(t) = 0$ with initial condition $x(t_0)$. In that case no noise is driving the shaping filter equation. This leads to constant samples in time and constant autocorrelation in τ.

$$\Psi_{xx}(\tau) = E\{x(t)x(t+\tau)\} = (P_0 + m_0^2) \tag{2.50}$$

This model is generally used for turn on to turn on biases of rate gyros that remains constant in single run. If any time varying error characteristics is desired to be modeled the "random walk" model is appropriate. Using that model slowly varying bias (unexpectedly due to failure or degradation of the sensor) can also be estimated. The random walk is the output of an integrator driven by white Gaussian noise. The defining relationship is $\dot{x}(t) = w(t)$ with initial condition $x(t_0) = 0$. Here $w(t)$ is zero mean and $E\{w(t)w(t+\tau)\} = Q\delta(t)$. The mean equation is the same as for the random constant and equal to $m_x(t) = m_x(t_0)$. However, the second order statistics is $\dot{P}_{xx}(t) = Q$ instead of $\dot{P}_{xx}(t) = 0$. This means that the estimated value of mean squared error is growing in time, i.e. $E\{x^2(t)\} = Q(t - t_0)$.

First order Gauss-Markov (exponentially time correlated) process models are first order lags driven by zero mean white Gaussian noise of strength Q ($E\{w(t)w(t+\tau)\} = Q\delta(t)$). The related autocorrelation is given as

$$\Psi_{xx}(\tau) = E\{x(t)x(t+\tau)\} = \sigma^2 e^{-|\tau|/T} \tag{2.51}$$

Here σ^2 is the mean squared value (with mean zero) and T is the correlation time. The model is described by $\dot{x}(t) = (-1/T)x(t) + w(t)$. In that case the second order statistics is defined as $\dot{P}_{xx}(t) = (-2/T)P_{xx}(t) + Q\delta(t)$. At the steady state condition (when $\dot{P}_{xx}(t) = 0$) it can be shown that $Q = (2/T)P_{ss}$ where $P_{ss} = E\{x^2(t)\} = \sigma^2$. Hence, once σ and τ for any output signal are known, the strength of the zero mean white Gaussian noise input signal, i.e. Q, can be calculated.

The bias instability signals in equation (2.46) (n_p, n_q, n_r) are modeled as they are generated using the first order Gauss-Markov process shaping filters. This is shown (for roll gyroscope) in the following figure and equation (2.52).

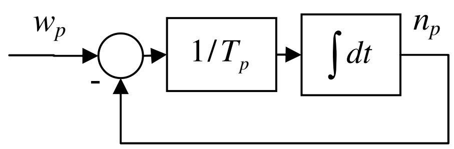

Figure 63. 1st Order Gauss-Markov Shaping Filter for a Single Gyroscope

$$\begin{aligned} T_p\dot{n}_p(t) + n_p(t) &= w_p(t) \\ T_q\dot{n}_q(t) + n_q(t) &= w_q(t) \\ T_r\dot{n}_r(t) + n_r(t) &= w_r(t) \end{aligned} \tag{2.52}$$

Here, T_p, T_q, T_r are the time constants of the first order Gauss-Markov process and w_p, w_q, w_r are the white Gaussian noises effecting on each of the gyroscopes.

An INS outputs the attitude of the vehicle that it is mounted onto. It measures the Euler angles ψ, θ, and ϕ. As expected these measurements have also some errors on them. Again neglecting the scale factor and the misalignment errors the attitude measurements can be expressed as

$$\begin{bmatrix} \phi_m \\ \theta_m \\ \psi_m \end{bmatrix} = \begin{bmatrix} \phi \\ \theta \\ \psi \end{bmatrix} + \begin{bmatrix} b_\phi \\ b_\theta \\ b_\psi \end{bmatrix} + \begin{bmatrix} n_\phi \\ n_\theta \\ n_\psi \end{bmatrix} \tag{2.53}$$

Here, b_ϕ, b_θ, b_ψ are the constant biases and n_ϕ, n_θ, n_ψ are the stochastic bias instability signals on the roll, pitch and yaw measurements. The b_ϕ, b_θ, b_ψ terms indicate the constant offset values on the Euler angle measurements and n_ϕ, n_θ, n_ψ are the bias instability signals. As for the gyroscopes, they are modeled to be generated by using the first order Gauss-Markov process shaping filters. This is shown in the following equation.

$$\begin{aligned} T_\phi \dot{n}_\phi(t) + n_\phi(t) &= w_\phi(t) \\ T_\theta \dot{n}_\theta(t) + n_\theta(t) &= w_\theta(t) \\ T_\psi \dot{n}_\psi(t) + n_\psi(t) &= w_\psi(t) \end{aligned} \tag{2.54}$$

Here, T_ϕ, T_θ, T_ψ are the time constants of the first order Gauss-Markov process and w_ϕ, w_θ, w_ψ are the white Gaussian noises effecting on the measurements of Euler angles.

The INS calculates the Euler angles by processing all the data that it gathers. In an attitude estimation algorithm primarily the output of the gyroscopes is used. Necessarily, the information coming from the gyroscopes is blended with the output of the accelerometers. Moreover, all data is processed in a Kalman filter estimating the attitude of the vehicle by using the position, velocity (and attitude) measurements coming from the external aiding devices such as GPS, Doppler radar, magnetometer, etc. When the calculation process is considered the Euler angle measurements coming from the INS takes longer time than reading the body angular velocities from the gyroscopes. Thus, first order time lag sensor dynamics models are introduced into equation (2.53).

$$\begin{aligned} T_{INS}\dot{\phi}' + \phi'(t) &= \phi(t) \\ T_{INS}\dot{\theta}' + \theta'(t) &= \theta(t) \\ T_{INS}\dot{\psi}' + \psi'(t) &= \psi(t) \end{aligned} \tag{2.55}$$

$$\begin{bmatrix} \phi_m \\ \theta_m \\ \psi_m \end{bmatrix} = \begin{bmatrix} \phi' \\ \theta' \\ \psi' \end{bmatrix} + \begin{bmatrix} b_\phi \\ b_\theta \\ b_\psi \end{bmatrix} + \begin{bmatrix} n_\phi \\ n_\theta \\ n_\psi \end{bmatrix} \tag{2.56}$$

Here T_{INS} is the assumed time constant of the INS and ψ', θ', and ϕ' are the lagged outputs driven by actual Euler angle values.

The angle of attack and sideslip sensor systems are used to provide stall warning, depict critical angles of attack during an approach and landing, assist in establishing optimum aircraft attitude for specific conditions of flight (such as maximum range or endurance) and verify airspeed indications or computations. An angle of attack (or sideslip) sensor system consists of sensors, transducers, indicators and stall-warning devices. Generally, there is one or more sensors protrude into the relative airflow.

The flow angles are typically measured with one of three sensors: flow vanes, fixed differential pressure probes, and null-seeking servo actuated differential pressure probes [46]. Flow vanes resemble small weather vanes and are connected to a potentiometer or other angle-measuring transducers. These vanes should be mass-balanced to remove biases and to improve precision in dynamic maneuvers. Flow vanes tend to be more sensitive than the other two sensors, especially at low speeds. On the other hand these vanes are more susceptible to damage than the other sensors are. Fixed differential pressure probes generally are hemispherical or pyramidal headed probes with two pressure ports for measuring the flow angle in each axis. When the two pressures are equal, the probe is aligned with the flow. A nonzero differential pressure can be converted to the angle of the flow to the probe. The null-seeking probe is similar to the fixed probe, except that a servo rotates the probe to achieve zero differential pressure. The angle to which the probe is rotated measures the local flow direction relative to the aircraft body datum.

All types of sensors, when aligning with the relative airflow, generate a signal, via a transducer, which is passed to the cockpit indicator either directly or through an air data system. There are various indicators that present the information in the form of actual angles, units or symbols. Most systems incorporate additional devices, such as electrically operated stick shakers and/or horns to warn of impending stalls and stick pushers which activate if stall recovery action is not initiated by the pilot.

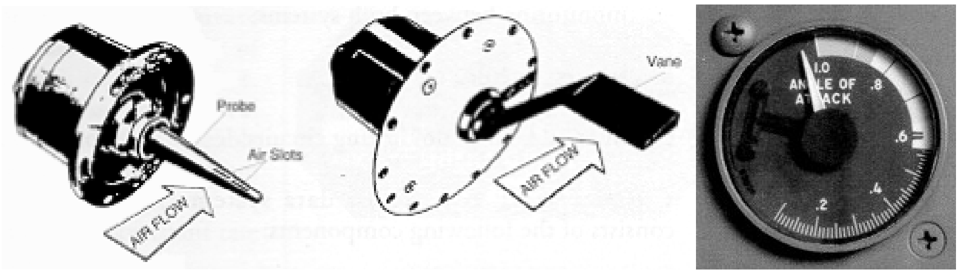

Figure 64. Probe and Vane Type AoA Sensors and an AoA Indicator [46]

The AoA or sideslip sensors are usually located ahead of the aircraft on the fuselage nose or on a wing tip. These are the most commonly used placements to mount the sensors since they should usually be the first part of the aircraft to be affected by the incoming airflow. Although these are the most common places to mount the sensors, they may be located on any part of the body of the aircraft as long as care is taken.

The locations of the flow angle sensors greatly affect their measurement. At subsonic speeds the local angle of attack is affected by flow around the body and wing of the airplane, which is termed “up-wash”. Up-wash affects the sensors near a lifting surface much more than it affects sensors on a nose boom. Wingtip-mounted sensors are greatly influenced by up-wash and side-wash, thus, they are rarely used.

True angle of attack can be determined during steady flight as the difference between the pitch attitude angle and flight path climb angle of the airplane. This analysis requires minimum effort, but the result may not be valid during unsteady flight. To obtain true angle of attack for unsteady flight the winds, airplane ground speed and true airspeed are combined. Assuming that the vertical winds are zero usually is valid for a non-turbulent atmosphere. Dynamic effects on the sensors must also be considered, including the bending of the airplane structure and the effects on accelerometers and flow vanes from angular rate and acceleration.

Typically, AoA sensors are mounted on the side of the fuselage forward of the wing. Upwash caused by wing lift should not affect the sensor in supersonic flow; however, the sensor may be affected by other local shock waves.

In theory, sideslip angle can be calibrated in the same manner as angle of attack. In practice, however, wind variability makes steady flight angle of sideslip calibration difficult because calculated true angle of sideslip is very sensitive to lateral winds [47]. This problem increases in difficulty as aircraft speed decreases. In a similar way that upwash affects AoA, sidewash affects the sideslip angle.

Quantities used to calibrate air data parameters are velocity, attitude, angular rates, angular and linear accelerations and atmospheric data. These quantities are recorded using digital recording. Several of the calibration calculations require earth relative position or velocity components. These data can be determined by an INS, ground based radar, laser, or optical tracker, or GPS. The Euler angles for aircraft attitude can also be measured by INS. An INS generally provides a complete earth relative data set. The angular rates and accelerations of the aircraft are also used in the calibration analyses. IMUs are used to determine these data. To convert the earth referenced data from INS the state of the atmosphere must be known. Measurements of the atmosphere can be made from ground based devices, upper-air weather balloons and satellite data. If direct atmospheric measurements cannot be made (for example, for a vehicle flying in near-space) a first order approximation can be made using a standard atmosphere [48].

The result of the flow angle sensors calibration processes are the calibration charts that give the information on flow angle measurement errors. These errors are generally plotted with respect to changing flow angle and free stream velocity values. Typical calibration charts are shown in Figure 65. Generally, typical flow angle sensor errors are within $\pm 0.2^{\circ}$ to $\pm 1^{\circ}$ bounds depending on the sensor type, aircraft velocity and weather conditions.

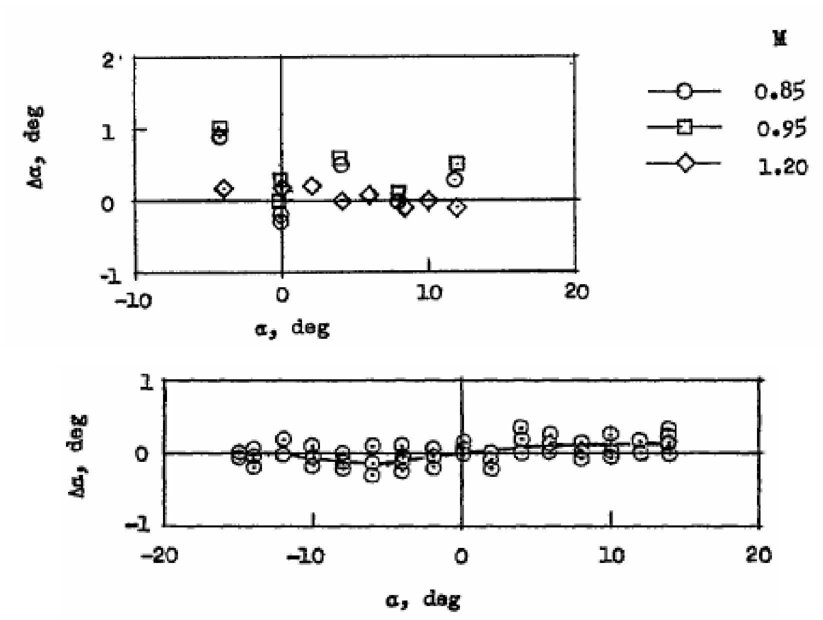

Figure 65. Example Calibration Charts for AoA Sensors [49]

The flow angle sensors have also measurement errors dependent on changing sideslip angles. In other words, although the angle of attack of the aircraft is remaining constant, it will be measured as it is changing with the varying sideslip angle. Thus, the measurement error in the longitudinal plane of motion is coupled with the motion in the lateral plane. This is illustrated in Figure 66.

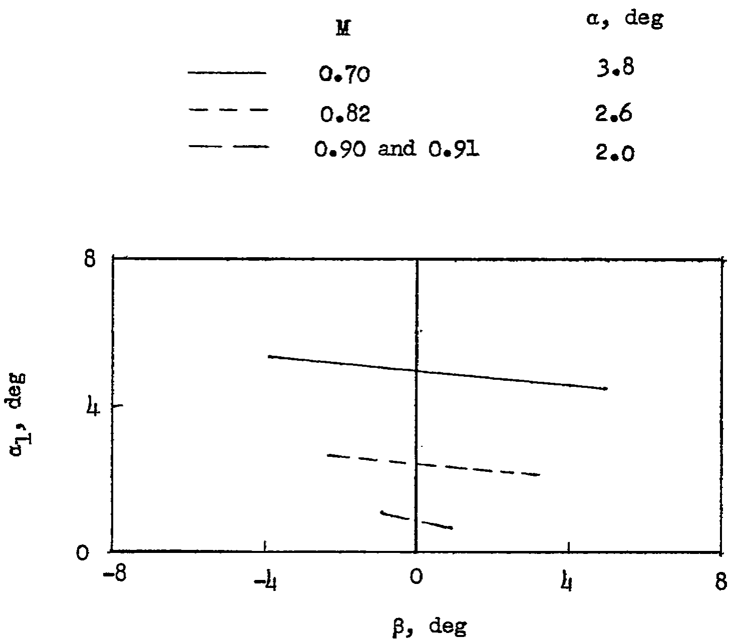

Figure 66. Effect of Sideslip on AoA Measurement [49]

In Figure 66 an AoA sensor is tested at different Mach numbers with varying sideslip angles [49]. The variation of AoA errors (α_1) with sideslip angle (β) turned out to be linear. This first order coupling can be formulated as $\Delta\alpha = (0.1^\circ)\beta$.

Using the aforementioned flow angle sensor error characteristics and neglecting linearity errors the flow angle errors can be expressed as

$$\begin{bmatrix} \alpha_m \\ \beta_m \end{bmatrix} = \begin{bmatrix} 1 & k_{\alpha\beta} \\ k_{\beta\alpha} & 1 \end{bmatrix} \begin{bmatrix} \alpha \\ \beta \end{bmatrix} + \begin{bmatrix} b_\alpha \\ b_\beta \end{bmatrix} + \begin{bmatrix} w_\alpha \\ w_\alpha \end{bmatrix} \tag{2.57}$$

Here, b_α, b_β are the constant biases and w_α, w_β are the white Gaussian noise signals on flow angles. The terms $k_{\alpha\beta}$, $k_{\beta\alpha}$ are used to define the cross-coupling effect of flow angles to each other.

The flow angles are indicated with certain amount of time lag. This is due to operation principles of measuring devices. They are generally potentiometer type of analog devices. Some of them (null-seeking probe type) have servo motors to nullify its own flow angle and measure the difference as the aircrafts flow angle. These are adding time lags on the measurement. Hence, a first order time lag flow angle sensor dynamics models are introduced into equation (2.57).

$$\begin{aligned} T_{FAS}\dot{\alpha}' + \alpha'(t) &= \alpha(t) \\ T_{FAS}\dot{\beta}' + \beta'(t) &= \beta(t) \end{aligned} \tag{2.58}$$

$$\begin{bmatrix} \alpha_m \\ \beta_m \end{bmatrix} = \begin{bmatrix} 1 & k_{\alpha\beta} \\ k_{\beta\alpha} & 1 \end{bmatrix} \begin{bmatrix} \alpha' \\ \beta' \end{bmatrix} + \begin{bmatrix} b_\alpha \\ b_\beta \end{bmatrix} + \begin{bmatrix} w_\alpha \\ w_\alpha \end{bmatrix} \tag{2.59}$$

Here T_{FAS} is the assumed time constant of the flow angle sensors and α', β' are the lagged outputs driven by actual flow angle values.

2.8. Modeling the Human Pilot

The mathematical models of the human operator are used to study the human pilot behavior in well defined tracking tasks and predict pilot to aircraft coupling problems such as *pilot induced oscillations* (PIO). Although the pilot is naturally adaptive the past research has shown that the pilot behaves in a predictable manner when the flying task is well defined. Example tasks are opponent aircraft tracking, landing and pursuit tracking for aerial refueling. In all of these cases a control-theoretic model can be developed.

In most of the classical human operator models the operator adjusts compensation such that the open loop man-machine system has the characteristics of a simple integrator with gain and time delay over a considerable frequency range. The model of that compensation has simple structure that usually includes a compensation gain (K_c), pure time delay (τ_d) and a neuro-motor lag (τ_n). Figure 67 shows a block diagram of a typical classical model of a single axis compensatory man-machine system.

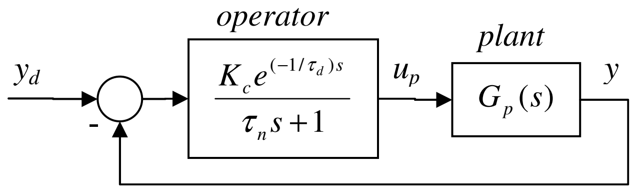

Figure 67. Model of a Single Axis Compensatory Man-Machine System

A unique operator model with a classical structure was proposed by Neal and Smith [50]. The Neal-Smith flying qualities criteria for pitch attitude tracking tasks are the first and only flying qualities criteria in Mil-Std 1797-A [35] that used “pilot in the loop" analysis to arrive at an estimate of an aircraft's flying qualities rating. The adjustment rules specified by Neal and Smith are used to obtain a unique representation of the human pilot.

A frequently used operator modeling is based on optimal control theory [51]. This formulation generates dynamic models for the time delay and neuro-motor lag of the human operator and an optimal controller synthesis used to generate the pilot commands. The overall modeling also includes the errors originating from noisy observations indicated from the displays and environmental disturbances such as engine noise, bad ambiance around the operator (hot cabin weather, high cabin pressure, etc.). Most of these models use a Padé approximation of the time delay so that the closed form transfer function representations of the operator can be obtained [52].

Modeling the pilot is important for opponent aircraft pointing and turn maneuvers control loops. A pilot steers the aircraft by giving commands to throttle (δ_{th}) and body axis roll, pitch and yaw rates (p, q, r). Hence, the pilot generates the desired body angular velocity commands (p_d, q_d, r_d) for the desired maneuvers of the aircraft. Hence, the block diagram of a pilot in the loop model for an aircraft can be constructed as shown in Figure 68.

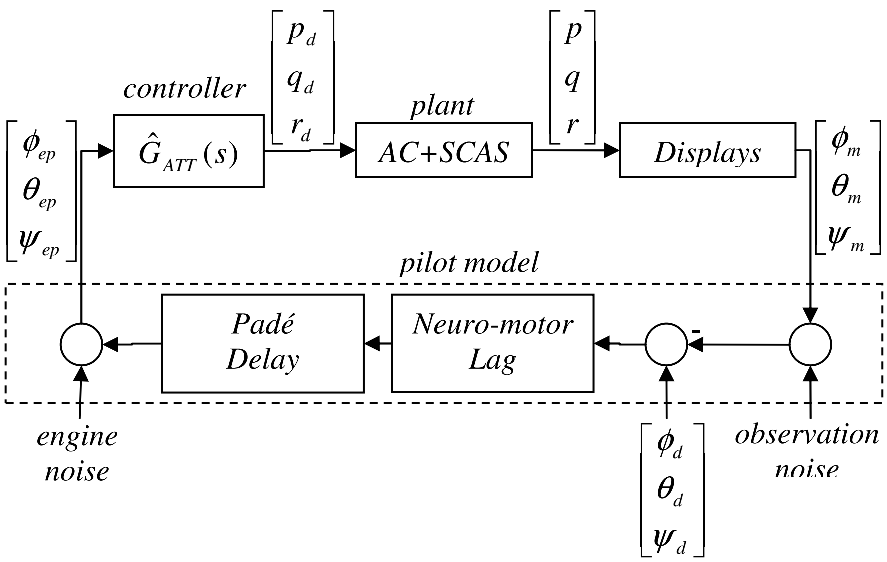

Figure 68. Conceptual Block Diagram of a Human Pilot Model

Here, $\hat{G}_{ATT}(s)$ represents the controller dynamics that generates the desired angular velocity commands. It operates on the pilot processed Euler angle error signals ($\phi_{ep}, \theta_{ep}, \psi_{ep}$) which are originally (before the human pilot procession) the errors between the desired Euler angle commands and the instantaneous values. The observation noise is originating from the cockpit displays (artificial horizon, azimuth direction indicator, etc.).

The desired body angular velocity commands are realized by the body angular velocity control loops. In the literature they are known as *stability and control augmentation systems* (SCAS). In Figure 69 the SCAS loop needed to realize the pilot commands is seen. Here, $\hat{G}_{SAS}(s)$ represents the SCAS controller dynamics, $\hat{G}_{IMU}(s)$ represents the sensor dynamics that measures the body angular velocities (INS, IMU or single gyroscopes) and $\hat{G}_a(s)$ represents the actuator dynamics that physically realizes the digital output signals of the controller (aerodynamic surfaces, TVC system, etc.).

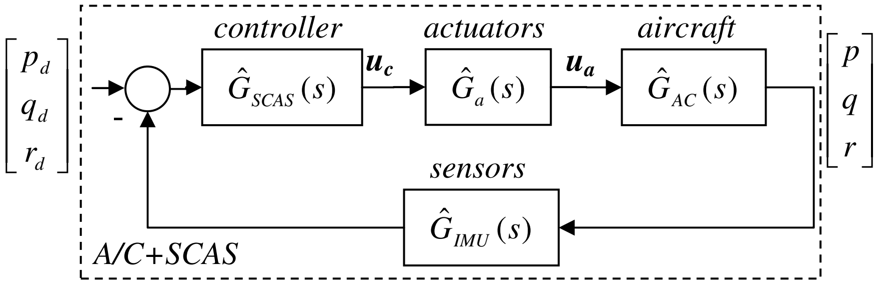

Figure 69. Block Diagram of a Stability and Control Augmentation Loop

In Figure 68 it should be noted that the outputs of the $\hat{G}_{ATT}(s)$ are not directly the desired body angular velocity commands (p_d, q_d, r_d). They are found by multiplying the real output of the $\hat{G}_{ATT}(s)$ (which are $\dot{\phi}_{com}(t)$, $\dot{\theta}_{com}(t)$ and $\dot{\psi}_{com}(t)$) with the matrix $\hat{J}^{(b,o)}$ as shown in equation (2.2). Using $\hat{J}^{(b,o)}$ earth fixed reference frame angular velocities are translated to the body fixed reference frame angular velocities. This is shown as

$$\hat{J}^{(b,o)} = \begin{bmatrix} 1 & 0 & -s\theta(t) \\ 0 & c\phi(t) & c\theta(t)s\phi(t) \\ 0 & -s\phi(t) & c\theta(t)c\phi(t) \end{bmatrix} \tag{2.60}$$

$$\begin{bmatrix} p_d(t) \\ q_d(t) \\ r_d(t) \end{bmatrix} = \begin{bmatrix} p_{com}(t) \\ q_{com}(t) \\ r_{com}(t) \end{bmatrix} = \hat{J}^{(b,o)} \begin{bmatrix} \dot{\phi}_{com}(t) \\ \dot{\theta}_{com}(t) \\ \dot{\psi}_{com}(t) \end{bmatrix} \tag{2.61}$$

The delay and neuro-motor lag dynamics, shown in the previous block diagrams, can be expressed using the time delay coefficients τ_d and τ_n. Here, the pure delay of the neuro-motor lag (τ_n) is expressed in 2nd order Padé approximation:

$$G_d(s) = \frac{1}{\tau_d s + 1} \tag{2.62}$$

$$G_n(s) = \frac{s^2 - 8/\tau_n s + 16/\tau_n^2}{s^2 + 8/\tau_n s + 16/\tau_n^2} \tag{2.63}$$

For the experienced fighter aircraft pilots (and test pilots) the pilot time delay (τ_d) is in between 0.08 sec to 0.15 sec, whereas, the neuro-motor lag (τ_n) is in between 0.08 sec to 0.13 sec.

CHAPTER 3

NONLINEAR INVERSE DYNAMICS CONTROLLER DESIGN

In this chapter, first, general aspects of nonlinear inverse dynamics controller design strategy will be discussed. Then, the nonlinear inverse dynamics controller design for the aircraft will be presented. The controller design based on the thrust vectoring controls will be investigated. Eventually, the constraining equation for the control effectors will be discussed and the stabilization controller and the attitude controller will be presented. Then, the chapter will carry on with the controller design based on aerodynamic control effectors and concluded with blending the aerodynamic and thrust vectoring controls.

3.1. Nonlinear Inverse Dynamics Control

The nonlinear dynamic inversion (NDI) process is explained in Chapter 1. Here, in this section, the mathematical preliminaries to design a controller based on NDI method will be given. In general, the dynamics of an air vehicle can be expressed as

$$\dot{\bar{x}} = \bar{f}(\bar{x}) + \hat{B}(\bar{x})\bar{u} \tag{3.1}$$

$$\bar{y} = \bar{h}(\bar{x}) \tag{3.2}$$

Here, $\bar{x} \in \Re^n$ is the state vector, $\bar{u} \in \Re^m$ is the control vector, $\bar{y} \in \Re^m$ is the output vector, m < n, $\bar{f}(\bar{x})$, $\hat{B}(\bar{x})$, and $\bar{h}(\bar{x})$ are nonlinear state-dependent functions. In order to obtain the direct relationship between $\bar{y}$ and $\bar{u}$, $\bar{y}$ is differentiated until the control input appears explicitly in the expression. In case of an aircraft, only one differentiation happens to be enough to reach such an explicit relationship. That is,

$$\dot{\bar{y}} = \left[\partial\bar{h}(\bar{x})/\partial(\bar{x})\right]\dot{\bar{x}} = \left[\partial\bar{h}(\bar{x})/\partial(\bar{x})\right]\bar{f}(\bar{x}) + \left[\partial\bar{h}(\bar{x})/\partial(\bar{x})\right]\hat{B}(\bar{x})\bar{u} \tag{3.3}$$

If $\left[\partial\bar{h}(\bar{x})/\partial(\bar{x})\right]\hat{B}(\bar{x})$ is invertible for all values of $\bar{x}$, then the inverse dynamics linearization is achieved by means of the following transformation:

$$\bar{u} = \bar{u}(\bar{x},\bar{r}) = \left\{\left[\partial\bar{h}(\bar{x})/\partial(\bar{x})\right]\hat{B}(\bar{x})\right\}^{-1}\left\{\bar{r} - \left[\partial\bar{h}(\bar{x})/\partial(\bar{x})\right]\bar{f}(\bar{x})\right\} \tag{3.4}$$

This transformation converts equation (3.3) into the following simple and linear form: $\dot{\bar{y}} = \bar{r}$. Here, $\bar{r}$ is the auxiliary control vector, which is used as the command vector on $\dot{\bar{y}}$ to force $\bar{y}$ to track a desired output vector $\bar{y}_d(t)$. It can be generated in order to impose the desired motion to the aircraft. In general, proportional (P) or proportional plus integral (PI) control laws turn out to be quite satisfactory for this purpose. In other words, $\bar{r}$ can be generated in one of the following ways:

$$\bar{r}(t) = \omega_{nd}\left[\bar{y}_d(t) - \bar{y}(t)\right] \tag{3.5}$$

$$\bar{r}(t) = 2\zeta_d \omega_{nd} \left[\bar{y}_d(t) - \bar{y}(t)\right] + \omega_{nd}^2 \int_0^t \left[\bar{y}_d(s) - \bar{y}(s)\right] ds \tag{3.6}$$

It is also very important that, if $\dim(\bar{y}) < \dim(\bar{x})$, which is so in general, the control action described above (which constitutes an outer loop for tracking purposes) may not be sufficient to stabilize the whole system. In that case, it will be necessary to use an additional inner control loop with state variable feedback for sake of stability augmentation.

Here, ω_{nd} is the desired natural frequency, and ζ_d is the desired damping coefficient of the closed loop dynamics. After the auxiliary control $\bar{r}$, in order to generate the actual control $\bar{u}$ according to equation (3.4), the state vector $\bar{x}$ has to be completely available and $\left[\partial\bar{h}(\bar{x}) / \partial(\bar{x})\right]\hat{B}(\bar{x})$ should be invertible for all values of $\bar{x}$. On the other hand, when it is invertible but has a small determinant, the control vector becomes large and the actuators may saturate. If this is the case and PI control law is used it is necessary to use an anti-wind up scheme and minimize the integral gain in order to control the accumulation of the error in the integral term.

3.2. Nonlinear Inverse Dynamics Controller Design for the Aircraft

For the aircraft considered here, two separate controllers are designed. One of the controllers manipulates the aerodynamic control effectors only and the other controller manipulates the thrust-vectoring paddles only. Afterwards, these two controllers are blended for the attitude controller which will be explained in detail in the following sections. The thrust vector controller is designed to be turned on whenever the aerodynamic controller loses its effectiveness due to excessive angle of attack values. Therefore, when the thrust vector controller is turned on, the aerodynamic controller is turned off and the aerodynamic control effectors are retracted to their neutral positions $(\delta_{an}, \delta_{en}, \delta_{rn})$ which are generally zero degrees for δ_{an} and δ_{rn} and zero degrees or trim values (δ_{e0}) for δ_{en}. In such a case, the aircraft is controlled only by using the total thrusts T_L and T_R created by the two engines and the thrust vector deviation angle pairs $\{\psi_L, \theta_L\}$ and $\{\psi_R, \theta_R\}$.

3.2.1. Controller Design for the Thrust Vectoring Control Phase

In the case of thrust vectoring controls, using the dynamic inversion control law in association with equations (3.4) and (2.10), the command values for the forces to be created by the left and right engines can be calculated using the following equation for a commanded acceleration state of the aircraft:

$$\hat{G}\begin{bmatrix} \overline{F}^{(b)}_{Lcom} \\ \overline{F}^{(b)}_{Rcom} \end{bmatrix} = \begin{bmatrix} [\dot{u}_{com}\ \dot{v}_{com}\ \dot{w}_{com}]^{\mathrm{T}} \\ [\dot{p}_{com}\ \dot{q}_{com}\ \dot{r}_{com}]^{\mathrm{T}} \end{bmatrix} - \overline{F} - \hat{H}\begin{bmatrix} \overline{F}^{(b)}_{a} \\ \overline{M}^{(b)}_{a} \end{bmatrix} \tag{3.7}$$

However, $\hat{G}$ happens to be an ever singular matrix. This is because it involves the skew symmetric cross-product matrices corresponding to the vectors $\overline{r}^{(b)}_{be_L}$ and $\overline{r}^{(b)}_{be_R}$. Each of these matrices is singular with rank 2. Therefore, $\hat{G}$ is also a rank-deficient matrix. This rank deficiency can be handled as described below. To start with, equation (3.7) can be written again as follows:

$$\begin{bmatrix} \hat{I} & \hat{I} \\ \tilde{r}^{(b)}_{be_L} & \tilde{r}^{(b)}_{be_R} \end{bmatrix}\begin{bmatrix} \overline{F}^{(b)}_{Lcom} \\ \overline{F}^{(b)}_{Rcom} \end{bmatrix} = \begin{bmatrix} \overline{F}^{(b)}_{com} \\ \overline{M}^{(b)}_{com} \end{bmatrix} \tag{3.8}$$

where $\overline{F}^{(b)}_{com}$ and $\overline{M}^{(b)}_{com}$ are the necessary force and moment vectors in order to realize the commanded accelerations completely. They are defined as

$$\begin{bmatrix} \overline{F}^{(b)}_{com} \\ \overline{M}^{(b)}_{com} \end{bmatrix} = \hat{H}^{-1}\left\{\begin{bmatrix} [\dot{u}_{com}\ \dot{v}_{com}\ \dot{w}_{com}]^{\mathrm{T}} \\ [\dot{p}_{com}\ \dot{q}_{com}\ \dot{r}_{com}]^{\mathrm{T}} \end{bmatrix} - \overline{F} - \hat{H}\begin{bmatrix} \overline{F}^{(b)}_{a} \\ \overline{M}^{(b)}_{a} \end{bmatrix}\right\} \tag{3.9}$$

As noted, the coefficient matrix in equation (3.8) is rank-deficient. Therefore, the consistency of that equation can be satisfied by allowing freedom for certain components of $\overline{F}^{(b)}_{com}$ and $\overline{M}^{(b)}_{com}$. Since the left and right engine nozzle exit locations are symmetric with respect to the center line of the aircraft, their position vectors can be expressed as $\overline{r}^{(b)}_{be_L}$ = $[e_x\ e_y\ e_z]^T$ and $\overline{r}^{(b)}_{be_R}$ = $[e_x\ \text{-}e_y\ e_z]^T$. Plugging these expressions into equation (3.8), the following constraint equation is found [58]:

$$M^{(b)}_{ycom} = -e_x F^{(b)}_{zcom} + e_z F^{(b)}_{xcom} \tag{3.10}$$

This, in turn, necessitates allowing freedom for certain components of the commanded translational and angular acceleration vectors. More specifically, only two of the three acceleration components ($\dot{u}, \dot{v}, \dot{w}$) can be commanded arbitrarily; the third one must obey the consistency constraint dictated by the constraint equation. That is;

$$J_y \dot{q}_{com} + e_x m\dot{w}_{com} - e_z m\dot{u}_{com} = -\Delta M_y - e_x \Delta F_z + e_z \Delta F_x \tag{3.11}$$

Furthermore, in return for this restriction, the y components of $\vec{F}_{Lcom}$ and $\vec{F}_{Rcom}$ can be chosen arbitrarily such that their sum will be equal to the y component of $\overline{F}^{(b)}_{com}$. Here, they are chosen to be equal to each other. In equation (3.11), J_y is the inertia component of the aircraft along the y direction of the body fixed frame, m is the mass of the aircraft and ΔM_y, ΔF_z and ΔF_x originate from equation (3.7). They are expressed as

$$\Delta F_x = mV\left[q\sin(\alpha)\cos(\beta) - r\sin(\beta)\right] + mg\sin(\theta) - F^{(b)}_{ax} \tag{3.12}$$

$$\Delta F_z = mV\left[p\sin(\beta) - q\cos(\alpha)\cos(\beta)\right] - mg\cos(\theta)\cos(\phi) - F^{(b)}_{az} \tag{3.13}$$

$$\Delta M_y = (J_x - J_z)pr + J_{xz}(p^2 - r^2) - M_{ay}^{(b)} \tag{3.14}$$

The angle of attack control necessitates specifying the acceleration command $\dot{w}_{com}$. Similarly, the pitching maneuver control for a desired pitch angle necessitates specifying the acceleration command $\dot{q}_{com}$. On the other hand, for the speed control of the aircraft in both of the previous control requirements, it is always necessary to specify the acceleration command $\dot{u}_{com}$. Therefore, in order to apply the angle of attack control, the acceleration commands $\dot{u}_{com}$ and $\dot{w}_{com}$ are generated and the corresponding $\dot{q}_{com}$ is found depending on them according to equation (3.11). Alternatively, if a pitching maneuver is required, the acceleration commands $\dot{u}_{com}$ and $\dot{q}_{com}$ are generated and the corresponding $\dot{w}_{com}$ is found depending on them again according to equation (3.11). Hence, $\overline{F}_{com}^{(b)}$ and $\overline{M}_{com}^{(b)}$ are determined using equation (3.9), which then lead to $\overline{F}_{Lcom}^{(b)}$ and $\overline{F}_{Rcom}^{(b)}$ according to equation (3.8) as shown in Table 1. Afterwards, $\{T_{Lcom}, \psi_{Lcom}, \theta_{Lcom}\}$ and $\{T_{Rcom}, \psi_{Rcom}, \theta_{Rcom}\}$ can be determined as explained in Chapter 2.

Table 1. Achievable Desired Forces and Moments by TVC Engines

Constraint Equation for q and/or θ Control ($AoACont$ =0)	Constraint Equation for α and/or w Control ($AoACont$ =1)
$F_{com\,z}^{(b)} = (-M_{com\,y}^{(b)} + e_z F_{com\,x}^{(b)}) / e_x$	$M_{com\,y}^{(b)} = -e_x F_{com\,z}^{(b)} + e_z F_{com\,x}^{(b)}$
$F_{Lcom\,x}^{(b)} = (F_{com\,x}^{(b)} - (M_{com\,z}^{(b)} - e_x F_{com\,y}^{(b)}) / e_y) / 2$	
$F_{Rcom\,x}^{(b)} = (F_{com\,x}^{(b)} + (M_{com\,z}^{(b)} - e_x F_{com\,y}^{(b)}) / e_y) / 2$	
$F_{Lcom_y}^{(b)} = F_{Rcom_y}^{(b)} = F_{com_y}^{(b)} / 2$	
$F_{Lcom\,z}^{(b)} = (F_{com\,z}^{(b)} + (M_{com\,x}^{(b)} + e_z F_{com\,y}^{(b)}) / e_y) / 2$	
$F_{Rcom\,z}^{(b)} = (F_{com\,z}^{(b)} - (M_{com\,x}^{(b)} + e_z F_{com\,y}^{(b)}) / e_y) / 2$	

3.2.1.1. The Stabilization Controller Design

The aim of the stabilization controller is to control the aircraft at undesired high AoA flight conditions for which the aerodynamic controls are inadequate to impose effective control power and bring the aircraft back to aerodynamically controllable flight regimes. Thus, this necessitates the usage of TVC for the stabilization controller.

In order to stabilize the aircraft at high-alpha flight conditions, first, the body angular acceleration components ($\dot{p}, \dot{q}, \dot{r}$) should be controlled and the stability of the aircraft should be augmented and enhanced. After the stability augmentation the linear acceleration components ($\dot{u}, \dot{v}, \dot{w}$) of the aircraft should be stabilized and brought to moderate levels that the aerodynamic controls will be adequate to control the aircraft at that flight regime. Thus, $\overline{F}_{com}^{(b)}$ and $\overline{M}_{com}^{(b)}$ are calculated using the commanded accelerations as shown in equation (3.9) and the relation of $\overline{F}_{com}^{(b)}$ and $\overline{M}_{com}^{(b)}$ to $\overline{F}_{Lcom}^{(b)}$ and $\overline{F}_{Rcom}^{(b)}$ will obey the constraint equation for α and/or w control shown in Table 1.

The desired accelerations (that stabilizes the aircraft) should be directly related to the body angular velocity (p, q, r) and body linear velocity (u, v, w) components of the aircraft. This relation is produced by designing a controller generating the commanded accelerations using the desired and actual body angular and linear velocities. For that purpose, the stabilization controller is structured to be composed of two parts. The first one generates the commanded angular accelerations using the desired and actual angular velocities and the second one generates the commanded linear accelerations using the desired and actual linear velocities.

Different controller structures can be used for this purpose. A commonly used one is the Proportional plus Integral (PI) control structure. It is particularly popular for its ease of implementation and for its proven performance in the NDI literature using fighter aircraft examples [26], [32], [43]. In this thesis, PI control structure is used for the linear acceleration controller and Proportional (P) control structure is used for the angular acceleration controller, i.e. the stability augmentation loop.

Using the desired angular velocity components p_d, q_d and r_d the error vector $\bar{e}_{av}(t)$ is defined as the difference between the desired (d) and the actual values of the body angular velocity components, i.e.

$$\bar{e}_{av}(t) = \begin{bmatrix} p_d(t) \\ q_d(t) \\ r_d(t) \end{bmatrix} - \begin{bmatrix} p(t) \\ q(t) \\ r(t) \end{bmatrix} \tag{3.15}$$

Implementing the P controller with the constant gain matrix $\hat{K}_d = diag(K_{d\phi}, K_{d\theta}, K_{d\psi})$ the commanded (com) angular accelerations $\dot{p}_{com}$, $\dot{q}_{com}$ and $\dot{r}_{com}$ can be expressed as

$$\begin{bmatrix} \dot{p}_{com}(t) \\ \dot{q}_{com}(t) \\ \dot{r}_{com}(t) \end{bmatrix} = \hat{K}_d \bar{e}_{av}(t) \tag{3.16}$$

After calculating $\dot{p}_{com}$, $\dot{q}_{com}$ and $\dot{r}_{com}$, $\overline{F}_{com}^{(b)}$ and $\overline{M}_{com}^{(b)}$ are determined using equation (3.8), which then lead to $\overline{F}_L^{(b)}$ and $\overline{F}_R^{(b)}$ according to Table 1. Since, the commanded pitch angular acceleration is generated the constraining equation for pitching maneuver should be used here. $\overline{F}_L^{(b)}$ and $\overline{F}_R^{(b)}$ are then used to calculate the left and right engine thrust magnitudes T_{Lcom} and T_{Rcom} and the thrust-vectoring angle pairs {ψ_{Lcom}, θ_{Lcom}} and {ψ_{Rcom}, θ_{Rcom}}. Finally, the throttle deflections and the six thrust-vectoring paddle deflection angles can be calculated from them.

For the linear acceleration controller instead of using the desired linear velocity components u_d, v_d and w_d, since, the total velocity, the angle of attack and the side slip angle can be measured directly on the aircraft and have direct relationship to piloting, desired total velocity, angle of attack and side slip angle (V_{Td}, α_d, β_d) are used. Using these values the error vector $\overline{e}_{lv}(t)$ is defined as the difference between the desired (d) and the actual values of the body linear velocity components, i.e.

$$\overline{e}_{lv}(t) = \begin{bmatrix} V_{Td}(t) \\ \alpha_d(t) \\ \beta_d(t) \end{bmatrix} - \begin{bmatrix} V_T(t) \\ \alpha(t) \\ \beta(t) \end{bmatrix} \tag{3.17}$$

Implementing the PI controller with the constant gain matrices $\hat{K}_{pl} = diag(K_{pV_T}, K_{p\alpha}, K_{p\beta})$ and $\hat{K}_{il} = diag(K_{iV_T}, K_{i\alpha}, K_{i\beta})$, the commanded total velocity, angle of attack and side slip angle rates can be expressed as

$$\begin{bmatrix} \dot{V}_{T\,com}(t) \\ \dot{\alpha}_{com}(t) \\ \dot{\beta}_{com}(t) \end{bmatrix} = \hat{K}_{pl}\overline{e}_{lv}(t) + \hat{K}_{il}\int_0^t \overline{e}_{lv}(t')\mathrm{d}t' \tag{3.18}$$

After calculating $\dot{V}_{T\,com}$, $\dot{\alpha}_{com}$ and $\dot{\beta}_{com}$, $\dot{u}_{com}$, $\dot{v}_{com}$ and $\dot{w}_{com}$ can be calculated using the following kinematic transformation given in Chapter 2.

$$\begin{bmatrix} \dot{u}_{com} \\ \dot{v}_{com} \\ \dot{w}_{com} \end{bmatrix} = \begin{bmatrix} c\alpha c\beta & -V_T s\alpha c\beta & -V_T c\alpha s\beta \\ s\beta & 0 & V_T c\beta \\ s\alpha c\beta & V_T c\alpha c\beta & -V_T s\alpha s\beta \end{bmatrix} \begin{bmatrix} \dot{V}_{Tcom} \\ \dot{\alpha}_{com} \\ \dot{\beta}_{com} \end{bmatrix} \tag{3.19}$$

Hence, $\overline{F}_{com}^{(b)}$ and $\overline{M}_{com}^{(b)}$ are determined using equation (3.8), which then lead to $\overline{F}_L^{(b)}$ and $\overline{F}_R^{(b)}$ according to Table 1. Since, the commanded vertical acceleration is generated the constraining equation for angle of attack control should be used here. The, $\overline{F}_L^{(b)}$ and $\overline{F}_R^{(b)}$ are used to calculate T_{Lcom} and T_{Rcom} and $\{\psi_{Lcom},\ \theta_{Lcom}\}$ and $\{\psi_{Rcom},\ \theta_{Rcom}\}$. Again, the throttle deflections and the six thrust-vectoring paddle deflection angles can be calculated using them.

The block diagram representation of the proposed stabilization controller based on thrust vectoring is shown in Figure 70. In the figure the block denoted by KC_l is the kinematic conversion given by equation (3.19).

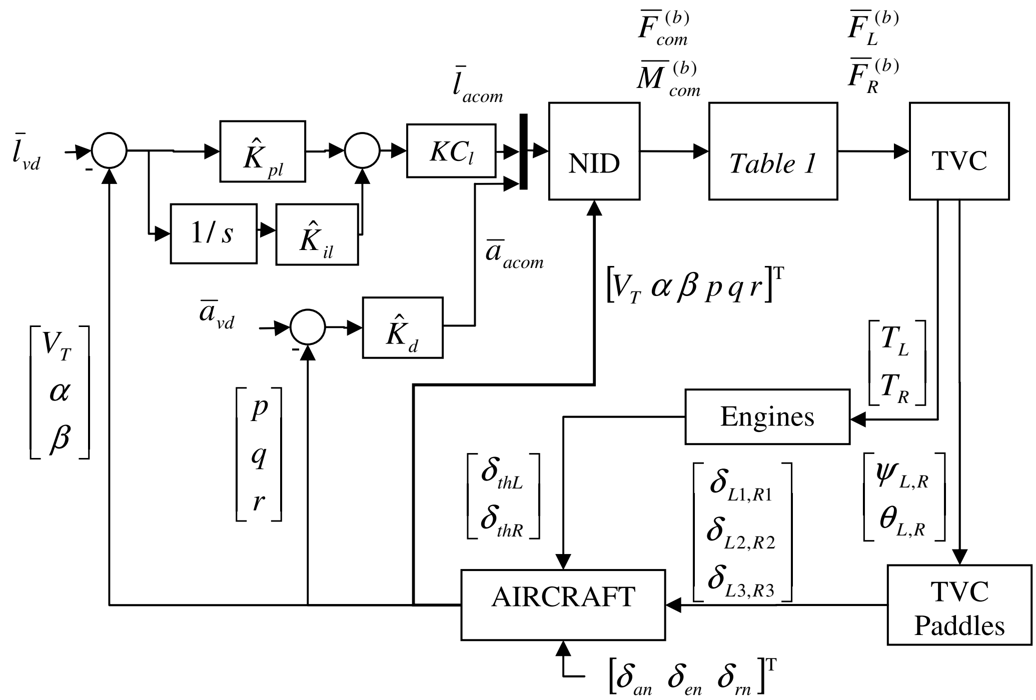

Figure 70. The Stabilization Controller Block Diagram

As it is mentioned before, the stabilization controller first augments the stability of the aircraft controlling the body angular acceleration components ($\dot{p},\dot{q},\dot{r}$). Then on the linear acceleration components ($\dot{u},\dot{v},\dot{w}$) of the aircraft are stabilized and brought to moderate levels that the aerodynamic controls will be adequate at that flight regime. Therefore, a parameter (*AoACont*) is defined to switch between the angular velocity controller and the linear velocity controller, i.e. choose control on p_d, q_d, r_d or $V_{Td}, \alpha_d, \beta_d$, during the operation of the stabilization controller. This is done by the structure given in block diagram in Figure 70 and using the following algorithm:

if $AoACont$ = 1 then

$$\bar{a}_{vd} = \begin{bmatrix} p_d = 0 \\ r_d = 0 \end{bmatrix}, \ \bar{l}_{vd} = \begin{bmatrix} V_{Td} \\ \alpha_d \\ \beta_d = 0 \end{bmatrix}, \ \begin{bmatrix} \dot{V}_{T\,com} \\ \dot{\alpha}_{com} \\ \dot{\beta}_{com} \end{bmatrix} = \hat{K}_{pl}\bar{e}_{lv}(t) + \hat{K}_{il}\int_0^t \bar{e}_{lv}(t')\mathrm{d}t',$$

$\bar{l}_{acom} = [\dot{u}_{com}\ \dot{v}_{com}\ \dot{w}_{com}]^{\mathrm{T}}$, $\bar{a}_{acom} = [\dot{p}_{com}\ \dot{r}_{com}]^{\mathrm{T}}$, and,

$M^{(b)}_{com\,y} = -e_x F^{(b)}_{com\,z} + e_z F^{(b)}_{com\,x}$

elseif $AoACont$ = 0 then

$$\bar{l}_{vd} = \begin{bmatrix} V_{Td} \\ \beta_d = 0 \end{bmatrix}, \ \bar{a}_{vd} = \begin{bmatrix} p_d = 0 \\ q_d = 0 \\ r_d = 0 \end{bmatrix}, \ \begin{bmatrix} \dot{p}_{com} \\ \dot{q}_{com} \\ \dot{r}_{com} \end{bmatrix} = \hat{K}_d \bar{e}_{av}(t),$$

$\bar{l}_{acom} = [\dot{u}_{com}\ \dot{v}_{com}]^{\mathrm{T}}$, $\bar{a}_{acom} = [\dot{p}_{com}\ \dot{q}_{com}\ \dot{r}_{com}]^{\mathrm{T}}$, and,

$F^{(b)}_{com\,z} = (-M^{(b)}_{com\,y} + e_z F^{(b)}_{com\,x}) / e_x$

3.2.1.2. The Attitude Controller Design

The aim of the attitude controller is to make the aircraft perform desired maneuvers at high AoA flight conditions. In order to maneuver the aircraft at high-alpha flight conditions yaw, pitch and roll attitude of the aircraft should be controlled. Thus, $\bar{F}^{(b)}_{com}$ and $\bar{M}^{(b)}_{com}$ are calculated using the commanded accelerations as shown in equation (3.9) and the relation of $\bar{F}^{(b)}_{com}$ and $\bar{M}^{(b)}_{com}$ to $\bar{F}^{(b)}_{Lcom}$ and $\bar{F}^{(b)}_{Rcom}$ will obey the constraint equation for q and/or θ control shown in Table 1.

These accelerations should be directly related to the desired roll, pitch and yaw angles of the aircraft. This relation is produced by designing a controller generating the commanded accelerations using the desired and actual attitude angles.

In order to calculate the commanded angular accelerations, the commanded angular velocities should be calculated first. Thus, the attitude controller is divided into two segments. First the commanded roll, pitch and yaw angular velocities are generated, and then, the commanded angular accelerations are generated using the commanded and actual angular velocities. Second segment of the controller is the same as the angular velocity controller of the stabilization controller and here it can be used for stability augmentation. Different from the angular velocity controller of the stabilization controller, the angular velocity commands will be generated by the first segment of the attitude controller. Here, for the slowly changing dynamics, because of the same reasons as in the case of linear velocity controller of the stabilization controller, again a PI control structure is used. As for the angular velocity controller a P control structure is used to support the first segment of the attitude controller with an effective derivative action.

Using the desired attitude angles of the aircraft ϕ_d, θ_d and ψ_d the error vector $\bar{e}_a(t)$ is defined as the difference between the desired (d) and the actual values of the attitude angles of the aircraft, i.e.

$$\bar{e}_a(t) = \begin{bmatrix} \phi_d(t) \\ \theta_d(t) \\ \psi_d(t) \end{bmatrix} - \begin{bmatrix} \phi(t) \\ \theta(t) \\ \psi(t) \end{bmatrix} \tag{3.20}$$

Implementing the PI controller with the constant gain matrices $\hat{K}_{pa} = diag(K_{p\phi}, K_{p\theta}, K_{p\psi})$ and $\hat{K}_{ia} = diag(K_{i\phi}, K_{i\theta}, K_{i\psi})$, the commanded roll, pitch and yaw angular velocities can be expressed as

$$\begin{bmatrix} \dot{\phi}_{com}(t) \\ \dot{\theta}_{com}(t) \\ \dot{\psi}_{com}(t) \end{bmatrix} = \hat{K}_{pa}\overline{e}_a(t) + \hat{K}_{ia}\int_0^t \overline{e}_a(t')\mathrm{d}t' \quad (3.21)$$

After calculating $\dot{\phi}_{com}$, $\dot{\theta}_{com}$ and $\dot{\psi}_{com}$, p_{com}, q_{com} and r_{com} can be calculated using the following kinematic transformation given in Chapter 2.

$$\begin{bmatrix} p_{com} \\ q_{com} \\ r_{com} \end{bmatrix} = \begin{bmatrix} 1 & 0 & -s\theta \\ 0 & c\phi & c\theta s\phi \\ 0 & -s\phi & c\theta c\phi \end{bmatrix} \begin{bmatrix} \dot{\phi}_{com} \\ \dot{\theta}_{com} \\ \dot{\psi}_{com} \end{bmatrix} \quad (3.22)$$

Once p_{com}, q_{com} and r_{com} are calculated they will be fed through the second segment of the controller and they will be used instead of p_d, q_d and r_d in equation (3.15). Hence, $\dot{p}_{com}$, $\dot{q}_{com}$ and $\dot{r}_{com}$ will be calculated and $\overline{F}^{(b)}_{com}$ and $\overline{M}^{(b)}_{com}$ will be determined using equation (3.8). Afterwards, $\overline{F}_L^{(b)}$ and $\overline{F}_R^{(b)}$ can be calculated according to Table 1. Since, the pitch acceleration is generated here the constraining equation for pitch angle and pitch rate control should be used. Then T_{Lcom} and T_{Rcom}, {ψ_{Lcom}, θ_{Lcom}} and {ψ_{Rcom}, θ_{Rcom}} (and the throttle deflections and the six thrust-vectoring paddle deflection angles) will be calculated using $\overline{F}_L^{(b)}$ and $\overline{F}_R^{(b)}$.

The block diagram representation of the proposed attitude controller based on thrust vectoring is shown in Figure 71. In the figure the block denoted by *KC* is the kinematic conversion given by equation (3.22).

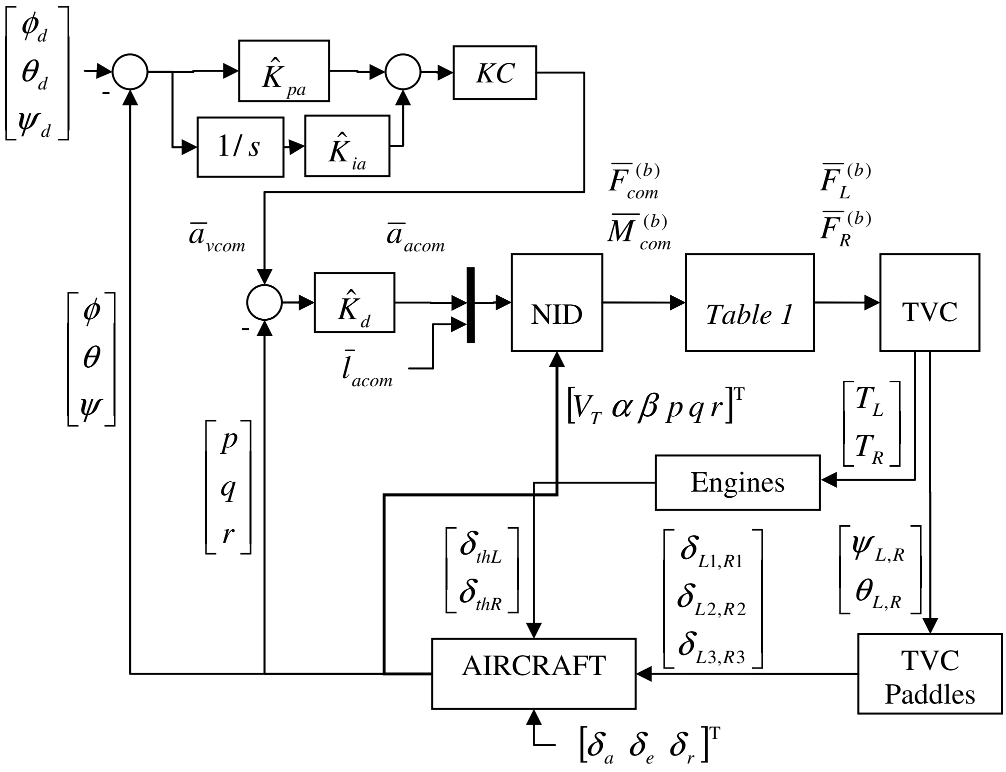

Figure 71. The Attitude Controller Block Diagram with TVC

As it is mentioned before, the purpose of the attitude controller is to achieve the desired maneuver by realizing the desired attitude angles. Therefore, ϕ_d, θ_d and ψ_d will be realized during the operation of the attitude controller. This is done by using

$$\overline{a}_{vcom} = \begin{bmatrix} p_{com} \\ q_{com} \\ r_{com} \end{bmatrix}, \begin{bmatrix} \dot{p}_{com} \\ \dot{q}_{com} \\ \dot{r}_{com} \end{bmatrix} = \hat{K}_d \overline{e}_{av}(t), \ \overline{a}_{acom} = [\dot{p}_{com}\ \dot{q}_{com}\ \dot{r}_{com}\ ]^T, \text{ and,}$$

$$\bar{l}_{ad} = \begin{bmatrix} \dot{u}_d = 0 \\ \dot{v}_d = 0 \end{bmatrix}$$ in the block diagram in Figure 71.

3.2.2. Controller Design for the Aerodynamic Control Phase

As previously mentioned, the aim of the stabilization controller is to control the aircraft at undesired high-alpha flight conditions for which the aerodynamic controls are inadequate to impose effective control power and bring the aircraft back to aerodynamically controllable flight regimes. Thus, TVC is designed to be turned on whenever the aerodynamic controller loses its effectiveness due to high angle of attack values. Therefore, the aerodynamic controller is not operative when the TVC is turned on. In such a case, the aerodynamic control effectors are retracted to their neutral positions and the aircraft is controlled only by using the total thrusts T_L and T_R and the thrust vector deviation angle pairs $\{\psi_L, \theta_L\}$ and $\{\psi_R, \theta_R\}$. Hence, a controller using the aerodynamic control effectors is not especially designed for the stabilization controller. However, the attitude control of the aircraft is desirable for every flight regime whether the angle of attack is low or high. For this purpose, the aerodynamic controller is designed for the attitude controller.

In the case of aerodynamic controls, using the dynamic inversion control law in association with equations (3.4) and (2.10), the command values for the aerodynamic forces and moments should be calculated. In this case, for commanded accelerations and un-deflected TVC paddles, following equation can be written.

$$\begin{bmatrix} \overline{F}^{(b)}_{acom} \\ \overline{M}^{(b)}_{acom} \end{bmatrix} = \hat{H}^{-1} \left\{ \begin{bmatrix} [\dot{u}_{com} & \dot{v}_{com} & \dot{w}_{com}]^{\mathrm{T}} \\ [\dot{p}_{com} & \dot{q}_{com} & \dot{r}_{com}]^{\mathrm{T}} \end{bmatrix} - \overline{F} - \hat{G} \begin{bmatrix} [T_L & 0 & 0]^{\mathrm{T}} \\ [T_R & 0 & 0]^{\mathrm{T}} \end{bmatrix} \right\} \tag{3.23}$$

For the attitude controller (realizing the yaw-pitch-roll maneuvers of the aircraft), the aerodynamic control surface deflections (δ_{acom}, δ_{ecom}, δ_{rcom}) should be found from $\overline{M}^{(b)}_{acom}$.

Using the aerodynamic moment coefficients (C_l, C_m, C_n) explained in Chapter 2.2 the aerodynamic moments are expressed as $M_{ax}^{(b)} = (Q_d Sb)C_l$, $M_{ay}^{(b)} = (Q_d S\bar{c})C_m$, $M_{az}^{(b)} = (Q_d Sb)C_n$. Here, Q_d is the dynamic pressure explained in Chapter 2.4, S is the surface area of the wing planform, $\bar{c}$ is the mean chord length and b is the span of the wing. As noted C_l, C_m and C_n are structured as:

$$C_l = C_l'(\alpha, \beta, p, q, r) + C_{l\delta_a}(\alpha, \beta)\delta_a + C_{l\delta_r}(\alpha, \beta)\delta_r \tag{3.24}$$

$$C_m = C_m'(\alpha, \beta, p, q, r) + C_{m\delta_e}(\alpha, \beta)\delta_e \tag{3.25}$$

$$C_n = C_n'(\alpha, \beta, p, q, r) + C_{n\delta_a}(\alpha, \beta)\delta_a + C_{n\delta_r}(\alpha, \beta)\delta_r \tag{3.26}$$

Thus, using the equations (3.23), (3.24), (3.25) and (3.26) the commanded aerodynamic control surface deflections for the commanded angular accelerations can be calculated as

$$\begin{bmatrix} \delta_{acom} \\ \delta_{ecom} \\ \delta_{rcom} \end{bmatrix} = \begin{bmatrix} C_{l\delta_a} & 0 & C_{l\delta_r} \\ 0 & C_{m\delta_e} & 0 \\ C_{n\delta_a} & 0 & C_{n\delta_r} \end{bmatrix}^{-1} \begin{bmatrix} M_{axcom}^{(b)} / (Q_d Sb) - C_l' \\ M_{aycom}^{(b)} / (Q_d S\bar{c}) - C_m' \\ M_{azcom}^{(b)} / (Q_d Sb) - C_n' \end{bmatrix} \tag{3.27}$$

The commanded angular accelerations for the desired yaw-pitch-roll maneuvers are calculated in the same way as explained in attitude controller design section in Chapter 3.2.1.2.

The block diagram representation of the proposed attitude controller based on aerodynamic controls is shown in Figure 72. In the figure the block denoted by *KC* is the kinematic conversion given by equation (3.22).

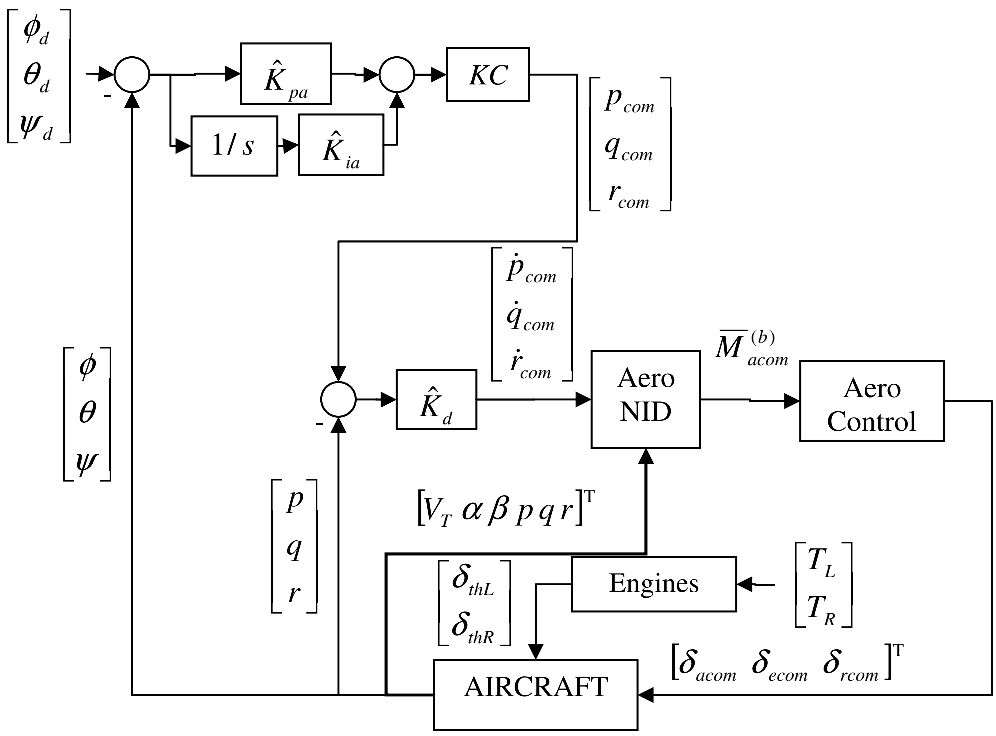

Figure 72. The Attitude Controller Block Diagram with Aerodynamic Controls

3.2.3. Blending the Thrust Vectoring and Aerodynamic Controls

The aerodynamic controls can effectively be used at low and moderate angle of attack flight regimes. However, they are ineffective at high angle of attack, stall and post-stall and thrust vectoring controls should be used at these flight regimes. Thus, for the attitude controller thrust vectoring and aerodynamic controls are blended and used together. The blending strategy is based on the following blender rules:

- Use conventional aerodynamic controls (aileron, elevator and rudder) and continuously monitor if any of the control surfaces (δ_a, δ_e, δ_r) saturates and check the value of the estimates of $C_{n\beta dyn}$ and *LCDP*.

- If aileron saturates, then command it to its neutral position (δ_{an}) and realize the desired roll or roll rate motion by using the thrust vectoring control until the new aileron command is unsaturated.
- If elevator saturates, then command it to its neutral position (δ_{en}) and realize the desired pitch or pitch rate motion by using the thrust vectoring control until the new elevator command is unsaturated. If the stall indication parameters ($C_{n\beta dyn}$, *LCDP*) indicate that the aircraft is in stall safe region (region A in Figure 54), then command the elevator to its trim position (δ_{e0}) for the instantaneous flight condition.
- If rudder saturates, then command it to its neutral position (δ_{rn}) and realize the desired yaw or yaw rate motion by using the thrust vectoring control until the new rudder command is unsaturated.

The rules situated above are also valid whenever any of the aerodynamic control surfaces saturate together. In that case, the desired roll, pitch and yaw motion will be realized by using the corresponding combination (given in Table 1) of thrust vectoring control effectors. The block diagram of the blended attitude controller is shown in Figure 73 and Figure 74.

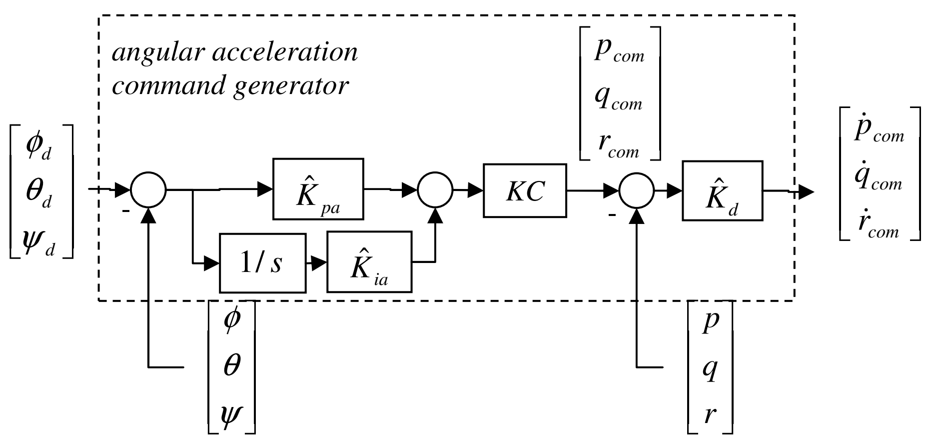

Figure 73. Angular Acceleration Command Generator for Attitude Controller

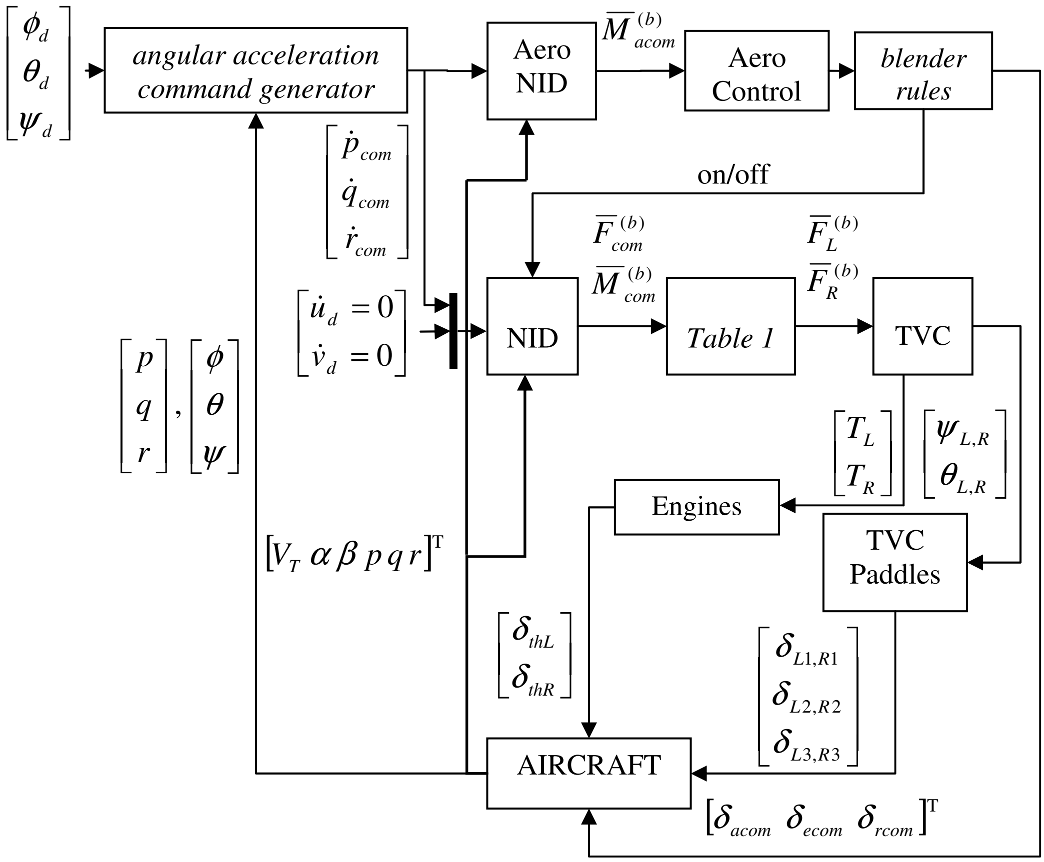

Figure 74. The Attitude Controller Block Diagram with Blended Controls

3.2.4. Designing the Controller Gain Matrices

Assuming that there are no uncertainties and no saturations due to control effectors limitations the NDI approach produces a linear system of three independent free integrators involving the linear accelerations $\dot{V}_{T\,com}$, $\dot{\alpha}_{com}$ and $\dot{\beta}_{com}$. Thus, the closed loop transfer functions for the linear velocity controller of the stabilization controller shown in Figure 70 can be written as

$$\frac{V_T(s)}{V_{Td}(s)} = \frac{K_{pV_T}s + K_{iV_T}}{s^2 + K_{pV_T}s + K_{iV_T}} \tag{3.28}$$

$$\frac{\alpha(s)}{\alpha_d(s)} = \frac{K_{p\alpha}s + K_{i\alpha}}{s^2 + K_{p\alpha}s + K_{i\alpha}} \tag{3.29}$$

$$\frac{\beta(s)}{\beta_d(s)} = \frac{K_{p\beta}s + K_{i\beta}}{s^2 + K_{p\beta}s + K_{i\beta}} \tag{3.30}$$

In order to calculate the matrices $\hat{K}_{pl}$ and $\hat{K}_{il}$ the poles of the desired closed loop dynamics for V_T, α and β should be specified. Here, these poles are specified as three sets where each one consists of a complex conjugate pole pair:

$$\left\{-\omega_{nV_T}(\zeta_{V_T} \pm j\sqrt{1-\zeta_{V_T}^2})\right\},\ \left\{-\omega_{n\alpha}(\zeta_{\alpha} \pm j\sqrt{1-\zeta_{\alpha}^2})\right\} \text{ and } \left\{-\omega_{n\beta}(\zeta_{\beta} \pm j\sqrt{1-\zeta_{\beta}^2})\right\}.$$

Using the selected poles and the defined closed loop transfer functions the controller gain matrices are found as follows:

$$\hat{K}_{pl} = \mathrm{diag}(2\zeta_{V_T}\omega_{nV_T},\ 2\zeta_{\alpha}\omega_{n\alpha},\ 2\zeta_{\beta}\omega_{n\beta}) \tag{3.31}$$

$$\hat{K}_{il} = \mathrm{diag}(\omega_{nV_T}^2,\ \omega_{n\alpha}^2,\ \omega_{n\beta}^2) \tag{3.32}$$

Same assumption is also true for the angular velocity controller of the stabilization (and the attitude) controller. Therefore, the NDI approach produces another linear system of three independent free integrators involving the angular accelerations $\dot{p}_{com}$, $\dot{q}_{com}$ and $\dot{r}_{com}$. Accordingly, the closed loop transfer functions for the angular velocity controller shown in Figure 70, Figure 71, Figure 72, Figure 73 and Figure 74 are written as

$$\frac{p(s)}{p_d(s)}=\frac{K_{d\phi}}{s+K_{d\phi}},\ \frac{q(s)}{q_d(s)}=\frac{K_{d\theta}}{s+K_{d\theta}},\ \frac{r(s)}{r_d(s)}=\frac{K_{d\psi}}{s+K_{d\psi}} \tag{3.33}$$

In order to calculate $\hat{K}_d$ the poles of the desired closed loop dynamics for p, q and r should be specified. Here, since the angular velocity controller will be the inner loop of the attitude controller and act as the stability augmentation loop, instead of designing $\hat{K}_d$ independently it is preferred to design the angular velocity controller in accordance with the attitude controller. Considering the attitude controller with the angular velocity controller and making the same assumptions as before the closed loop transfer functions for the attitude controller shown in Figure 71, Figure 72, Figure 73, Figure 74 can be written as shown:

$$\frac{\phi(s)}{\phi_d(s)}=\frac{K_{d\phi}(K_{p\phi}s+K_{i\phi})}{s^3+K_{d\phi}s^2+K_{p\phi}K_{d\phi}s+K_{i\phi}K_{d\phi}} \tag{3.34}$$

$$\frac{\theta(s)}{\theta_d(s)}=\frac{K_{d\theta}(K_{p\theta}s+K_{i\theta})}{s^3+K_{d\theta}s^2+K_{p\theta}K_{d\theta}s+K_{i\theta}K_{d\theta}} \tag{3.35}$$

$$\frac{\psi(s)}{\psi_d(s)}=\frac{K_{d\psi}(K_{p\psi}s+K_{i\psi})}{s^3+K_{d\psi}s^2+K_{p\psi}K_{d\psi}s+K_{i\psi}K_{d\psi}} \tag{3.36}$$

In order to calculate $\hat{K}_{pa}$, $\hat{K}_{ia}$ and $\hat{K}_d$ the poles of the desired closed loop dynamics of the attitude angles should be specified. Here, these poles are specified as three sets where each one consists of a complex conjugate pole pair and a real pole:

$$\left\{-\omega_{n\phi}(\zeta_\phi \pm j\sqrt{1-\zeta_\phi^2}),-\omega'_{n\phi}\right\},\ \left\{-\omega_{n\theta}(\zeta_\theta \pm j\sqrt{1-\zeta_\theta^2}),-\omega'_{n\theta}\right\} \text{ and } \left\{-\omega_{n\psi}(\zeta_\psi \pm j\sqrt{1-\zeta_\psi^2}),-\omega'_{n\psi}\right\}.$$

Using the selected poles and the transfer functions the controller gain matrices are found as follows:

$$\hat{K}_d = \mathrm{diag}(2\zeta_\phi \omega_{n\phi} + \omega'_{n\phi}, 2\zeta_\theta \omega_{n\theta} + \omega'_{n\theta}, 2\zeta_\psi \omega_{n\psi} + \omega'_{n\psi}) \tag{3.37}$$

$$\begin{aligned}\hat{K}_{pa} = \mathrm{diag}(&\frac{\omega_{n\phi}(\omega_{n\phi} + 2\zeta_\phi \omega'_{n\phi})}{2\zeta_\phi \omega_{n\phi} + \omega'_{n\phi}}, \frac{\omega_{n\theta}(\omega_{n\theta} + 2\zeta_\theta \omega'_{n\theta})}{2\zeta_\theta \omega_{n\theta} + \omega'_{n\theta}}, \\ &\frac{\omega_{n\psi}(\omega_{n\psi} + 2\zeta_\psi \omega'_{n\psi})}{2\zeta_\psi \omega_{n\psi} + \omega'_{n\psi}})\end{aligned} \tag{3.38}$$

$$\hat{K}_{ia} = \mathrm{diag}(\frac{\omega_{n\phi}{}^2 \omega'_{n\phi}}{2\zeta_\phi \omega_{n\phi} + \omega'_{n\phi}}, \frac{\omega_{n\theta}{}^2 \omega'_{n\theta}}{2\zeta_\theta \omega_{n\theta} + \omega'_{n\theta}}, \frac{\omega_{n\psi}{}^2 \omega'_{n\psi}}{2\zeta_\psi \omega_{n\psi} + \omega'_{n\psi}}) \tag{3.39}$$

The poles of the desired closed loop dynamics for stabilization and attitude controls should be selected considering the robustness of the closed loop, the agility and flying qualities of the aircraft during the desired maneuvers and the control power limitations. The robustness analysis and the selection of closed loop poles are explained in Chapter 4. Then, the agility and flying qualities performance of the aircraft with the selected poles for stabilization and attitude controllers is demonstrated with simulations for different scenarios in Chapter 5 and Chapter 6.

CHAPTER 4

ROBUST PERFORMANCE ANALYSIS

In this chapter, first, the general aspects of the trim analysis and linearization of the nonlinear dynamics of the aircraft will be discussed. Then, the modeling of the uncertainties and the disturbances on the aircraft will be presented. Eventually, the robust performance analysis of the controller loops with and without the pilot model will be constituted. At the end of the chapter, the performance of the designed stabilization and attitude controllers will be analyzed with simulations.

4.1. Trim Analysis and Linearization

The robust performance (RP) analysis is done by linearizing the nonlinear aircraft dynamics at the desired flight condition. For that purpose, a trimming algorithm that trims the aircraft at the desired flight conditions is generated. This algorithm calculates the trim values of total thrust (T_0), angle of attack (α_0), the side slip angle (β_0), aileron (δ_{a0}), elevator (δ_{e0}) and rudder (δ_{r0}) deflections for $\dot{u} = \dot{v} = \dot{w} = \dot{p} = \dot{q} = \dot{r} = 0$ at the desired altitude (h_0), Mach number (M_0), pitch angle (θ_0), roll angle (ϕ_0) and body angular velocities (p_0, q_0, r_0). The trim equations are originated from the Newton-Euler equations explained in Chapter 2.

$$\bar{f}_0 = \begin{bmatrix} -mg\sin(\theta_0) + T_0 + Fa_{x0} \\ mg\cos(\theta_0)\sin(\phi_0) + Fa_{y0} \\ mg\cos(\theta_0)\cos(\phi_0) + Fa_{z0} \\ Ma_{x0} \\ Ma_{y0} \\ Ma_{z0} \end{bmatrix} = \bar{0} \tag{4.1}$$

$$\begin{bmatrix} Fa_{x0} \\ Fa_{y0} \\ Fa_{z0} \\ Ma_{x0} \\ Ma_{y0} \\ Ma_{z0} \end{bmatrix} = Q_{d0} S \begin{bmatrix} C_x(\alpha_0, \beta_0, p_0, q_0, r_0, \delta_{a0}, \delta_{e0}, \delta_{r0}) \\ C_y(\alpha_0, \beta_0, p_0, q_0, r_0, \delta_{a0}, \delta_{e0}, \delta_{r0}) \\ C_z(\alpha_0, \beta_0, p_0, q_0, r_0, \delta_{a0}, \delta_{e0}, \delta_{r0}) \\ bC_l(\alpha_0, \beta_0, p_0, q_0, r_0, \delta_{a0}, \delta_{e0}, \delta_{r0}) \\ \bar{c}C_m(\alpha_0, \beta_0, p_0, q_0, r_0, \delta_{a0}, \delta_{e0}, \delta_{r0}) \\ bC_n(\alpha_0, \beta_0, p_0, q_0, r_0, \delta_{a0}, \delta_{e0}, \delta_{r0}) \end{bmatrix} \tag{4.2}$$

Here, $Q_{d0} = 1/2\rho_0 h_0 V_{T0}^2$ and ρ_0, V_{T0} are the air density and total velocity at which the trim values are calculated. S is the surface area of the wing planform, $\bar{c}$ is the mean chord length and b is the span of the wing. Also, $C_x, C_y, C_z, C_l, C_m, C_n$ are the aerodynamic coefficients and functions of $\alpha_0, \beta_0, p_0, q_0, r_0, \delta_{a0}, \delta_{e0}, \delta_{r0}$ as explained in Chapter 2.

Equation (4.1) is a coupled nonlinear set of static equations. There are various solution methods for that type of equations. Here, the trim equations are solved by using the Newton-Raphson method. In order to apply that method, first, the perturbation matrix for the nonlinear equation set is found:

$$\Delta\hat{f}_0 = [\partial\bar{f}_0/\partial T \;\; \partial\bar{f}_0/\partial\alpha \;\; \partial\bar{f}_0/\partial\beta \;\; \partial\bar{f}_0/\partial\delta_a \;\; \partial\bar{f}_0/\partial\delta_e \;\; \partial\bar{f}_0/\partial\delta_r] \tag{4.3}$$

Then on the initial conditions for the unknown trim values (T_0, α_0, β_0, δ_{a0}, δ_{e0}, δ_{r0}) are set that the algorithm starts the iteration from these values. At each of the iteration steps $\bar{f}_0$ is calculated and updated with the current values of the unknown trim conditions.

Defining a standard deviation σ_r on the solution of the nonlinear equations the covariance matrix $\hat{R} = \sigma_r \hat{I}$ is written. Thus, the perturbation vector is written as $d\bar{x}_0 = (\Delta\hat{f}_0^{\,T} R^{-1} \Delta\hat{f}_0)^{-1} \Delta\hat{f}_0^{\,T} R^{-1} \bar{f}_0$. Then the unknowns are updated at each iteration step k using $d\bar{x}_0$:

$$[T_0\ \alpha_0\ \beta_0\ \delta_{a0}\ \delta_{e0}\ \delta_{r0}]_{k+1}^{\mathrm{T}} = [T_0\ \alpha_0\ \beta_0\ \delta_{a0}\ \delta_{e0}\ \delta_{r0}]_{k}^{\mathrm{T}} - d\bar{x}_0 \tag{4.4}$$

Hence, whenever the condition $\|d\bar{x}_0\| \leq \varepsilon$ (the error bound for $d\bar{x}_0$) is satisfied the values of the trim conditions are found within the defined error bound ε.

Since equation (4.1) is nonlinear the solutions of the trim values may not be unique. In order to handle the right solution some conditional checks are integrated into the Newton-Raphson iteration algorithm. As explained in Chapter 2 the aerodynamic coefficients are defined for the following intervals; $-15^\circ \leq \alpha \leq 15^\circ$, $15^\circ < \alpha < 30^\circ$, $30^\circ \leq \alpha \leq 55^\circ$. For $\alpha > 55^\circ$ same aerodynamic coefficients for $30^\circ \leq \alpha \leq 55^\circ$ interval are used. Thus, the trim algorithm is executed separately for each of these intervals and three different trim angles of attack (α_0) solutions are found. Then, they are checked if they are really in the interval that they are solved for. The solution that matches with its corresponding interval is chosen as the right solution. There are some cases that the algorithm finds more than one α_0 matches. Whenever this is the case, the smallest matched α_0 solution is counted for the right solution. There are also some cases that the algorithm could not find any matching α_0 solution. In that case any α_0 is not found and the aircraft cannot be trimmed at the desired flight condition due to the angle of attack limitation.

Furthermore, the trim values of the aerodynamic surface deflections are also checked if they are in the designated intervals, i.e. if $-21^{\circ} \le \delta_{e0} \le 7^{\circ}$, $-16^{\circ} \le \delta_{a0} \le 16^{\circ}$ and $-30^{\circ} \le \delta_{r0} \le 30^{\circ}$. If these conditions are altered the aircraft cannot be trimmed at the desired flight condition. Also, the trim value of the total thrust (T_0) is checked whether P_{a0} found using equation (2.29) is less than and equal to 100%. If this condition is altered then the aircraft cannot be trimmed at the desired flight condition due to the thrust limitation.

Applying the proposed algorithm the trim points for the desired flight conditions are calculated for the altitudes in between 0 m to 15000 m, for the Mach numbers in between 0.1 to 1.5 and $\phi_0 = \theta_0 = p_0 = q_0 = r_0 = 0$ (wings level flight). For each point of the flight envelope the iterations are started from the initial values of $T_0 = 1000\text{N}$ and $\alpha_0 = \beta_0 = \delta_{a0} = \delta_{e0} = \delta_{r0} = 0$. Whenever α_0, δ_{e0}, δ_{a0}, δ_{r0} and T_0 conditional checks are altered the corresponding flight conditions are treated as the "border" conditions for the desired flight condition.

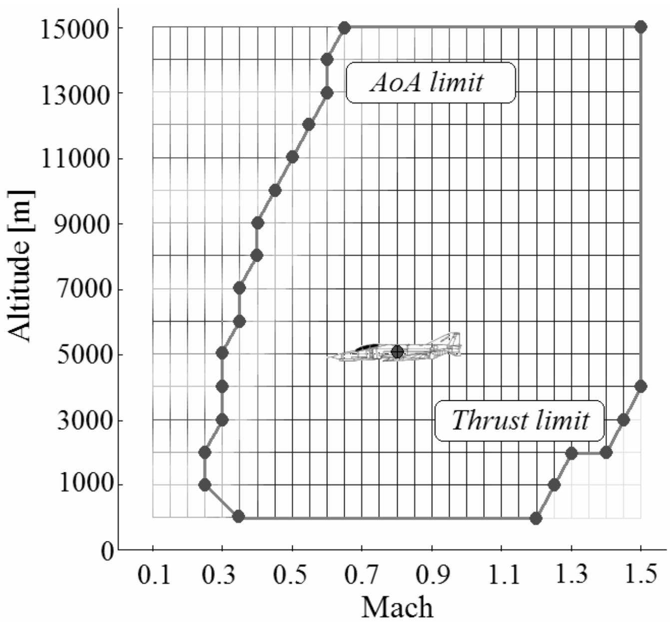

Figure 75. The Flight Envelope for the Wings Level Flight

As it is mentioned before, the trim algorithm will be used to find the equilibrium point around which the nonlinear aircraft dynamics will be linearized and used in the RP analysis.

For the analysis the nonlinear plant is chosen as the total plant composed of the NID, TVC, Engines, TVC paddles, Aero NID, Aero Control plants and the rules in Table 1. This is done in order to see the affect of NID coupled nonlinear aircraft dynamics in the RP analysis. For the analysis of the attitude controller the multiple plants are seen in Figure 76.

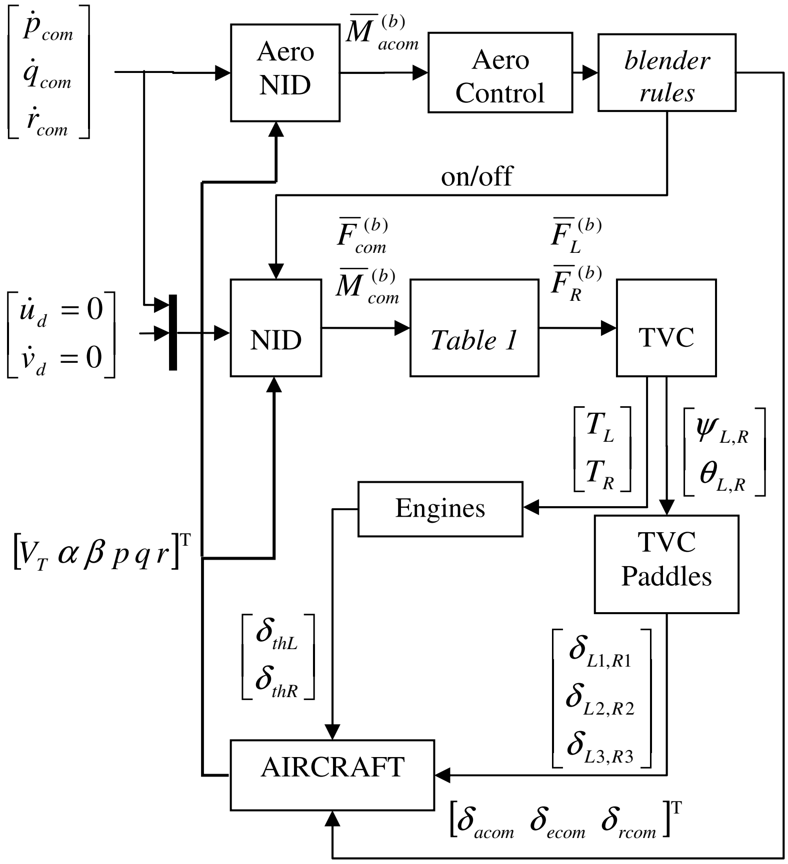

Figure 76. The Angular Acceleration Command Loop for Attitude Controller

Also, the resultant compact nonlinear plant is shown in Figure 77. Here, the translational motion outputs of the aircraft are chosen as the aircraft linear velocity components at the body fixed reference frame (u, v, w) instead of V_T, α and β. Hence, the output matrix of the resultant linear plant expression becomes an identity matrix.

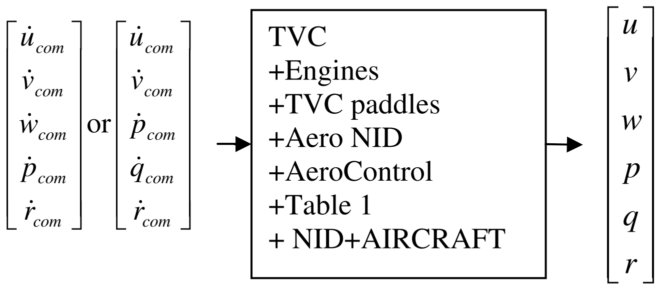

Figure 77. The Compact Nonlinear Dynamics

The compact nonlinear dynamics and its 1st order Taylor series expansion are expressed as:

$$\begin{bmatrix}\dot{u}_{com}\\ \dot{v}_{com}\\ \dot{w}_{com}\\ \dot{p}_{com}\\ \dot{q}_{com}\\ \dot{r}_{com}\end{bmatrix} = \bar{f}_c(\begin{bmatrix}u\\ v\\ w\\ p\\ q\\ r\end{bmatrix}) \tag{4.5}$$

$$\begin{bmatrix} \dot{u}_{com0} \\ \dot{v}_{com0} \\ \dot{w}_{com0} \\ \dot{p}_{com0} \\ \dot{q}_{com0} \\ \dot{r}_{com0} \end{bmatrix} + \begin{bmatrix} \Delta\dot{u} \\ \Delta\dot{v} \\ \Delta\dot{w} \\ \Delta\dot{p} \\ \Delta\dot{q} \\ \Delta\dot{r} \end{bmatrix} = \bar{f}_c\left(\begin{bmatrix} u_0 \\ v_0 \\ w_0 \\ p_0 \\ q_0 \\ r_0 \end{bmatrix}\right) + \hat{A}_c \begin{bmatrix} \Delta u \\ \Delta v \\ \Delta w \\ \Delta p \\ \Delta q \\ \Delta r \end{bmatrix} + \text{H.O.T.} \tag{4.6}$$

Here, $\bar{f}_c$ is the nonlinear function that represents the compact nonlinear dynamics.

$$\begin{aligned} \hat{A}_c = \big[&\partial\bar{f}_c / \partial u \; \partial\bar{f}_c / \partial v \; \partial\bar{f}_c / \partial w \\ &\partial\bar{f}_c / \partial p \; \partial\bar{f}_c / \partial q \; \partial\bar{f}_c / \partial r\big]_{u_0, v_0, w_0, p_0, q_0, r_0} \end{aligned} \tag{4.7}$$

Ignoring the higher order terms (H.O.T) following linear dynamics is found:

$$\begin{bmatrix} \Delta\dot{u} \\ \Delta\dot{v} \\ \Delta\dot{w} \\ \Delta\dot{p} \\ \Delta\dot{q} \\ \Delta\dot{r} \end{bmatrix} = \hat{A}_c \begin{bmatrix} \Delta u \\ \Delta v \\ \Delta w \\ \Delta p \\ \Delta q \\ \Delta r \end{bmatrix} \tag{4.8}$$

Equation (4.8) is the state space representation of the linearized compact nonlinear dynamics. Using the property $\hat{G}_{nom}(s) = (s\hat{I} - \hat{A}_c)^{-1}$ equation (4.8) can be expressed in Laplace domain. Thus, the linear transfer matrix ($\hat{G}_{nom}(s)$) is found:

$$\begin{bmatrix} \Delta u(s) \\ \Delta v(s) \\ \Delta w(s) \\ \Delta p(s) \\ \Delta q(s) \\ \Delta r(s) \end{bmatrix} = \hat{G}_{nom}(s) \begin{bmatrix} \Delta \dot{u}(s) \\ \Delta \dot{v}(s) \\ \Delta \dot{w}(s) \\ \Delta \dot{p}(s) \\ \Delta \dot{q}(s) \\ \Delta \dot{r}(s) \end{bmatrix} \tag{4.9}$$

Here, using the rules in Table 1 for the stabilization (*AoACont* =1) and attitude (*AoACont* =0) controllers two different linear transfer matrices are found. The transfer matrix for the stabilization controller is:

$$\hat{G}^{sta}_{nom}(s) = \begin{bmatrix} G_{uu}(s) & 0 & 0 & 0 & G_{uq}(s) & 0 \\ 0 & G_{vv}(s) & 0 & 0 & 0 & 0 \\ 0 & 0 & G_{ww}(s) & 0 & G_{wq}(s) & 0 \\ 0 & 0 & 0 & G_{pp}(s) & 0 & 0 \\ 0 & 0 & 0 & 0 & 0 & 0 \\ 0 & 0 & 0 & 0 & 0 & G_{rr}(s) \end{bmatrix} \tag{4.10}$$

Here, the transfer functions representing the dynamic cross-coupling between channels are $G_{uq}(s)$ and $G_{wq}(s)$. The output channel Δu is excited by $\Delta \dot{u}$ and $\Delta \dot{q}$ input channels. Similarly, the output channel Δw is excited by $\Delta \dot{w}$ and $\Delta \dot{q}$ input channels. Also, Δq is not excited by any of the input channels. This is originated from the constraint equation for α and/or w control, i.e. $M^{(b)}_{com\,y} = -e_x F^{(b)}_{com\,z} + e_z F^{(b)}_{com\,x}$.

Similarly, the transfer matrix for the attitude controller is:

$$\hat{G}_{nom}^{att}(s) = \begin{bmatrix} G_{uu}(s) & 0 & G_{uw}(s) & 0 & 0 & 0 \\ 0 & G_{vv}(s) & 0 & 0 & 0 & 0 \\ 0 & 0 & 0 & 0 & 0 & 0 \\ 0 & 0 & 0 & G_{pp}(s) & 0 & 0 \\ 0 & 0 & G_{qw}(s) & 0 & G_{qq}(s) & 0 \\ 0 & 0 & 0 & 0 & 0 & G_{rr}(s) \end{bmatrix} \tag{4.11}$$

Here, the transfer functions representing the dynamic cross-coupling between channels are $G_{uw}(s)$ and $G_{qw}(s)$. The output channel Δu is excited by $\Delta\dot{u}$ and $\Delta\dot{w}$ input channels. Similarly, the output channel Δq is excited by $\Delta\dot{q}$ and $\Delta\dot{w}$ input channels. Also, Δw is not excited by any of the input channels. This is originated from the constraint equation for q and/or θ control, i.e. $F_{com\,z}^{(b)} = (-M_{com\,y}^{(b)} + e_z F_{com\,x}^{(b)}) / e_x$.

The trim algorithm and the linearization is tested for the flight condition at which $h_0 = 7{,}500\,\text{m}$, $M_0 = 0.95$ and $\phi_0 = \theta_0 = p_0 = q_0 = r_0 = 0$. Using the trim algorithm the equilibrium points at the specified flight condition are found as $\beta_0 = \delta_{a0} = \delta_{r0} = 0$ and $T_0 = 26{,}428\,\text{N}$, $\alpha_0 = 0.33^\circ$ and $\delta_{e0} = \text{-}1.14^\circ$. Applying first order Taylor series expansion around the equilibrium points, $\hat{G}_{nom}^{sta}(s)$ and $\hat{G}_{nom}^{att}(s)$ are found. For the stabilization controller the transfer functions in $\hat{G}_{nom}^{sta}(s)$ are:

$$G_{uu}(s) = G_{vv}(s) = G_{ww}(s) = G_{pp}(s) = G_{rr}(s) = \frac{(s+211)}{s(s+211)} \tag{4.12}$$

$$G_{uq}(s) = \frac{0.10}{s(s+211)} \tag{4.13}$$

$$G_{wq}(s) = \frac{0.72s + 0.49}{s(s+211)} \tag{4.14}$$

Here, the transfer functions in equation (4.12) are pure integrators. This result is actually originating from the application of the nonlinear dynamic inversion, i.e. the feedback linearization.

As for the attitude controller the transfer functions in $\hat{G}_{nom}^{att}(s)$ are:

$$G_{uu}(s) = G_{vv}(s) = G_{ww}(s) = G_{pp}(s) = G_{rr}(s) = \frac{(s+0.69)}{s(s+0.69)} \tag{4.15}$$

$$G_{uw}(s) = \frac{-0.14}{s(s+0.69)} \tag{4.16}$$

$$G_{qw}(s) = \frac{1.40s+295}{s(s+0.69)} \tag{4.17}$$

Here, the transfer functions in equation (4.15) are also pure integrators.

In order to test $\hat{G}_{nom}^{sta}(s)$ and $\hat{G}_{nom}^{att}(s)$ they are simultaneously simulated with the compact nonlinear dynamics with the same $\dot{u}_{com}, \dot{v}_{com}, \dot{w}_{com}$ and $\dot{p}_{com}, \dot{q}_{com}, \dot{r}_{com}$ inputs. The block diagram of the simulation structure is shown in the following figure.

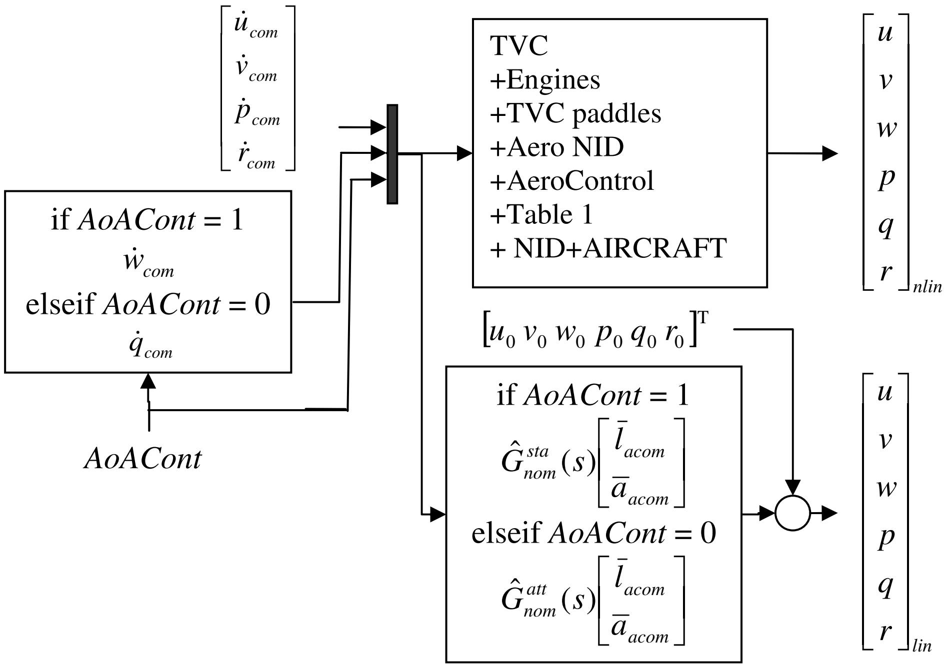

Figure 78. The Compact Nonlinear Dynamics and Linear Transfer Matrices

As mentioned before the trim values are found for $\dot{u}_{com0} = \dot{v}_{com0} = \dot{w}_{com0} = 0$ and $\dot{p}_{com0} = \dot{q}_{com0} = \dot{r}_{com0} = 0$. Thus, same inputs are used for the linear transfer matrix and the compact nonlinear plant, i.e. $[\Delta\dot{u}_{com}\ \Delta\dot{v}_{com}\ \Delta\dot{w}_{com}]^{\mathrm{T}} = [\dot{u}_{com}\ \dot{v}_{com}\ \dot{w}_{com}]^{\mathrm{T}}$ and $[\Delta\dot{p}_{com}\ \Delta\dot{q}_{com}\ \Delta\dot{r}_{com}]^{\mathrm{T}} = [\dot{p}_{com}\ \dot{q}_{com}\ \dot{r}_{com}]^{\mathrm{T}}$. Also, the inputs of $\hat{G}^{sta}_{nom}(s)$ and $\hat{G}^{att}_{nom}(s)$ are dependent on *AoACont*. If *AoACont* = 1, then $\bar{l}_{acom} = [\dot{u}_{com}\ \dot{v}_{com}\ \dot{w}_{com}]^{\mathrm{T}}$ and $\bar{a}_{acom} = [\dot{p}_{com}\ \dot{r}_{com}]^{\mathrm{T}}$, on the contrary, if *AoACont* = 0, then $\bar{l}_{acom} = [\dot{u}_{com}\ \dot{v}_{com}]^{\mathrm{T}}$ and $\bar{a}_{acom} = [\dot{p}_{com}\ \dot{q}_{com}\ \dot{r}_{com}]^{\mathrm{T}}$.

For the stabilization controller $\hat{G}^{sta}_{nom}(s)$ and the compact nonlinear dynamics are simulated simultaneously with $\dot{p}_{com} = \dot{q}_{com} = \dot{r}_{com} = 0$. $\dot{u}_{com}, \dot{v}_{com}$ and $\dot{w}_{com}$ are chosen as zero mean white noise signals with Gaussian distribution and standard deviation values of $\dot{u}_{std} = \dot{v}_{std} = \dot{w}_{std} = 100$ m/sec. Figure 79 and Figure 80 shows the simulation results. The values drawn with dotted lines are the outputs of

$\hat{G}_{nom}^{sta}(s)$ and the values drawn with continuous lines are the outputs of the compact nonlinear dynamics.

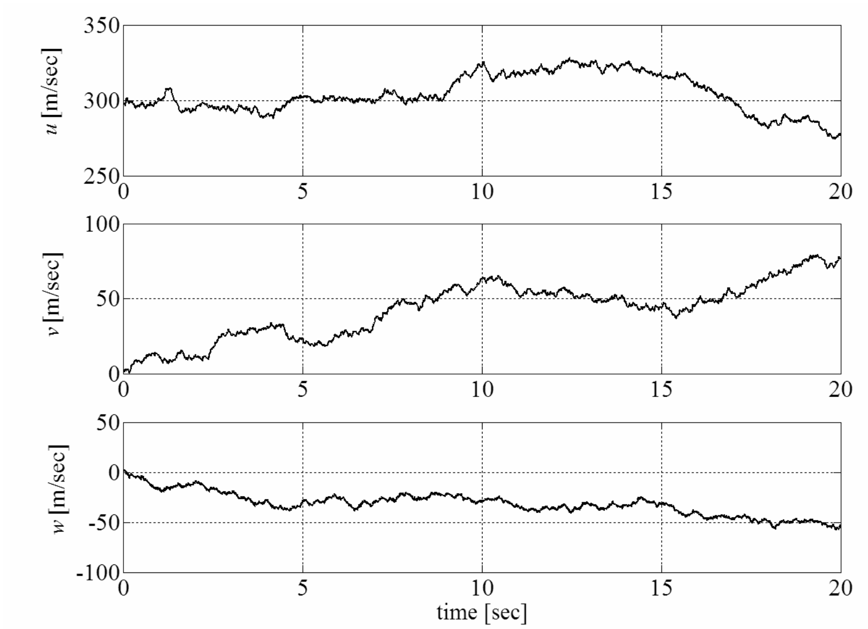

Figure 79. u, v, w Outputs of the ND and the Linear TM for Stab. Control

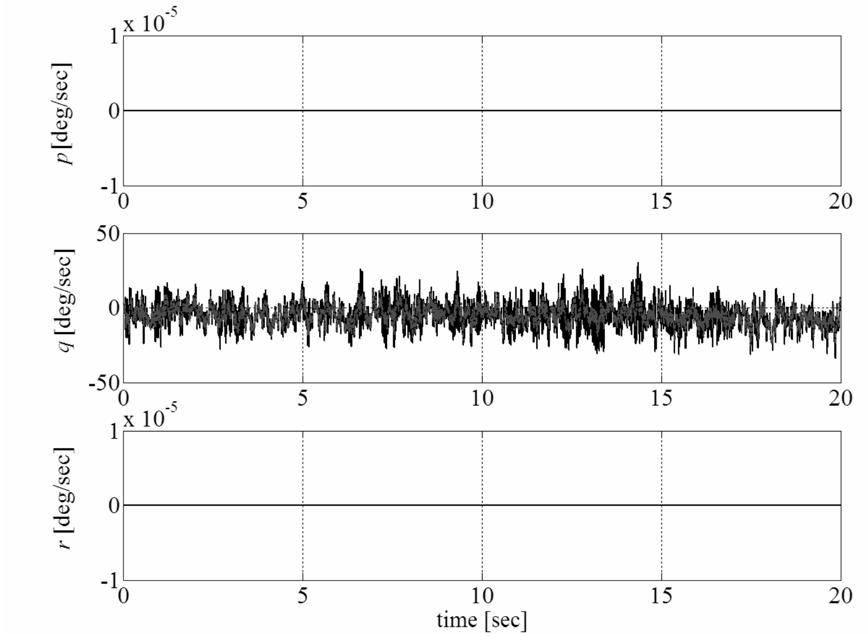

Figure 80. p, q, r Outputs of the ND and the Linear TM for Stab. Control

Figure 79 and Figure 80 show that the translational velocity component outputs (u, v, w) of $\hat{G}_{nom}^{sta}(s)$ and the compact nonlinear dynamics are perfectly matched. However, since $AoACont = 1$, q cannot be controlled.

Figure 80 shows that q output of $\hat{G}_{nom}^{sta}(s)$ (dotted line) is not exactly the same with that of the compact nonlinear dynamics (continuous line). However, they show similar characteristics and vary around the trim value $q_0 = 0$ in between $\pm 30^\circ$/sec.

In the simulations p and r components of the angular velocity are desired to be kept constant at their trim values (p_0, r_0). Inspecting p and r outputs of the compact nonlinear dynamics it is seen that there is not any dynamical coupling between $\Delta\dot{u}_{com}, \Delta\dot{v}_{com}, \Delta\dot{w}_{com}$ and $\Delta p, \Delta r$ channels. This is also true for $\hat{G}_{nom}^{sta}(s)$ since p and r outputs of $\hat{G}_{nom}^{sta}(s)$ are zero. Here, the linearization pursued by applying the 1st order Taylor series expansion inherently reflects the characteristics of the compact nonlinear dynamics.

Similarly for the attitude controller, $\hat{G}_{nom}^{att}(s)$ and the compact nonlinear dynamics are simultaneously simulated with $\dot{u}_{com} = \dot{v}_{com} = 0$. $\dot{p}_{com}, \dot{q}_{com}, \dot{r}_{com}$ are chosen as zero mean white noise signals with *Gaussian* distribution and standard deviation values of $\dot{p}_{std} = \dot{q}_{std} = \dot{r}_{std} = 100^{\circ}$/sec. Figure 81 and Figure 82 show the simulation results. The values drawn with dotted lines are the outputs of $\hat{G}_{nom}^{att}(s)$ and the values drawn with continuous lines are the outputs of the compact nonlinear dynamics.

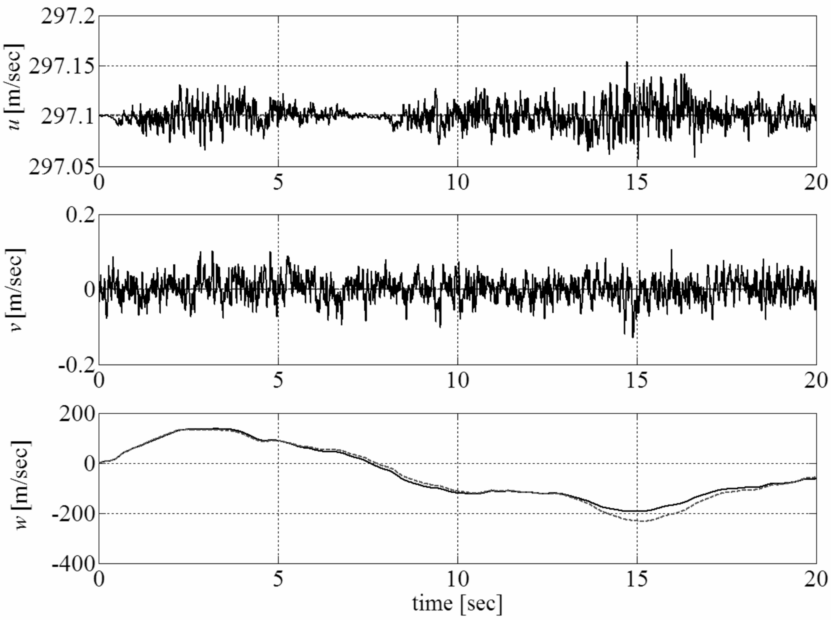

Figure 81. u, v, w Outputs of the ND and the Linear TM for Att. Control

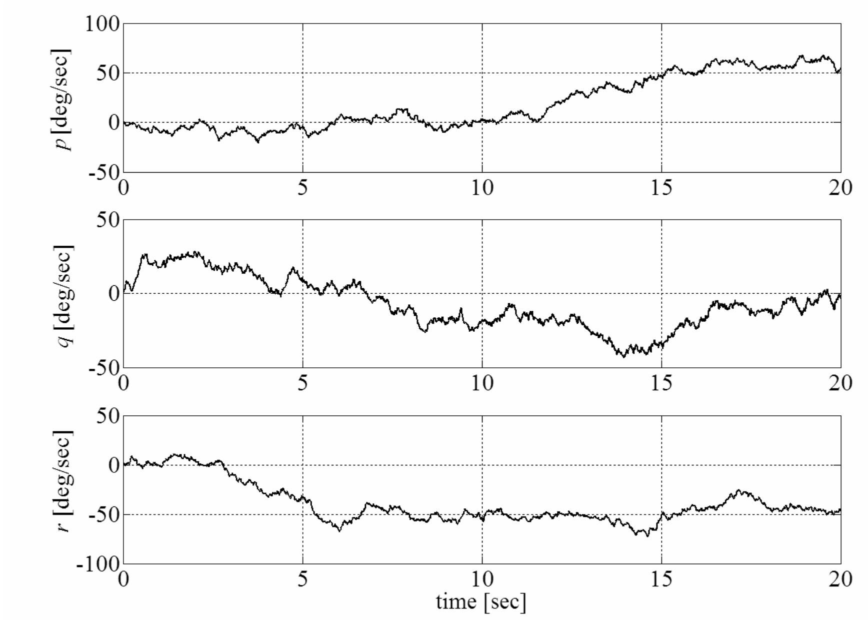

Figure 82. p, q, r Outputs of the ND and the Linear TM for Att. Control

Figure 81 and Figure 82 show that the angular velocity component outputs (p, q, r) of $\hat{G}_{nom}^{att}(s)$ and the compact nonlinear dynamics are perfectly matched. However, since $AoACont = 0$, w cannot be controlled.

Figure 81 shows that w outputs of $\hat{G}_{nom}^{att}(s)$ and the compact nonlinear dynamics highly deviate from the trim value $w_0 = 0$ and reach up to ± 200 m/sec. This leads to w output of $\hat{G}_{nom}^{att}(s)$ (dotted line) differ from w output of the compact nonlinear dynamics (continuous line) in certain amount. This is a presumable result since w output of $\hat{G}_{nom}^{att}(s)$ is highly deviated from its trim value and the linearized dynamics is not completely representing the compact nonlinear dynamics.

In the simulations u and v components of the translational velocity are desired to be kept constant at the trim values (u_0, w_0). However, inspecting u and v outputs of the compact nonlinear dynamics, it is seen that there is still small dynamic coupling between $\dot{p}_{com}, \dot{q}_{com}, \dot{r}_{com}$ and u, v. Here, $\dot{p}_{com}, \dot{q}_{com}, \dot{r}_{com}$ inputs slightly activates u and v outputs that they vary around the trim values within ± 0.1 m/sec. On the other hand, analyzing $\hat{G}_{nom}^{att}(s)$ there is no dynamical coupling between $\Delta\dot{p}_{com}, \Delta\dot{q}_{com}, \Delta\dot{r}_{com}$ and $\Delta u, \Delta v$ channels, and, u and v outputs of $\hat{G}_{nom}^{att}(s)$ are zero. This is because of the fact that the linearization pursued by applying the 1st order Taylor series expansion cannot represent the complete dynamics of the compact nonlinear plant. However, the dynamic coupling effect on u and v channels is very small. Thus, in the RP analysis (that uses $\hat{G}_{nom}^{att}(s)$) u and v channels are assumed to be uncoupled from $\Delta\dot{p}_{com}, \Delta\dot{q}_{com}, \Delta\dot{r}_{com}$.

4.2. Uncertainty Estimation for Robust Performance Analysis

The uncertainty estimation for RP analysis is pursued by applying the linearization of the compact nonlinear dynamics mentioned in the previous section. In order to estimate the uncertainty, the compact nonlinear dynamics is divided into two separate parts. The first part consists of the nonlinear dynamic inversion using the aerodynamic and thrust vectoring control effectors and the second part consists of the nonlinear dynamics with the engine and aircraft dynamics.

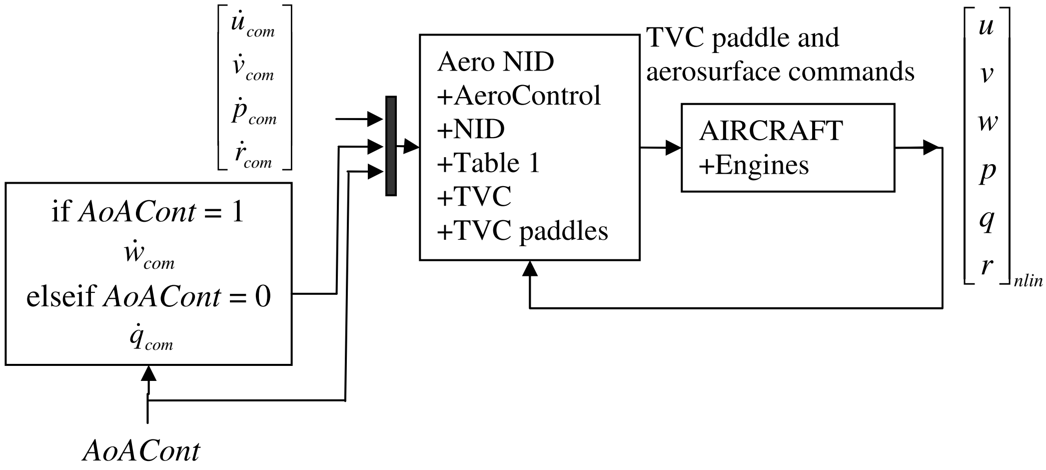

Figure 83. The Compact Nonlinear Dynamics Separated in 2-Parts

$\hat{G}^{sta}_{nom}(s)$ and $\hat{G}^{att}_{nom}(s)$ are calculated at the condition that the first part is exactly the inverse of the second part. Thus, for a proper inversion, it is very crucial to identify the parameters of the nonlinear dynamics exactly. The most important parameters of the nonlinear plant dynamics are the aerodynamic coefficients which are explained in Chapter 2. They are conventionally estimated by using the databases (aided by semi-empirical methods) of similar air vehicles, wind tunnel tests, computational fluid dynamics (CFD) design tools and flight tests. All of these methods have certain estimation errors dependent on several factors. That is, the technique and methodology of estimation, the flight conditions at which the estimations are made and the geometry of the aircraft are very important factors affecting the estimation accuracy.

The estimation errors on the aerodynamic coefficients are generally specified with percentages. Figure 84 shows an example for comparison of some aerodynamic coefficient derivatives estimated by using JKay Vortex Lattice Method (a CFD method based on vortex rings assignment) [53] and USAF Digital DATCOM [54] for an F-18 type configuration. The deviations of the aerodynamic coefficient derivatives from the nominal (Data) are different for two of the methods and flight conditions.

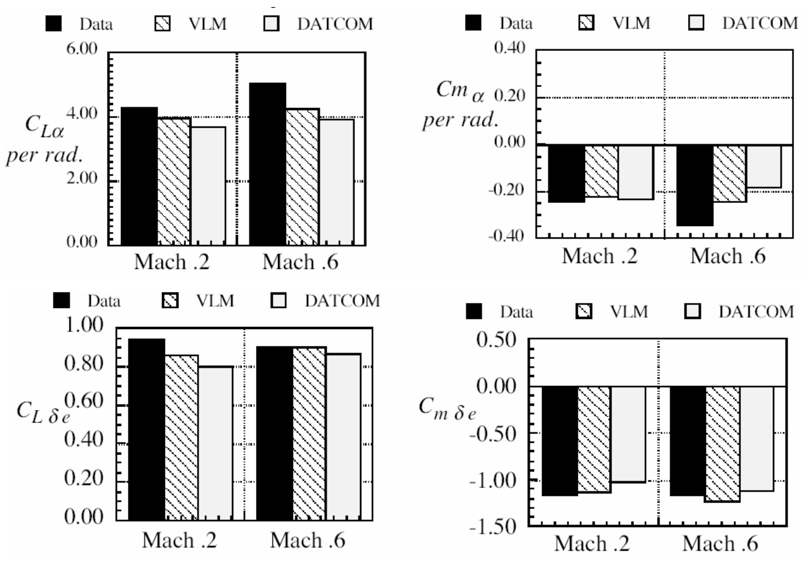

Figure 84. Aerodynamic Coefficient Uncertainties for F-18 [53]

Recall that, as explained in Chapter 3, the commanded forces and moments ($\overline{F}_{com}^{(b)}$ and $\overline{M}_{com}^{(b)}$) are calculated by using the aerodynamic forces and moments ($\overline{F}_a$ and $\overline{M}_a$) as defined by equation (3.9). Also remember that $\overline{F}_a$ and $\overline{M}_a$ are functions of the aerodynamic coefficients. Hence, the estimation errors of the aerodynamic coefficients will directly effect $\overline{F}_{com}^{(b)}$ and $\overline{M}_{com}^{(b)}$ which then lead to $\overline{F}_{Lcom}{}^{(b)}$ and $\overline{F}_{Rcom}{}^{(b)}$ according to equation (3.8). Also, as explained in Chapter 2, the thrust deflection angles $\{\psi_{Lcom},\ \theta_{Lcom}$ and $\psi_{Rcom},\ \theta_{Rcom}\}$ are calculated using $\overline{F}_{Lcom}{}^{(b)}$ and $\overline{F}_{Rcom}{}^{(b)}$ and the TVC paddle deflection angles ($\delta_{L1}, \delta_{L2}, \delta_{L3}$, and, $\delta_{R1}, \delta_{R2}, \delta_{R3}$) are calculated using the thrust deflection angles. Eventually, the estimation errors of the aerodynamic coefficients will directly effect the commanded TVC paddle deflections and degrade the performance of the designed controller or even cause improper operation. Therefore, it is crucial to analyze the effects of the aerodynamic coefficient uncertainties on the controller performance.

The effects of the estimation errors are analyzed by using the trimming and linearization method explained in the previous section. Here, the compact nonlinear dynamics separated into two parts (shown in Figure 83) is also used.

The analysis starts with a very marginal assumption. Suppose that the aerodynamic coefficients, thus the aerodynamic forces and moments, are completely unknown. Hence, the effects of the aerodynamic control surfaces are neglected and the nonlinear dynamic inversion is done with $\overline{F}_a = \overline{M}_a = \overline{0}$. In that case the aerodynamic NID is non-operative and the whole control should be realized by the TVC. The compact nonlinear dynamics separated into two parts (with $\overline{F}_a = \overline{M}_a = \overline{0}$) is shown in Figure 85.

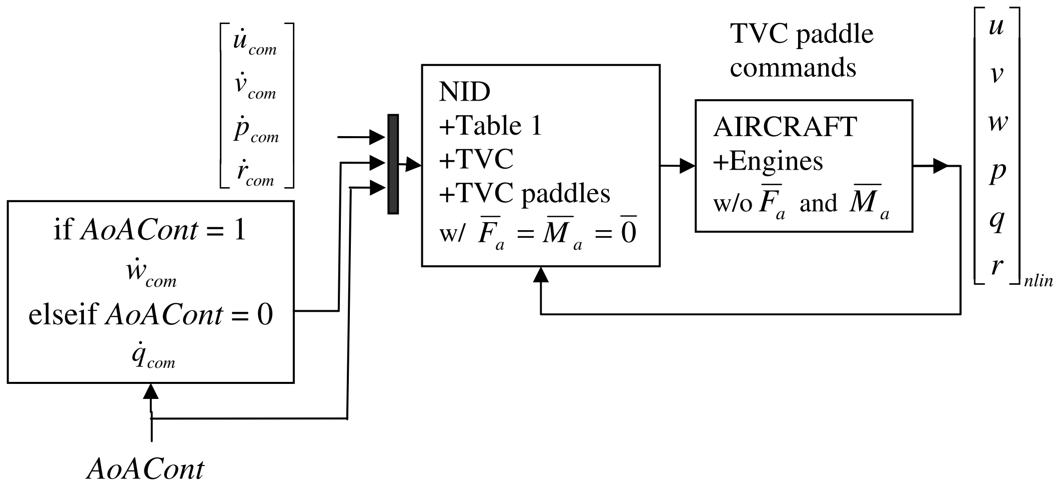

Figure 85. The Compact ND Separated in 2-Parts ($\overline{F}_a = \overline{M}_a = \overline{0}$)

The block diagram in Figure 85 is linearized by using the trimming and linearization methods explained in the previous section. As expected, this linearization lead to the *perturbed* transfer matrices ($\hat{G}^{sta}(s)$, $\hat{G}^{att}(s)$) which are different than the nominal transfer matrices ($\hat{G}^{sta}_{nom}(s)$, $\hat{G}^{att}_{nom}(s)$). The block diagrams of the linearized perturbed compact nonlinear dynamics, $\hat{G}_{nom}^{sta}(s)$ and $\hat{G}_{nom}^{att}(s)$ with the additive uncertainty transfer matrices, for the stabilization and the attitude controllers are shown in the following figures.

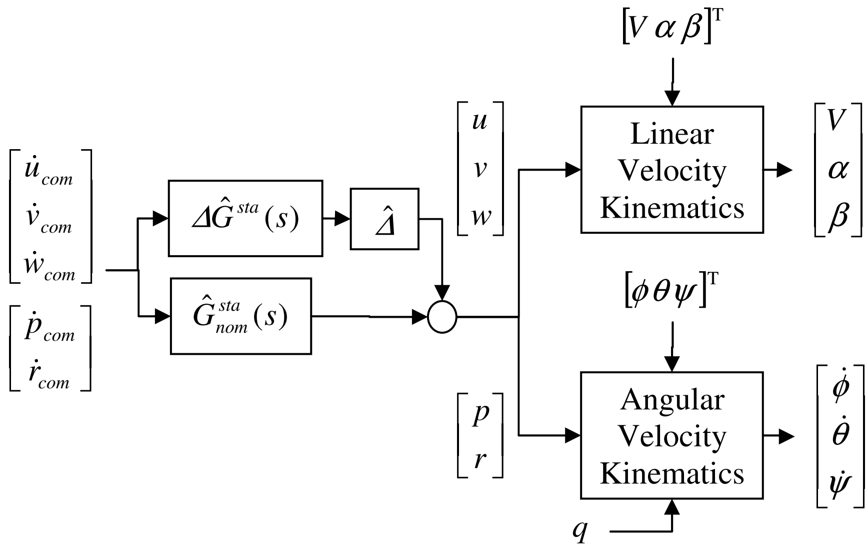

Figure 86. $\dot{u}_{com}$, $\dot{v}_{com}$, $\dot{w}_{com}$ Command Loop for the Stabilization Controller

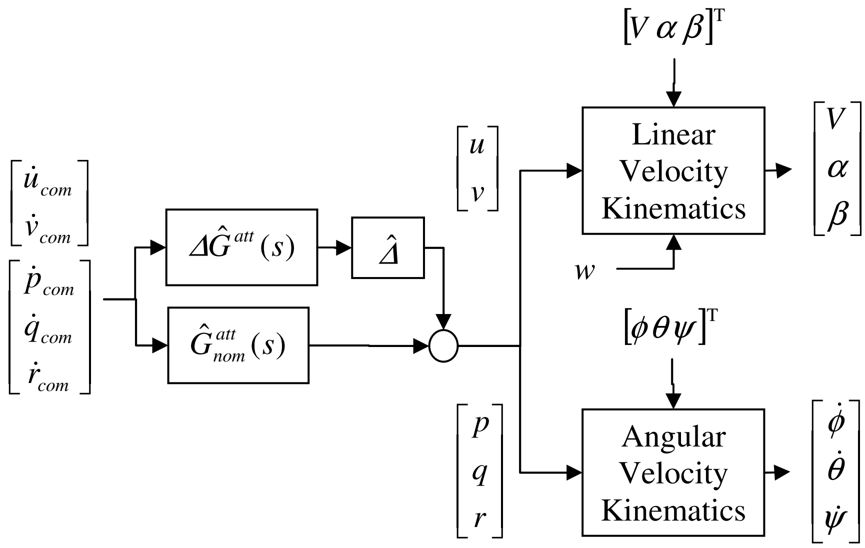

Figure 87. $\dot{p}_{com}$, $\dot{q}_{com}$, $\dot{r}_{com}$ Command Loop for the Attitude Controller

The nominal transfer matrices ($\hat{G}^{sta}_{nom}(s)$, $\hat{G}^{att}_{nom}(s)$) and the perturbed transfer matrices ($\hat{G}^{sta}(s)$, $\hat{G}^{att}(s)$) are presented by using the Bode magnitude plots of the nominal and perturbed transfer functions. The plots are drawn for the flight condition at which the Mach number is 0.95 and the altitude is 7,500 m. $\dot{u}_{com}$, $\dot{v}_{com}$, $\dot{w}_{com}$ command loop plots for the stabilization controller are shown in Figure 88 to Figure 92. The dashed lines refer to the nominal transfer functions and the continuous lines refer to the perturbed transfer functions.

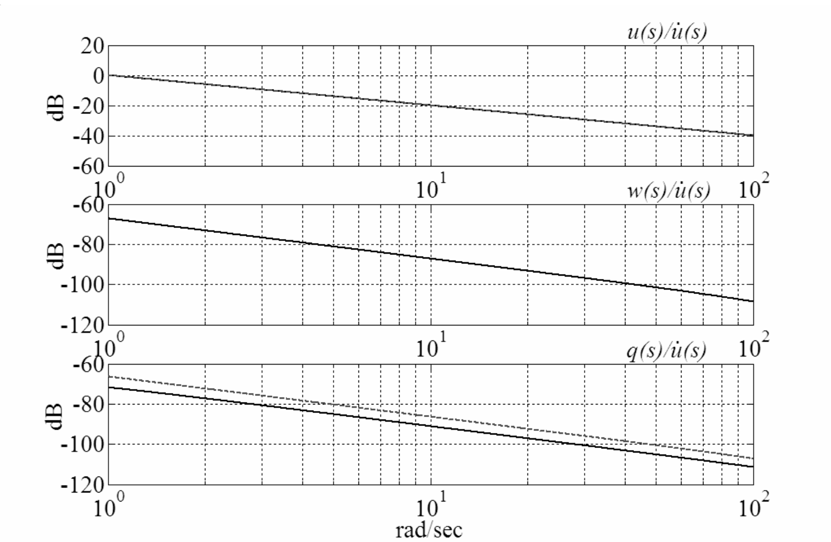

Figure 88. $\dot{u}$ Channel Nominal and Perturbed TFs (Stabilization Controller)

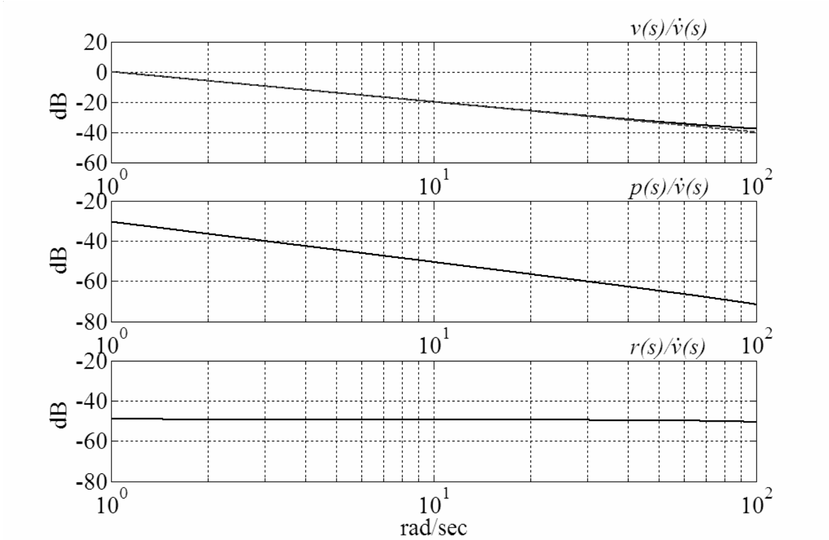

Figure 89. $\dot{v}$ Channel Nominal and Perturbed TFs (Stabilization Controller)

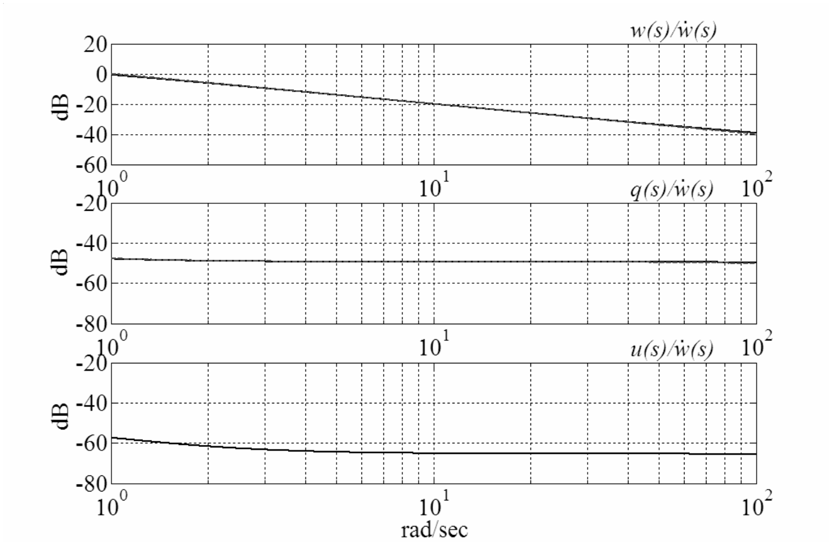

Figure 90. $\dot{w}$ Channel Nominal and Perturbed TFs (Stabilization Controller)

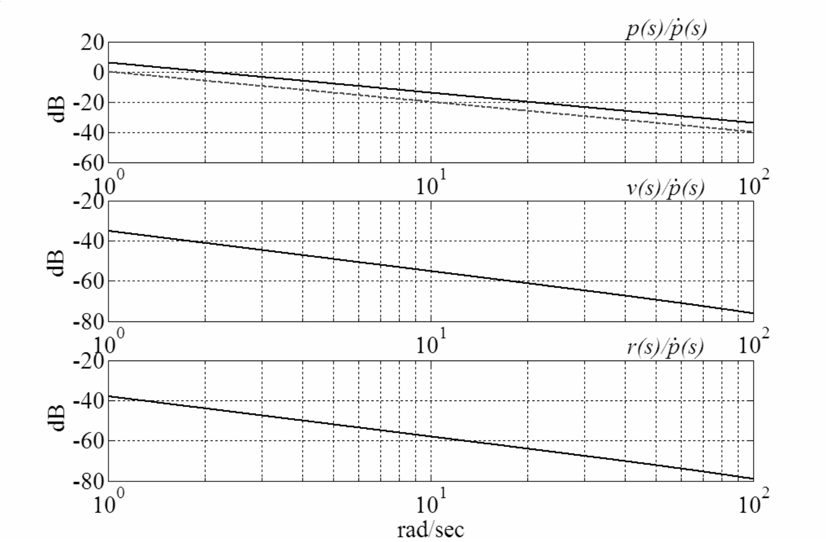

Figure 91. $\dot{p}$ Channel Nominal and Perturbed TFs (Stabilization Controller)

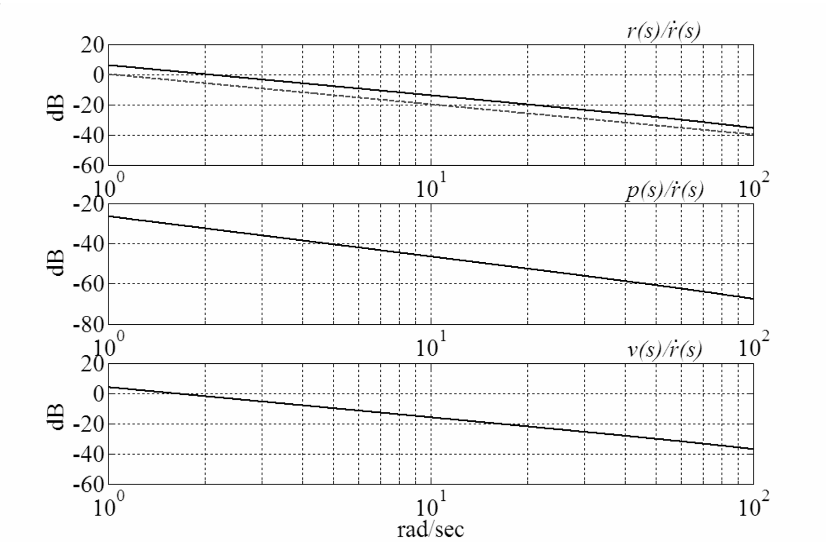

Figure 92. $\dot{r}$ Channel Nominal and Perturbed TFs (Stabilization Controller)

The analysis of the stabilization control loop showed that for $u(s)/\dot{u}(s)$, $v(s)/\dot{v}(s)$ and $w(s)/\dot{w}(s)$ the nominal and perturbed transfer functions are almost the same.

The transfer functions; $w(s)/\dot{u}(s)$, $p(s)/\dot{v}(s)$, $r(s)/\dot{v}(s)$, $u(s)/\dot{w}(s)$, $v(s)/\dot{p}(s)$, $r(s)/\dot{p}(s)$, $p(s)/\dot{r}(s)$ and $v(s)/\dot{r}(s)$ are uncoupled in $\hat{G}^{sta}_{nom}(s)$. However, the nonlinear dynamic inversion with $\overline{F}_a = \overline{M}_a = \overline{0}$ induces small dynamic couplings between these channels in $\hat{G}^{sta}(s)$. On the other hand, the nonlinear dynamic inversion with $\overline{F}_a = \overline{M}_a = \overline{0}$ strongly effects the transfer functions $q(s)/\dot{u}(s)$, $p(s)/\dot{p}(s)$ and $r(s)/\dot{r}(s)$. Here, nearly 100% dc-gain differences between the nominal and perturbed transfer functions are seen.

Similar analysis is done for $\dot{p}_{com}$, $\dot{q}_{com}, \dot{r}_{com}$ command loop for the attitude controller and the Bode magnitude plots are drawn. Similar to the previous analysis the dashed lines refer to the nominal transfer functions and the continuous lines refer to the perturbed transfer functions.

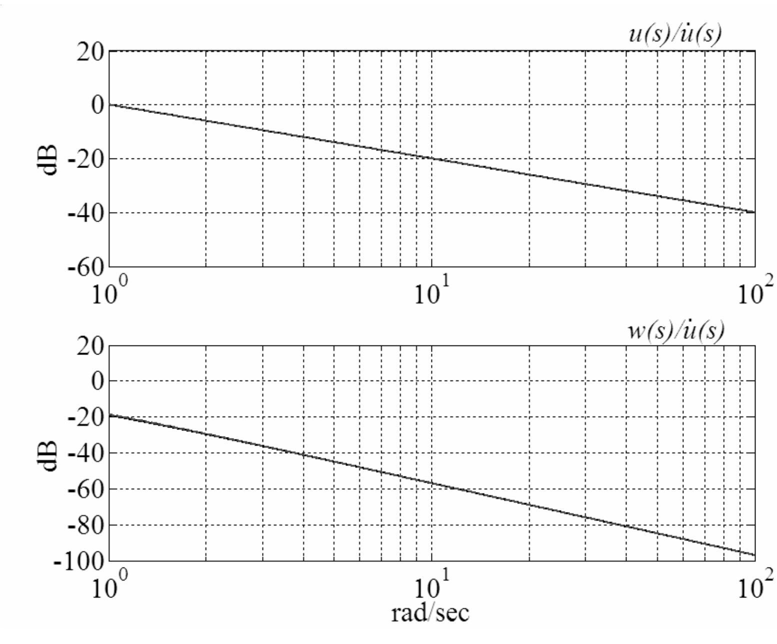

Figure 93. $\dot{u}$ Channel Nominal and Perturbed TFs (Attitude Controller)

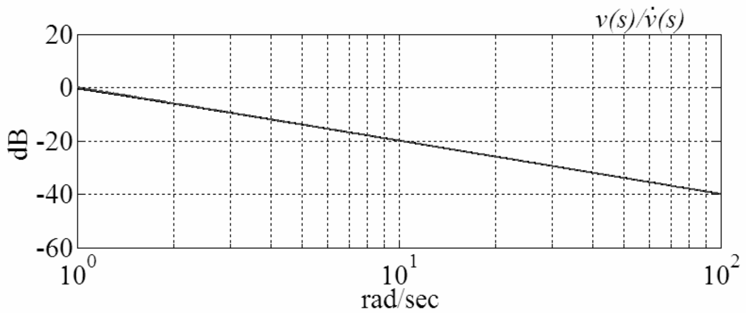

Figure 94. $\dot{v}$ Channel Nominal and Perturbed TFs (Attitude Controller)

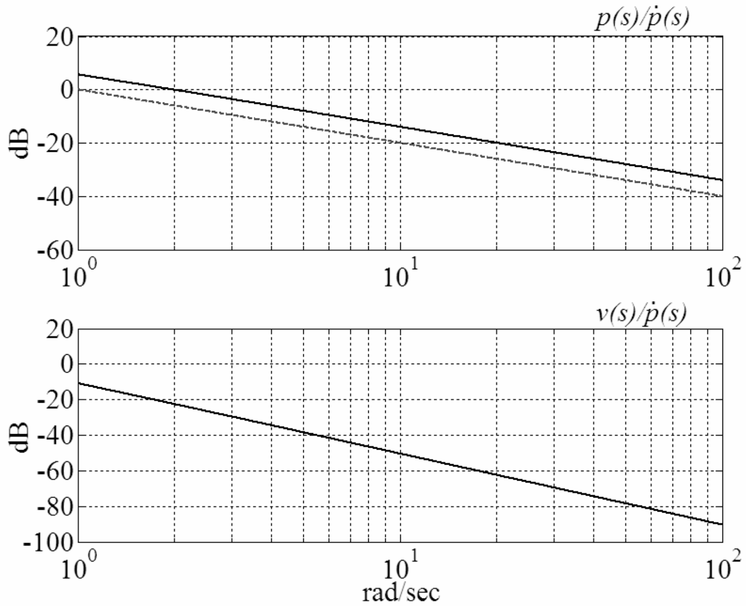

Figure 95. $\dot{p}$ Channel Nominal and Perturbed TFs (Attitude Controller)

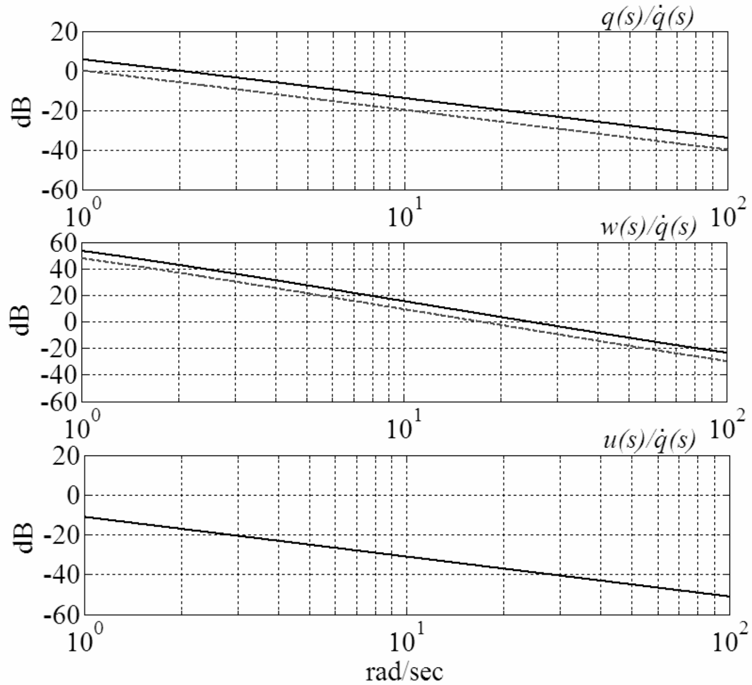

Figure 96. $\dot{q}$ Channel Nominal and Perturbed TFs (Attitude Controller)

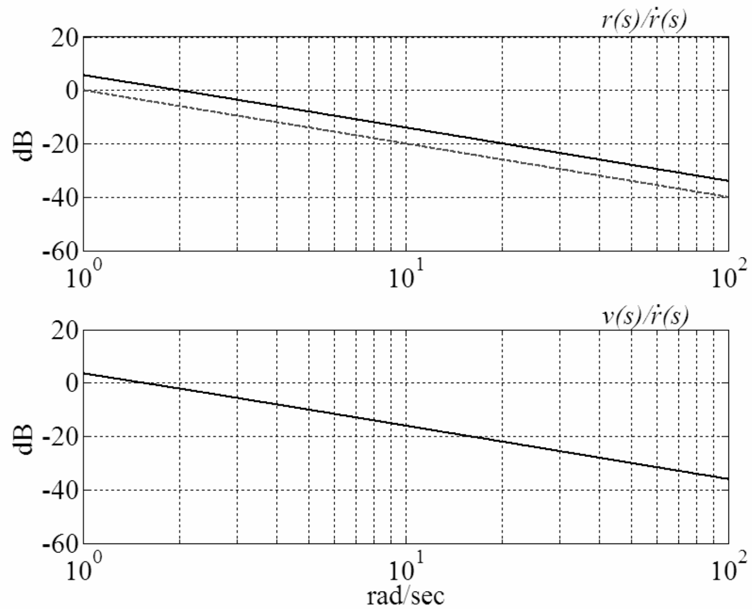

Figure 97. $\dot{r}$ Channel Nominal and Perturbed TFs (Attitude Controller)

The analysis on the attitude controller showed that for $u(s)/\dot{u}(s)$, $w(s)/\dot{u}(s)$ and $v(s)/\dot{v}(s)$ the nominal and perturbed transfer functions are the same. Also, the transfer functions; $v(s)/\dot{p}(s)$, $u(s)/\dot{q}(s)$ and $v(s)/\dot{r}(s)$ are uncoupled in $\hat{G}^{att}_{nom}(s)$. However, for $\hat{G}^{att}(s)$ the nonlinear dynamic inversion with $\overline{F}_a = \overline{M}_a = \overline{0}$ induces small dynamic couplings between these channels. On the other hand, the nonlinear dynamic inversion with $\overline{F}_a = \overline{M}_a = \overline{0}$ strongly effected the transfer functions $p(s)/\dot{p}(s)$, $q(s)/\dot{q}(s)$, $w(s)/\dot{q}(s)$ and $r(s)/\dot{r}(s)$. Here, nearly 100% dc-gain differences between the nominal and perturbed transfer functions are seen.

The differences between the perturbed and the nominal transfer matrices are the uncertainties on the nominal transfer matrices:

$$\Delta\hat{G}^{sta}(s) = \hat{G}^{sta}(s) - \hat{G}^{sta}_{nom}(s) \tag{4.18}$$

$$\Delta\hat{G}^{att}(s) = \hat{G}^{att}(s) - \hat{G}^{att}_{nom}(s) \tag{4.19}$$

Here, $\Delta\hat{G}^{sta}(s)$ and $\Delta\hat{G}^{att}(s)$ are the transfer matrices defining the *additive uncertainty* on the nominal transfer matrices. They are composed of additive uncertainty transfer functions:

$$\Delta\hat{G}^{sta}(s) = \begin{bmatrix} 0 & 0 & \Delta G^{sta}_{w\dot{u}}(s) & 0 & \Delta G^{sta}_{q\dot{u}}(s) & 0 \\ 0 & 0 & 0 & \Delta G^{sta}_{p\dot{v}}(s) & 0 & \Delta G^{sta}_{r\dot{v}}(s) \\ \Delta G^{sta}_{u\dot{w}}(s) & 0 & 0 & 0 & 0 & 0 \\ 0 & \Delta G^{sta}_{v\dot{p}}(s) & 0 & \Delta G^{sta}_{p\dot{p}}(s) & 0 & \Delta G^{sta}_{r\dot{p}}(s) \\ 0 & 0 & 0 & 0 & 0 & 0 \\ 0 & \Delta G^{sta}_{v\dot{r}}(s) & 0 & \Delta G^{sta}_{p\dot{r}}(s) & 0 & \Delta G^{sta}_{r\dot{r}}(s) \end{bmatrix} \tag{4.20}$$

$$\Delta\hat{G}^{att}(s)=\begin{bmatrix} 0 & 0 & 0 & 0 & 0 & 0 \\ 0 & 0 & 0 & 0 & 0 & 0 \\ 0 & 0 & 0 & 0 & 0 & 0 \\ 0 & \Delta G_{v\dot{p}}^{att}(s) & 0 & \Delta G_{p\dot{p}}^{att}(s) & 0 & 0 \\ \Delta G_{u\dot{q}}^{att}(s) & 0 & \Delta G_{w\dot{q}}^{att}(s) & 0 & \Delta G_{q\dot{q}}^{att}(s) & 0 \\ 0 & \Delta G_{v\dot{r}}^{att}(s) & 0 & 0 & 0 & \Delta G_{r\dot{r}}^{att}(s) \end{bmatrix} \quad (4.21)$$

For the stabilization controller the transfer functions forming $\Delta\hat{G}^{sta}(s)$ are:

$$\Delta G_{w\dot{u}}^{sta}(s)=\frac{-30.08}{s(s^2+553.07s+68857)} \quad (4.22)$$

$$\Delta G_{q\dot{u}}^{sta}(s)=\frac{0.11s+19.08}{s(s^2+553.07s+68857)} \quad (4.23)$$

$$\Delta G_{p\dot{v}}^{sta}(s)=\frac{5.62s+2050.80}{s(s^2+553.07s+68857)} \quad (4.24)$$

$$\Delta G_{r\dot{v}}^{sta}(s)=\frac{-0.63s^2-231.32s-88.66}{s(s^2+553.07s+68857)} \quad (4.25)$$

$$\Delta G_{u\dot{w}}^{sta}(s)=\frac{-0.20s^2-37.90s-85.74}{s(s^2+553.07s+68857)} \quad (4.26)$$

$$\Delta G_{v\dot{p}}^{sta}(s)=\frac{-3.40s-1202.60}{s(s^2+553.07s+68857)} \quad (4.27)$$

$$\Delta G_{p\dot{p}}^{sta}(s)=\frac{2s^2+1106.20s+137710}{s(s^2+553.07s+68857)} \quad (4.28)$$

$$\Delta G_{r\dot{p}}^{sta}(s) = \frac{2.35s + 868.51}{s(s^2 + 553.07s + 68857)} \tag{4.29}$$

$$\Delta G_{v\dot{r}}^{sta}(s) = \frac{297.05s + 108340}{s(s^2 + 553.07s + 68857)} \tag{4.30}$$

$$\Delta G_{p\dot{r}}^{sta}(s) = \frac{-8.86s - 3232.40}{s(s^2 + 553.07s + 68857)} \tag{4.31}$$

$$\Delta G_{r\dot{r}}^{sta}(s) = \frac{s^2 + 364.60s + 137710}{s(s^2 + 553.07s + 68857)} \tag{4.32}$$

For the attitude controller the transfer functions forming $\Delta\hat{G}^{att}(s)$ are:

$$\Delta G_{v\dot{p}}^{att}(s) = \frac{0.30s + 0.21}{s^2(s + 0.79)} \tag{4.33}$$

$$\Delta G_{p\dot{p}}^{att}(s) = \frac{2s^2 + 1.59s + 0.15}{s^2(s + 0.79)} \tag{4.34}$$

$$\Delta G_{u\dot{q}}^{att}(s) = \frac{\text{s}(-0.28s - 0.22)}{s^2(s + 0.79)} \tag{4.35}$$

$$\Delta G_{w\dot{q}}^{att}(s) = \frac{3.33s^2 + 589.78s + 62.91}{s^2(s + 0.79)} \tag{4.36}$$

$$\Delta G_{q\dot{q}}^{att}(s) = \frac{2s^2 + 1.59s + 0.15}{s^2(s + 0.79)} \tag{4.37}$$

$$\Delta G_{v\dot{r}}^{att}(s) = \frac{s(-1.58s - 1.08)}{s^2(s+0.79)} \tag{4.38}$$

$$\Delta G_{r\dot{r}}^{att}(s) = \frac{2s^2 + 1.59s + 0.15}{s^2(s+0.79)} \tag{4.39}$$

4.3. Robust Performance Analysis of the Controllers

The robust performance analysis starts by constructing the block diagrams for the stabilization and attitude controllers. The following figures show the stabilization controller block diagrams for the analysis:

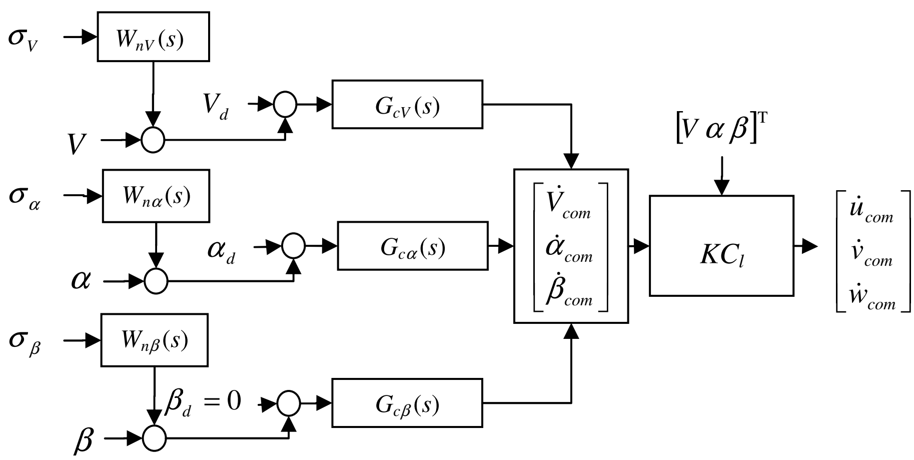

Figure 98. The Stabilization Controller Block Diagram

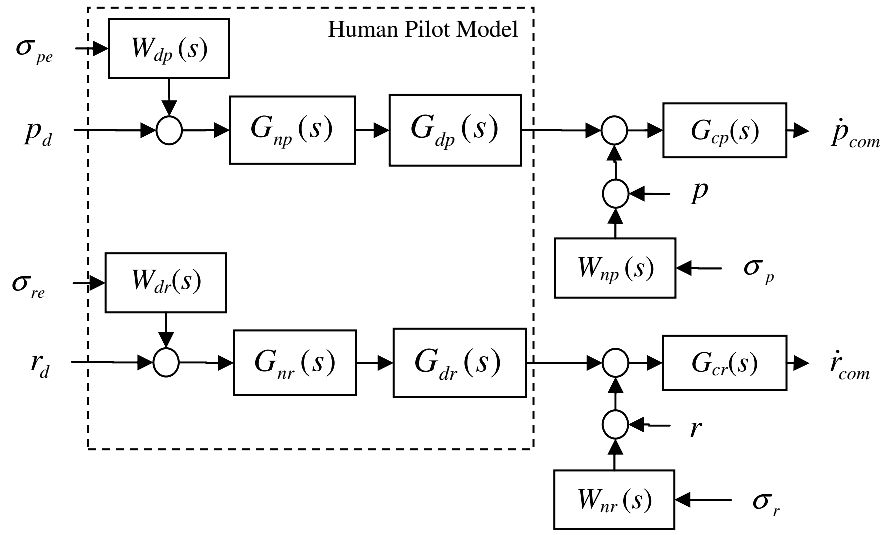

Figure 99. The Stabilization Controller Block Diagram (cont'd)

In the stabilization controller block diagrams $G_{cV}(s)$, $G_{c\alpha}(s)$ and $G_{c\beta}(s)$ are the PI controller transfer functions structured by using the gain matrices $\hat{K}_{pl}$ and $\hat{K}_{il}$ and $G_{cp}(s)$ and $G_{cr}(s)$ are the P controller transfer functions structured by the gain matrix $\hat{K}_d$ as discussed in Chapter 3.

The shaping filters of the measurement noises (discussed in Chapter 2.7) on the total velocity and the angular velocity measured by means of an on-board INS are denoted by $W_{nV}(s)$ and $W_{np}(s)$, $W_{nr}(s)$. Similarly, the shaping filters of the measurement noises on the angle of attack and side slip angles measured by means of the on-board flow angle measurement devices are denoted by $W_{n\alpha}(s)$ and $W_{n\beta}(s)$. As for the human pilot model (discussed in Chapter 2.8), $W_{dp}(s)$, $W_{dr}(s)$ are used for the transfer functions of the shaping filters of the disturbance noise (the engine noise) effecting the pilot in the cockpit. In the analysis all of the shaping filters of the random noise signals are set to unity.

Also, the neuro-motor lag and the second order Padé delay transfer functions for the angular velocity control channels are denoted by $G_{np}(s)$, $G_{nr}(s)$ and $G_{dp}(s)$ and $G_{dr}(s)$ for the stabilization controller.

Similar block diagrams are also constructed for the robust performance analysis of the attitude controller:

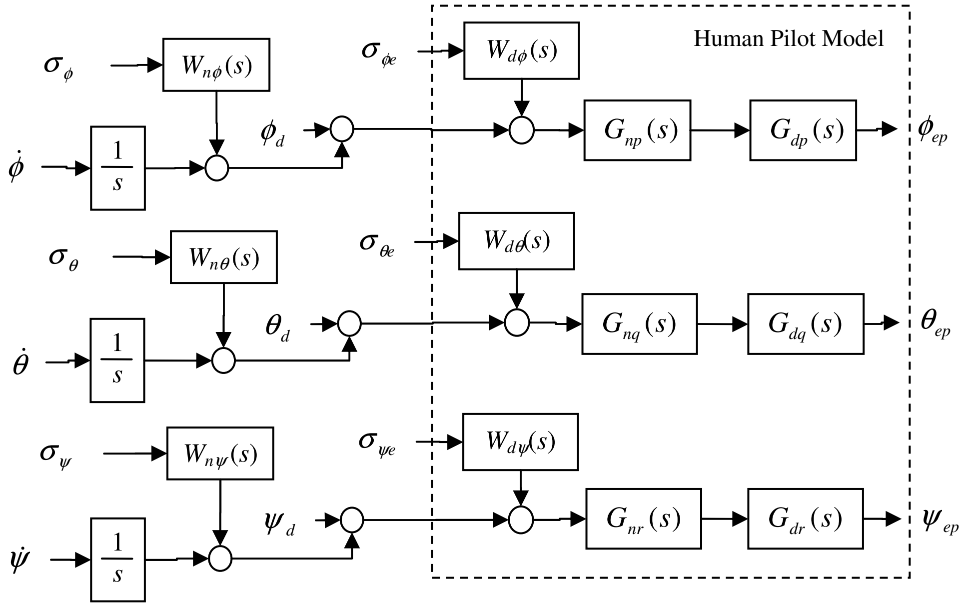

Figure 100. The Attitude Controller Block Diagram

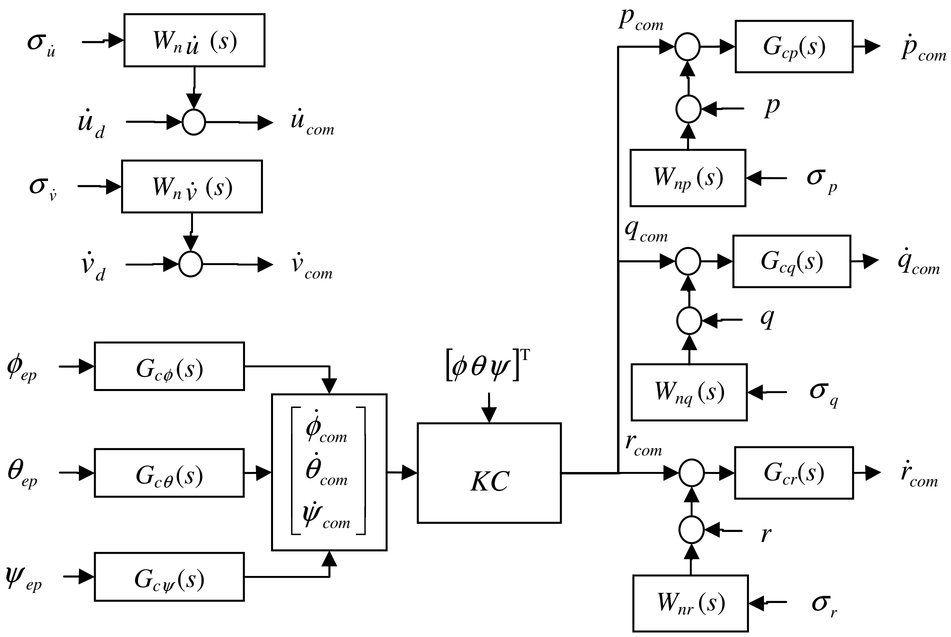

Figure 101. The Attitude Controller Block Diagram (cont'd)

In the attitude controller block diagrams $G_{c\phi}(s)$, $G_{c\theta}(s)$ and $G_{c\psi}(s)$ are the PI controller transfer functions structured by using the gain matrices $\hat{K}_{pa}$ and $\hat{K}_{ia}$ and $G_{cp}(s)$, $G_{cq}(s)$ and $G_{cr}(s)$ are the P controller transfer functions structured by the gain matrix $\hat{K}_d$ as discussed in Chapter 3.

The shaping filters of the measurement noises on the linear acceleration, attitude and the angular velocity measured by means of an on-board INS are denoted by $W_{n\dot{u}}(s)$, $W_{n\dot{v}}(s)$ and $W_{n\phi}(s)$, $W_{n\theta}(s)$, $W_{n\psi}(s)$ and $W_{np}(s)$, $W_{nq}(s)$, $W_{nr}(s)$. As for the human pilot model, $W_{d\phi}(s)$, $W_{d\theta}(s)$ and $W_{d\psi}(s)$ are used for the transfer functions of the shaping filters of the disturbance noise (the engine noise) effecting the pilot in the cockpit. In the RP analysis all of the shaping filters of the random noise signals are set to unity.

Also, the neuro-motor lag and the second order Padé delay transfer functions for the angular velocity control channels are denoted by $G_{np}(s)$, $G_{nq}(s)$, $G_{nr}(s)$ and $G_{dp}(s)$, $G_{dq}(s)$, $G_{dr}(s)$ for the attitude controller.

The performances of the designed controllers are examined by comparing the controlled output with the output of the desired closed loop dynamics. It represents the *desired matching model* of the controlled linearized perturbed compact nonlinear dynamics. The transfer matrices for the desired matching model of the stabilization and attitude controlled loops are denoted by $\hat{G}_{des}^{sta}(s)$ and $\hat{G}_{des}^{att}(s)$. The errors between the desired matching model outputs and the controlled outputs are processed with the *performance weight transfer matrices* ($\hat{W}_p^{sta}(s)$, $\hat{W}_p^{att}(s)$) and the structured singular values (μ) of the outputs are calculated.

For the stabilization controller the structured singular value calculation is based on the outputs of $\hat{W}_p^{sta}(s)$ ($\delta V, \delta\alpha, \delta\beta, \delta p, \delta r$) and for the attitude controller the structured singular value calculation is based on the outputs of $\hat{W}_p^{att}(s)$ ($\delta\phi, \delta\theta, \delta\psi$). The stabilization and attitude control loops, the desired matching models and the performance weight transfer matrices outputs are shown in Figure 102 and Figure 103.

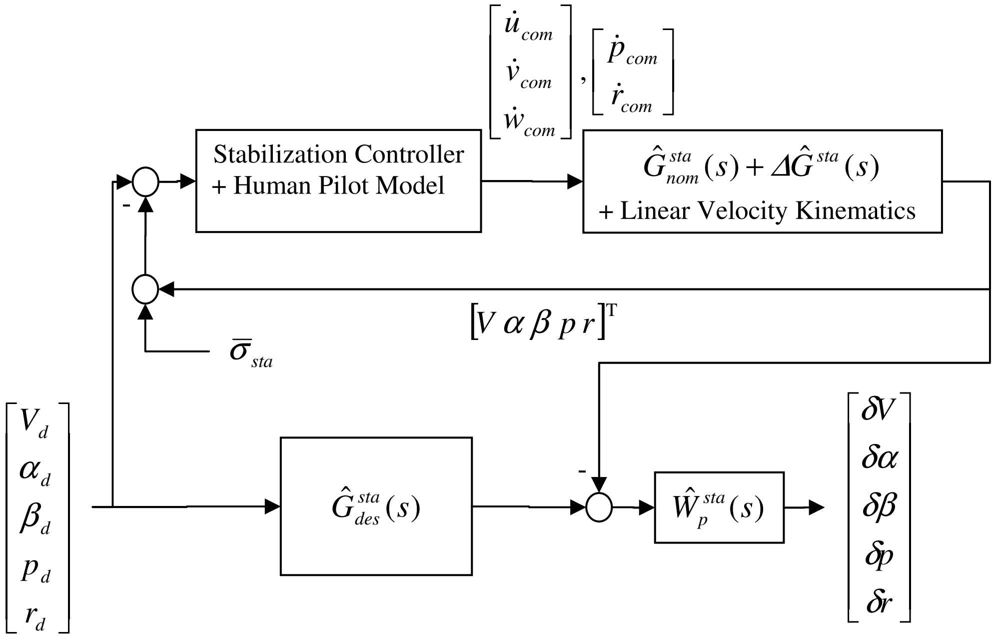

Figure 102. The Stabilization Control Loop and the Desired Matching Model

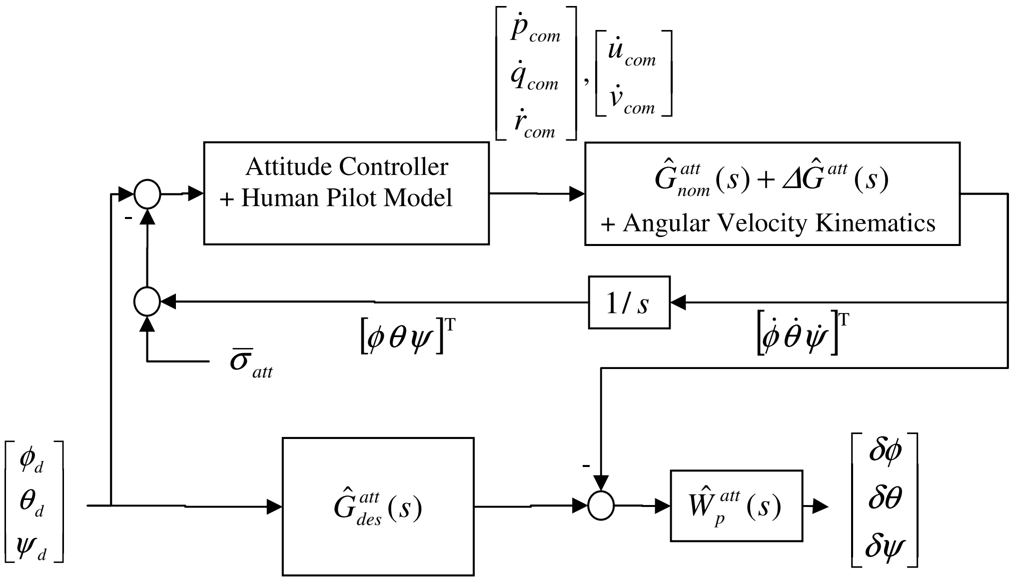

Figure 103. The Attitude Control Loop and the Desired Matching Model

Here, $\overline{\sigma}_{sta}$ and $\overline{\sigma}_{att}$ vectors are used for the collection of the random noise signal on the stabilization and attitude control loops. Here, $\overline{\sigma}_{sta}$ consists of $\sigma_V, \sigma_\alpha, \sigma_\beta, \sigma_p, \sigma_r, \sigma_{pe}, \sigma_{re}$ and $\overline{\sigma}_{att}$ consists of $\sigma_\phi, \sigma_\theta, \sigma_\psi, \sigma_p, \sigma_q, \sigma_r, \sigma_{pe}, \sigma_{qe}, \sigma_{re}$ and $\sigma_{\dot{u}}, \sigma_{\dot{v}}$ signals.

The RP analysis of the stabilization and the attitude control loops (the calculation of the structured singular values) are done for the flight condition at which the Mach number is 0.95 and the altitude is 7,500 m.

As it is mentioned previously in Chapter 3, the poles of the desired closed loop dynamics are specified by using $\omega_{nV_T}, \omega_{n\alpha}, \omega_{n\beta}$, $\omega_{n\phi}, \omega_{n\theta}, \omega_{n\psi}$, $\omega'_{n\phi}, \omega'_{n\theta}, \omega'_{n\psi}$ and $\zeta_{V_T}, \zeta_\alpha, \zeta_\beta$, $\zeta_\phi, \zeta_\theta, \zeta_\psi$. Thus, for the stabilization controller, $\omega_{nV_T}, \omega_{n\alpha}, \omega_{n\beta}$, $\omega'_{n\phi}, \omega'_{n\psi}$ and $\zeta_{V_T}, \zeta_\alpha, \zeta_\beta$, ζ_ϕ, ζ_ψ should be chosen to specify the desired closed loop dynamics.

Considering the robust stability and nominal performance characteristics, under the effect of the described plant uncertainties and disturbances, the parameters defining the closed loop dynamics are set as:

Table 2. The Desired Closed Loop Parameters of the Stabilization Control

Autopilot (A/P)	Human Pilot (H/P)
$\omega_{nV_T} = \omega_{n\alpha} = \omega_{n\beta} = 1\,\text{Hz}$ $\zeta_{V_T} = \zeta_\alpha = \zeta_\beta = 1$	$\omega_{nV_T} = \omega_{n\alpha} = \omega_{n\beta} = 0.15\,\text{Hz}$ $\zeta_{V_T} = \zeta_\alpha = \zeta_\beta = 1$
$\omega'_{n\phi} = \omega'_{n\psi} = 9\,\text{Hz}$ $\zeta_\phi = \zeta_\psi = 1$	$\omega'_{n\phi} = \omega'_{n\psi} = 9\,\text{Hz}$ $\zeta_\phi = \zeta_\psi = 1$

As for the analysis, the transfer matrix for the desired matching model of the stabilization controller loop is chosen as:

$$\hat{G}_{des}^{sta}(s) = \text{diag}(\frac{\omega_{nV_T}}{s+\omega_{nV_T}}, \frac{\omega_{n\alpha}}{s+\omega_{n\alpha}}, \frac{\omega_{n\beta}}{s+\omega_{n\beta}}, \frac{\omega'_{n\phi}}{s+\omega_{n\phi}}, \frac{\omega'_{n\psi}}{s+\omega_{n\psi}}) \tag{4.40}$$

Also, the performance weighting transfer matrix of the stabilization controller loop is chosen as:

$$\hat{W}_{p}^{sta}(s) = \text{diag}(\frac{s+30\,\omega_{nV_T}}{10(s+3\,\omega_{nV_T})}, \frac{s+30\,\omega_{n\alpha}}{10(s+3\,\omega_{n\alpha})}, \frac{s+30\,\omega_{n\beta}}{10(s+3\,\omega_{n\beta})}, \frac{s+30\,\omega'_{n\phi}}{10(s+3\,\omega'_{n\phi})}, \frac{s+30\,\omega'_{n\psi}}{10(s+3\,\omega'_{n\psi})}) \tag{4.41}$$

Here, the performance weight transfer functions are chosen in the form of a lead-lag filter that suppresses the frequencies higher than the desired matching model and the stabilization control closed loop natural frequencies. The Bode plot of the performance weight transfer function for $\omega_{ni} = 2\pi$ rad/sec is:

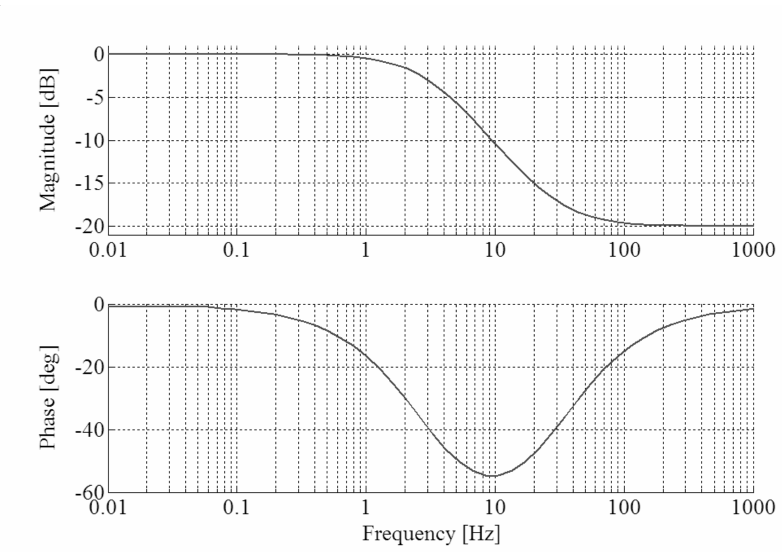

Figure 104. The Bode Plot of the Performance Weight ($\omega_{ni} = 2\pi$ rad/sec)

Using the parameter set in Table 2 μ upper bound, the robust stability and the nominal performance graphics are drawn for the stabilization controller (with $\overline{F}_a = \overline{M}_a = \overline{0}$) and the autopilot and the human pilot in the loop cases:

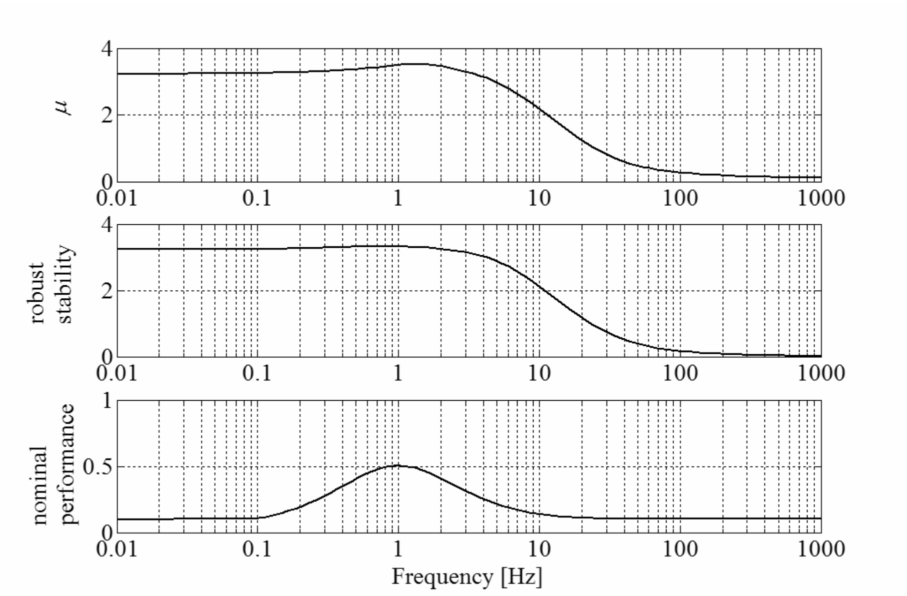

Figure 105. RP Plots of the Stabilization Control Loop w/ A/P (0% Aero.)

The peak of the μ-plot is 3.52. This means that for all perturbation matrices $\overline{\sigma}\left[\hat{\Delta}(j\omega)\right] < 1/3.52$ and $\left\|\hat{F}_u(\hat{M},\hat{\Delta})\right\|_\infty \leq$ 3.52. The assigned uncertainties alter the RP of the closed loop system. The system can satisfy RP only to $1/3.52$ of the assigned disturbances and uncertainties.

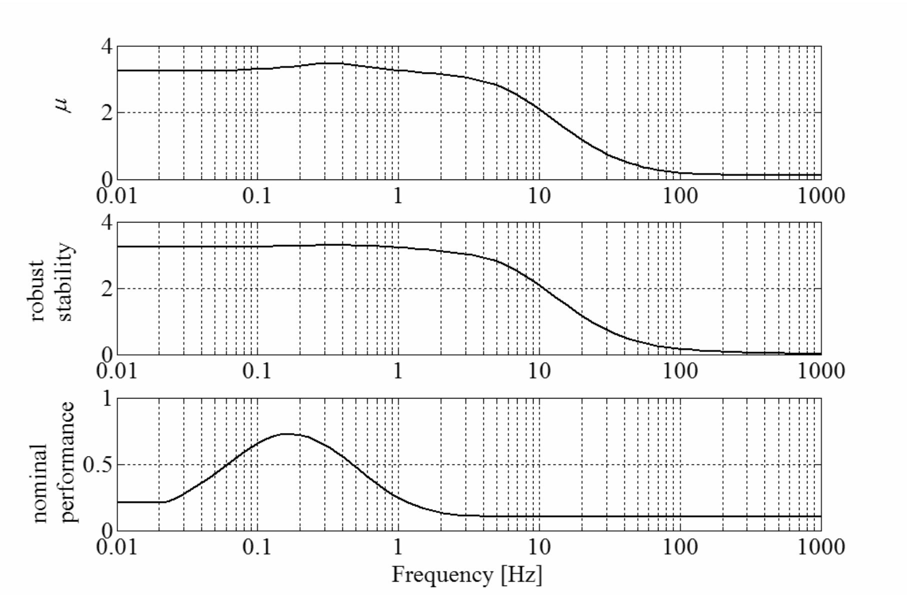

Figure 106. RP Plots of the Stabilization Control Loop w/ H/P (0% Aero.)

The peak of the μ-plot is 3.46. This means that for all perturbation matrices $\overline{\sigma}\left[\hat{\Delta}(j\omega)\right] < 1/\,3.46$ and $\left\|\hat{F}_u(\hat{M},\hat{\Delta})\right\|_\infty \leq 3.46$. The assigned uncertainties alter the RP of the closed loop system. The system can satisfy RP only to 1/ 3.46 of the assigned disturbances and uncertainties.

The analysis obviously showed that the robust performance can not be achieved for the stabilization controller with $\overline{F}_a = \overline{M}_a = \overline{0}$. In order to handle the robust performance the aerodynamic parameter uncertainty of the model should be decreased. In other words, the aerodynamic properties of the aircraft should be modeled (or identified) with better accuracy.

Hence, instead of totally ignoring the aerodynamic forces and moments (and assigning $\overline{F}_a = \overline{M}_a = \overline{0}$) it is necessary that, with certain amount of error, they should be included in the dynamic inversion. As it is mentioned previously the aerodynamic coefficients are estimated by using different methods (databases with semi-empirical prediction tools, CFD, wind tunnel tests, flight tests, etc.) all of which have certain estimation errors. The error percentages are mostly dependent on the estimation method, the geometry of the vehicle and the flight conditions. Also, the errors on a single aerodynamic coefficient set (C_x, C_y, C_z and C_l, C_m, C_n) may differ under the same conditions.

Thus, for the RP analysis, the aerodynamic coefficient set in the aircraft dynamics is modified. During the modification 30% uncertainty on the aerodynamic coefficients of the aircraft is assumed, i.e. the aerodynamic coefficients used in the aircraft dynamics are 70% accurate. Here, it should be noted that, 30% uncertainty is relatively high when the accuracy of the estimation methods (typically 10%-20% depending on the coefficient type) are considered. Here, in the analysis, the coefficients are modified in order to degrade the dynamic inversion performance. That is, all of the aerodynamic coefficients except C_x are decreased to 70% of their nominal values. Hence, the lifting and maneuvering capabilities of the aircraft are degraded. However, C_x is increased to 130% in order to induce additional total drag on the estimated value.

The compact nonlinear dynamics separated into two parts (second part has 30% degraded $\overline{F}_a$ and $\overline{M}_a$ performance) is shown in the following figure.

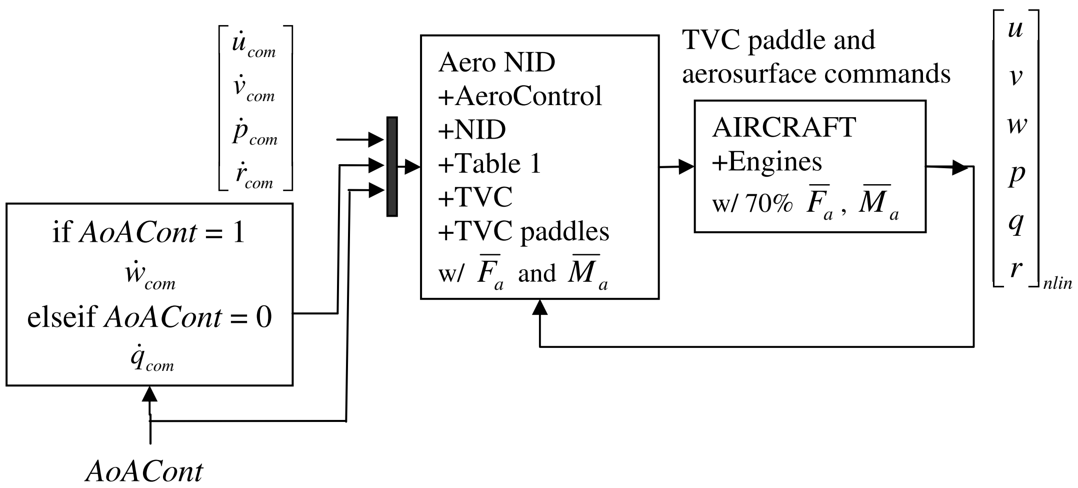

Figure 107. The Compact ND Separated into Two Parts with 70% $\overline{F}_a$ and $\overline{M}_a$

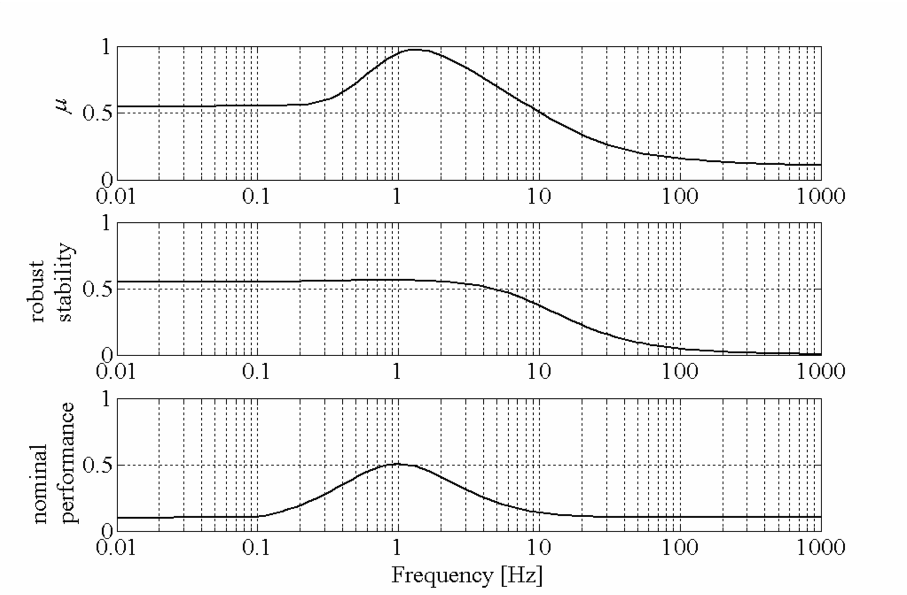

Figure 108. RP of Stabilization Controller w/ 70% $\overline{F}_a$, $\overline{M}_a$ and A/P

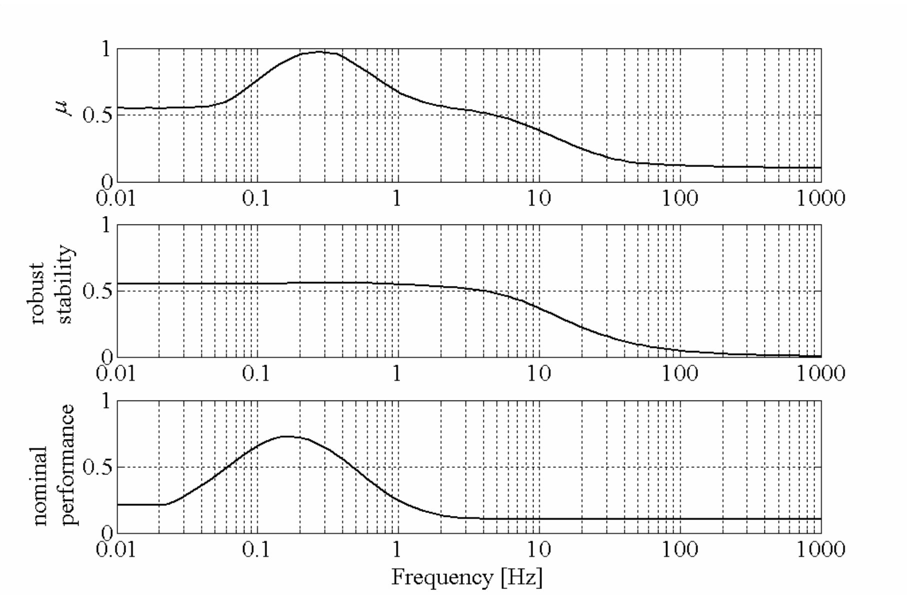

Figure 109. RP of Stabilization Controller w/ 70% $\overline{F}_a$, $\overline{M}_a$ and H/P

The plots show that the RP is achieved with the designed stabilization controller for 30% aerodynamic capability degradation.

As for the attitude controller, considering the robust stability and nominal performance characteristics, under the effect of the described plant uncertainties and disturbances, the parameters defining the closed loop dynamics are set as:

Table 3. The Desired Closed Loop Parameters of the Attitude Control

Autopilot (A/P)	Human Pilot (H/P)
$\omega_{n\phi} = \omega_{n\theta} = \omega_{n\psi} = 1\,\text{Hz}$ $\omega'_{n\phi} = \omega'_{n\theta} = \omega'_{n\psi} = 7\,\text{Hz}$ $\zeta_{\phi} = \zeta_{\theta} = \zeta_{\psi} = 1$	$\omega_{n\phi} = \omega_{n\theta} = \omega_{n\psi} = 0.22\,\text{Hz}$ $\omega'_{n\phi} = \omega'_{n\theta} = \omega'_{n\psi} = 7\,\text{Hz}$ $\zeta_{\phi} = \zeta_{\theta} = \zeta_{\psi} = 1$

In the analysis of the attitude controller the transfer matrix for the desired matching model ($\hat{G}_{des}^{sta}(s)$) and the transfer matrix of the performance weighting ($\hat{W}_{p}^{sta}(s)$) are the same as in the analysis of the stabilization controller.

Using the parameter set in Table 3 μ upper bound, the robust stability and the nominal performance graphics are drawn for the attitude controller for 30% aerodynamic capability degradation and the autopilot and the human pilot in the loop cases:

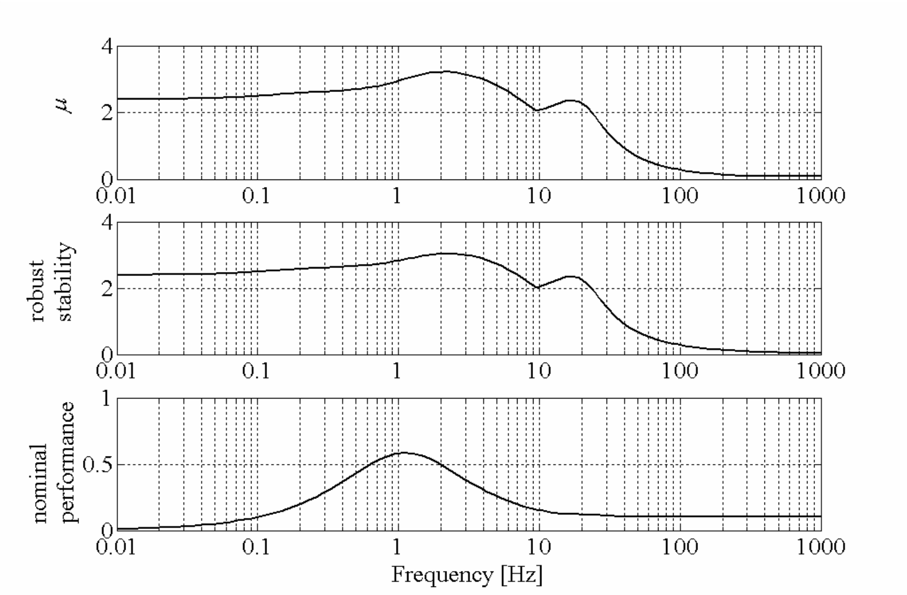

Figure 110. RP of Attitude Controller w/ $\overline{F}_a = \overline{M}_a = \overline{0}$ and A/P

The peak of the μ-plot is 3.21. This means that for all perturbation matrices $\overline{\sigma}\left[\hat{\Delta}(j\omega)\right] < 1/\,3.21$ and $\left\|\hat{F}_u(\hat{M},\hat{\Delta})\right\|_\infty \leq 3.21$. The assigned uncertainties alter the RP of the closed loop system. The system can satisfy RP only to 1/ 3.21 of the assigned disturbances and uncertainties.

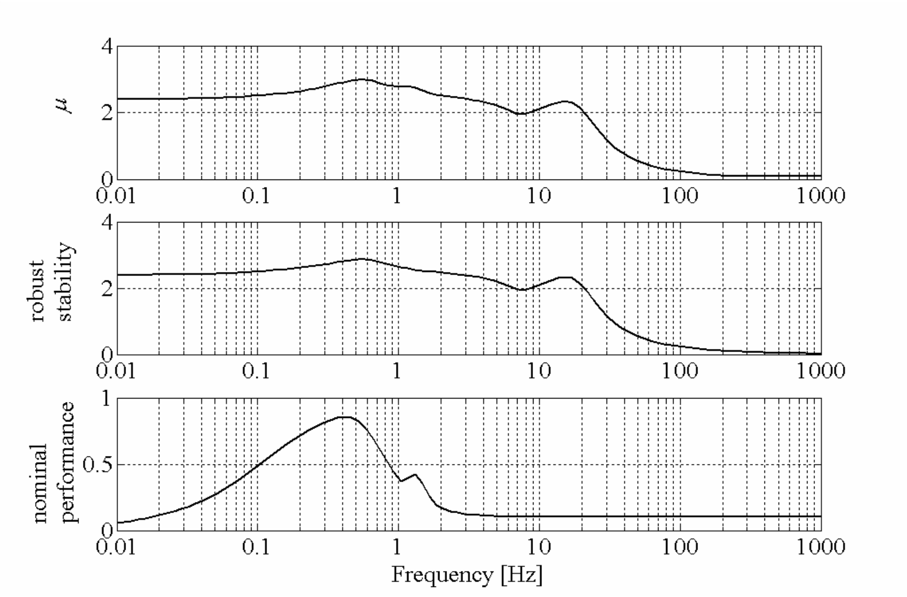

Figure 111. RP of Attitude Controller w/ $\overline{F}_a = \overline{M}_a = \overline{0}$ and H/P

Here, the peak of the μ-plot is 2.98. This means that for all perturbation matrices $\overline{\sigma}\left[\hat{\Delta}(j\omega)\right] < 1/2.98$ and $\left\|\hat{F}_u(\hat{M},\hat{\Delta})\right\|_\infty \leq 2.98$. The assigned uncertainties alter the RP of the closed loop system. The system can satisfy RP only to 1/ 2.98 of the assigned disturbances and uncertainties.

Hence, instead of totally ignoring the aerodynamic forces and moments 30% aerodynamic capability degradation is applied as in the case of the stabilization controller (the aerodynamic coefficients of the aircraft dynamics are 70% accurate).

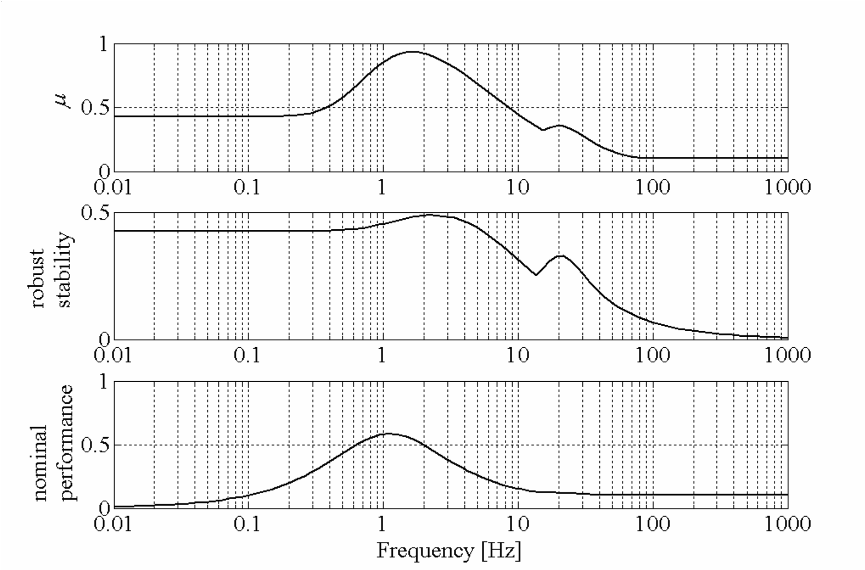

Figure 112. RP of Attitude Controller w/ 70% $\overline{F}_a$, $\overline{M}_a$ and A/P

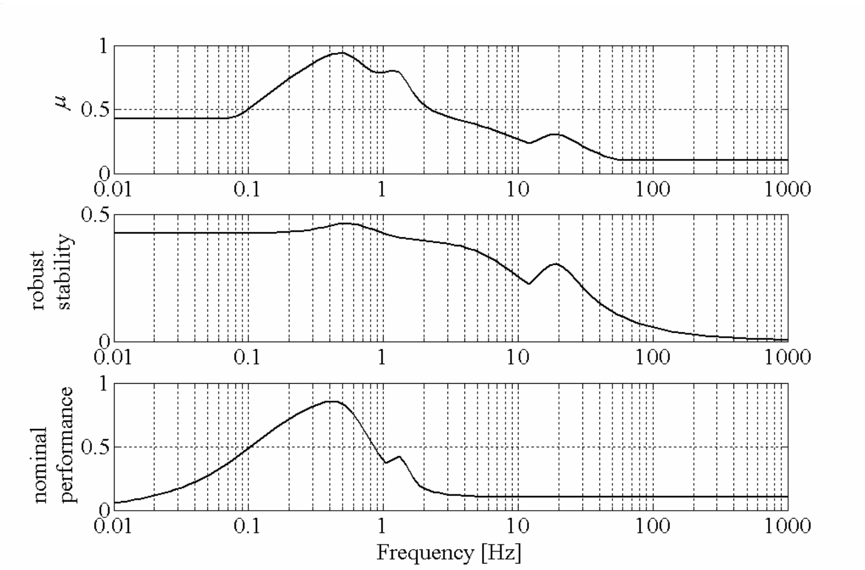

Figure 113. RP of Attitude Controller w/ 70% $\overline{F}_a$, $\overline{M}_a$ and H/P

The plots show that the RP is achieved with the designed attitude controller for 30% aerodynamic capability degradation.

The RP analysis results are also verified by simulating the designed stabilization controller with the compact nonlinear plant dynamics. The stabilization control loop is simulated using the control parameter set given in Table 2 and 30% aerodynamic capability degradation in the aircraft dynamics.

For the simulations of the stabilization controller the reference inputs are chosen as $p_d = r_d = \beta_d = 0$ and V_{Td}, α_d are the trim values at the desired flight condition. The disturbances arising from the sensor and engine noises ($\bar{\sigma}_{sta}$) are chosen as zero mean white noise signals with Gaussian distribution and standard deviation values of $\sigma_{V\,std} = 1$m/sec, $\sigma_{\alpha\,std} = \sigma_{\beta\,std} = 1^\circ$, $\sigma_{p\,std} = \sigma_{r\,std} = 1^\circ$/hr and $\sigma_{pe\,std} = \sigma_{re\,std} = 10^\circ$/hr. Figure 114, Figure 115 and Figure 116 show the simulation results for the stabilization controller. In the figures the dotted lines are the reference inputs.

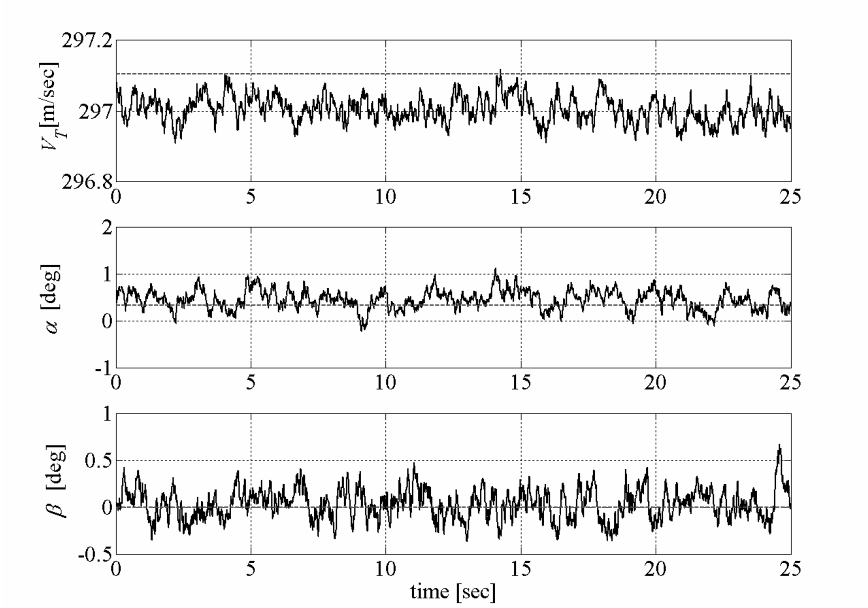

Figure 114. Stab. Controller V_T, α, β Output for 30% Aero. Perturbation w/A/P

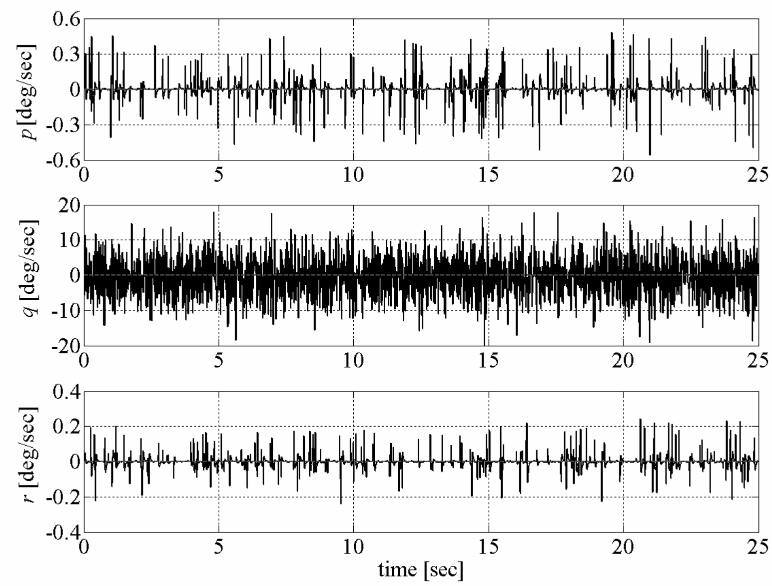

Figure 115. Stab. Controller p, q, r Outputs for 30% Aero. Perturbation w/A/P

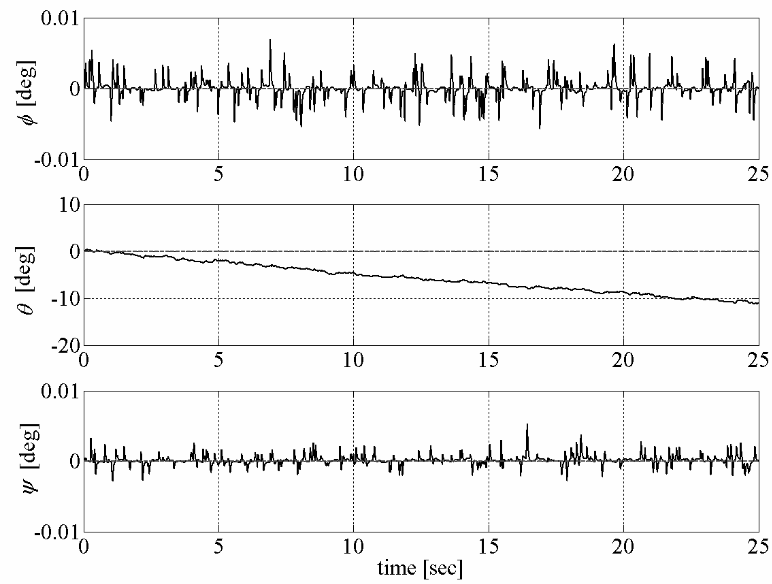

Figure 116. Stab. Controller ϕ, θ, ψ Outputs for 30% Aero. Perturbation w/A/P

The RP analysis results are also verified by simulating the designed attitude controller with the compact nonlinear plant dynamics. The attitude control loop is simulated using the control parameter set given in Table 3 and 30% aerodynamic capability degradation in the aircraft dynamics.

For the simulations of the attitude controller the reference inputs V_{Td}, α_d are the trim values at the desired flight condition and $\beta_d = 0$. Since, the aim of the attitude controller is to make rapid maneuvers the attitude angle commands are generated in order to achieve a desired rapid maneuver. The maneuver is defined such that the aircraft pulls-up to 85° from 0° pitch attitude and turns back to its original (level) position at the end of the maneuver. Simultaneously, the aircraft makes a full heading reversal (180° yaw angle change). The whole maneuver is completed in 20 seconds. Here, the reference attitude commands for pitch and yaw motions are specified to be composed of two different half-cycloid motions:

$$\theta_d(t) = \frac{\theta_{\max}}{2}(1 - \cos(2\pi \frac{t}{t_{\max}})) \tag{4.42}$$

$$\psi_d(t) = \psi_{final}(\frac{t}{t_{\max}} - \frac{1}{2\pi}\sin(2\pi \frac{t}{t_{\max}})) \tag{4.43}$$

Here, $\theta_{\max} = 85^\circ$, $\psi_{final} = 180^\circ$ and $t_{\max} = 20$ sec. Since the attitude controller simultaneously controls the roll, pitch and yaw attitude of the aircraft a reference input for the roll attitude should be defined. It is originated from the relationship between the roll angle and the yaw rate during the constant altitude and turn rate lateral turn. It can be proved that during this maneuver following equation holds [33]:

$$\dot{\psi}(t) = \frac{g}{V_T}\tan(\phi(t)) \tag{4.44}$$

Here, the turn rate of the aircraft is dependent on the total velocity and the bank angle of the aircraft together with the gravitational acceleration. Hence, this equality can be modified for a lateral turn maneuver simultaneous with a pitch maneuver:

$$\phi_d(t) = k_{tailor} \tan^{-1}\left(\frac{g}{V_T \dot{\psi}(t)}\right) \tag{4.45}$$

Here, k_{tailor} is a constant tailoring parameter used to induce the turn performance degrading effect (when compared with the constant altitude turn) of the motion in the longitudinal plane. It is chosen as 0.6 to give a feasible roll command coordinated with the heading reversal maneuver.

The disturbances arising from the sensor and engine noises ($\overline{\sigma}_{att}$) are chosen as zero mean white noise signals with Gaussian distribution and standard deviation values of $\sigma_{\phi\, std} = \sigma_{\theta\, std} = 0.3^\circ$ and $\sigma_{\psi\, std} = 0.1^\circ$, $\sigma_{p\, std} = \sigma_{q\, std} =$ $\sigma_{r\, std} = 1^\circ$/hr, $\sigma_{\phi e\, std} = \sigma_{\theta e\, std} =$ $\sigma_{\psi e\, std} = 0.5^\circ$ and $\sigma_{\dot{u}\, std} = \sigma_{\dot{v}\, std} = 1$ m/sec^2. Figure 117, Figure 118 and Figure 119 show the simulation results for the attitude controller. The dotted lines are the reference inputs.

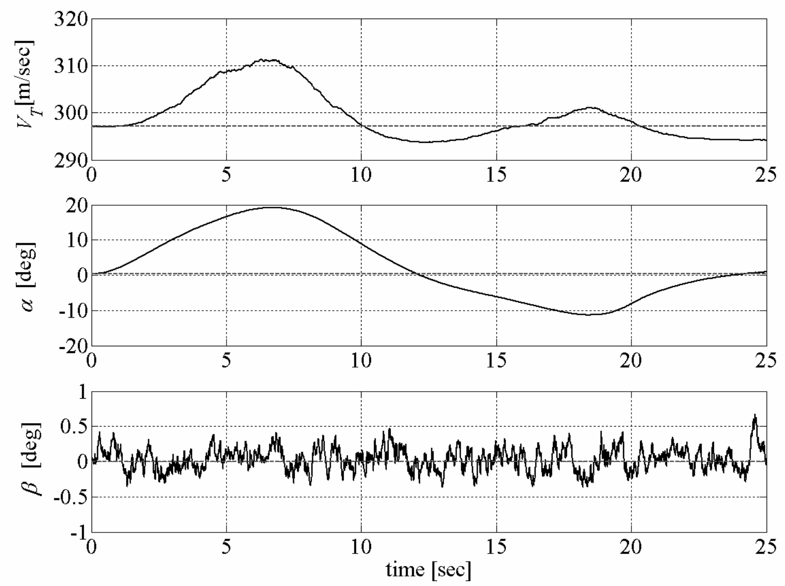

Figure 117. Att. Controller V_T, α, β Outputs for 30% Aero. Perturbation w/A/P

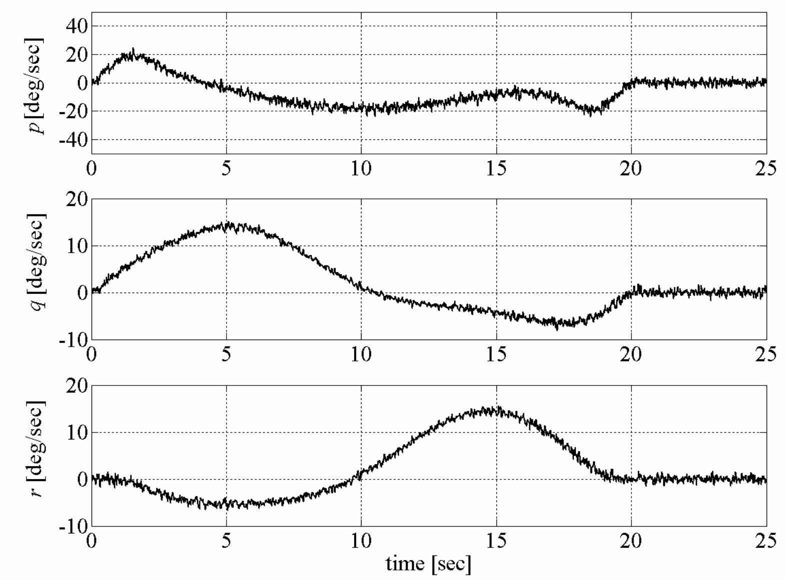

Figure 118. Att. Controller p, q, r Outputs for 30% Aero. Perturbation w/A/P

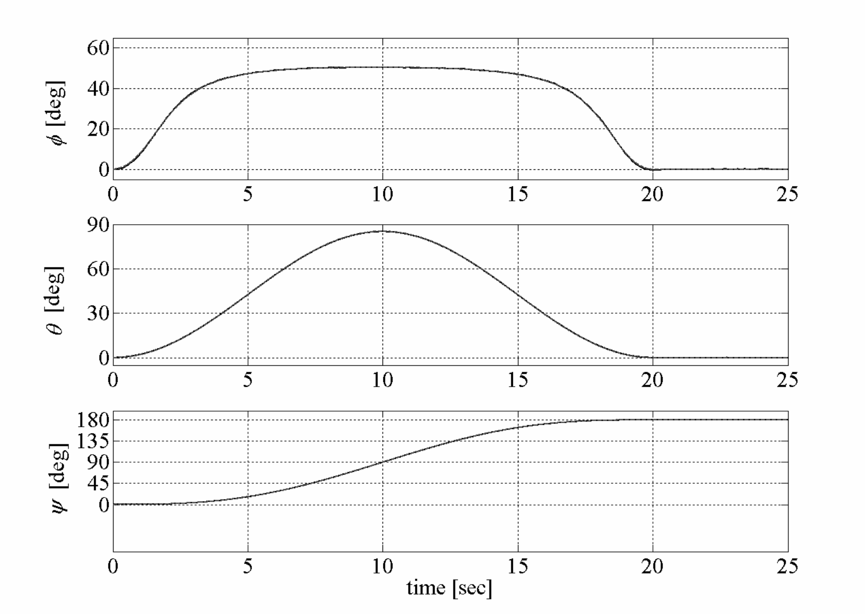

Figure 119. Att. Controller ϕ, θ, ψ Outputs for 30% Aero. Perturbation w/A/P

The RP of the designed attitude controller is also simulated with the human pilot dynamics. In the simulations instead of using second order Padé approximation for the time delay in the human pilot model, pure time delay representations are used, i.e. $G_{dp}(s) = G_{dq}(s) = G_{dr}(s) = e^{-\tau_d s}$. Figure 120, Figure 121 and Figure 122 show the simulation results for the attitude controller with the human pilot model. The dotted lines are the reference inputs.

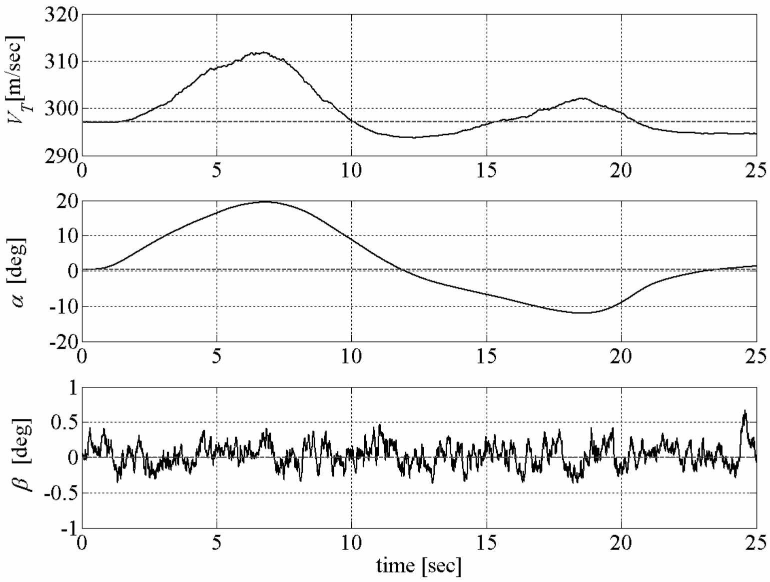

Figure 120. Att. Controller V_T, α, β Outputs for 30% Aero. Perturbation w/H/P

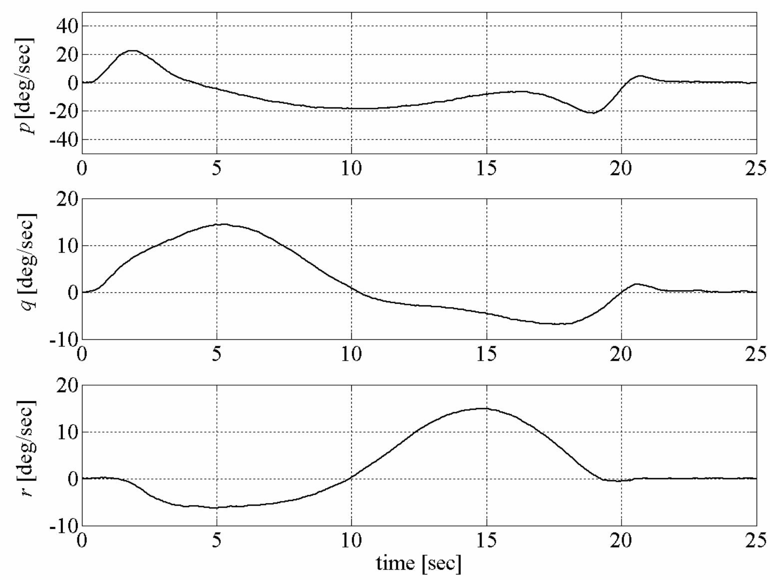

Figure 121. Att. Controller p, q, r Outputs for 30% Aero. Perturbation w/H/P

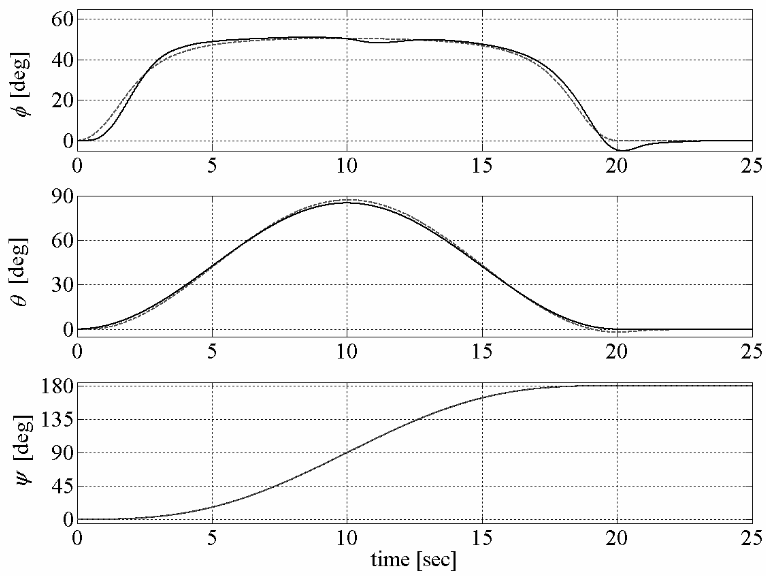

Figure 122. Att. Controller ϕ, θ, ψ Outputs for 30% Aero. Perturbation w/H/P

CHAPTER 5

STABILIZATION AT HIGH ANGLE OF ATTACK

In this chapter, the performance of the designed stabilization controller will be investigated. For that purpose, first, a pull-up maneuver to bring the aircraft manually into stall condition will be introduced. Then, the stall indication trigger to activate the stabilization controller will be discussed. Eventually, the trim angle of attack calculation and trim angle of attack control will be constituted. Afterwards, two stabilization control cases the Euler angle rate stabilization with trim angle of attack control and the reference Euler angle tracking with trim angle of attack control cases will be analyzed with simulations.

The idea behind the stabilization at high angle of attack is to use the stabilization controller (designed in Chapter 3 and Chapter 4) in order to recover the aircraft from the dangerous stall regions using the TVC (since the aerodynamic control effectors are inoperative here). Thus, the controller will bring the aircraft to safer flight conditions and the pilot can use the aerodynamic controls to steer the aircraft.

5.1. The Pull-Up Maneuver for Stall Testing

The stall stabilization control analysis is done for the initial condition of the aircraft at which the aircraft is at wings level steady flight at 5,000 m altitude and 0.75 Mach. Applying the trim algorithm discussed in Chapter 4 the equilibrium points at the specified flight condition are found as $\beta_0 = \delta_{a0} = \delta_{r0} = 0$ and $T_{L0} = T_{R0} = 22{,}860\,\mathrm{N}$, $\alpha_0 = 0.7^\circ$, $\delta_{e0} = -1.29^\circ$ and $\delta_{Lth} = \delta_{Rth} = 0.54$.

The simulation of the pull-up maneuver is desirable in order to identify the stall effective regions described in Section 2. The maneuver is realized using the elevator deflection command (δ_{ecom}) so that the aircraft starts to climb up from the initial altitude. The time histories of the total velocity (V_T), the angle of attack (α), the pitch angle (θ) and the the elevator command for this maneuver are shown in the following figures.

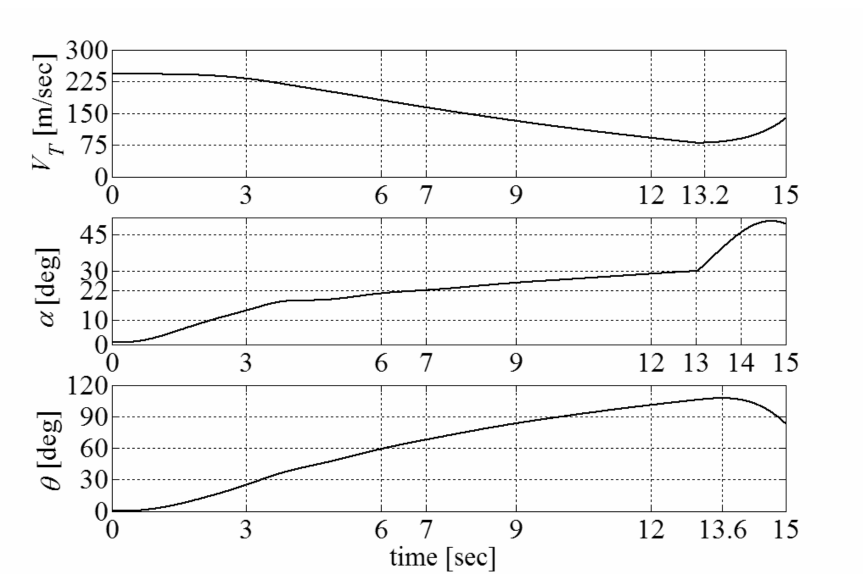

Figure 123. Stall Manipulation Simulation Results for V_T, α, θ

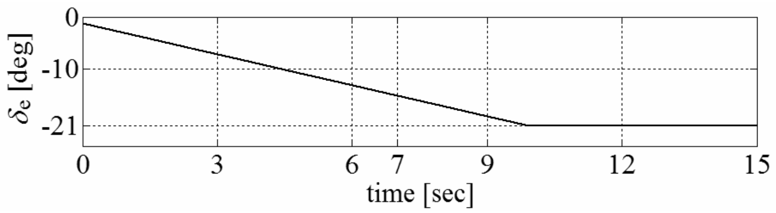

Figure 124. Elevator Deflection Command for Stall Manipulation Simulation

For the initial conditions considered here, the simulation shows that, the aircraft is in stall (region D_1) after 7th second up to 13th second. Afterwards, the aircraft is in the post-stall (region D_1 and D_2). Then on, at 14th second, it enters the deep-stall (region C). Note that the aircraft passes the post-stall very rapidly (in one second) and enters the deep-stall region. This is shown on the integrated Bihrle-Weissmann chart in Figure 125.

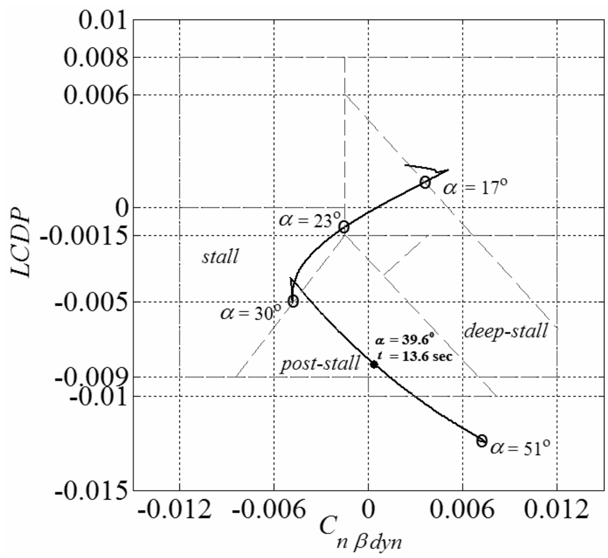

Figure 125. Stall Manipulation Shown on IBW Chart

When the aircraft is at the mids of the post-stall region (t = 13.6 sec), although there is still an elevator command trying to pull the aircraft up, there occurs the undesired nose down pitching motion which develops very rapidly. This simulation suggests that the stabilization controller should start at latest just before this situation is confronted.

5.2. The Stall Indication Trigger

The stall stabilization controller is desired to start operation automatically whenever the aircraft encounters dangerous stall regions. The logic of the stall indication trigger is based on the regions stated in Figure 125 and the values of the stall indication parameters $C_{n\beta dyn}$ and $LCDP$.

If the undesired nose down pitching motion occurs (at $\alpha = 39.6^\circ$, $t = 13.6\,\text{sec}$ and the early start of region D_2) the stall stabilization controller is activated. Remember that at region D_2 there are strong departures, roll reversals and spin tendencies. Thus, the entrance to region D_2 is treated as the upper most tolerable point for the stabilization controller to start. Here, at $\alpha = 39.6^\circ$, the values of the stall indication parameters are $C_{n\beta\,dynT} = 0.0004$ and $LCDP_T = -0.0083$. Throughout the motion of the aircraft both $C_{n\beta\,dyn}$ and $LCDP$ are monitored and whenever the condition $C_{n\beta\,dyn} \geq C_{n\beta\,dynT}$ and $LCDP \leq LCDP_T$ is achieved the stall stabilization controller automatically starts its operation.

5.3. The Trim Angle of Attack Control

As it is mentioned in Chapter 3 the angle of attack (α) of the aircraft, which is measured by the angle of attack sensor, is controlled in the stabilization controller. Therefore it is necessary to generate the angle of attack command (α_{com}) when the stabilization is started.

The mission of the stall stabilization controller is to bring the aircraft to safer flight conditions at which the aerodynamic controls are effective. Thus, the angle of attack commands for the stabilization control are chosen as the trim angle of attack (α_0) values. They are calculated by applying the trim algorithm explained in Chapter 4 and for the altitudes in between 0 m to 15,000 m, the Mach numbers in between 0.1 to 1.5 and $\phi_0 = \theta_0 = p_0 = q_0 = r_0 = 0$.

Then, a 2-D look up table is formed and the trim angle of attack values are structured as a function of altitude and Mach number. During the operation of the stabilization controller the commanded angle of attack values are calculated by linear interpolation on the 2-D look-up table at the instantaneous altitudes and Mach numbers. Hence, the reference angle of attack values are the instantaneous trim angle of attack values that the aircraft will be in wings level flight at which the aerodynamic controls are strongly effective and the aircraft is easily controlled.

The samples of angle of attack command values for different Mach numbers and altitudes are seen in Table 4. Note that the trim angle of attack values are higher for low Mach numbers and decrease as the velocity of the aircraft increases. Also, they are higher for high altitudes and decrease as the altitude decreases. In the table the values in the shaded cells are showing the flight conditions at which the trim angle of attack values are higher and the aircraft is in transition to high angle attack flight regions. Thus, these values are not used in the trim angle of attack control. Whenever the trim angle of attack value is higher than 17°, to be in the safe region according to Figure 125, instead of the real values $\alpha_0 = 17^\circ$ is used.

Table 4. Sample Angle of Attack Commands for the Stabilization Controller

α_0 [deg]		Mach Numbers							
		0.1	**0.3**	**0.5**	**0.7**	**0.9**	**1.1**	**1.3**	**1.5**
Altitudes [km]	**0**	12.58	8.01	1.33	-0.51	-1.27	-1.65	-1.87	-2.01
	3	27.79	12.63	3.01	0.34	-0.75	-1.31	-1.62	-1.82
	6	29.87	29.87	5.63	1.68	0.06	-0.76	-1.23	-1.54
	9	20.65	20.65	9.94	3.88	1.39	0.13	-0.59	-1.05
	12	21.04	21.04	21.04	7.50	3.58	1.59	0.45	-0.26
	15	26.47	26.47	26.47	13.18	7.02	3.90	2.11	0.97

The trim angle of attack values, i.e. the angle of attack commands of the stabilization controller, are also shown in the following mesh plot. Here, the trim angle of attack values which are higher than 17° are not shown.

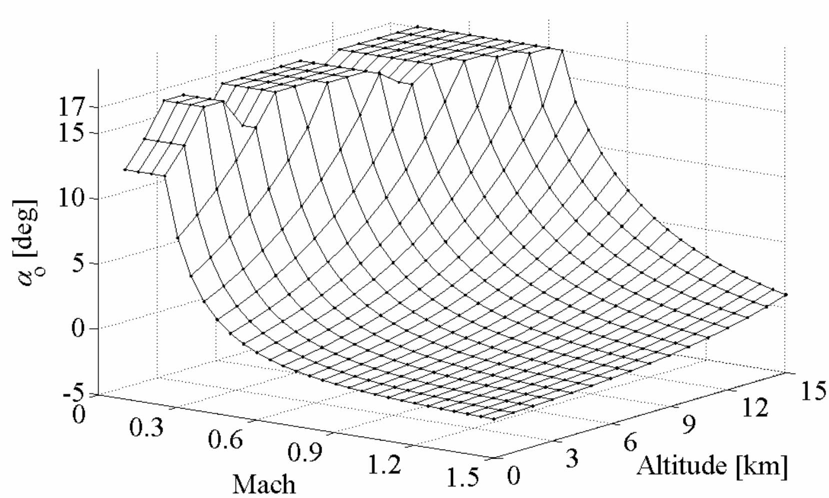

Figure 126. The Angle of Attack Commands of the Stabilization Controller

The plot is drawn for $\Delta M = 0.05$ Mach number and $\Delta h = 1000\,\mathrm{m}$ altitude intervals. From the plot it is clear that the trim angle of attack values are getting higher at low Mach number flight regime. They decrease to moderate levels when the velocity of the aircraft increases. Similarly, the low altitude flight also decreases the trim angle of attack.

5.4. Stall Stabilization with Trim Angle of Attack Tracking and Angular Velocity Regulation Control

At stall conditions, in general, the aerodynamic control surfaces are not effective and the desired control authority cannot be achieved only by applying the aerodynamic controls. However, thrust vectoring control will successfully help the aircraft to recover from undesired stall and cause rapid movements. Thus, for the stall stabilization of the aircraft only TVC is applied. The aim of the controller is to get the aircraft into stable flight conditions at which the aerodynamic control surfaces operate successfully.

The stall stabilization controller is a hybrid controller composed of the attitude and stabilization controllers explained in Chapter 3. In the first phase of the stable flight recovery maneuver from stall condition the pitch angular velocity component is nullified ($q_d = 0$). Thus, the growth of the pitch angle (θ) is controlled and kept at constant level. During this phase the instantaneous attitude angle rates ($\dot{\phi}, \dot{\theta}, \dot{\psi}$) of the aircraft is continuously monitored and the mean of the norm of the vector $[\dot{\phi}, \dot{\theta}, \dot{\psi}]^{\mathrm{T}}$ is calculated at the end of every 1 second period. Here the length of the check period is chosen to be 1 sec to be consistent with the closed loop design frequency (1 Hz) given in Table 2.

At every second the difference between the recently calculated mean and one second earlier value is checked if it is less than a pre-specified threshold error. In other words, it is checked if the one second period mean of the norm is the "same" as the previous second. That condition gives the indication that the angular velocity components are regulated and the attitude angles remain unchanged.

Then on, in the second phase of the stall stabilization, the control switches the operation from the body angular velocity components to the angle of attack and side slip angle control. The aim of that phase is to get the aircraft into the aerodynamically controllable and stable flight condition. As it is mentioned before the angle of attack commands for that phase are the trim angle of attack values ($\alpha_d = \alpha_0$). Also, the side slip angle commands are zero in order to prevent any possible lateral acceleration of the aircraft ($\beta_d = 0^\circ$).

From the beginning of the stall stabilization control (both in the first and the second phases) the roll attitude angle of the aircraft is nullified ($\phi_d = 0^\circ$) such that the aircraft will get into wings level condition at the end of the stall stabilization maneuver. Also, the yaw attitude of the aircraft is commanded to turn back to its original condition ($\psi_d = \psi_0$).

All of the angular commands ($\alpha_d, \beta_d, \phi_d$ and ψ_d) are generated by using the time dependent half-cycloid motion form:

$$\mu_d(t) = \mu_i + (\mu_{df} - \mu_i)\left[\frac{t}{t_f} - \frac{1}{2\pi}\sin(2\pi\frac{t}{t_f})\right] \tag{5.1}$$

Here, μ_i denotes the initial values of the angles under control. ϕ_i and ψ_i are the initial values of the roll and yaw attitudes of the aircraft at the instant that the first phase (attitude controller) of the stall stabilization controller is started. α_i and β_i are the initial values of the angle of attack and side slip angles at the instant that the second phase (stabilization controller) of the stall stabilization controller is started. Also, μ_{df} is the desired final values of the angles ($\alpha_{df}, \beta_{df}, \phi_{df}$ and ψ_{df}) that the aircraft will reach at the end of the stabilization maneuver. t_f is the desired amount of time in which the aircraft will recover the desired final angular values starting from the instantaneous values (initial values) at the start of the stabilization maneuver. Figure 127 shows the half-cycloid motion profile for $\mu_i = 45^\circ$, $\mu_{df} = 0^\circ$ and $t_f = 10$ sec.

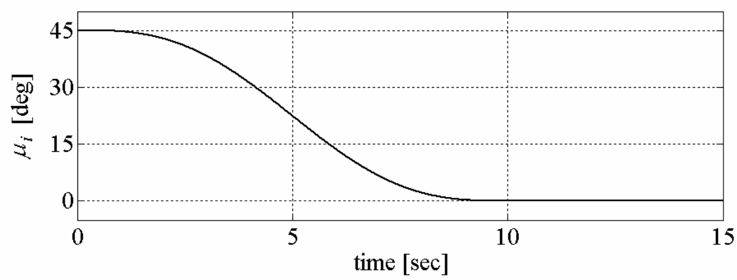

Figure 127. Half-Cycloid Motion Used in Stall Stabilization Controller

The simulations for the stall stabilization controller are started at the flight condition for which the aircraft is at wings level steady flight at 5,000 m altitude and 0.75 Mach. Starting from this initial condition the pull-up maneuver is started using the elevators as shown in Figure 124.

In order to give disturbance on the stall stabilization controller the aircraft is subjected to the air turbulence. Thus, the aircraft's longitudinal components of translational velocity (*u, w*) and longitudinal component of angular velocity (*q*) are disturbed using the *Dryden wind turbulence model* as explained in Chapter 2.6. The turbulence scale lengths used in the modeling are $L_u = L_w = 530$ m and the probability that the high altitude intensities to be exceeded of are chosen as 10^{-5} (severe). Also, the aerodynamic coefficients are disturbed by applying the uncertainties explained in Chapter 4.3.

During the simulation whenever the condition $C_{n\beta\,dyn} \geq C_{n\beta\,dynT}$ and $LCDP \leq LCDP_T$ is achieved the stall stabilization controller is automatically started. Then on, the attitude angles (ϕ, θ, ψ) of the aircraft are monitored. If the time difference of the mean of the norm of the vector $[\dot{\phi}, \dot{\theta}, \dot{\psi}]^T$ is below 1°/sec (the pre-specified threshold value) the angle of attack and side slip angle control is started. As mentioned before, the desired final value of the angle of attack command is the instantaneous trim angle of attack values. The value of t_f is chosen as 0.1 sec such that the aircraft immediately reaches the trim angle of attack values.

The simulation results, i.e. the time histories of the total velocity (V_T), the angle of attack (α), the pitch angle (θ), the thrust vectoring paddle deflections ($\delta_{L1}, \delta_{L2}, \delta_{L3}$ and $\delta_{R1}, \delta_{R2}, \delta_{R3}$) and the throttle deflections ($\delta_{Lth}, \delta_{Rth}$) for the stall stabilization maneuver are shown in the following figures.

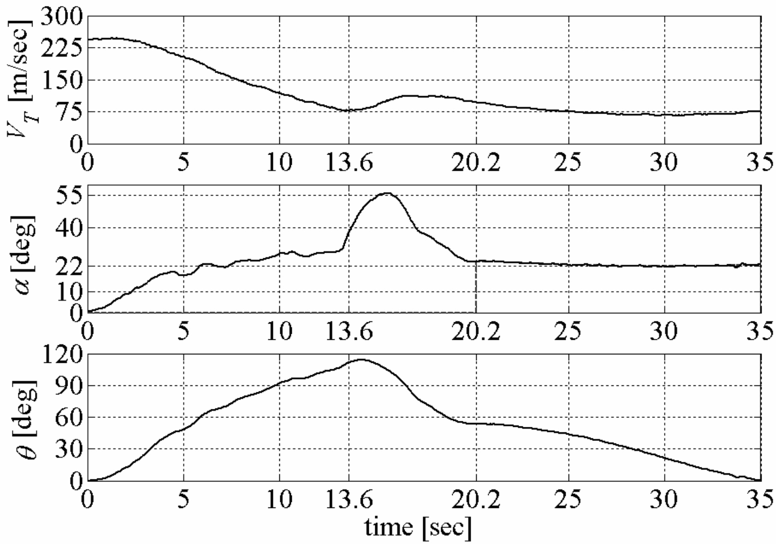

Figure 128. Longitudinal Plane Stall Stabilization Results for V_T, α, θ

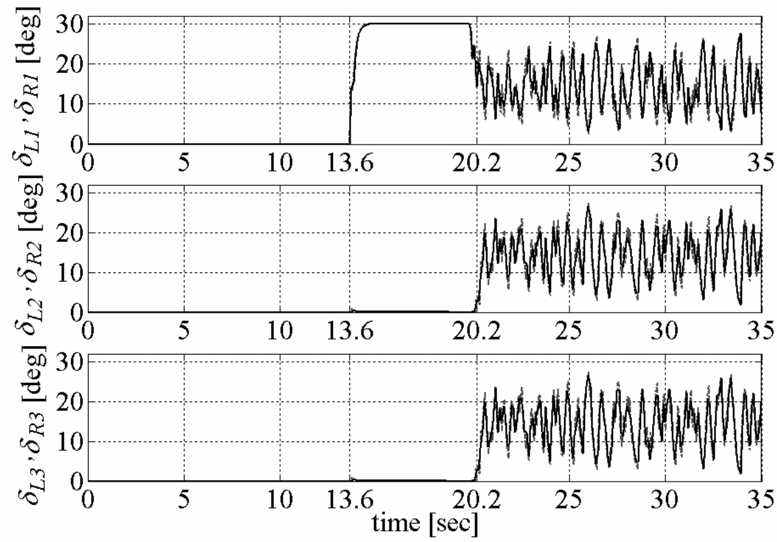

Figure 129. Longitudinal Plane Stall Stabilization Results for δ_L and δ_R

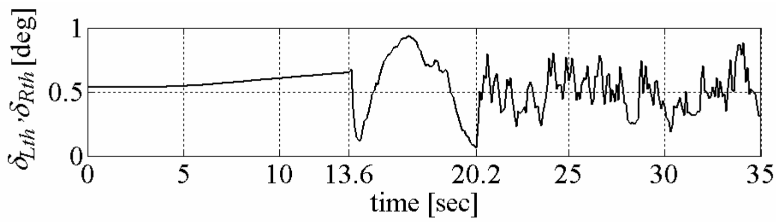

Figure 130. Longitudinal Plane Stall Stabilization Results for δ_{th}

As it is seen from the above figures the longitudinal stall stabilization maneuver is started at t = 13.6 sec and the first phase of the stabilization controller ($q_d = 0$) is lasted for 6.6 seconds. Then on, the pitch angle of the aircraft (θ) is stabilized and the second phase of the stabilization controller ($\alpha_d = \alpha_0, \beta_d = 0^\circ$) is started. At the end of that phase the trim angle of attack command is around 22°, i.e. region F. At this region the resistance to departures and spins is started and roll reversals do not occur, i.e. this is the start of the stall safe region. The integrated

Bihrle-Weissmann chart for the whole period of the longitudinal stall stabilization maneuver is shown in Figure 131.

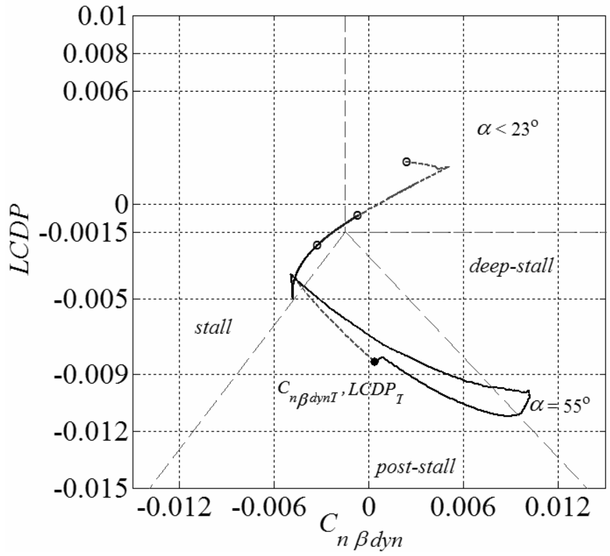

Figure 131. Longitudinal Plane Stall Stabilization Shown on IBW Chart

The dashed line (starting with the symbol "o") in Figure 131 is the stall manipulation part of the maneuver which is activated by using the elevator commands. When the aircraft is nearly at the middle of the post-stall region the stall stabilization control is started automatically since the condition $C_{n\beta\,dyn} \geq C_{n\beta\,dynT}$ and $LCDP \leq LCDP_T$ is achieved. Then, the aircraft makes a stability recovery maneuver that it starts to get back to stall region from the post-stall region. This recovery lasts approximately 5 seconds. During the recovery maneuver the aircraft also passes through the deep-stall region for some short period of time. At the end of the recovery maneuver (shown with the symbol "o") the aircraft is in the stall region and the pitch attitude of the aircraft is stabilized. Thus, the trim angle of attack controller is started when $\alpha = 24^\circ$. At the end of that phase the aircraft moves to the stall safe region at which $\alpha = 22^\circ$ (also shown with the symbol "o").

During the stability recovery phase of the stall stabilization maneuver the aircraft visits the deep-stall region and then recover to the stall region and this phase lasts approximately for 5 seconds. Actually, this is not a desired phenomenon. The recovery phase should be less than that and the aircraft should not visit deep-stall region. However, at the beginning of that phase the thrust vectoring paddles at the upper orientation (δ_{L1}, δ_{R1}) are saturated at their maximum deflection values (30°). It takes approximately 5 seconds that the paddles get free from saturation. This is the cause of the recovery phase to last longer than expected. The saturation of the paddles is shown in Figure 129.

The stall stabilization of the aircraft in the directional and lateral planes of motion is also simulated. The simulation is started at the same flight condition, i.e. wings level steady flight at 5,000 m altitude and 0.75 Mach, and the same pull-up maneuver as in the previous case.

Also, the air turbulence model is the same as in the previous case study. However, all of the translational (*u*, *v*, *w*) and angular (*p*, *q*, *r*) velocity components are disturbed using the Dryden wind turbulence model as explained in Chapter 2.6. The turbulence parameters are the same as used in the previous modeling, i.e. $L_u = L_v = L_w = 530$ m and the probability that the high altitude intensities to be exceeded of are 10^{-5} (severe). The aerodynamic uncertainties are also applied on the aerodynamic coefficients as described in Chapter 4.3.

Since the aim of that simulation is to test the stall stabilization performance especially in the directional and lateral planes of motion, a sideward rate gust (r_g) is applied at the 3rd second of the simulation. The parameters of the gust model, presented in Chapter 2.6, are chosen as 20 meters for the gust length and $r_g = 0.55$ rad/sec for the gust amplitude.

The desired final value of the angle of attack command (α_{df}) is the instantaneous trim angle of attack values and the desired final value of the side slip angle (β_{df}) is zero. The value of t_f for angle of attack and side slip angle stabilization is chosen as 2 seconds. As for the roll and yaw attitude of the aircraft the desired final values are both zero. For the roll attitude stabilization $t_f = 5.5$ sec and yaw attitude stabilization $t_f = 2$ sec are chosen.

The simulation results for the time histories of the total velocity (V_T), the angle of attack (α), the side slip angle (β), the roll, pitch and yaw angles (ϕ, θ, ψ), the thrust vectoring paddle deflections ($\delta_{L1}, \delta_{L2}, \delta_{L3}$ and $\delta_{R1}, \delta_{R2}, \delta_{R3}$) and the throttle deflections ($\delta_{Lth}, \delta_{Rth}$) for the stall stabilization maneuver with side gust are shown in the following figures.

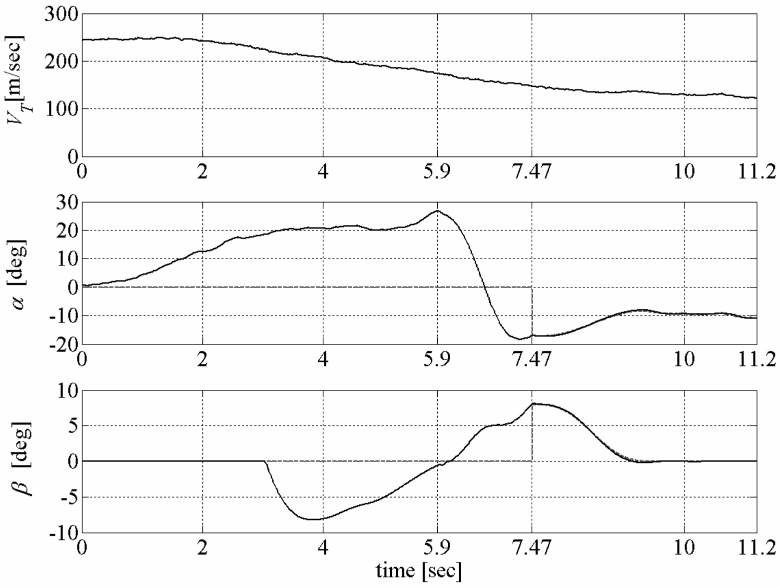

Figure 132. Stall Stabilization Simulation Results for V_T, α , β

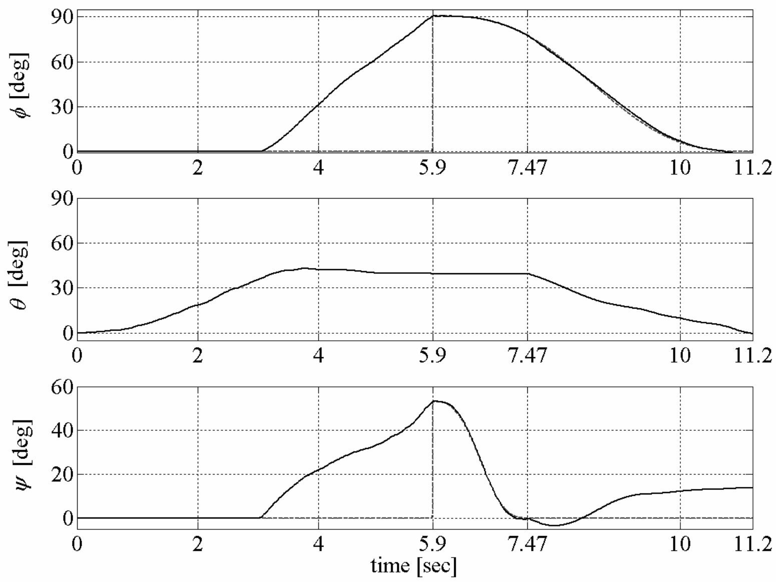

Figure 133. Stall Stabilization Simulation Results for ϕ, θ, ψ

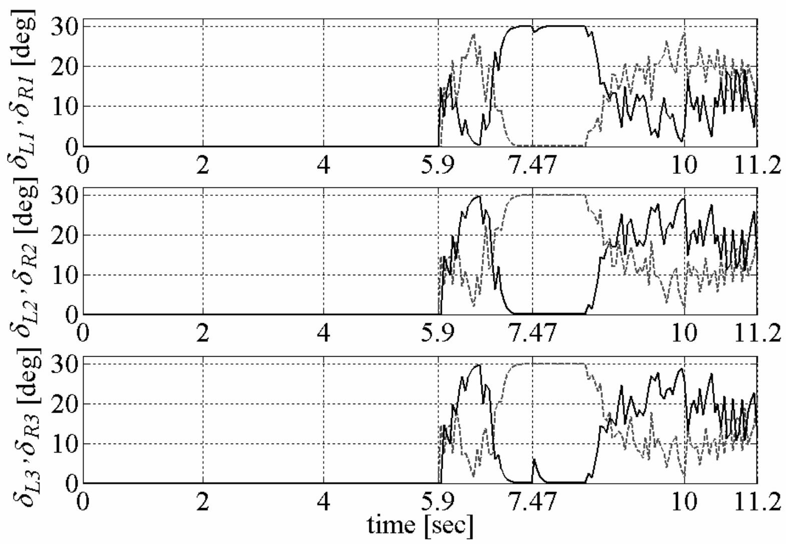

Figure 134. Stall Stabilization Simulation Results for δ_L and δ_R

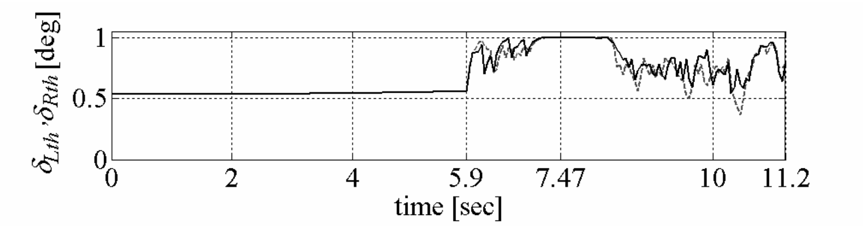

Figure 135. Stall Stabilization Simulation Results for δ_{th}

As it is seen from the above figures the stall stabilization maneuver is started at $t = 5.9$ sec and the first phase of the stabilization controller is lasted for 1.57 seconds. Then on, the pitch and yaw angles of the aircraft are stabilized and the second phase of the stabilization controller ($\alpha_{df} = \alpha_0, \beta_{df} = 0^\circ$) is started. The integrated Bihrle-Weissmann (IBW) chart for the whole period of the stall stabilization maneuver is shown in Figure 136.

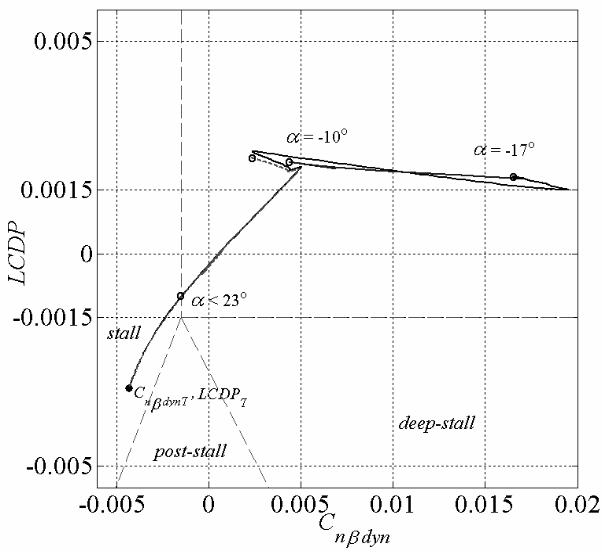

Figure 136. Stall Stabilization Maneuver Shown on IBW Chart

The dashed line (starting with the symbol "o") in Figure 136 is the stall manipulation part of the maneuver which is activated by using the elevator commands. When $t = 3\sec$ the side gust is activated. After 2.9 seconds when $C_{n\beta dyn}$ = -0.0043 and $LCDP = -0.0032$ the stall stabilization controller is triggered. Different than the previous case the stall stabilization maneuver is started earlier here. This is mandatory since the side gust caused approximately 90° roll departure in 2.9 seconds and drags the aircraft into the stall region. This is a very high roll departure rate and if the stabilization is not started here it will be impossible to stabilize it even with the TVC.

In the stall region the stall stabilization control is started automatically and the aircraft makes a stability recovery maneuver that it starts to get back to stall free region in 1.57 seconds (shown with the symbol “o”). Here, the pitch and yaw attitudes of the aircraft are stabilized and the trim angle of attack controller is started when the trim angle of attack command is $\alpha_0 = -17^\circ$. At the end of that phase the aircraft stays in the stall safe region with $\alpha_0 = -10^\circ$ (also shown with the symbol “o”).

Note that, in the previous simulations, at the first phase of the stall stabilization controller, the pitch rate component (q) of the body angular velocity is nullified in order to stabilize the pitch attitude of the aircraft. On the other hand the yaw attitude of the aircraft is directly driven to a desired final yaw attitude value ($\psi_{df} = 0$). The reason for that is, it is more logical to stabilize the aircraft at the original heading (before the gust) rather than stabilizing the yaw rate and end up with a constant but arbitrary heading.

Similar approach can be followed in order to stabilize the pitch attitude of the aircraft in the first phase. Thus, instead of nullifying the pitch rate, a desired pitch attitude profile for the stabilization recovery of the motion in the pitch plane can be defined.

Thus, another simulation can be made by changing the pitch command and keeping the final values of the desired commands of the angle of attack, the side slip angle, the roll and yaw attitudes of the aircraft and the corresponding stabilization final time (t_f) values the same. The final value of the desired pitch command is chosen as zero ($\theta_{df} = 0$) and $t_f = 5.5$ seconds. However, the pitch attitude command (with yaw attitude command) is only activated for 2 seconds and then the stabilization controller switches to the angle of attack and side slip angle stabilization (the second phase). The simulation results are shown in the following figures.

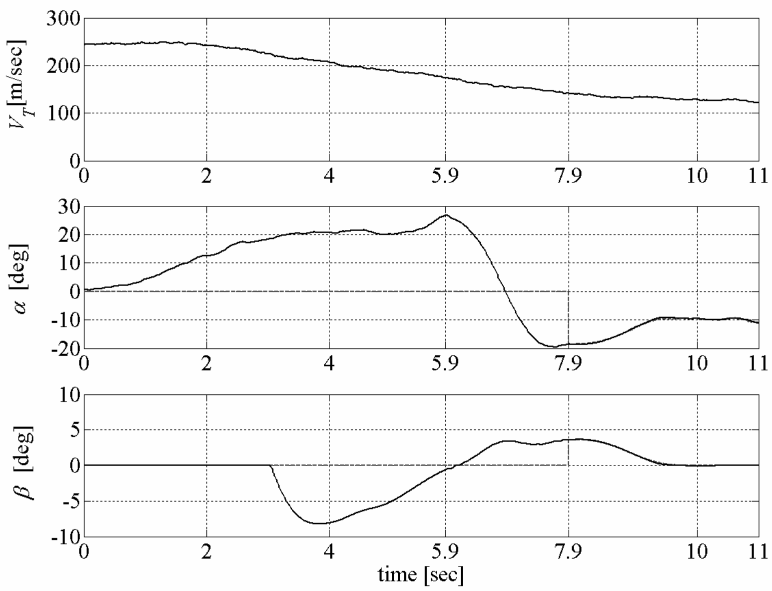

Figure 137. Stall Stabilization Simulation Results for V_T, α, β

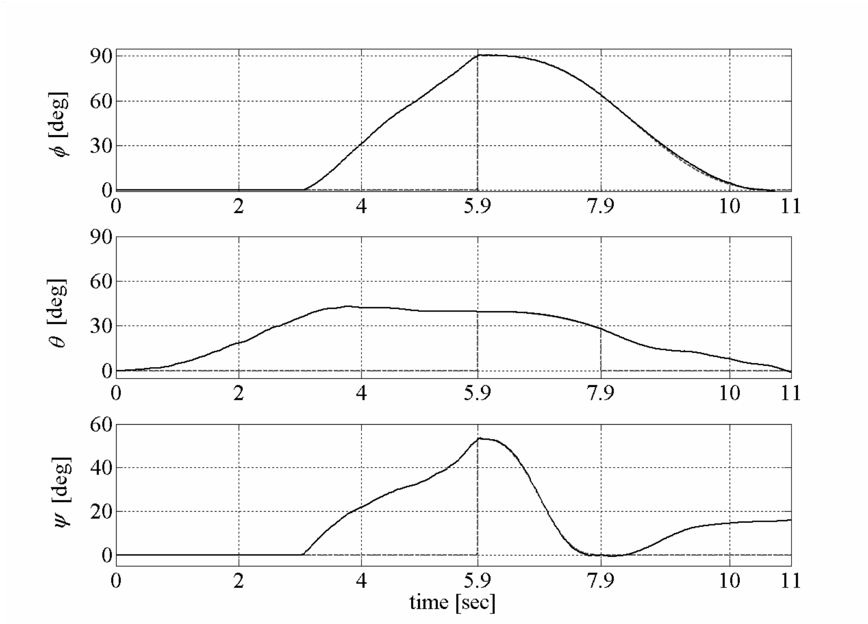

Figure 138. Stall Stabilization Simulation Results for ϕ, θ, ψ

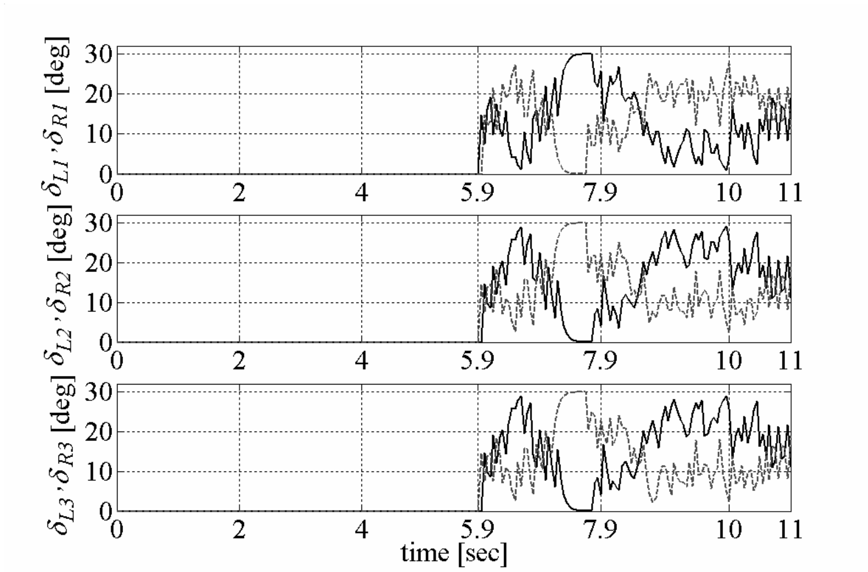

Figure 139. Stall Stabilization Simulation Results for δ_L and δ_R

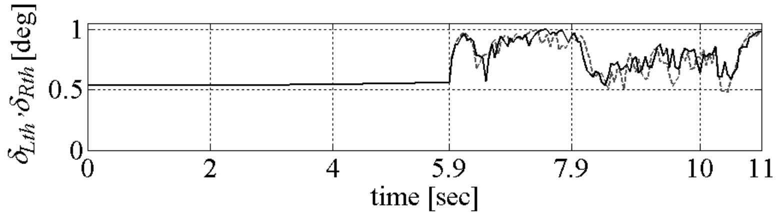

Figure 140. Stall Stabilization Simulation Results for δ_{th}

The stall stabilization maneuver is started at $t = 5.9$ sec and the first phase of the stabilization controller is designed to last for 2 seconds. During this time period, the pitch and yaw angles of the aircraft are stabilized by applying the desired motion command profile. Then on, the second phase of the stabilization controller ($\alpha_{df} = \alpha_0, \beta_{df} = 0^\circ$) is started. The integrated Bihrle-Weissmann chart is not shown here since it is very similar to that of the previous case.

After the last two simulations it is concluded that in order to stabilize the aircraft under the stall conditions all of the stabilization methods can be used. For example, if the aim is to stabilize the angular velocity components and to recover to constant but arbitrary attitude angles then the angular velocity components (q, r) of the aircraft are regulated. Similarly, if the linear velocity components are desired to be regulated then the angle of attack and the side slip angles (α, β) are controlled in the stabilization controller. If the aim is to have direct control on the attitude angles (θ, ψ) of the aircraft then it is possible to define desired attitude motion profiles. In all cases it is necessary to stabilize the roll attitude (ϕ) of the aircraft to get the aircraft in wings level position at the end of the stall stabilization control.

CHAPTER 6

HIGH ANGLE OF ATTACK MANEUVERS

In this chapter, the performance of the attitude controller (designed in Chapter 3 and Chapter 4) will be investigated. For that purpose, first, the Cobra maneuver will be analyzed by using the aerodynamic controls only and TVC only. Then, the Herbst maneuver will be introduced and analyzed similarly by using the aerodynamic controls only and TVC only. Eventually, different attitude control maneuvers as velocity vector roll maneuver, fixed ground target attack maneuvers, tail chase acquisition maneuver and target aircraft pointing maneuver will be introduced and analyzed by simulations.

6.1. Cobra Maneuver

The Cobra maneuver was first demonstrated by the famous Russian pilot Pougachev. This maneuver is composed of two successive phases. In the first *pull-up phase* the pilot makes a nose-up maneuver until the aircraft gets into stall and therefore slows down dramatically. In the second *recovery phase* the pilot starts the nose-down maneuver and returns the aircraft to a desired pitch angle. The pull-up phase of the maneuver is realized by the aerodynamic control surfaces and the recovery phase of the maneuver can be realized by means of either aerodynamic control only or TVC only. The performances of these two controls are compared in the sequel.

6.1.1. Aerodynamic Control Only

In this case, for commanded accelerations and un-deflected TVC paddles, equation (3.23) is solved for the aerodynamic forces and moments. Thus, the commanded aerodynamic control surface deflections can be calculated by using equation (3.27).

In the simulations, the pull-up phase of the Cobra maneuver is started at the specified initial condition and the aircraft climbs up from the initial altitude. After 8^{th} second, when the aircraft is in stall with $\alpha = 23^{\circ}$ and $\theta = 76^{\circ}$, the recovery phase of the maneuver is started using the aerodynamic controls only. In the recovery phase the pitch angle of the aircraft is brought to a desired value of -5° in 18 seconds. The simulations showed that, if the recovery phase is started beyond $\alpha = 23^{\circ}$, the desired maneuver cannot be achieved without any saturation of the elevator deflection. Hence, considering the specified initial conditions, the recovery phase should start at latest when $\alpha = 23^{\circ}$ so that the desired maneuver can be achieved using the aerodynamic controls only. The time histories of the total velocity, the angle of attack, the pitch angle, and the elevator deflection are shown in the following figures where the aerodynamic controls are used successfully in the recovery phase.

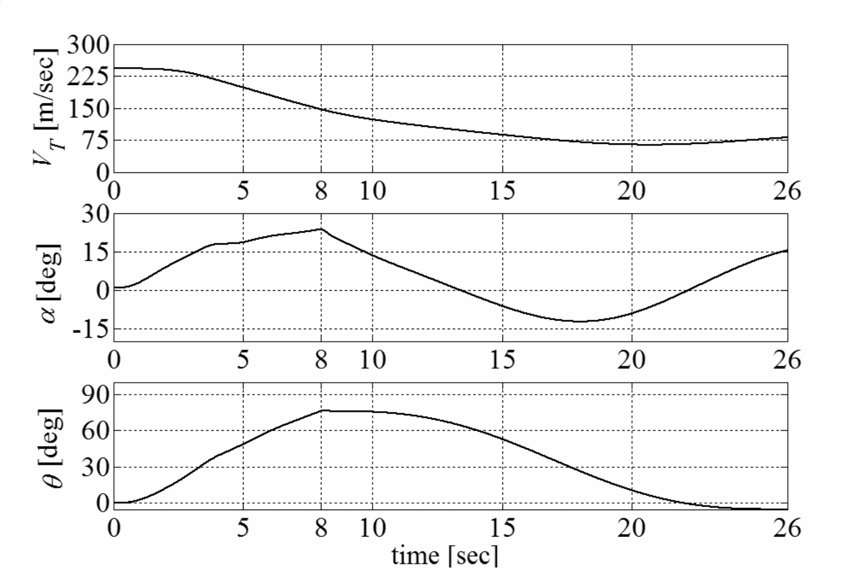

Figure 141. Cobra Maneuver Aero. Control Results for V_T, α , θ

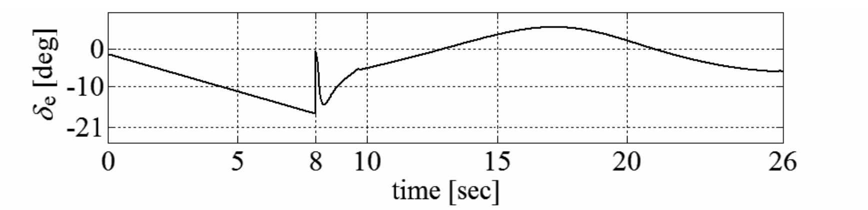

Figure 142. Cobra Maneuver Aero. Control Results for δ_e

6.1.2. Thrust Vector Control Only

In the simulations, the pull-up phase of the maneuver is started at the same initial condition and the aircraft climbs up from the initial altitude. After 13th second when the aircraft gets into the deep stall region, with $\alpha = 30^\circ$ and $\theta = 105^\circ$, the recovery phase of the maneuver is started using TVC only. In the recovery phase, the pitch angle of the aircraft is brought to a desired value of -5° in 18 seconds. The simulations showed that, using TVC instead of aerodynamic control, the maneuvering capability of the aircraft is enhanced and the recovery phase of the maneuver could be started at higher angles of attack when the pitch angles are also higher than the case with "aerodynamic control only". The time histories of the total velocity, the angle of attack, the pitch angle, and the thrust-vectoring paddle deflections are shown in the following figures.

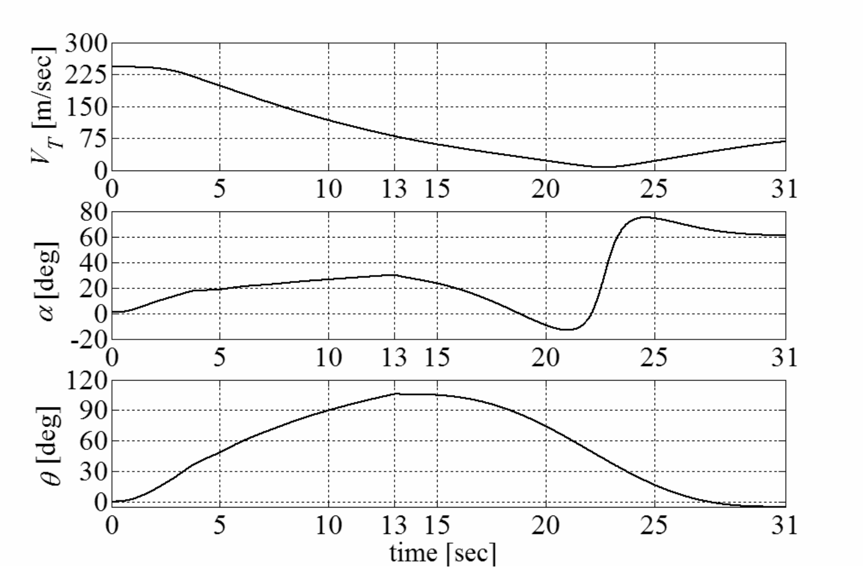

Figure 143. Cobra Maneuver TVC Results for V_T, α, θ

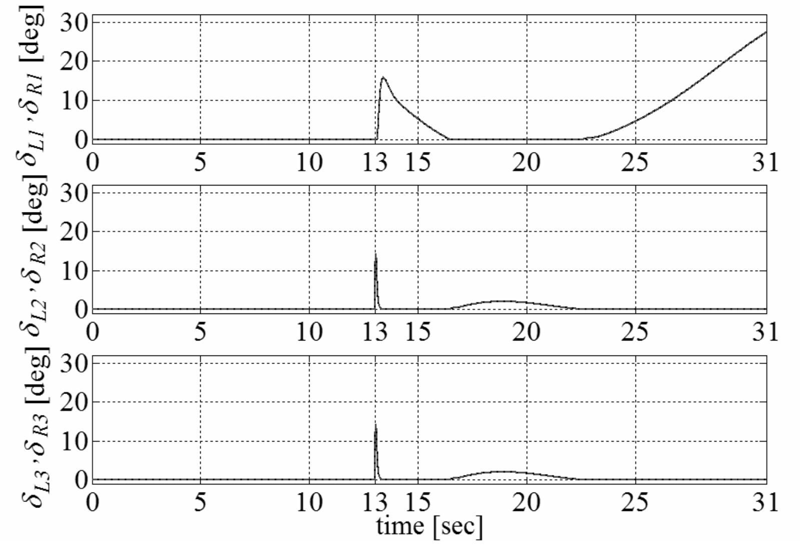

Figure 144. Cobra Maneuver TVC Results for δ_L and δ_R

6.2. Herbst Maneuver

The Herbst maneuver is named after Dr. W.B. Herbst, proponent of using post-stall flight in air combat. It is used for heading reversal of the aircraft with downward nose pointing for a possible dive attack in close air combat.

The Herbst maneuver is composed of two successive phases. In the first *pull-up phase*, the aircraft makes a nose-up maneuver until it gets into stall and therefore slows down dramatically. In the second *heading reversal phase*, the aircraft starts a roll motion coordinated with a yaw motion in order to change its heading and to lower its pitch angle. At the end of the maneuver, the aircraft turns 180° and thus reverses its initial heading direction at the beginning of the maneuver and meanwhile assumes a desired pitch angle. The pull-up phase of the maneuver is realized by the aerodynamic control surfaces. However, the heading reversal phase of the maneuver can only be realized by means of TVC. This conclusion has been reached based on the results of the simulations explained in the sequel.

6.1.1. Thrust Vector Control Only

In the simulations, the pull-up phase of the Herbst maneuver is started at the same initial condition and the aircraft climbs up from the initial altitude. After 12th second when the aircraft is in post-stall region, with $\alpha = 28^\circ$ and $\theta = 101^\circ$, the heading reversal phase of the maneuver is started using TVC only. In the heading reversal phase, a coordinated lateral maneuver is realized by commanding the roll angle to -30° and the yaw rate to -18°/sec in 15 seconds. At the same time, the pitch angle of the aircraft is brought to a desired value of -12° in 18 seconds.

The time histories of the total velocity, the angle of attack, the side slip angle, the roll, pitch and yaw angles, and the thrust-vectoring paddle deflections for this maneuver are shown in the following figures.

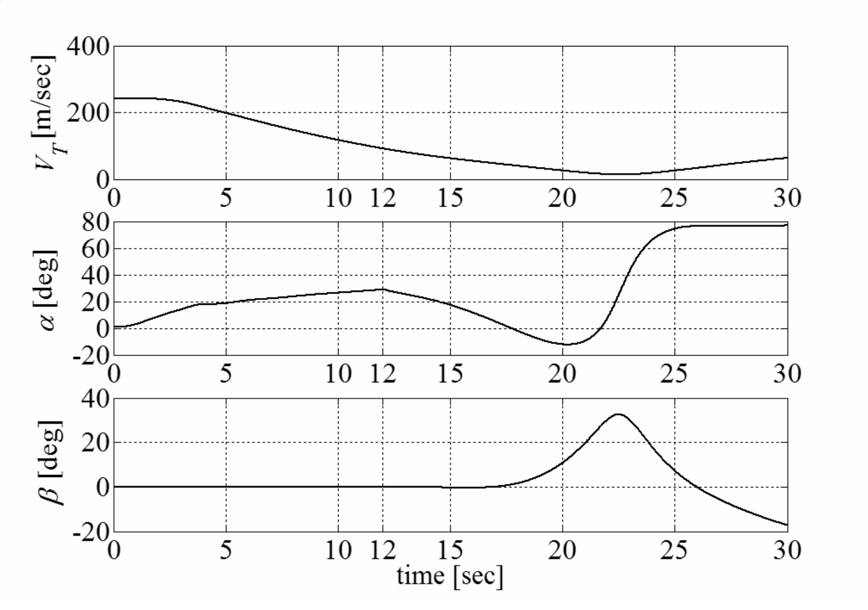

Figure 145. Herbst Maneuver TVC Results for V_T, α, β

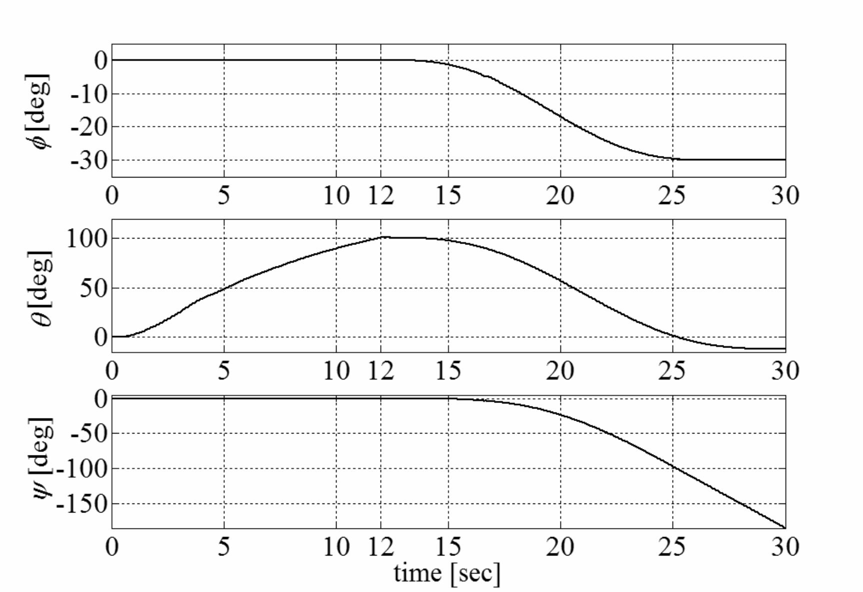

Figure 146. Herbst Maneuver TVC Results for ϕ, θ, ψ

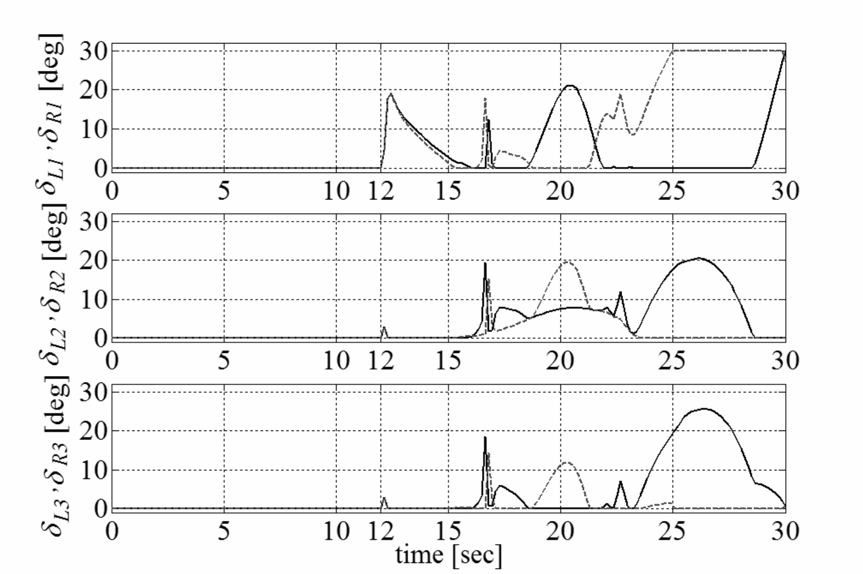

Figure 147. Herbst Maneuver TVC Results for δ_L and δ_R

6.1.2. Aerodynamic Control Only

In the simulations, the pull-up phase of the Herbst maneuver is started at the specified initial condition and the aircraft climbs up from the initial altitude. The simulations showed that, if the heading reversal phase is started beyond $\alpha = 14^\circ$, the desired maneuver cannot be achieved without any saturation of the aerodynamic control surfaces. Hence, considering the specified initial conditions, the second phase of the maneuver can be started when $\alpha \leq 14^\circ$. It is also noticed that, although the desired roll and pitch angles are achieved at the end of the maneuver, a complete heading reversal cannot be realized as desired. This is because the yaw rate can only be commanded up to a limited value without any saturation of the aerodynamic control surfaces. This is demonstrated with a specific simulation, where the second phase is started when $\alpha = 14^\circ$ and $\theta = 26^\circ$. In this simulation, the roll angle is commanded to a desired value of -30° at 15 seconds and the pitch attitude is commanded to a desired value of -12° at 18 seconds. However, it is seen that the yaw rate can only be commanded at most to a value of -4.5°/sec due to saturations, which happens to be insufficient for a complete heading reversal. The time histories of the total velocity, the angle of attack, the side slip angle, the roll, pitch and yaw angles, and the commanded aileron, elevator and rudder deflections are shown in the following figures.

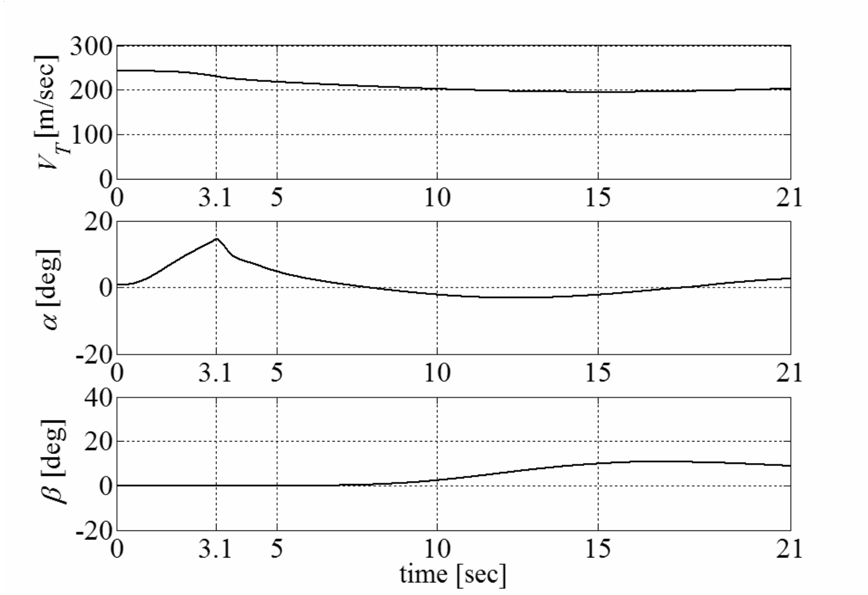

Figure 148. Herbst Maneuver Aero. Control Results for V_T, α, β

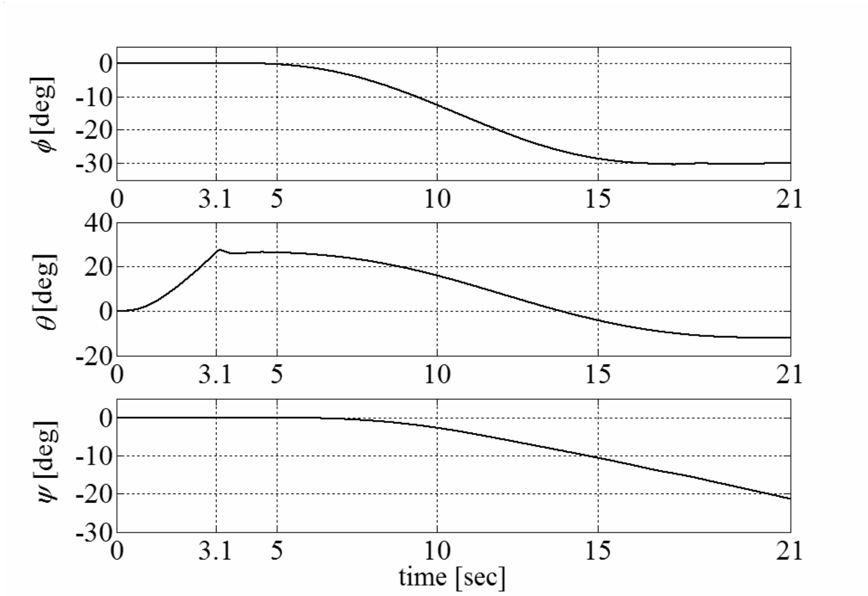

Figure 149. Herbst Maneuver Aero. Control Results for ϕ, θ, ψ

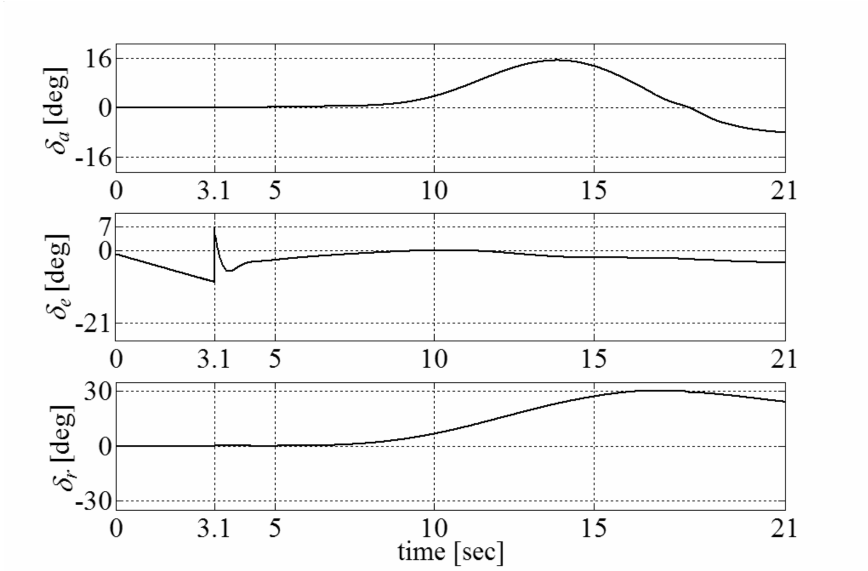

Figure 150. Herbst Maneuver Aero. Control Results for $\delta_a, \delta_e, \delta_r$

As verified by simulations, the achieved maneuvering capability using the "aerodynamic control only" is very low when compared to the case with “TVC only”. A desired maneuver with complete heading reversal cannot be realized by using the aerodynamic control surfaces only. The aerodynamic control surfaces turn out to be extremely inadequate for this purpose.

6.3. Velocity Vector Roll Maneuver

The velocity vector roll is one of the crucial parts of the “post-stall flight tests”. It is known as the milestone to demonstrate the performance of a successful high alpha maneuvering fighter aircraft. In that maneuver, the aircraft is brought to a relatively high angle of attack and velocity vector roll is demanded from the aircraft. Consequently, the aircraft turns a whole revolution around its velocity vector while keeping its angle of attack at the desired values. An illustrative sketch for velocity vector roll maneuvers can be seen at the following figure.

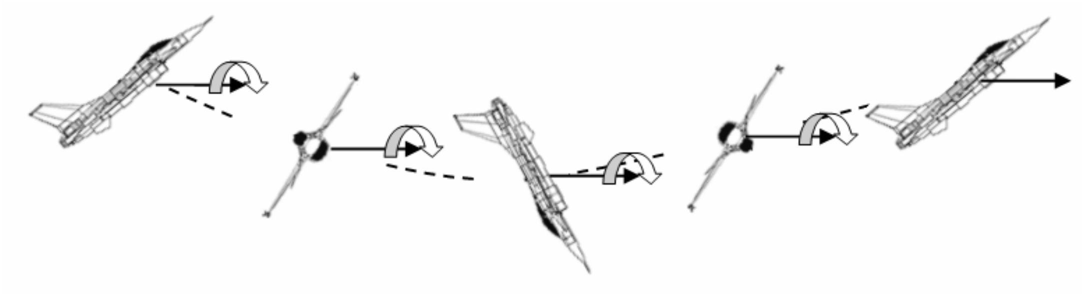

Figure 151. Definition of the Velocity Vector Roll Maneuver

In order to command the aircraft's velocity vector, the orientation angles of the velocity of the aircraft should be controlled. Thus, the flight path angles (γ_y, γ_z) and the velocity vector roll angle (γ_x) should be calculated. Recall that, the Euler angles define the rotations from the earth fixed reference frame to the body fixed reference frame, i.e. $\hat{C}^{(o,b)} = R_3(\psi)R_2(\theta)R_1(\phi)$. Similarly, γ_z, γ_y and γ_x define the rotations from the earth fixed reference frame to the wind axis reference frame, i.e. $\hat{C}^{(o,w)} = R_3(\gamma_z)R_2(\gamma_y)R_1(\gamma_x)$. Also, two successive rotations, made by angle of attack and side slip angles, defines the rotation sequence from the body fixed reference frame to the wind axis reference frame. Thus, $\hat{C}^{(b,w)} = R_2(-\alpha)R_3(\beta)$ is the rotation matrix from body fixed reference frame to the wind axis reference frame. Since, $\hat{C}^{(o,b)}\hat{C}^{(b,w)} = \hat{C}^{(o,w)}$, the flight path angles are:

$$\begin{bmatrix} \gamma_x \\ \gamma_y \\ \gamma_z \end{bmatrix} = \begin{bmatrix} \tan^{-1}(\hat{C}_{32}^{(o,w)}, \hat{C}_{33}^{(o,w)}) \\ \tan^{-1}(-\hat{C}_{31}^{(o,w)}, (1-\hat{C}_{31}^{(o,w)2})^{(1/2)}) \\ \tan^{-1}(\hat{C}_{21}^{(o,w)}, \hat{C}_{11}^{(o,w)}) \end{bmatrix} \tag{6.1}$$

Also, the angular velocity of the aircraft, expressed at wind axis coordinates, with respect to the earth fixed reference frame, $\vec{\omega}_{w/o}$, can be found by differentiating $\hat{C}^{(o,w)}$ with respect to time:

$$\overline{\omega}_{w/o}^{(o)} = \hat{C}^{(o,b)}\,\overline{\omega}_{b/o}^{(b)} - \dot{\alpha}\,\hat{C}^{(o,b)}\,\overline{u}_2 + \dot{\beta}\,\hat{C}^{(o,b)} R_2(-\alpha)\overline{u}_3 \tag{6.2}$$

Similarly, differentiating $\hat{C}^{(o,w)}$ with respect to time $\overline{\omega}_{w/o}^{(o)}$ is found:

$$\overline{\omega}_{w/o}^{(o)} = \dot{\gamma}_z\,\overline{u}_3 + \dot{\gamma}_y R_3(\gamma_z)\overline{u}_2 + \dot{\gamma}_x\, R_3(\gamma_z) R_2(\gamma_y)\overline{u}_1 \tag{6.3}$$

$$\overline{\omega}_{w/o}^{(o)} = \hat{J}^{(o,w)}\begin{bmatrix}\dot{\gamma}_x\\ \dot{\gamma}_y\\ \dot{\gamma}_z\end{bmatrix} = \begin{bmatrix} c\gamma_z c\gamma_y & -s\gamma_z & 0\\ s\gamma_z c\gamma_y & c\gamma_z & 0\\ -s\gamma_y & 0 & 1\end{bmatrix}\begin{bmatrix}\dot{\gamma}_x\\ \dot{\gamma}_y\\ \dot{\gamma}_z\end{bmatrix} \tag{6.4}$$

Combining equation (6.3) and (6.4) the time derivatives of velocity vector orientation angles can be found.

$$\begin{bmatrix}\dot{\gamma}_x\\ \dot{\gamma}_y\\ \dot{\gamma}_z\end{bmatrix} = \hat{J}^{(w,o)}\hat{C}^{(o,b)}\begin{bmatrix}p\\ q\\ r\end{bmatrix} + \begin{bmatrix} -\hat{J}^{(w,o)}\hat{C}^{(o,b)}\,\overline{u}_2\\ \hat{J}^{(w,o)}\hat{C}^{(o,b)} R_2(-\alpha)\overline{u}_3\end{bmatrix}^T \begin{bmatrix}\dot{\alpha}\\ \dot{\beta}\end{bmatrix} \tag{6.5}$$

Pursuing a similar way as in the case of attitude controller design described in Chapter 3.2 the velocity vector attitude controller can be designed. The desired velocity vector roll angle and the flight path angles are defined as γ_{xd}, γ_{yd} and γ_{zd}. Also, the error vector $\overline{e}_r(t)$ is defined as the difference between the desired (d) and the actual values of the velocity vector attitude angles of the aircraft, i.e.

$$\overline{e}_r(t) = \begin{bmatrix}\gamma_{xd}(t) - \gamma_x(t)\\ \gamma_{yd}(t) - \gamma_y(t)\\ \gamma_{zd}(t) - \gamma_z(t)\end{bmatrix} \tag{6.6}$$

Implementing the PI with velocity feed-forward controller with the constant gain matrices $\hat{K}_{pr} = diag(K_{p\gamma_x}, K_{p\gamma_y}, K_{p\gamma_z})$ and $\hat{K}_{ir} = diag(K_{i\gamma_x}, K_{i\gamma_y}, K_{i\gamma_z})$ the commanded velocity vector roll, pitch and yaw angular velocities can be expressed:

$$\begin{bmatrix} \dot{\gamma}_{xcom}(t) \\ \dot{\gamma}_{ycom}(t) \\ \dot{\gamma}_{zcom}(t) \end{bmatrix} = \hat{K}_{pr}\bar{e}_r(t) + \hat{K}_{ir}\int_0^t \bar{e}_r(t')dt' + \begin{bmatrix} \dot{\gamma}_x(t) \\ \dot{\gamma}_y(t) \\ \dot{\gamma}_z(t) \end{bmatrix} \tag{6.7}$$

After calculating the velocity vector roll, pitch and yaw angular velocities, p_{com}, q_{com} and r_{com} can be calculated:

$$\begin{bmatrix} p_{com}(t) \\ q_{com}(t) \\ r_{com}(t) \end{bmatrix} = \hat{C}^{(b,o)}\hat{J}^{(o,w)}\left(\begin{bmatrix} \dot{\gamma}_{xcom}(t) \\ \dot{\gamma}_{ycom}(t) \\ \dot{\gamma}_{zcom}(t) \end{bmatrix} - \begin{bmatrix} -\hat{J}^{(w,o)}\hat{C}^{(o,b)}\bar{u}_2 \\ \hat{J}^{(w,o)}\hat{C}^{(o,b)}R_2(-\alpha)\bar{u}_3 \end{bmatrix}^{\mathrm{T}} \begin{bmatrix} \dot{\alpha}(t) \\ \dot{\beta}(t) \end{bmatrix}\right) \tag{6.8}$$

Once p_{com}, q_{com} and r_{com} are calculated they will be fed through the second segment of the controller and they will be used instead of p_d, q_d and r_d in equation (3.15). Hence, $\dot{p}_{com}$, $\dot{q}_{com}$ and $\dot{r}_{com}$ will be calculated and $\bar{F}^{(b)}_{com}$ and $\bar{M}^{(b)}_{com}$ will be determined using equation (3.8). Afterwards, $\bar{F}_L^{(b)}$ and $\bar{F}_R^{(b)}$ can be calculated according to Table 1. Since, the pitch acceleration is generated here the constraining equation for pitch angle and pitch rate control should be used. Then T_{Lcom} and T_{Rcom}, {ψ_{Lcom}, θ_{Lcom}} and {ψ_{Rcom}, θ_{Rcom}} (and the throttle deflections and the six thrust-vectoring paddle deflection angles) will be calculated using $\bar{F}_L^{(b)}$ and $\bar{F}_R^{(b)}$.

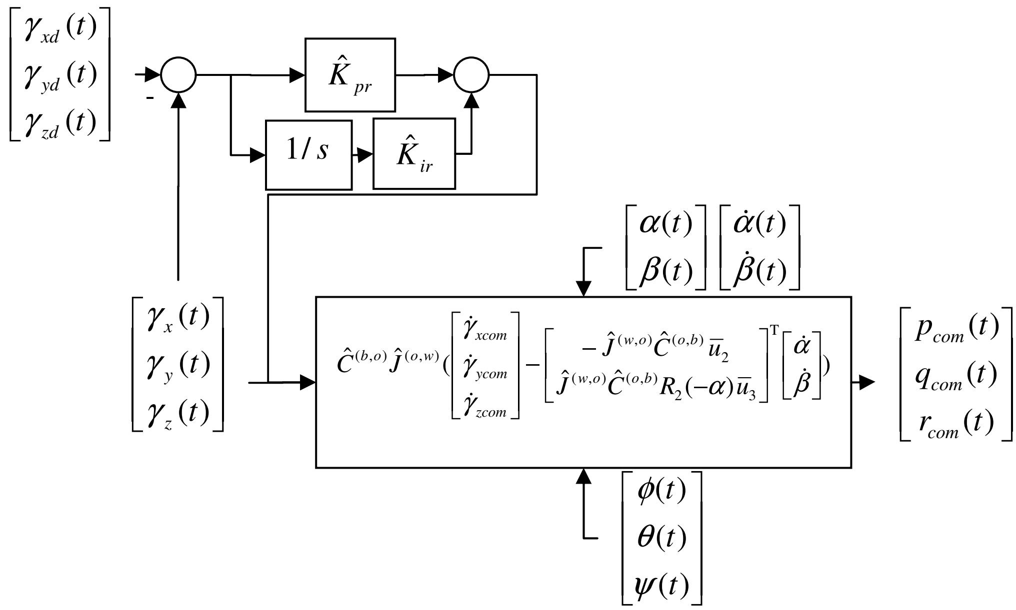

Figure 152. The Velocity Vector Controller Block Diagram

The controller gain matrices ($\hat{K}_{pr}, \hat{K}_{ir}$) are calculated pursuing the same approach described in Chapter 3.2. Also, the same desired closed loop parameter set (ω_n's and ζ's) is used as shown in Table 3 in Chapter 4.3.

The velocity vector roll maneuver simulation is started from the initial condition at which the aircraft is at 10,000 m altitude at 0.8 Mach at $\theta_0 = 10^\circ$ climb. Applying the trim algorithm discussed in Chapter 4.1 the equilibrium points at the specified flight condition are found as $\beta_0 = \delta_{a0} = \delta_{r0} = 0^\circ$ and $T_{L0} = T_{R0} = 26{,}314\,\text{N}$, $\alpha_0 = 3.11^\circ$, $\delta_{e0} = \text{-}2.19^\circ$ and $\delta_{Lth} = \delta_{Rth} = 0.85$.

The velocity vector roll angle is commanded to perform a full turn (0° to 360°) in 19 seconds. Here, similar to the stall stabilization controller, a hybrid controller composed of the velocity vector roll attitude and angle of attack and side slip angle controllers (explained in Chapter 3.2) are used.

When the velocity vector roll command is started the angle of attack (α) and side slip angle (β) are stabilized (by regulating $\dot{\alpha}$ and $\dot{\beta}$ for 9 seconds). At the last 10 seconds, of the velocity vector roll control, the angle of attack and side slip angles are commanded to 10° and 0° respectively. The aircraft's motion during the velocity vector roll control is given in the following figure.

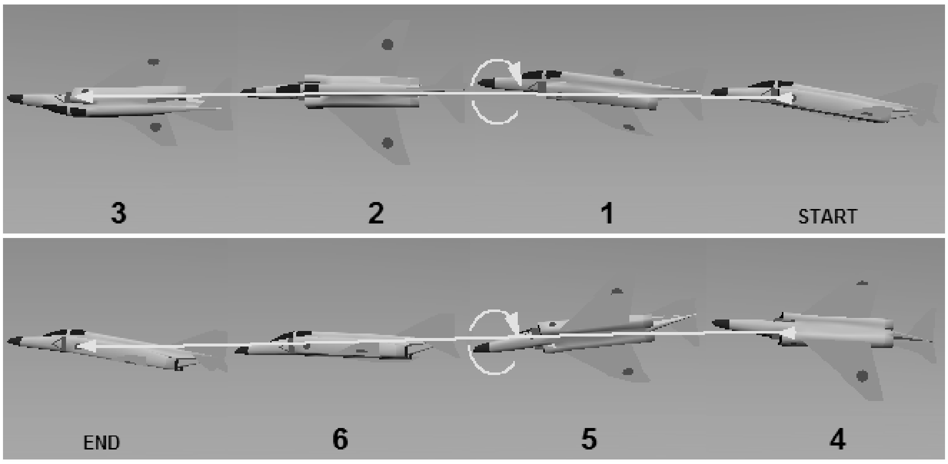

Figure 153. Phases of the Velocity Vector Roll Maneuver

The time histories of the total velocity, the angle of attack, the side slip angle, the roll, pitch and yaw angles, the thrust-vectoring paddle deflections and aerodynamic control surfaces for this maneuver are shown in the following figures.

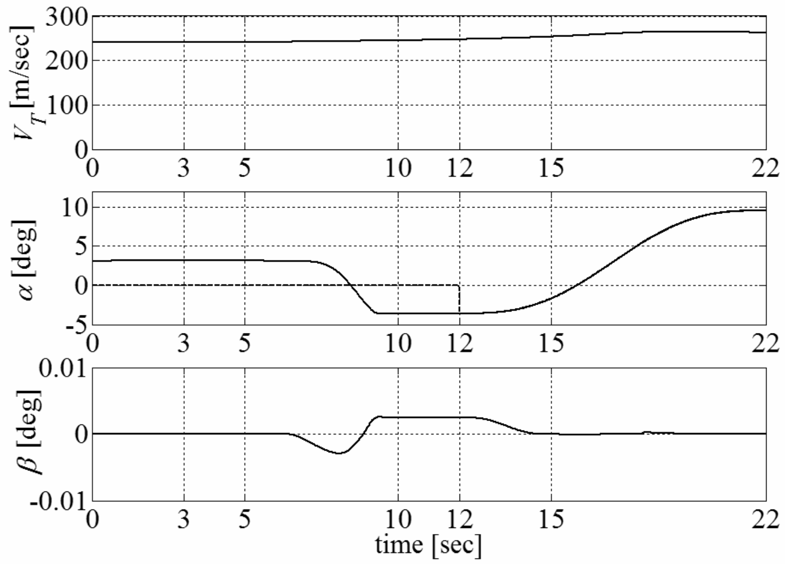

Figure 154. Velocity Vector Roll Maneuver Results for V_T, α, β

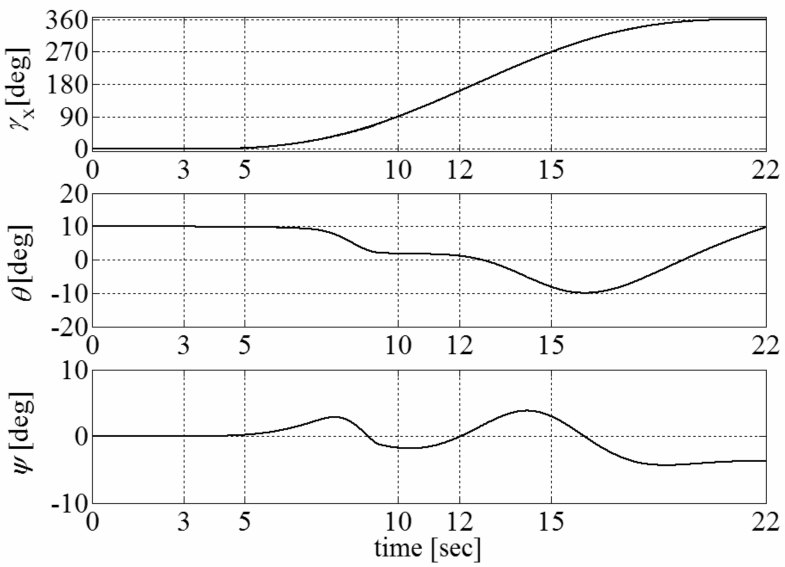

Figure 155. Velocity Vector Roll Maneuver Results for γ_x, θ, ψ

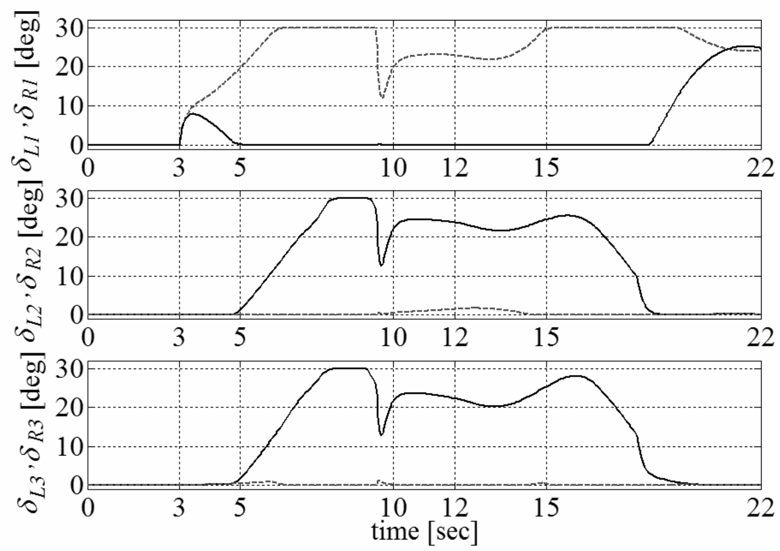

Figure 156. Velocity Vector Roll Maneuver Results for δ_L and δ_R

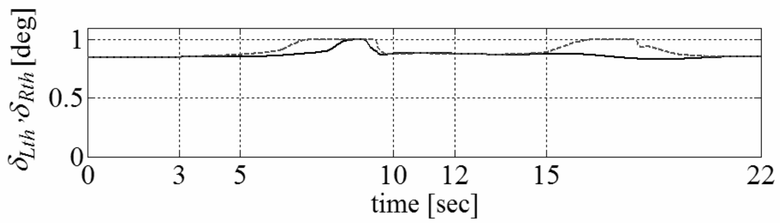

Figure 157. Velocity Vector Roll Maneuver Results for δ_{th}

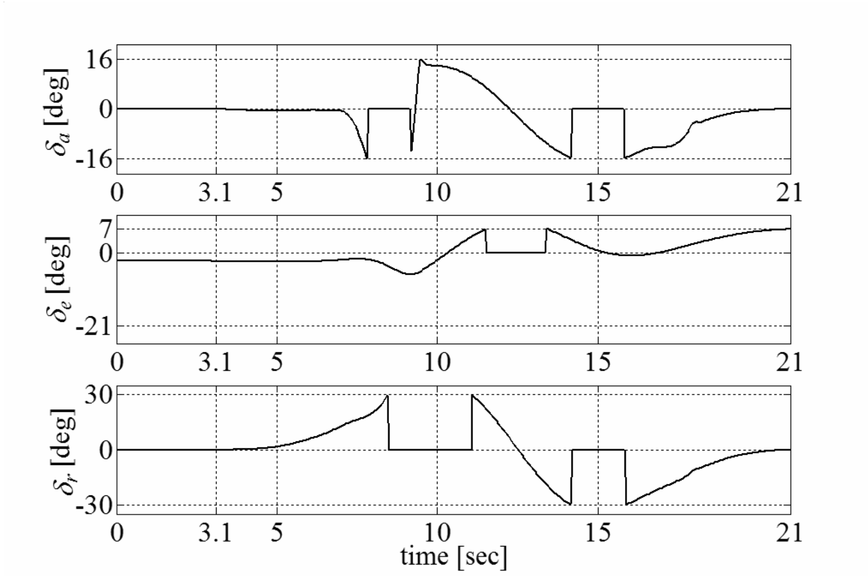

Figure 158. Velocity Vector Roll Maneuver Results for $\delta_a, \delta_e,\ \delta_r$

6.4. Fixed Ground Target Attack Maneuvers

The fixed ground target attack maneuvers are in a group of important offense maneuvers. In such a maneuver the aircraft should directly charge on to the fixed ground target rapidly (in the defense zone of the target), attack the target and leave the zone with a sharp turn leaving the target behind. Thus, the attack aircraft should remain in the defense zone of the target for a short time with an effective offense and without being hit.

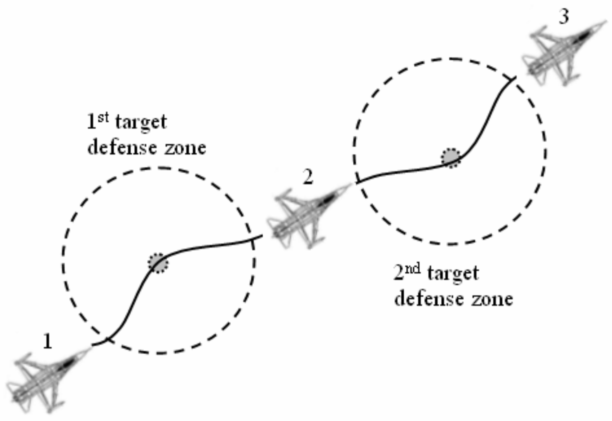

Figure 159. Waving between the Targets

In order to simulate the fixed ground target attack scenario the desired yaw angle command (ψ_d) is generated to wave between the targets. The yaw angle commands are generated that the aircraft rapidly turns to the center of the target defense zone and after it passes the target rapidly, turns to its original flight path, i.e. the flight leg before entering the zone. The proposed steering algorithm is explained below.

Defining the zone circular radius as R_{dz}, the steering law for maneuvering in the zone is stated as:

if $(d_{dz} - R_{dz}) \leq d_{dz\min}$, then:

$\text{TAttack}_{in} = on$ and hold $x_{in} = x(t)$, $y_{in} = y(t)$ and $\psi_{in} = \psi(t)$.

Calculate the coordinate to steer after leaving the zone which is on the original route before entering the zone:

$$x_{out} = x_{in} + 2R_{dz} \tag{6.9}$$

$$y_{out} = y_{in} + \tan(\psi_{in})(x_{out} - x_{in}) \tag{6.10}$$

if $\text{TAttack}_{in} = on$, then:

$$\psi_d = \tan^{-1}((y_{do} - y(t)),(x_{do} - x(t))) \tag{6.11}$$

if $\text{TAttack}_{in} = on$ and $d_{dz} \leq d_{dz\min}$ (the aircraft reaches on the target), then:

$\text{TAttack}_{center} = on$ and

$$\psi_d = \tan^{-1}((y_d - y(t)),(x_d - x(t))) \tag{6.12}$$

if $\text{TAttack}_{center} = on$ and $\left| y_d - y(t) \right| \leq d_{dz\min}$ |, then:

$\text{TAttack}_{in} = off$ and $\psi_d = \psi_{in}$.

Here, d_{dz} is the lateral distance between the aircraft's position and the position of the center of the target defense zone. It is calculated by using the lateral position components of the aircraft body position ($x(t), y(t)$) and the lateral position components of the center of the zone (x_{dz}, y_{dz}):

$$d_{dz} = ((x_{dz} - x(t))^2 + (y_{dz} - y(t))^2)^{1/2} \tag{6.13}$$

Also, $d_{dz\min}$ is the threshold value of the distance in order to decide that the aircraft is in the zone.

Here, note that, after reaching to the center of the defense zone the aircraft switches to a desired recovery point ($\begin{bmatrix} x_d & y_d \end{bmatrix}^T$) which is actually on its original flight leg before entering the zone.

Pursuing the stated steering algorithm the aircraft maneuvers in order to attack a fixed ground target in its defense zone and then recovers its original heading.

For the fixed ground target attack maneuver simulations the attitude controller described in Chapter 3.2 and designed in Chapter 4.3 is used. The simulations are started from the initial condition at which the aircraft is at 5,000 m. altitude at 0.45 Mach at wings level flight. Applying the trim algorithm discussed in

Chapter 4.1 the equilibrium points at the specified flight condition are found as $\beta_0 = \delta_{a0} = \delta_{r0} = 0^\circ$ and $T_{L0} = T_{R0} = 6{,}047\,\mathrm{N}$, $\alpha_0 = 6.27^\circ$, $\delta_{e0} = \text{-}3.31^\circ$ and $\delta_{Lth} = \delta_{Rth} = 0.14$.

In order to simulate the fixed ground target attack scenario a ground target defense zone whose radius is equal to 4,000m and the target which is located at $[x_{do}\ y_{do}]^{\mathrm{T}} = [5{,}000\ 2{,}000]^{\mathrm{T}}\,\mathrm{m}$ is defined. Then on, three different scenarios are simulated by changing the initial position and yaw attitude of the aircraft in each. As for Case I $[x_0\ y_0]^{\mathrm{T}} = [0\ 0]^{\mathrm{T}}\,\mathrm{m}$ and $\psi_0 = 0^\circ$, for Case II $[x_0\ y_0]^{\mathrm{T}} = [0\ 5{,}500]^{\mathrm{T}}\,\mathrm{m}$ and $\psi_0 = 0^\circ$ and for Case III $[x_0\ y_0]^{\mathrm{T}} = [0\ -2{,}000]^{\mathrm{T}}\,\mathrm{m}$ and $\psi_0 = 30^\circ$. The simulation results showing the lateral track of the aircraft waving in the defense zone is shown in the following figure.

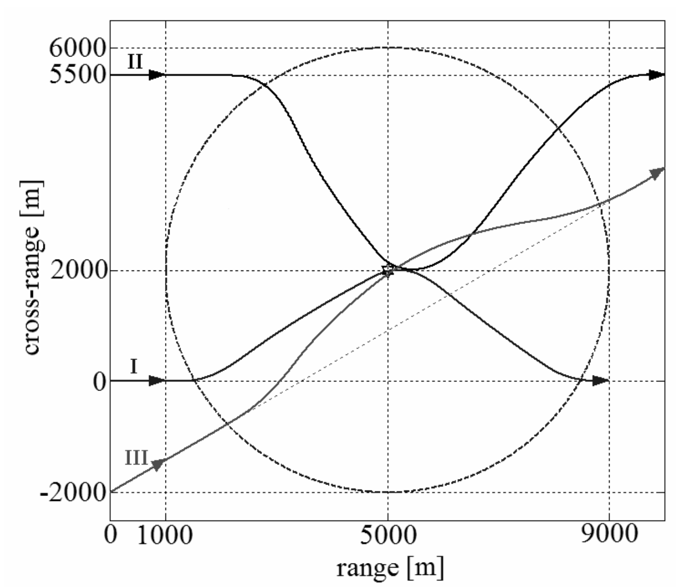

Figure 160. Lateral Tracks for the Fixed Ground Target Attack Maneuvers

As it is mentioned before, during the fixed ground target attack maneuvers the attitude controller which is designed in Chapter 4.3 is used. Here, the yaw attitude command (ψ_d) is generated using the proposed defense zone maneuvering algorithm. Also, the time rate of change of the yaw attitude command ($\dot{\psi}_d$) can be generated from the same algorithm as a by-product and used to calculate the roll attitude command (ϕ_d). Here, it is assumed that the aircraft makes coordinated turn maneuvers (also discussed in Chapter 2.1) and the commanded roll angle of the aircraft during that maneuver is calculated by using $\phi_d = \tan^{-1}(V_T\dot{\psi}_d / g)$. Also, the pitch attitude command (θ_d) is generated in order to increase the altitude and avoid getting closer to the target at the center of the zone.

The time histories of the total velocity, the angle of attack, the side slip angle, the roll, pitch and yaw angles, the thrust-vectoring paddle deflections and aerodynamic control surfaces are shown in the following figures. Here, since it acquires more rapidity, the results of Case I are presented.

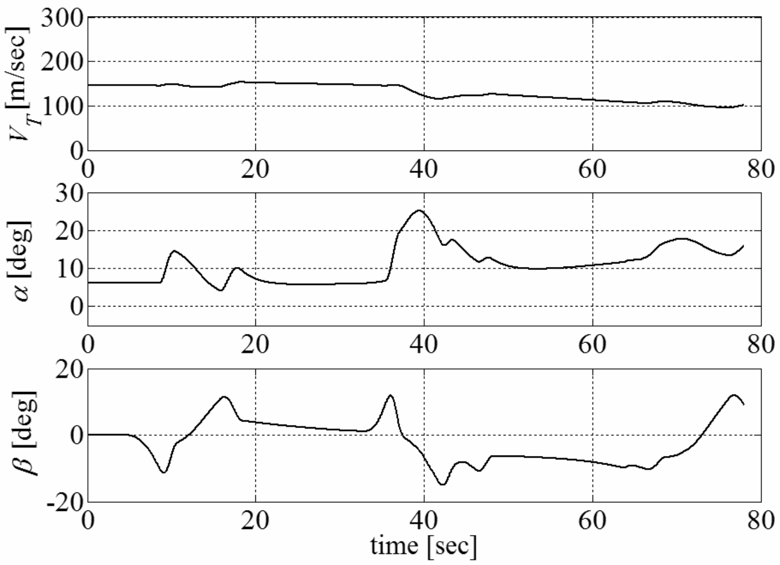

Figure 161. Fixed Ground Target Attack Maneuver Results for V_T, α, β

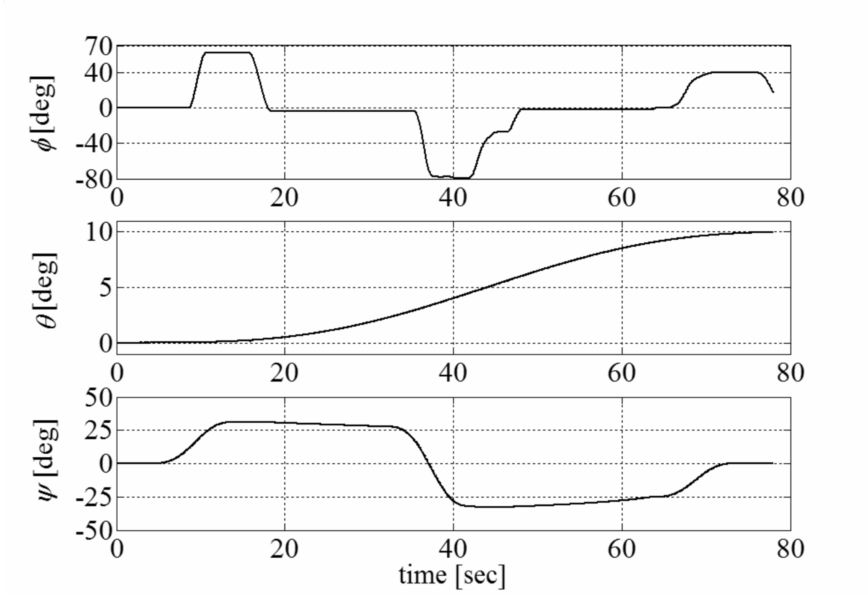

Figure 162. Fixed Ground Target Attack Maneuver Results for ϕ, θ, ψ

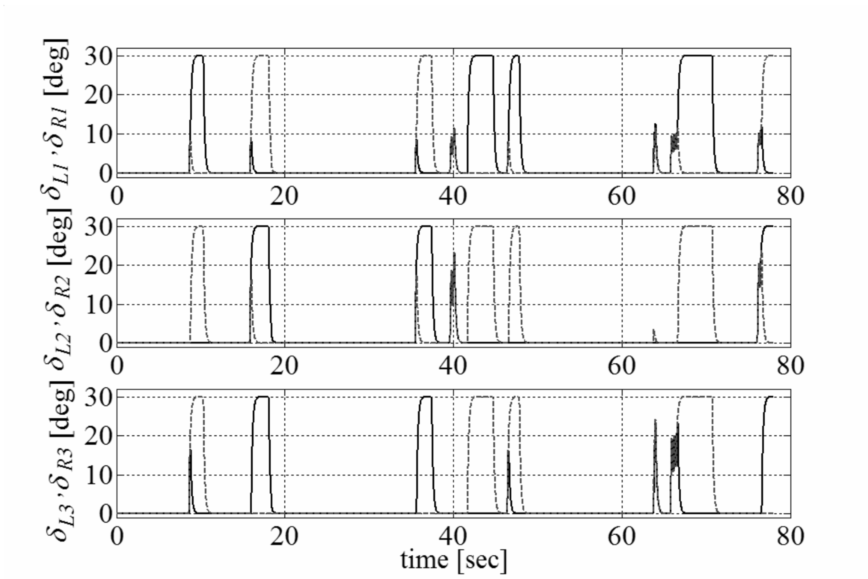

Figure 163. Fixed Ground Target Attack Maneuver Results for δ_L and δ_R

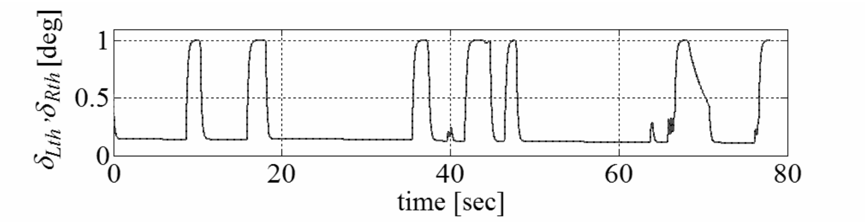

Figure 164. Fixed Ground Target Attack Maneuver Results for δ_{th}

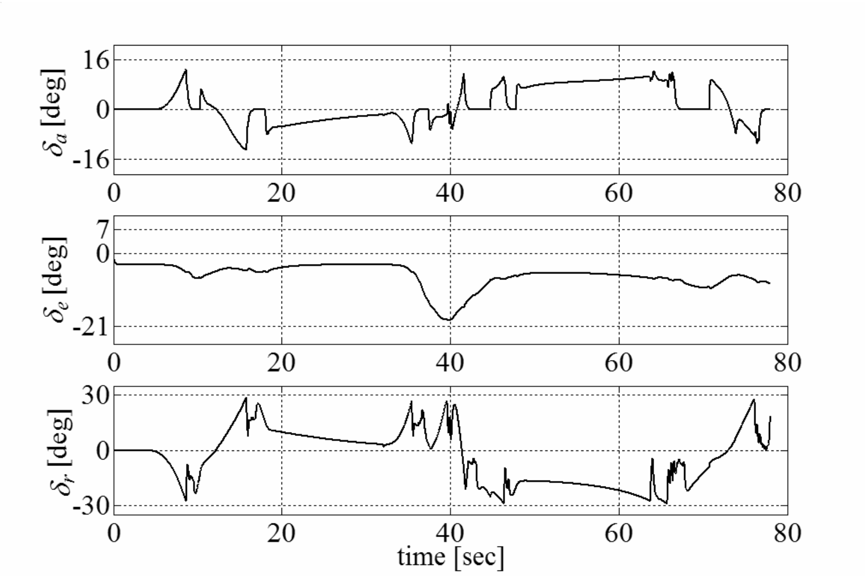

Figure 165. Fixed Ground Target Attack Maneuver Results for δ_a, δ_e, δ_r

6.5. The Offensive BFM - Tail Chaise Acquisition Maneuvers

The offensive BFM are very important for effectively directing the guns and the missiles towards the opponent aircraft. In that case, the target aircraft makes series of aggressive s-turns and tries to stay in non-line of sight. Thus, in order to maintain air-superiority in such a scenario, the attack aircraft should perform agile roll maneuvers to capture the target and keep it in line of sight (LOS) repeatedly.

In order to simulate that scenario a target aircraft is introduced in the simulations and programmed to fly a pre-defined s-turn trajectory. Thus, it tries to get away from the offensive aircraft with decreasing the probability of a possible target lock. The target aircraft is modeled and simulated as a point mass flown by steering its velocity vector in the lateral and vertical flight path. The pre-programmed desired flight path angles of the target are:

$$\gamma_{ztd}(t) = \gamma_{zref}(\sin(2\pi \frac{t}{t_{z\max}}) + \sin(4\pi \frac{t}{t_{z\max}}) + \sin(14\pi \frac{t}{t_{z\max}})) \tag{6.14}$$

$$\gamma_{ytd}(t) = \gamma_{yfinal}(\frac{t}{t_{y\max}} - \frac{1}{2\pi}\sin(2\pi \frac{t}{t_{y\max}})) \tag{6.15}$$

Here, $\gamma_{zref} = 45^\circ$, $\gamma_{yfinal} = -20^\circ$ and $t_{z\max} = 100\,\text{sec}$ and $t_{y\max} = 55\,\text{sec}$.

The desired flight path angles are filtered using first order low-pass filters ($f_n = 1\,\text{Hz}$) in order to account for the vertical and lateral flight path dynamics of the target aircraft. Thus, the flight path angles of the target are calculated:

$$\dot{\gamma}_{zt}(t) = (2\pi f_n)(\gamma_{ztd}(t) - \gamma_{zt}(t)) \tag{6.16}$$

$$\dot{\gamma}_{yt}(t) = (2\pi f_n)(\gamma_{ytd}(t) - \gamma_{yt}(t)) - \frac{g}{V_{Tt}}\cos(\gamma_{yt}(t)) \tag{6.17}$$

The effect of the gravitational acceleration is also included in the vertical flight path angle dynamics. Here, g is the gravity and V_{Tt} is the total velocity of the target aircraft. The total velocity of the target aircraft is calculated using $V_{Tt} = V_T + 30$. Here, it is assumed that the speed of the target aircraft is 30 m/sec higher than the attack aircraft in every situation.

The velocity components of the target aircraft are calculated by using V_{Tt} and $\gamma_{zt}(t), \gamma_{yt}(t)$:

$$\dot{x}_t(t) = \cos(\gamma_{yt}(t))\cos(\gamma_{zt}(t)) \tag{6.18}$$

$$\dot{y}_t(t) = \cos(\gamma_{yt}(t))\sin(\gamma_{zt}(t)) \tag{6.19}$$

$$\dot{z}_t(t) = -\sin(\gamma_{yt}(t)) \tag{6.20}$$

Hence, integrating the velocity components the position of the target aircraft can be calculated.

Knowing the position of the target aircraft the desired pitch and yaw angles (the line of sight angles) in order to point the target aircraft can be calculated:

$$\psi_d = \tan^{-1}(\Delta y, \Delta x) \tag{6.21}$$

$$\theta_d = \tan^{-1}(-\Delta z, (\Delta x^2 + \Delta y^2)^{1/2}) \tag{6.22}$$

Here, $\Delta x, \Delta y$ are the lateral components and Δz is the vertical component of the distance between the positions of the target and the attack aircraft and calculated from $[\Delta x\ \Delta y\ \Delta z]^{\mathrm{T}} = [x_t\ \ y_t\ \ z_t]^{\mathrm{T}} - [x_b\ \ y_b\ \ z_b]^{\mathrm{T}}$.

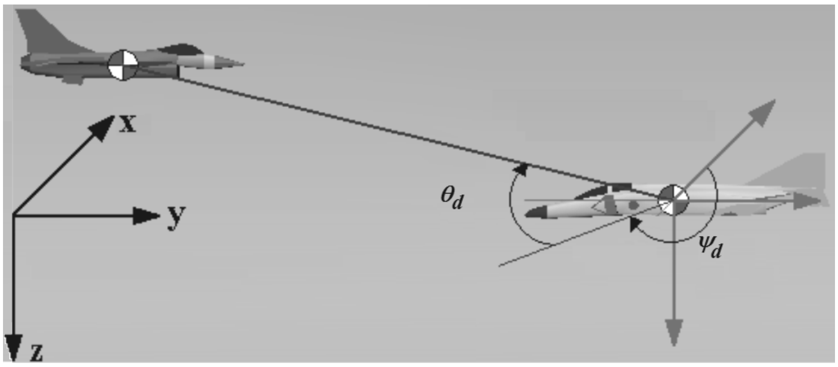

Figure 166. The Pointing Geometry and LOS Angles

Hence, the pitch and yaw angle errors (that will be fed to the attitude controller) are calculated, i.e. $\theta_e(t) = \theta_d(t) - \theta(t)$ and $\psi_e(t) = \psi_d(t) - \psi(t)$. Here, ψ_e should be modified in order to achieve the short-cut steering. For example, if the yaw angle error is greater then 180° or less than -180°, ψ_e is modified for the shorter way turn:

$$\psi_e = \begin{cases} \psi_d(t) - \psi(t) - 2\pi, & \psi_d(t) - \psi(t) > \pi \\ \psi_d(t) - \psi(t), & \psi_d(t) - \psi(t) \leq \pi \ and\ \psi_d(t) - \psi(t) \geq -\pi \\ \psi_d(t) - \psi(t) + 2\pi, & \psi_d(t) - \psi(t) < -\pi \end{cases} \tag{6.23}$$

For the tail chase acquisition maneuver simulations the attitude controller described in Chapter 3.2 and designed in Chapter 4.3 is used. The simulations are started from the initial condition at which the attack aircraft is at 5,000 m altitude at 0.45 Mach at wings level flight. Initially the target and the attack aircraft are at the same altitude and the initial lateral position components of the aircrafts are $[x_0\ y_0]^T = [0\ 0]^T$ and $[x_{t0}\ y_{t0}]^T = [-1{,}000\ 0]^T$ m. The simulation results for the lateral and vertical tracks of the target and attack aircrafts are shown in the following figures.

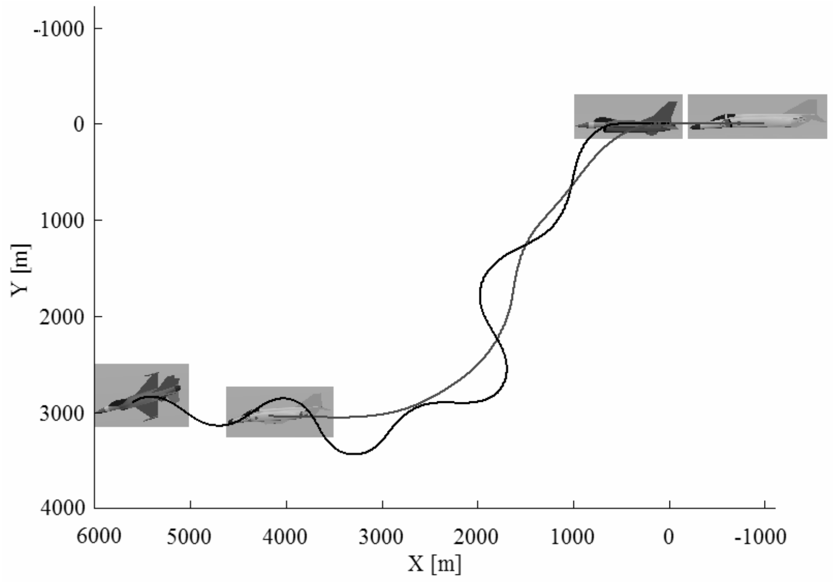

Figure 167. Lateral Track of the A/C for the Tail Chase Acq. Maneuver

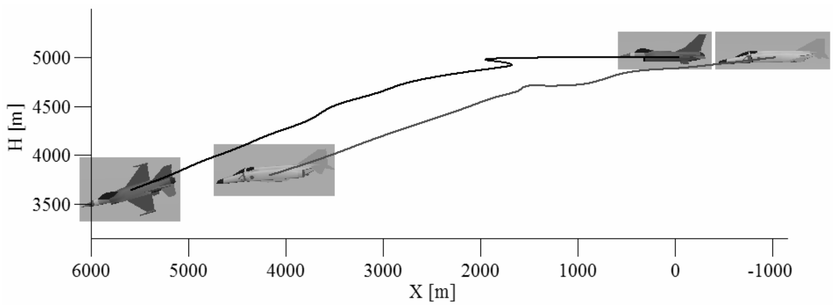

Figure 168. Vertical Track of the A/C for the Tail Chase Acq. Maneuver

The line of sight vectors during the maneuver are shown in the following figure.

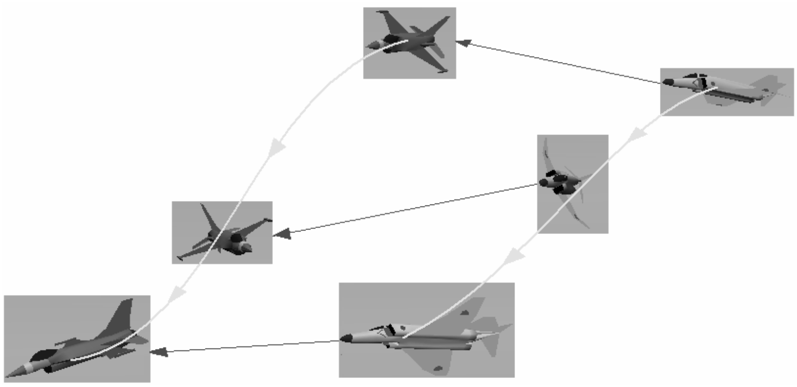

Figure 169. Tail Chase Acquisition between the Two Aircrafts

The tail chase acquisition maneuver simulation is done for 1 min. During the simulation the aircrafts positions and attitudes are interconnected with a virtual reality modeling environment to visualize the performance of the pointing control. In the following figure the snap-shots of the aircrafts at different times of the simulation can be seen. The pictures on the right hand side of the figure are the visualizations from a virtual camera assumed to be aligned with the attack aircraft and mounted behind its tail.

Figure 170. The Snap-shots from the Tail Chase Acquisition Simulation

During the tail chase acquisition maneuvers ψ_d and θ_d are generated using equation (6.21) and equation (6.22). Also, the desired roll attitude of the aircraft is left free with maintaining $\dot{\phi}_d = 0$. The time histories of the total velocity, the angle of attack, the side slip angle, the roll, pitch and yaw angles, the thrust-vectoring paddle deflections and aerodynamic control surfaces of the attack aircraft for the tail chase acquisition maneuver simulation are shown in the following figures.

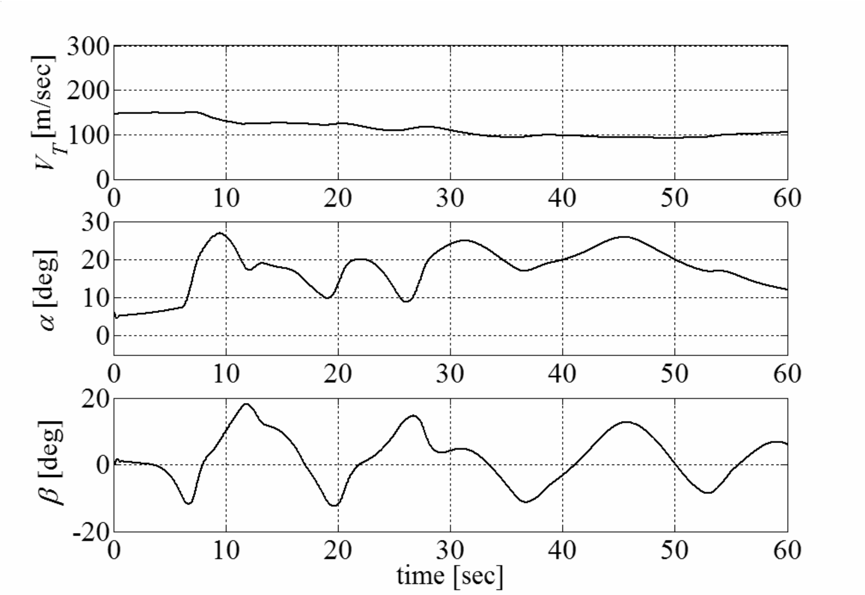

Figure 171. Tail Chase Acquisition Maneuver Results for V_T, α, β

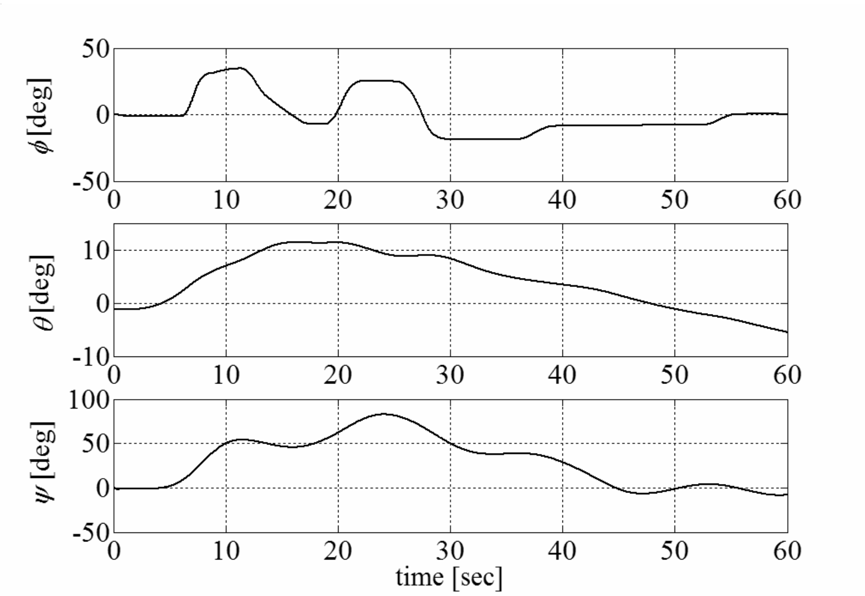

Figure 172. Tail Chase Acquisition Maneuver Results for ϕ, θ, ψ

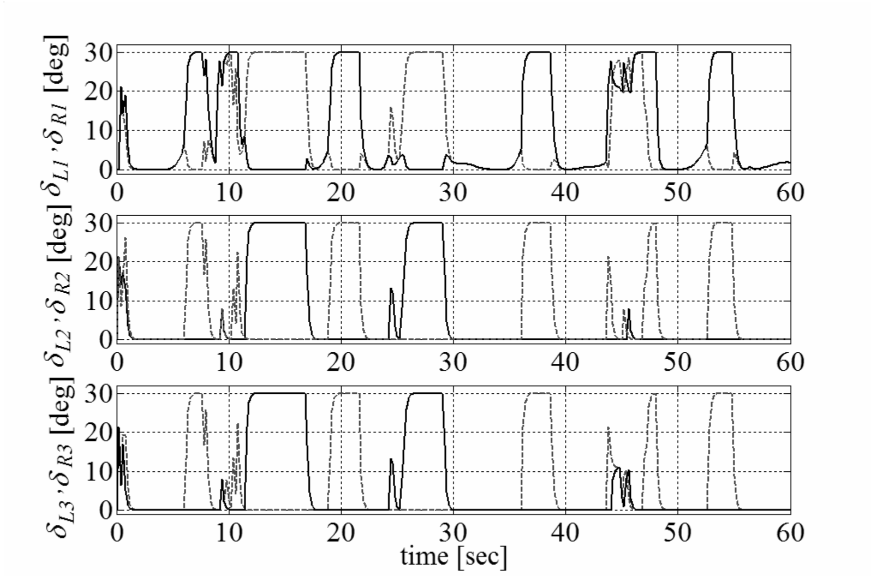

Figure 173. Tail Chase Acquisition Maneuver Results for δ_L and δ_R

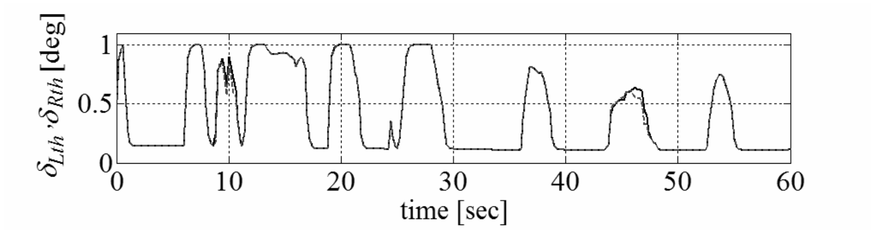

Figure 174. Tail Chase Acquisition Maneuver Results for δ_{th}

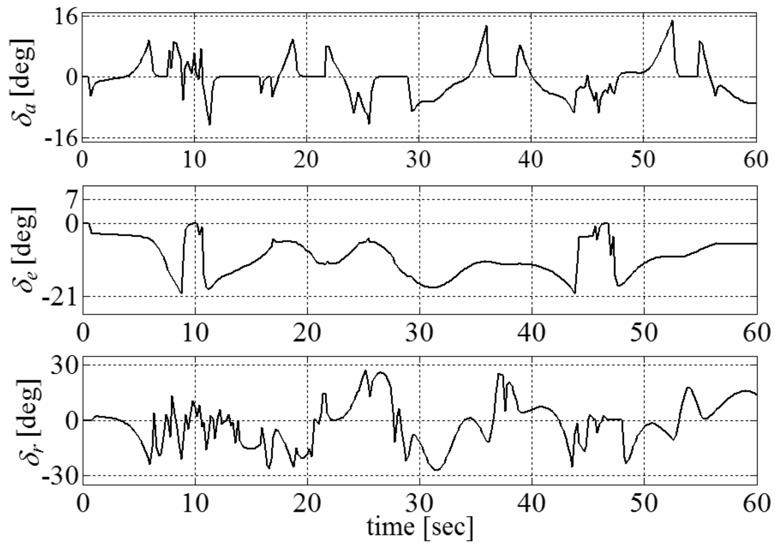

Figure 175. Tail Chase Acquisition Maneuver Results for δ_a, δ_e, δ_r

6.6. The Head-on BFM - Target Aircraft Pointing Maneuvers

As it is mentioned in Chapter 6.2 Herbst maneuver is used for aggressive coupled motion of the aircraft both in pitch and yaw planes of motion. The aim of the maneuver is to perform a heading reversal with desired pitch motion in a comparably short amount of time. Thus, the attack aircraft can direct the armament towards the target aircraft in a head to head close air combat.

In order to simulate that scenario, similar to the tail chase acquisition maneuver described in the previous chapter, a target aircraft is programmed to fly a pre-defined aggressive escape maneuver. Thus, it tries to decrease the probability of target lock rapidly. The pre-programmed desired flight path angles of the target are:

$$\gamma_{ztd}(t) = -9\frac{\gamma_{zref}}{t_{z\max}}(1-\cos(2\pi\frac{t}{t_{z\max}})) + \pi \tag{6.24}$$

$$\gamma_{ytd}(t) = \gamma_{yfinal}\left(\frac{t}{t_{y\max}} - \frac{1}{2\pi}\sin(2\pi\frac{t}{t_{y\max}})\right) \tag{6.25}$$

Here, $\gamma_{zref} = 30^\circ$, $\gamma_{yfinal} = -25^\circ$ and $t_{z\max} = 10$ sec and $t_{y\max} = 10$ sec. Also, the desired flight path angles are filtered using first order low-pass filters ($f_n = 1$ Hz) and the flight path angles of the target are calculated using equation (6.16) and equation (6.17). The total velocity of the target aircraft is chosen as $V_{Tt} = 250$ m/sec. The velocity components of the target aircraft are calculated by using equation (6.18) to equation (6.20) and integrating them the position of the target aircraft can be calculated. Knowing the position of the target aircraft the desired pitch and yaw line of sight angles can be calculated using equation (6.21) and equation (6.22). Hence, the pitch and yaw angle errors ($\theta_e(t), \psi_e(t)$) are calculated as mentioned in the previous chapter.

Here, ψ_e is modified in order to achieve the short-cut steering. However, in some cases it is necessary to make the long-way turn. For example, if the target aircraft is approaching towards the tail of the attack aircraft, although it is on the right or left side of the aircraft, it is proper to turn from the opposite side. The following figure is showing such cases.

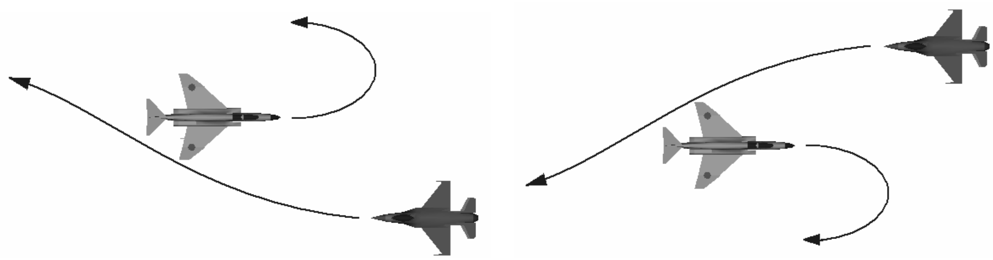

Figure 176. Left or Right Turn Decision

This situation is handled by implementing the following logic in the simulations:

$$\begin{cases} \text{turnRight}\,, \pi/2 < \psi_{e0} < \pi \\ \text{turnLeft}\ , \quad \text{otherwise} \end{cases} \tag{6.26}$$

$$\begin{cases} \qquad \psi_d \qquad\qquad , \text{turnRight} \\ \psi_d + 2\pi\,\text{sign}(\psi_d),\ \text{turnLeft} \end{cases} \tag{6.27}$$

Here, ψ_{e0} is the yaw angle error at the beginning of the capture maneuver.

For the target aircraft pointing maneuver simulations the attitude controller described in Chapter 3.2 and designed in Chapter 4.3 is used. The simulations are started from the initial condition at which the attack aircraft is at 5,000 m altitude at 0.75 Mach at wings level flight. Initially the altitude of the target aircraft is 6,000 m and the initial lateral position components of the aircrafts are $[x_0\ \ y_0]^{\mathrm{T}}$ = $[-1{,}000\ 0]^{\mathrm{T}}$ and $[x_{t0}\ \ y_{t0}]^{\mathrm{T}}$ = $[2{,}500\ -1{,}000]^{\mathrm{T}}$ m.

Before the start of the maneuver the range between the target and the attack aircraft is repeatedly observed. Whenever the range is less than or equal to 1,500 m the attack aircraft observes the route of the target for one second (for left or right turn decision) and starts performing the maneuver. At the beginning of the maneuver the pilot manually pulls-up the aircraft (using the elevator only) to high angle of attack values climbing from the initial altitude. The simulation results for the lateral and vertical tracks of the target and attack aircrafts are shown in the following figures.

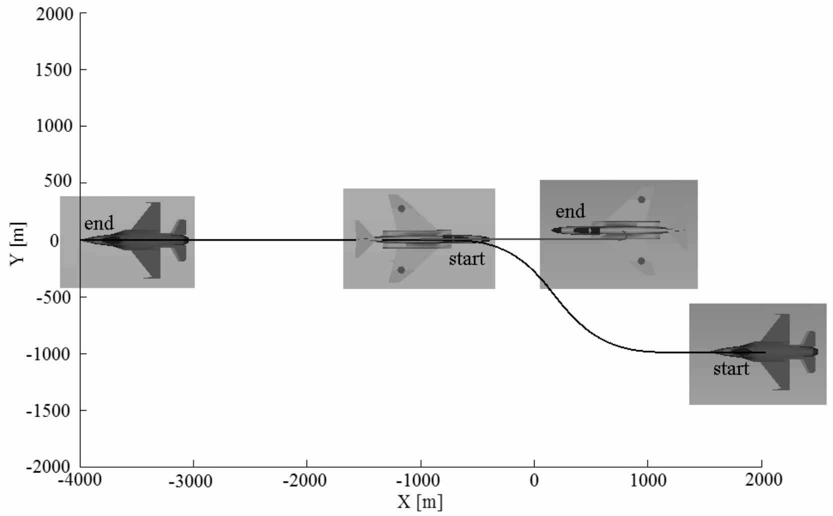

Figure 177. Lateral Track of the A/C for the Target A/C Point. Maneuver

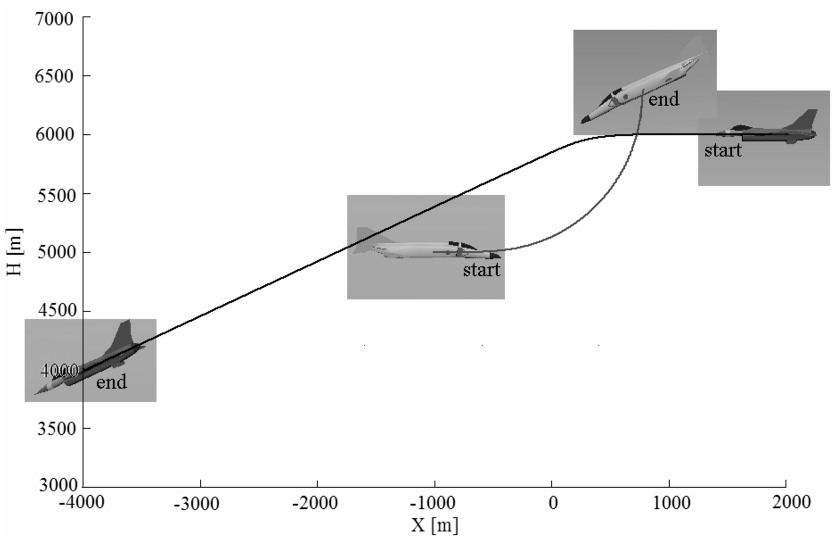

Figure 178. Vertical Track of the A/C for the Target A/C Point. Maneuver

The target aircraft pointing maneuver simulation is done for 30 seconds. During the simulation the aircrafts positions and attitudes are interconnected with a virtual reality modeling environment to visualize the performance of the pointing control. In the following figure the snap-shots of the aircrafts at different times of the simulation can be seen. The pictures on the right hand side of the figure are the visualizations from a virtual camera assumed to be aligned with the attack aircraft and mounted behind its tail.

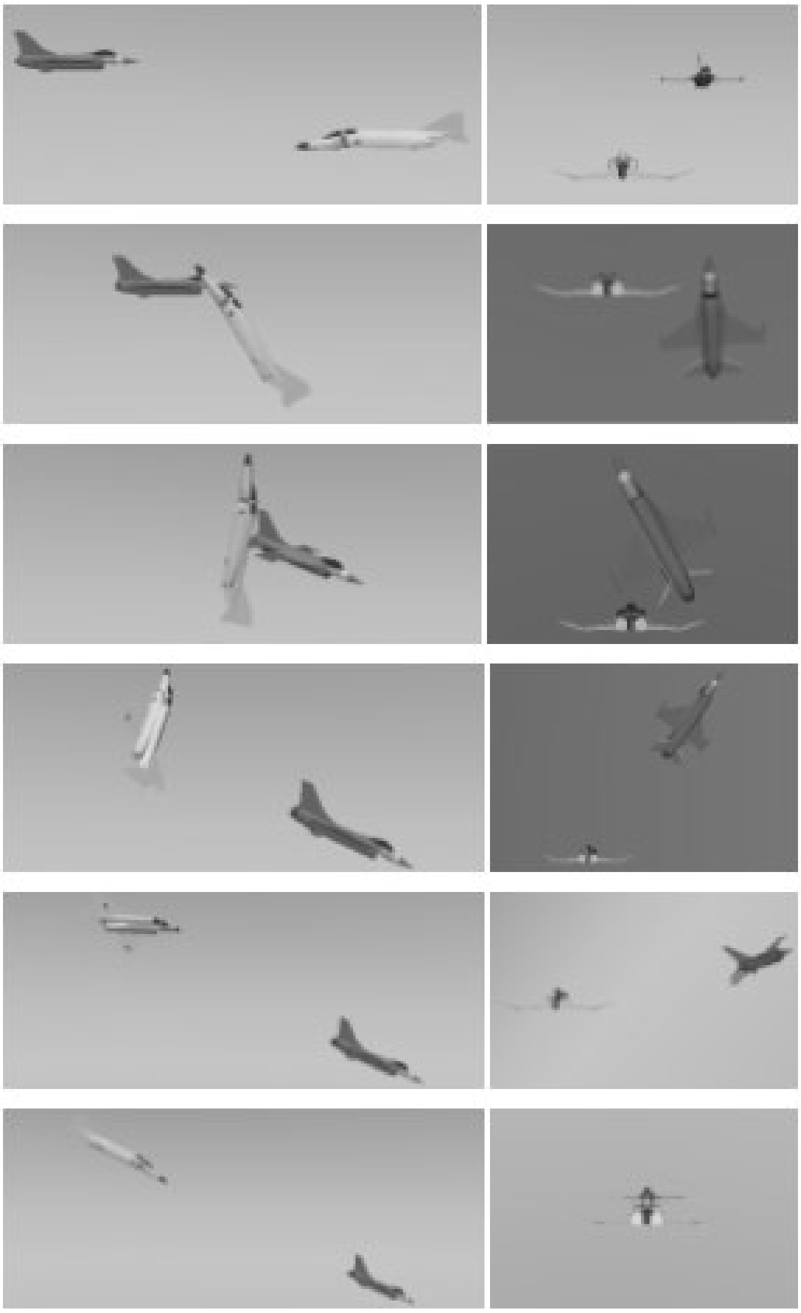

Figure 179. The Snap-shots from the Target A/C Point. Maneuver

During the target aircraft pointing maneuvers ψ_d and θ_d are generated using equation (6.21) and equation (6.22). Also, the desired roll attitude of the aircraft is commanded maintaining $\phi_d = 3\dot{\psi}_d$. The time histories of the total velocity, the angle of attack, the side slip angle, the roll, pitch and yaw angles, the thrust-vectoring paddle deflections and aerodynamic control surfaces of the attack aircraft for the target aircraft pointing maneuver simulation are shown in the following figures.

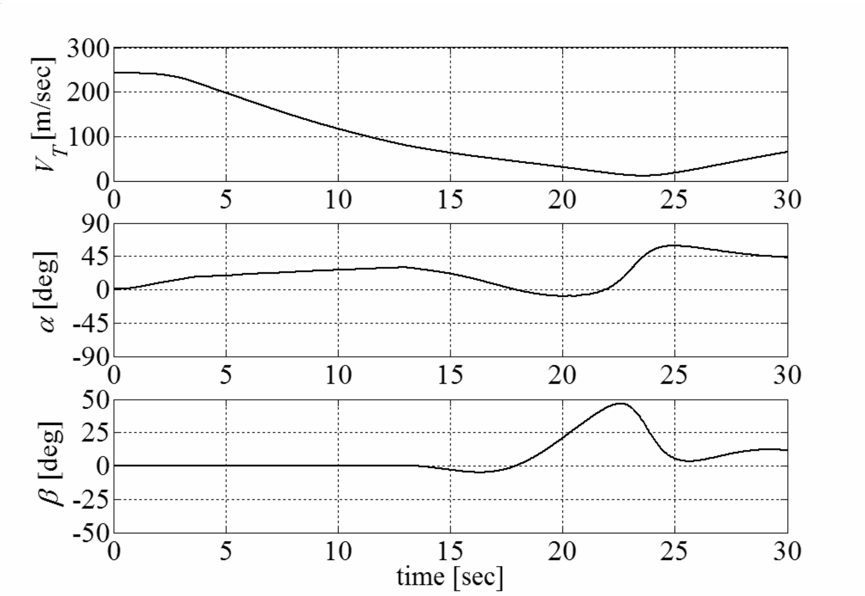

Figure 180. Target A/C Point. Maneuver Results for V_T, α, β

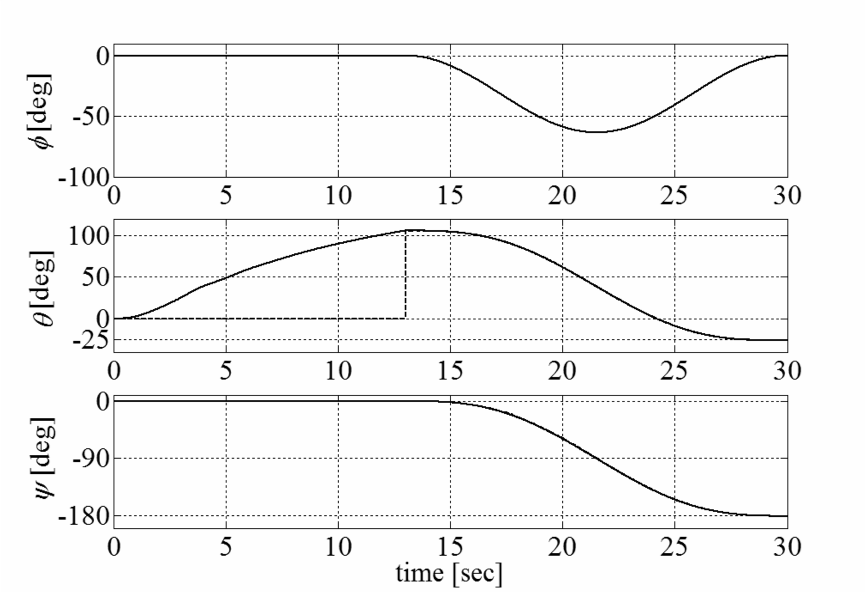

Figure 181. Target A/C Point. Maneuver Results for ϕ, θ, ψ

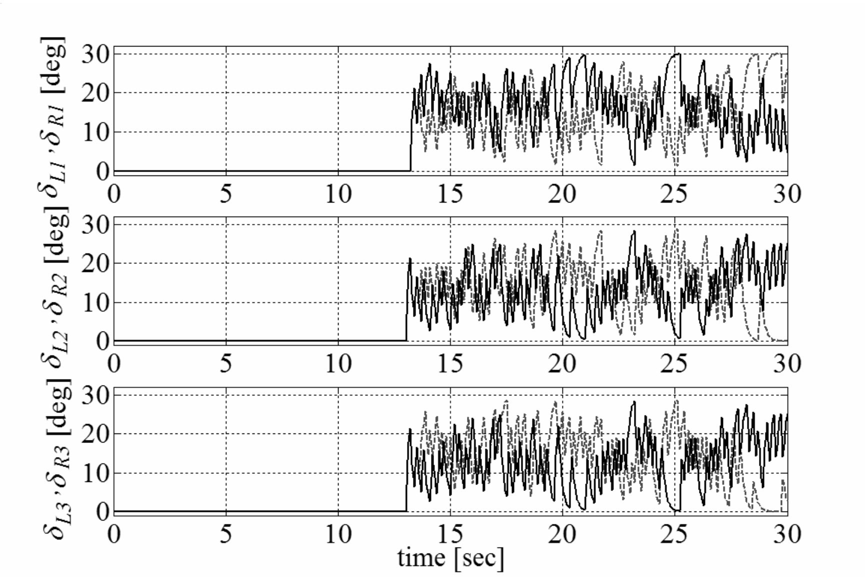

Figure 182. Target A/C Point. Maneuver Results for δ_L and δ_R

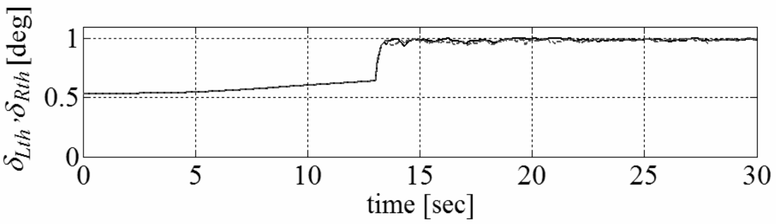

Figure 183. Target A/C Point. Maneuver Results for δ_{th}

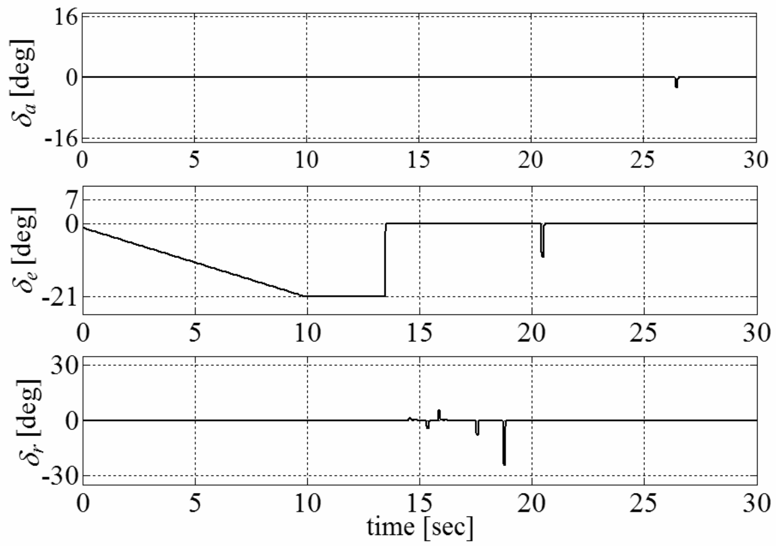

Figure 184. Target A/C Point. Maneuver Results for $\delta_a, \delta_e,\ \delta_r$

Here, note that, almost the entire pointing maneuver is performed by using the TVC. The aerodynamics surfaces are retracted to their neutral positions since the commands generated by using the aerodynamic surface controller (Chapter 3.2) are saturated most of the time throughout the maneuver.

The target aircraft pointing maneuvers are generally done under the control of the pilot rather than performing them with the autopilot. Thus, in order to investigate the effect of human pilot interaction on the pointing maneuver performance human pilot model integrated simulations are done. The human pilot model (described in Chapter 2.8) is integrated in the control loop. However, the desired control loop design parameters are adjusted according to Table 3. These parameters are already designed to maintain the robustness of the attitude control loop as mentioned in Chapter 4.3 before.

The time histories of the total velocity, the angle of attack, the side slip angle, the roll, pitch and yaw angles, the thrust-vectoring paddle deflections and aerodynamic control surfaces of the attack aircraft for the human pilot integrated target aircraft pointing maneuver simulation are shown in the following figures.

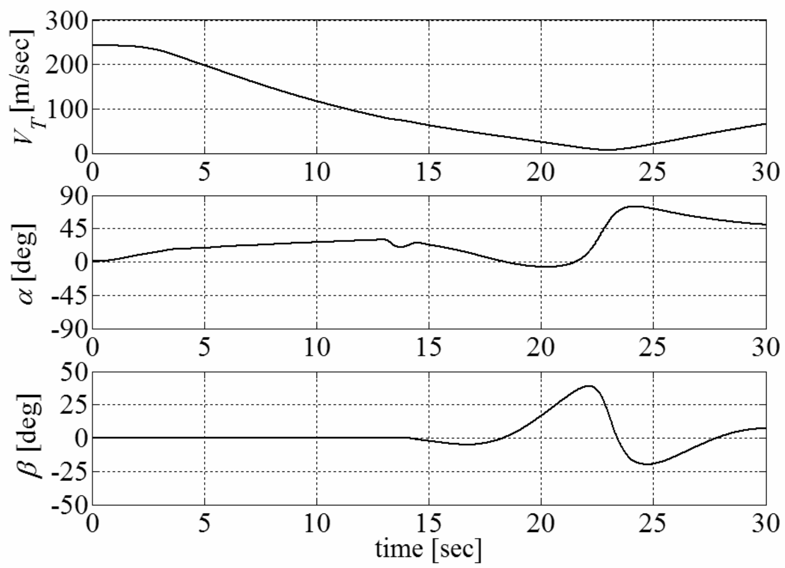

Figure 185. H/P Integrated Target A/C Point. Maneuver Results for V_T, α, β

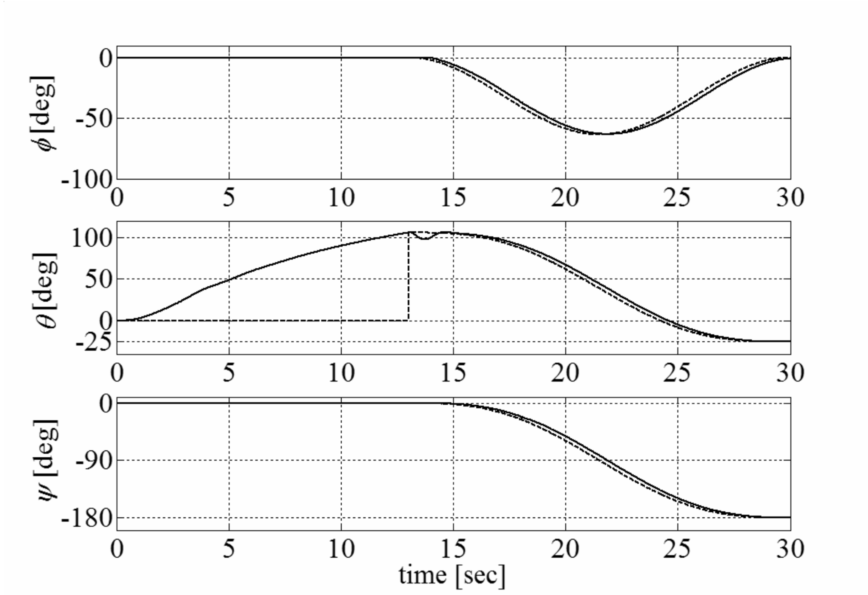

Figure 186. H/P Integrated Target A/C Point. Maneuver Results for ϕ, θ, ψ

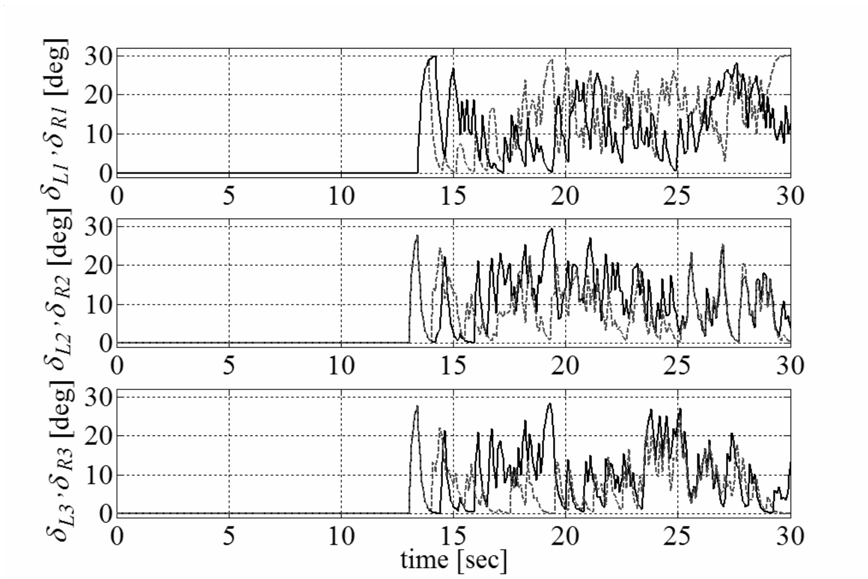

Figure 187. H/P Integrated Target A/C Point. Maneuver Results for δ_L and δ_R

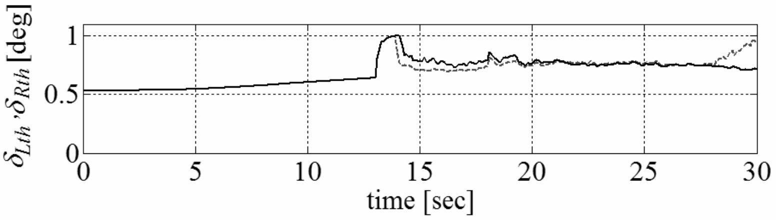

Figure 188. H/P Integrated Target A/C Point. Maneuver Results for δ_{th}

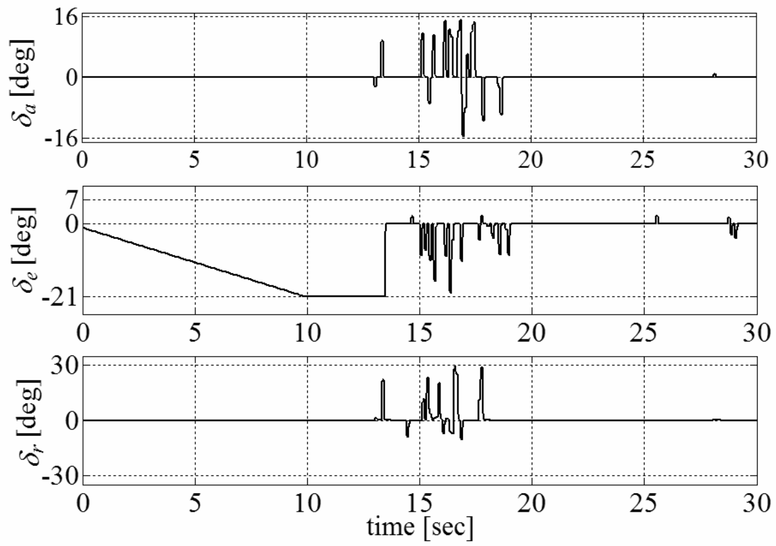

Figure 189. H/P Integrated Target A/C Point. Maneuver Results for δ_a, δ_e, δ_r

As for the human pilot integrated simulations, again, most of the pointing maneuver is performed by using the TVC. Only at the beginning of the maneuver the aerodynamic control surfaces are used. The performance of the maneuver, as expected, is not good as it was in the autopilot case. Nevertheless, the pilot manages to recover the target aircraft exactly at the end of the maneuver. During the transient phase of the maneuver the desired line of sight angle commands are tracked with certain latency originating from the neuro-motor lag and pure time delay of the pilot. Here, also note that, the noise of the sensors and the noise originating from the engine are also integrated in the simulations (both the autopilot and human pilot). All of these noise signals are zero mean white noise and their standard deviations are $\sigma_{\phi\,std} = \sigma_{\theta\,std} = 0.3^\circ$, $\sigma_{\psi\,std} = 0.1^\circ$, $\sigma_{p\,std} = \sigma_{q\,std} = \sigma_{r\,std} = 1^\circ$/hr and $\sigma_{\phi e\,std} = \sigma_{\theta e\,std} = \sigma_{\psi e\,std} = 0.5^\circ$.

CHAPTER 7

DISCUSSION AND CONCLUSION

In this study the stabilization and maneuvering control of aircraft at high angle of attack flight regimes are dealt with. The proposed control structures are applied on a two engine fighter-bomber aircraft implementing different flight scenarios. The simulation scenarios are divided into two main parts as the stabilization and recovery from undesired high angle of attack flight and the desired high angle of attack flight for defensive and offensive maneuvering.

The study starts with the detailed modeling of the aircraft. The aircraft kinematics and dynamics is described. Here, the effect of engine angular momentum is also included since the two engines of the aircraft under study are spinning at high velocities in the same direction to maintain the interchangeability purpose. After the dynamic modeling the detailed aerodynamic modeling of the aircraft including the high angle of attack effects is studied. The high angle of aerodynamics is very important for a super-maneuverable fighter aircraft. The ability to control the aircraft at high angle of attack maneuvering and flight without departure are the major concerns. In the same section the stall prediction parameters $C_{n\beta dyn}$ and *LCDP* are also introduced and their importance on stall, post-stall and deep-stall indication is described on the Bihrle-Weissmann chart. This chart indicates the stall resistant and weak regions based on the angle of attack values in different regimes of flight. The aerodynamic coefficients of the aircraft are highly nonlinear and divided into three different groups for different angle of attack values ranging from $\alpha = -15^{\circ}$ to $\alpha = 55^{\circ}$ and beyond. Using these values the stall, post-stall and deep-stall regions of the aircraft under study is defined on the integrated Bihrle-Weissmann chart. The engine model of the aircraft is modeled using the dynamics of the commanded (P_c) and actual (P_a) power and the engine time constant (τ_{eng}). The total thrust of the engine is based on P_a and the idle, military, and maximum thrust values that are the functions of the instantaneous Mach number and altitude. The thrust vectoring paddles are used in order to deviate the total thrust of the engines and achieve TVC. The three paddles are moved in conjunction with each other and their resultant effect deviate the total thrust in the lateral and vertical directions with respect to the body of the aircraft. Each paddle is modeled to move 30° at most and using the coordinated movement of the paddles the thrust deviation angles envelope is formed.

In Chapter 2, the flight environment of the aircraft is also modeled. Here, the *Dryden* wind turbulence model in longitudinal, lateral and vertical directions are used. The turbulence intensities are determined from a lookup table that gives the turbulence intensity as a function of altitude and the probability of the exceeded turbulence intensities. Also, in order to assess the aircraft response to large rotation rate disturbances, a discrete rate gust model in the form of standard "1-cosine" shape is implemented.

In the same chapter, the detailed modeling of the onboard sensors is also conducted. Here, INS, IMU and the AoA, the sideslip sensors are introduced with their dynamic and error modeling. The modeling of accelerometers and gyroscopes are also described since they are the prime elements of the INS or the IMU. The error sources both in deterministic and stochastic nature are defined and their effects on the measurements are defined. As for the stochastic error sources the definition of some shaping filter configurations for process modeling are given. The detailed models of the AoA and side slip sensors are constructed and different types of angle sensors including flow vanes, fixed pressure probes and servo actuated pressure probes are introduced. Finally, in the same chapter, the human pilot model is constructed. The pilot is modeled as a compensatory man-machine interface. This model is composed of the pilot compensation gain (K_c), pure time delay (τ_d), approximated as a second order Padé approximation, and a neuro-motor lag (τ_n) of the human operator.

Chapter 3 is dedicated to nonlinear inverse dynamics (NID) control structure design. In this chapter, NID controller design based on the thrust vectoring controls is presented. The constraining equation which is effective on the used control effectors (thrust vectoring paddles) is described and this constraint leads to two different controller designs; the stabilization controller and the attitude controller. The stabilization controller is designed to stabilize the aircraft and recover it from the undesired high angle of attack flight regimes. Thus, it especially works on the flight angles; i.e. AoA and the side slip angle. As for the attitude controller, it is designed to rapidly maneuver the aircraft in the high angle of attack flight. Consequently, it directly controls the attitude angles of the aircraft; the roll, pitch and yaw angles. The chapter is concluded with the explanation of the blending of the TVC with the conventional aerodynamic control effectors; i.e. the aileron, elevator and rudder.

As a following work, the robust performance analysis of the designed controllers is conducted in Chapter 4. In the first part of the chapter the trim analysis and the linearization is discussed. For that purpose a special trimming algorithm is generated. This algorithm calculates the trim values of total the thrust (T_0), the angle of attack (α_0), the side slip angle (β_0), the angle of aileron (δ_{a0}), elevator (δ_{e0}) and rudder (δ_{r0}) deflections for $\dot{u} = \dot{v} = \dot{w} = \dot{p} = \dot{q} = \dot{r} = 0$ at the desired altitude (h_0), Mach number (M_0), pitch angle (θ_0), roll angle (ϕ_0) and body angular velocities (p_0, q_0, r_0). The algorithm reduces the Newton-Euler equations describing the dynamics of the aircraft (defined in Chapter 2) to a nonlinear set of coupled static equations, i.e. the trim equations. These equations are solved by using the Newton-Raphson method. Here, it is noted that, since the equations are nonlinear there are possibilities for the existence of the multiple solutions. In order to handle the “right” solution some conditional checks are introduced and integrated into the solution algorithm. As explained before, the nonlinear aerodynamic coefficients are described in three different intervals. In the solution of the trim equations the multiple trim angle of attack (α_0) solutions are checked if they are really in the same interval in which the solutions are carried out. The solution that matches with its corresponding interval is chosen as the right solution. There are some cases that the algorithm finds more than one match. If this is the case, the smallest matched solution is counted for the right solution. There are also some cases that the algorithm could not find any matching α_0 solution and the aircraft cannot be trimmed at that desired flight condition. In the tailoring of the trim algorithm, the trim values of the aerodynamic surface deflections are also checked if they are in the designated intervals. Similarly, the trim value of the actual power level (P_{a0}) is checked to be less than or equal to 100%. Applying the proposed trim procedure the wings level flight envelope for the aircraft is constructed. This trim algorithm is used to find the equilibrium point around which the nonlinear aircraft dynamics is linearized. This linear dynamics is used in the robust performance analysis.

The robust performance analysis is done by using the nonlinear total plant composed of the NID, TVC, Engines, TVC paddles, Aero NID and the Aero Control plants. Applying the trim algorithm and linearization on this nonlinear total plant gives the transfer matrices that relate the perturbed body accelerations ($\Delta\dot{u}, \Delta\dot{v}, \Delta\dot{w}, \Delta\dot{p}, \Delta\dot{q}, \Delta\dot{r}$) to the perturbed body velocities ($\Delta u, \Delta v, \Delta w, \Delta p, \Delta q, \Delta r$) both for the stabilization and the attitude controllers. In order to test the linearization the calculated transfer matrices ($\hat{G}_{nom}^{sta}(s)$, $\hat{G}_{nom}^{att}(s)$) are simultaneously simulated with the compact nonlinear dynamics with the same $\dot{u}_{com}, \dot{v}_{com}, \dot{w}_{com}$ and $\dot{p}_{com}, \dot{q}_{com}, \dot{r}_{com}$ inputs and the results are presented graphically. The results are very satisfactory regarding that the nonlinear total plant outputs matched with the linear plant outputs. For the stabilization controller only the uncontrolled q output of

$\hat{G}_{nom}^{sta}(s)$ is not exactly the same with that of the nonlinear compact dynamics. However, they show similar characteristics and vary around the trim value $q_0 = 0$ in between $\pm 30^{\circ}$/sec. As for the attitude controller, w outputs of $\hat{G}_{nom}^{att}(s)$ and the compact nonlinear dynamics highly deviate from the trim value ($w_0 = 0$) and the uncontrolled w output of $\hat{G}_{nom}^{att}(s)$ differ from w output of the compact nonlinear dynamics. This is a presumable result since w output of $\hat{G}_{nom}^{att}(s)$ is highly deviated from its trim value and the linearized dynamics is no longer representing the nonlinear dynamics. After these series of analysis the uncertainty estimation for the robust performance analysis is done by dividing the compact nonlinear dynamics into two segments composed of nonlinear dynamic inversion and the nonlinear dynamics itself. For a proper inversion the identification of the parameters of the nonlinear dynamics is very crucial and the most important parameters of the nonlinear plant dynamics are the aerodynamic coefficients. However, there is certain estimation errors generally specified with percentages. This estimation error directly effects the commanded forces and moments ($\overline{F}_{com}^{(b)}$, $\overline{M}_{com}^{(b)}$) used in the NDI controller. This effect is directly seen on the commanded TVC paddle deflections and degrades the performance of the designed controller or even cause improper operation. Thus, the robustness of the designed controller to the uncertain aerodynamics is very crucial.

The uncertainty assignment is started with a very marginal assumption that the aerodynamic coefficients are completely unknown, i.e. $\overline{F}_a = \overline{M}_a = \overline{0}$. With this assumption the perturbed transfer matrices ($\hat{G}^{sta}(s)$, $\hat{G}^{att}(s)$) which are different than the nominal transfer matrices ($\hat{G}_{nom}^{sta}(s)$, $\hat{G}_{nom}^{att}(s)$) are calculated. For the stabilization controller plant, the transfer functions $q(s)/\dot{u}(s)$, $p(s)/\dot{p}(s)$ and $r(s)/\dot{r}(s)$ are strongly effected. As for the attitude controller plant, the transfer functions $p(s)/\dot{p}(s)$, $q(s)/\dot{q}(s)$, $w(s)/\dot{q}(s)$ and $r(s)/\dot{r}(s)$ are strongly effected.

Here, nearly 100% DC gain differences between the nominal and perturbed transfer functions are seen.

The differences between the perturbed and nominal transfer matrices are defined as the additive uncertainties related to the defined situation of totally uncertain aerodynamics, and, the robust performance analysis is done for the stabilization and attitude controllers.

The inspection on the structured singular value (μ), the robust stability and the nominal performance of the stabilization and the attitude controllers for the autopilot and human pilot cases showed that, for the totally uncertain aerodynamics case, the peak of the upper bound μ-plots are higher than 1.

Thus, the assigned total aerodynamic uncertainty alters the robust performance of the closed loop systems. The analysis obviously showed that the robust performance cannot be achieved for the controllers with $\overline{F}_a = \overline{M}_a = \overline{0}$. In order to achieve the robust performance the aerodynamic parameter uncertainty of the model should be decreased. Thus, the aerodynamic coefficient set is modified and 30% uncertainty, which is still very high, on the aerodynamic coefficients is assumed. Here, all of the aerodynamic coefficients except C_x are decreased to 70% of their nominal values and the analysis are repeated. In that case, for the same controller parameter sets, the upper bound μ-plots are calculated to be less than 1 both for the stabilization and attitude controllers and for A/P and H/P cases. Hence, the RP is achieved with the designed stabilization and attitude controllers for 30% aerodynamic capability degradation. The analysis is also verified by simulating the designed stabilization and attitude controllers for the A/P and H/P cases. All of these time domain simulation results showed that the designed controllers are stable and robust to the defined 30% aerodynamic uncertainties and the disturbances arising from the sensor and engine noises.

In Chapter 5, the performance of the stabilization controller is investigated. Here, the designed stabilization controller is used to stabilize the aircraft at high angle of attack flight in order to recover it from the dangerous stall regions using the TVC (since the aerodynamic control effectors are inoperative here). Thus, the controller will bring the aircraft to safer flight conditions and the pilot can use the aerodynamic controls to steer the aircraft. For that purpose, the aircraft is manually driven into stall by the application of a pull-up maneuver. Here, a special stall indication trigger is designed to start the operation of the stabilization controller. The stabilization controller commands the aircraft to the trim angle of attack values corresponding to the instantaneous flight velocity and altitude of the aircraft. Two different stabilization control strategies are studied here. First one is based on the stabilization of the rates of the Euler angles and the second one is based on tracking the desired Euler angles commands.

The logic of the stall indication trigger is based on the stall safe and critical regions of the Bihrle-Weissmann chart and the stall indication parameters; $C_{n\beta\,dyn}$ and $LCDP$. Throughout the motion of the aircraft both parameters are monitored and whenever $C_{n\beta\,dyn} \geq C_{n\beta\,dynT}$ and $LCDP \leq LCDP_T$ are achieved the stall stabilization controller is automatically started. Here, the subscript T denotes the values which are the upper most tolerable points for the stabilization controller to start. The stall stabilization controller is a hybrid controller composed of the attitude and stabilization controllers. In the first phase of the stable flight recovery maneuver from stall condition the body angular velocity components are nullified and the growths of the attitude angles are controlled. During this phase the attitude angles are continuously monitored. In the second phase of the stall stabilization the control switches the operation from the body angular velocity components to the angle of attack and side slip angle control. The aim of that phase is to get the aircraft into the aerodynamically controllable and stable flight condition. The angle of attack commands for that phase are the trim angle of attack values and the side slip angle commands are zero. The simulation results of the stabilization controller are also presented on the integrated Bihrle-Weissmann chart for the whole period of the stabilization maneuver. The tracks on the charts definitely show that the aircraft starts from a stall free region and then travels to stall and post-stall regions. At the mids of the post-stall region the designed stall trigger starts the operation of the stabilization controller and recovers the aircraft back to the stall free and safe flight regimes. In all of the simulations the air turbulence and the aerodynamic coefficient uncertainties are also included. Additionally, in order to present the performance of the lateral stabilization an additive sideward rate gust (r_g) is applied. The results of the simulations showed that in order to stabilize the aircraft under the stall conditions the designed stabilization controller can be used either to stabilize the angular velocity components or the attitude angles together with controlling the angle of attack and the side slip angles. In all cases it is necessary to stabilize the roll attitude of the aircraft to get the aircraft in wings level position at the end of the stall stabilization maneuver.

In Chapter 6, the performance of the attitude controller is investigated at various high angle of attack rapid maneuvers. The *Cobra* and *Herbst* maneuvers are treated as reference maneuvers and the performances of the TVC only and the aerodynamic controls only are analyzed. Under limited conditions, the desired Cobra maneuver can be achieved by using the aerodynamic control only. For example, for the simulated aircraft, the desired maneuver cannot be realized without the elevator deflection saturation beyond $\alpha = 23^\circ$. Hence, it is concluded that the elevator control is ineffective to realize the desired maneuver at higher values of angle of attack and therefore TVC should be used instead. As for the Herbst maneuver, the simulations have shown that the aerodynamic control by itself is totally unqualified. The highest angle of attack value that the second phase of the maneuver can be started and continued without saturations is $\alpha = 14^\circ$ and at that value the aircraft is not even in stall yet. Even then the desired complete heading reversal cannot be achieved, because the yaw rate commands are not necessary enough.

Both of the maneuvers are then simulated using the integrated TVC system. Integration of the thrust-vectoring paddles within the system created notably superior performance on the high angle of attack controllability and rapid maneuverability of the aircraft. It is observed that the recovery phase of the Cobra maneuver can be started even when the aircraft gets into deep stall and the pitch attitude can be commanded from a high value such as 105° to -5° rapidly at 18 seconds. As also observed, the heading reversal phase of the Herbst maneuver can be started even when $\alpha = 28^\circ$ and a complete heading reversal maneuver can be successfully realized. At the same time the pitch attitude can be commanded from a high value such as 101° to -12° again rapidly at 18 seconds.

Consecutively, different high angle of attack maneuver simulations are realized by the blended thrust vectoring and aerodynamics control effort. First of these maneuvers is the velocity vector roll maneuver which is known as a performance demonstrator maneuver of a successfully maneuvering fighter aircraft. In that maneuver the velocity vector roll angle (γ_x) should be commanded. Hence, here, the aircraft flight path angles ($\gamma_x, \gamma_y, \gamma_z$) and time rate of change of these angles ($\dot{\gamma}_x, \dot{\gamma}_y, \dot{\gamma}_z$) are calculated. Then on, the designed attitude controller, designed for the attitude angles, is adapted to the flight path angles and the commanded body angular rates are calculated. Afterwards, γ_x is commanded to perform a full turn (0° to 360°) in 19 seconds. Here, similar to the stall stabilization controller, a hybrid controller composed of the velocity vector roll attitude and angle of attack and side slip angle controllers are used by regulating $\dot{\alpha}$ and $\dot{\beta}$ for 9 seconds. At the last 10 seconds, of the velocity vector roll control, the angle of attack and side slip angles are commanded to 10^o and 0^o respectively. Throughout the maneuver the velocity of the aircraft is approximately kept constant and undesired lateral accelerations are mostly suppressed by the side slip angle control. At some certain stages of the maneuver the TVC paddles are saturated and remained at 30° for some seconds. These saturations did not affect the whole performance of the maneuver, however, it is seen from the side slip angle and yaw attitude time histories that the aircraft got a little side-slip throughout the maneuver and ended up the maneuver with approximately 3° heading change. The aerodynamic control effectors ($\delta_a, \delta_e, \delta_r$) helped the TVC paddles however they are saturated at some certain stages of the maneuver and retracted to their neutral positions. As a result, the desired maneuver is successfully realized and at the end of the maneuver the velocity vector is turned to its original position at the start of the maneuver.

The second maneuver is the fixed ground target attack maneuver. Here, the aircraft attacks a fixed ground target and makes rapid maneuvers in the defense zone of the target. Here, first, the aircraft directly moves head on to and offenses the target. Then, after passing the target, it makes a rapid maneuver and leaves the defense zone of the target. Finally, the aircraft captures its original flight path that is before the target defense zone entrance.

The fixed ground target attack maneuver simulations are generated by using the attitude controller and commanding the desired yaw angle (ψ_d) to wave in the defense zone of the target. For that purpose a special lateral steering algorithm is proposed. That algorithm generates lateral commands whenever the aircraft starts the attack maneuver. After attacking the target, the aircraft is commanded to its original heading (or a recovery point). The simulation results showed that the fixed ground target attack maneuver is mostly done by the aerodynamic control effectors. However, in certain stages of the maneuver the aerodynamic controls are saturated and the TVC paddles are deflected to their maximum positions. These regions are the start of the maneuver, reaching the center of the zone making a turn maneuver and recovering the original flight path at the end of the zone. From the time history plot of the angle of attack it is seen that at these regions the angle of attack values are comparably higher with respect to the other stages of the maneuver. Especially, when the aircraft reaches the target (where a most rapid turn is needed) the angle of attack value is greater than 25°. This shows that the rapid maneuvers are successfully realized at high angle of attack values using TVC rather than aerodynamic control effectors.

Afterwards, the tail chase acquisition maneuver which is one sort of an offensive Basic Fighter Maneuver (BFM) is implemented and simulated. In order to maintain air-superiority in such a scenario the attack aircraft should perform agile roll maneuvers to capture the target and keep it continuously in line of sight. In order to simulate that scenario a target aircraft is introduced in the simulations and programmed to fly a pre-defined s-turn trajectory. The simulations are generated by using the attitude controller and commanding the desired yaw and pitch angles (ψ_d, θ_d) to point the target aircraft. The tail chase acquisition maneuver simulation is done for 60 seconds. During the simulation the positions and attitudes of the attacking and target aircrafts are interconnected with a custom designed virtual reality modeling environment to visualize the performance of the pointing control. Throughout the maneuver during the s-turns the angle of attack values are jumped approximately to 30° and the side-slip angles are waved between $\pm 20^\circ$. The aircraft comes perpendicular to its initial yaw attitude at the mids of the maneuver and then comes to its original attitude at the end of the maneuver. The aerodynamic control effectors helped the maneuver; however, most of the agile turns are realized in conjunction with TVC paddles. At the sharp s-turns the aerodynamic controls are saturated and the TVC paddles are deflected to their maximum positions. As a result, the desired maneuver is successfully realized and the virtual reality environment showed that the attack aircraft pointed the target aircraft throughout the whole maneuver.

After the offensive BFM case, the target aircraft pointing at head-on BFM is implemented and simulated. This scenario is simulated similarly to the previous scenario and a target aircraft is programmed to fly a pre-defined aggressive escape maneuver and trying to decrease the probability of target lock. The simulations are generated by using the attitude controller and commanding the desired yaw and pitch angles (ψ_d, θ_d) to point the target aircraft. Before the start of the maneuver the range between the target and the attack aircraft is repeatedly observed. Whenever the range is less than a prescribed value the attack aircraft starts performing the maneuver with giving a turn direction decision. At the initial phase of the maneuver the pilot manually pulls-up the aircraft to stall region and then the turning maneuver is started. The target aircraft pointing maneuver simulation is done for 30 seconds. During the simulation the positions and attitudes of the attacking and target aircrafts are interconnected with the designed virtual reality modeling environment and the performance of the pointing control is visualized.

Throughout the maneuver, when the aircraft is capturing the target, the angle of attack and the side-slip angle values reach up to very high values as 60° and 50° respectively. Also, at that stage, the aircraft almost stopped and the total velocity of the aircraft slowed down to 30m/sec. This is a very aggressive maneuver, and, can be described in a way such that "the aircraft stopped and turned". Almost the entire maneuver is realized with TVC paddles. The aerodynamic control effectors are operated at some certain stages of the maneuver, but, rapidly saturated and retracted their neutral positions.

The same maneuver is also simulated with the pilot in the loop to investigate the effect of the human pilot interaction on the pointing maneuver performance. Hence, the human pilot model is integrated in the control loop and the desired control loop design parameters are adjusted to maintain the robustness of the attitude control loop with the integrated pilot. Similar time history plots are obtained for the total velocity, angle of attack and side-slip angles. However, the roll, pitch and yaw attitude results are different than the auto piloted case. Due to the noise and lag associated with the human pilot dynamics at the start of the maneuver the pilot gave higher turn command than needed and the desired pitch attitude cannot be captured instantly. Although this is the case at the beginning of the maneuver, the desired roll, pitch and yaw attitudes are captured with some certain time lag (approximately 0.35 sec) throughout the maneuver. This time lag causes approximately at most 5° tracking error in all attitude angles. Considering the all weapons envelope of the attack aircraft 5° (maximum) error is not expected to cause any deficiency on effectively directing the armament towards the target aircraft. The human pilot integrated pointing maneuver is performed by using the TVC paddles most of the time. The aerodynamic control surfaces are especially deflected at the beginning of the maneuver. The entire performance of the maneuver is not good as the autopilot case as expected. Nevertheless, the pilot manages recovering the target exactly at the end of the maneuver.

The contributions and innovations of this study can be listed briefly as follows:

- The thrust vectoring control (using the TVC paddles) blended with the conventional aerodynamic controls is applied to the fighter-bomber aircraft under study for the first time.
- A special hexagonal shaped jet turning envelope calculation is proposed and implemented for the cooperative operation of the three TVC paddles.
- In the NID controller design, the achievable desired forces and moments are structured by using the constraining equation related to the positional geometry of the TVC effectors; which inherently dictates the design of the stabilization and the attitude controllers.
- A special trim algorithm is implemented to account for the multiple solutions and discriminate the proper solution by checking the trim values of the angle of attack, aerodynamic control surface deflections and the engine actual power setting.
- The uncertainty calculation is done by linearizing the “uncertain” total plant (composed of the TVC, engines, TVC paddles and aerodynamic controls) together with the “nominal” TVC NID and aerodynamic NID. Hence, this leads to the calculation of additive uncertainty transfer functions which are the differences from the free integrators in the diagonal channels and zeros in the off-diagonal channels of the transfer matrix found for the nominal total plant linearized together with the nominal inverse dynamics.
- In this study the idea of treating the aerodynamic coefficients (thus the aerodynamic forces and moments) as they are completely unknown is analyzed for the first time. This unusual assumption is pursued in order to eliminate the lengthy and cost consuming aerodynamic analyses and ease the control design whenever the TVC is existent. Hence, the entire control action is desired to be realized by the TVC in a way trying to suppress the “disturbance” coming from the aerodynamics of the aircraft. However, the robustness analysis showed that it is impossible to achieve the desired performance without any knowledge of the aerodynamics. Thus, it is

concluded that the aerodynamic model accuracy (up to some certain level) should be maintained although TVC is the major control effector.

- The integration of the human pilot in the robustness analysis is another innovation conducted in this study. The pilot is integrated in the stabilization and attitude controller loops and a robust fly-by-wire controller design is developed.
- The stabilization control for recovering the aircraft from the undesired stall, where the aerodynamic control effectors are inoperative, using the TVC is another contributive part of this study. Here, a special and hybrid controller architecture, operating on the Euler angle rates and then switching to trim angle of attack control, is proposed and implemented.
- The usage of integrated Bihrle-Weissmann chart is highly populated in this study. Using the stall indication parameters of the aircraft, the static (before the simulation) and the dynamic (through the simulation) analysis of the stall, post-stall and deep-stall regions are done. Also, the high angle of attack stabilization control triggering logic is based on the travel of the stall indication track on the mentioned chart.
- The TVC integrated aircraft is tested for a group of high angle of attack rapid maneuvers such as Cobra, Herbst, velocity vector roll, fixed ground target attack, tail chase acquisition and target aircraft pointing maneuvers. Here, a special purpose virtual reality modeling environment to visualize the performance of the pointing control is developed and interconnected with the simulations.
- As for the fixed ground target attack maneuver, in order to charge directly on to the target and be effective in the defense zone of the target, a special algorithm is proposed and implemented in the simulations.
- The human pilot is integrated in the head-on BFM and the performance of the attitude controller for the fly-by-wire target aircraft pointing maneuver is investigated.

As for the future work the following recommendations can be proposed:

- The proposed TVC enhancement can be applied on some different aircraft configurations including the single engine fighters and the resulting performances can be analyzed.
- The enhancement presented in this study can be tested in some different scenarios including the very short take-off and landing (VSTOL). Here, also the ground effects on the performance of the designed controller can be analyzed.
- The controller design methodology conducted in this study can be tested in a pursuer-evader scenario. Thus, the performance of the TVC enhanced aircraft evading from a missile or gun-shot can be compared with the conventionally configured aircraft.
- The human pilot model can be enhanced and some prediction capabilities can be added to the existing model. These predictions may originate from the visual interpretations or the force feedbacks on the control manipulators. Also, a discrete and fuzzy pilot modeling can be conducted to reflect the cognitive characteristics of the human pilot.

REFERENCES

[1] FAA, "Instrument Flying Handbook", Department of Transportation, Federal Aviation Administration, AC 61-27C, pp. 4-1, 4-3, 1980.

[2] Department of the Air Force, "*Flying Operations: Instrument Flight Procedures*", AFMAN 11-217, Vol. 1, pp. 14-16, April, 1996.

[3] Crenshaw, D., "How to Live and Die in the Virtual Sky", http://www.combatsim.com/, November, 1998, last accessed March, 2006.

[4] Mason, W.H., "*High Angle-of-Attack Aerodynamics*", AOE 4124 Configuration Aerodynamics Course Notes, Aerospace and Ocean Engineering, Virginia Tech., March, 2006.

[5] Chambers, J.R., Grafton, S.B., "*Aerodynamics of Airplanes at High Angles of Attack*", NASA TM 74097, Dec. 1977.

[6] Chambers, J.R., "*High-Angle-of-Attack Aerodynamics: Lessons Learned*", AIAA Paper 86-1774, June 1986.

[7] Well, K.H., Faber, B., Berger, E., "*Optimization of Tactical Aircraft Maneuvers Utilizing High Angles of Attack*", Journal of Guidance, Control, and Dynamics 1982, 0731-5090 vol.5 no.2 (131-137).

[8] Greer, H.D., "Summary of Directional Divergence Characteristics of Several High-Performance Aircraft Configurations", NASA TN D-6993, Nov. 1972.

[9] Chambers, J.R., "*Overview of Stall/Spin Technology*", AIAA Paper 80-1580, August, 1980.

[10] Nguyen, L.T., Ogburn, M.E., Gilbert, W.P., Kibler, K.S., Brown, P.W., Deal, P.L., "*Simulator Study of Stall/Post-Stall Characteristics of a Fighter Airplane with Relaxed Static Stability*", NASA TP-1538, December, 1979.

[11] Chambers, J.R., "*High-Angle-of-Attack Technology: Progress and Challenges*", High-Angle-of-Attack Technology, NASA CP-3149, vol. 1, May 1992, pp. 1–22.

[12] Herbst, W.B., "*X-31A at First Flight*", Flying Qualities, AGARD CP-508, Feb. 1991, pp. 29-1–29-8.

[13] Canter, Dave E., "*X-31 Post-Stall Envelope Expansion and Tactical Utility Testing*", Fourth High Alpha Conference, NASA CP-10143, vol. 2, July 1994.

[14] Kidman, D.S., Vickers, J.E., Olson, B.P., and Gerzanics, M.A., "*Evaluation of the F-16 Multi-Axis Thrust Vectoring Aircraft*", AFFTC-TR-95-12, Sept. 1995.

[15] Smith, W., "*X-29 High AOA Flight Test Results: An Overview*", SAE Aerospace Atlantic Conference and Exposition, SAE International, Washington, DC, USA, Apr. 1993.

[16] Gilbert, W.P., Nguyen, L.T., and Gera, J., "*Control Research in the NASA High-Alpha Technology Program*", Aerodynamics of Combat Aircraft Controls and of Ground Effects, AGARD-CP-465, pp. 3-1 -3-18, Apr. 1990.

[17] Ogburn, M.E.; and Foster, J.V., "*Development of High-Angle-of-Attack Nose-Down Pitch Control Margin Design Guidelines for Combat Aircraft*", NASA CP-10127, December 1993, pp. 293-322.

[18] "Cooperative Program on Dynamic Wind Tunnel Experiments for Maneuvering Aircraft", AGARDAR- 305, Oct. 1996.

[19] Foster, J.V., "*Investigation of the Susceptibility of Fighter Airplanes to the Out-of-Control Falling Leaf Mode*", In NASA Langley Research Center, editor, NASA High Angle of Attack Conference, ITAR, Hampton, VA, Sept. 1996.

[20] Kalviste, J., "*Math Modeling of Aero Data for Aircraft Dynamic Motion*", AIAA Atmospheric Flight Mechanics Conference, AIAA Paper 94-AFM-26-7, August 1994.

[21] Smith, P.R., "*Functional Control Law Design Using Exact Non-Linear Dynamic Inversion*", AIAA Atmospheric Flight Mechanics Conference, AIAA Paper 94-3516- CP, pp. 481-486, August 1994.

[22] Smith, P.R., and Patel, Y., "*Translational Motion Control Of VSTOL Aircraft Using Nonlinear Dynamic Inversion*", AIAA Atmospheric Flight Mechanics Conference, AIAA Paper 95-3452-CP, pp. 238-252, August 1995.

[23] Ostroff A.J., and Bacon B.J., "*Force and Moment Approach for Achievable Dynamics using Nonlinear Dynamic Inversion*", AIAA Guidance, Navigation, and Control Conference, AIAA Paper 99-4001, August 1999.

[24] Isidori, A., Nonlinear Control Systems, 2nd ed., Springer-Verlag, New York, 1995, Chaps 3, 4 and 5.

[25] Bugajski, J. D., and Enns, F.D., "Nonlinear Control Law with Application to High Angle of Attack Flight," Journal of Guidance, Control, and Dynamics, Vol. 15, No. 3, 1992, pp. 761–767.

[26] Enns, D., Bugajski, D., Hendrick, R., and Stein, G., "*Dynamic Inversion: an Evolving Methodology for Flight Control Design*", International Journal of Control, Vol. 59, No. 1, 1992, pp. 71–91.

[27] Patel, Y., and Smith, P.R., "Translational Motion Control of Vertical Takeoff Aircraft Using Nonlinear Dynamic Inversion," Journal of Guidance, Control, and Dynamics, Vol. 21, No. 1, 1998, pp. 179–182.

[28] Smith, P.R., and Berry, A., "Flight Test Experience of a Non-Linear Dynamic Inversion Control Law on the VAAC Harrier," AIAA Paper 2000-3914, Aug. 2000.

[29] Littleboy, D. M., and Smith, P.R., "Using Bifurcation Methods to Aid Nonlinear Dynamic Inversion Control Law Design," Journal of Guidance, Control, and Dynamics, Vol. 21, No. 4, 1998, pp. 632–638.

[30] Snell, A., "*Decoupling Control with Applications to Flight*" Journal of Guidance, Control, and Dynamics, Vol. 21, No. 4, 1998, pp. 647–655.

[31] Durham, W., "*Dynamic Inversion and Model-Following Control*", AIAA Paper 96-3690, July 1996.

[32] Honeywell Technology Center, Lockheed Martin Skunk Works, and Lockheed Martin Tactical Aircraft Systems, “*Application of Multivariable Control Theory to Aircraft Control Laws: Final Report: Multivariable Control Design Guidelines*”, WL-TR-96-3099, Flight Dynamics Directorate, Wright Laboratory, Air Force Materiel Command, Wright-Patterson AFB, OH 45433-7562, May, 1996.

[33] Nelson, R., Flight Stability and Automatic Control, 2nd ed., McGraw-Hill, ISBN 9780070462731, October 1997.

[34] Balas, G.J., Garrard, W.L. and Reiner, J., “*Robust Dynamic Inversion Control Laws for Aircraft Control*”, AIAA Paper 92-4329, Proceedings of the AIAA Guidance, Navigation and Control Conference, Hilton Head Island, SC, Aug. 1992, pp. 192-205.

[35] Anon., “Military Standard Flying Qualities of Piloted Aircraft”, Mil-STD-1797A, January, 1990.

[36] Zames, G., “Feedback and Optimal Sensitivity: Model Reference Transformation, Multiplicative Seminorms, and Approximate Inverses”, IEEE Transactions on Automatic Control, 26:301-320, 1981.

[37] Skogestad, S., Postlethwaite, I., Multivariable Feedback Control, Analysis and Design, John Wiley & Sons, ISBN 0471943304, August 2001.

[38] Doyle, J., Glover, K., Khargonekar, P., “*State Space Solutions to Standard H_2 and H_∞ Control Problems*”, IEEE Transactions on Automatic Control, 34(8):831-846, 1989.

[39] Doyle, J., "*Analysis of Feedback Systems with Structured Uncertainties*", IEE Proceedings, Part D, 133(2):45-46, March 1982.

[40] Nalbantoğlu, V., "Robust Control and System Identification for Flexible Structures", PhD Thesis, University of Minnesota, Minneapolis, MN, July 1998.

[41] Doyle, J., Wall, J.E., Stein, G., "*Performance and Robustness Analysis for Structured Uncertainty*", In Proc. of IEEE Control Decision Conf., pp 629-636, 1982.

[42] Balas, G.J., Doyle, J., Glover, K., Packard, A., Smith, R., "*μ-Analysis and Synthesis Toolbox*", MUSYN Inc. and Mathworks Inc., Minneapolis, MN, 1993.

[43] Ito, D., Georgie, J., Valasek, J., Ward, D.T., "Re-Entry Vehicle Flight Controls Design Guidelines: Dynamic Inversion", Flight Simulation Laboratory, Texas Engineering Experiment Station, Texas A&M University, Final Technical Report, NAG9-1085, May 2001.

[44] Anon., "Military Specification Flying Qualities of Piloted Airplanes", Mil-F-8785-C, November, 1980.

[45] Maybeck, P.S., Stochastic Models, Estimation, and Control Volume 1, Academic Press Inc., ISBN 0 12 480701 1, 1979.

[46] Haering, E.A., "Airdata Measurement and Calibration", NASA Technical Memorandum 104316, NASA Dryden Flight Research Center, Edwards, CA, 1995.

[47] Lawford, J.A., Nippress, K.R., “Calibration of Air-Data Systems and Flow Direction Sensors,” AGARD-AG-300, vol. 1, Sep. 1983.

[48] National Oceanic and Atmospheric Administration, National Aeronautics and Space Administration, and United States Air Force, “U.S. Standard Atmosphere, 1976,” NOAAS/T 76-1562, U.S. Government Printing Office, Washington DC, 1976.

[49] Gracey, W., “Summary of Methods of Measuring Angle of Attack on Aircraft”, NACA TN 4531, Langley Aeronautical Lab., Langley Field, VA, 1958.

[50] Neal, T.P., Smith, R.E., “An In-Flight Investigation to Develop Control System Design Criteria for Fighter Aircraft”, AFFDL-TR-70-74, Vol. I, December 1970.

[51] Davidson, J.B., Schmidt, D.K., “Modified Optimal Control Pilot Model for Computer-Aided Design and Analysis”, NASA TM-4384, NASA Langley Research Center, VA, 1992.

[52] Phillips, J.M., “Variable Strategy Model of the Human Operator”, PhD Thesis, Virginia Polytechnic Institute and State University, Blacksburg, VA, 2000.

[53] Kay, J., Mason, W. H., Durham, W., Lutze, F., “*Control Authority Assessment in Aircraft Conceptual Design*”, AIAA Paper 93-3968, Virginia Tech, VA.

[54] Williams, J.E., Vukelich, S.R., “The USAF Stability and Control Datcom”, AFFDL-TR-79-3032, Volume I, Users Manual, McDonnell Douglas

Astronautics Company, St. Louis Division, St Louis, Missouri 63166, April 1979.

[55] Garza, F. R., Morelli, E. A., “*A Collection of Nonlinear Aircraft Simulations in MATLAB*”, NASA/TM-2003-212145, January 2003.

[56] Bowers, A., Noffz, G., Grafton, S.B., Mason, M.L., Peron, L.R., “Multiaxis Thrust Vectoring Using Axisymmetric Nozzles and Post-exist Vanes on an F-18 Configuration Vehicle”, NASA-TM-101741, Dyden Flight Research Facility, Edwards, CA, 1991.

[57] Anon., “Manual of the ICAO Standard Atmosphere (extended to 80 KM)”, International Civil Aviation Organization, Doc 7488-CD, Third Edition, 1993, ISBN 92-9194-004-6.

[58] Ateşoğlu, Ö., Özgören, M.K., “High-α Flight Maneuverability Enhancement of a Twin Engine Fighter-Bomber Aircraft for Air Combat Superiority Using Thrust-Vectoring Control”, AIAA-2006-6056, AIAA Guidance, Navigation and Control Conference, Keystone, CO, Aug. 21-24, 2006.

[59] Stalford, H., Hoffman, E., “*Thrust Vectoring Effect on Time-optimal 90 degrees Angle of Attack Pitch Up Maneuvers of a High Alpha Fighter Aircraft*”, AIAA-1989-3521, AIAA Guidance, Navigation and Control Conference, Boston, MA, Aug. 14-16, 1989.

[60] Schneider, G., Garret, L.W., George, W., “*Minimum Time Turns Using Vectored Thrust*”, AIAA-1988-4070, AIAA Guidance, Navigation and Control Conference, Minneapolis, MN, Aug. 15-17, 1988.

[61] Young, J., "*X-31 VECTOR Program Summary*", AIAA-2004-5026, AIAA Guidance, Navigation, and Control Conference and Exhibit, Providence, Rhode Island, Aug. 16-19, 2004.

[62] Tamrat, B., "The X-31: A Post-Stall Technology (PST) Fighter Close-In-Combat Results Assessment, And A Look At New CIC Performance Evaluation Metrics", AIAA-2004-5173, AIAA Atmospheric Flight Mechanics Conference and Exhibit, Providence, Rhode Island, Aug. 16-19, 2004.

[63] Carlos, M., Selmon, T., Trujillo, J., Steven, M., "*An Air Combat Simulation Model Suitable for the Evaluation of Agility and EFM*", AIAA-1989-3311, AIAA Flight Simulation Technologies Conference and Exhibit, Boston, MA, Aug. 14-16, 1989.

[64] Gallaway, C. R., Osborn, R.F., "*Aerodynamics Perspective of Supermaneuverability*", AIAA-1985-4068 Applied Aerodynamics Conference, 3rd, Colorado Springs, CO, Oct. 14-16, 1985.

[65] Kish, B.A., Mittlestead, D.R., Wunderlich, G., Tokar, J.M., Hooper, T., "*Practical Limits of Supermaneuverability and Full Envelope Agility*", AIAA-1996-3493, AIAA Flight Simulation Technologies Conference, San Diego, CA, July 29-31, 1996.

[66] Berrier, B., Mason, L., "*Static Investigation of Post-exit Vanes for Multiaxis Thrust Vectoring*", SAE, ASME, and ASEE, Joint Propulsion Conference, 23rd, San Diego, CA, June 29-July 2, 1987.

[67] Yupu, L., Fuying, G., Lan, C.E., "*Estimation of Aircraft Models in Cobra Maneuvers Through Dynamic Inversion*", AIAA-1994-3494, AIAA Atmospheric Flight Mechanics Conference, Scottsdale, AZ, Aug. 1-3, 1994.

[68] Horie, K., Conway, B.A., "*Optimization for Fighter Aircraft Vertical-Plane Maneuvering Using Poststall Flight*", Journal of Aircraft, 0021-8669, vol.37 no.6 (pp. 1017-1021), 2000.

[69] Murayama, K., Hull, D.G., "*The Cobra Maneuver as a Minimum Time Problem*", AIAA-1997-3586, AIAA Atmospheric Flight Mechanics Conference, New Orleans, LA, Aug. 11-13, 1997.

[70] Komduur, H. J., Visser, H.G., "*Optimization of Vertical Plane Cobra-like Pitch Reversal Maneuvers*", AIAA-2001-4134, AIAA Atmospheric Flight Mechanics Conference and Exhibit, Montreal, Canada, Aug. 6-9, 2001.

[71] Goman, M.G., Kolesnikov, E.N., "*Robust Nonlinear Dynamic Inversion Method for an Aircraft Motion Control*", AIAA-1998-4208, AIAA Guidance, Navigation, and Control Conference and Exhibit, Boston, MA, Aug. 10-12, 1998.

[72] Smit, M.Z., Craig, I.K., "*Robust Flight Controller Design using H-infinity Loop-shaping and Dynamic Inversion Techniques*", AIAA-1998-4132, AIAA Guidance, Navigation, and Control Conference and Exhibit, Boston, MA, Aug. 10-12, 1998.

[73] Richard, A.J., Buffington, J.M., Banda, S.S., "*Design of Nonlinear Control Laws for High-angle-of-attack Flight*", Journal of Guidance, Control, and Dynamics 1994, 0731-5090 vol.17 no.4 (pp. 737-746).

[74] Herbst, W.B., Krogull, B., "*Design for Air Combat*", AIAA-1972-749, American Institute of Aeronautics and Astronautics, Aircraft Design, Flight Test, and Operations Meeting, 4th, Los Angeles, CA, Aug. 7-9, 1972.

[75] Herbst, W.B., "*Dynamics of Air Combat*", Journal of Aircraft 1983, 0021-8669 vol.20 no.7 (594-598).

[76] Herbst, W.B., "*Future Fighter Technologies*", Journal of Aircraft 1980, 0021-8669 vol.17 no.8 (561-566).

[77] Shinar, J., "*Concept of Automated Aircraft Guidance System for Air-to-air Missions*", AIAA-1986-2285, Atmospheric Flight Mechanics Conference, Williamsburg, VA, August 18-20, 1986.

[78] Beh, H., van den Bunt, R., Fischer, B., "*High Angle of Attack Approach and Landing Control Law Design for the X-31A*", AIAA-2002-247, AIAA Aerospace Sciences Meeting and Exhibit, 40th, Reno, NV, Jan. 14-17, 2002.

[79] Reigelsperger, W., Hammett, K.D., Banda, S.S., "*Lateral-directional, Full Envelope Control Law Design for F-16 with Thrust Vectoring*", AIAA-1995-3249, AIAA Guidance, Navigation and Control Conference, Baltimore, MD, Aug. 7-10, 1995.

[80] Innocenti, M., Carnasciali, G., Nasuti, F., "*Angle of Attack Guidance via Robust Approximate Inversion*", AIAA-1998-4113, AIAA Guidance, Navigation, and Control Conference and Exhibit, Boston, MA, Aug. 10-12, 1998.

[81] Fisher, D.F., Cobleigh, B.R., Banks, D.W., Hall, R.M., Wahls, R.A., "*Reynolds Number Effects at High Angles of Attack*", AIAA-1998-2879, Advanced Measurement and Ground Testing Technology Conference, 20th, Albuquerque, NM, June 15-18, 1998.

CURRICULUM VITAE

PERSONAL INFORMATION:

Surname, Name:	ATEŞOĞLU, Özgür
Nationality:	Turkish
Date and Place of Birth:	July 12, 1971, Konya, TÜRKİYE
Work Address:	Navigation and Guidance Systems Design Dept.
	MGEO, Aselsan Inc.
	06750, Akyurt, Ankara, TÜRKİYE
	Tel: +90 (312) 847 53 00
	Fax: +90 (312) 847 53 20
	E-mail: oatesoglu@mgeo.aselsan.com.tr

EDUCATION:

Degree	**Institution**	**Year of Graduation**
MS	METU Aerospace Engineering	1996
BS	METU Aerospace Engineering	1994
High School	Ankara Fen Lisesi, Ankara	1989

WORK EXPERIENCE:

Year	Place	Enrollment
2000 Sept. – Present	ASELSAN, MGEO, Navigation and Guidance Systems Design Dept., Ankara, Türkiye	Lead Design Engineer Chief Engineer
1999 Apr. – 2000 Sept.	Turkish Aerospace Industries (TAI), Avionics Div. and Flight Mechanics Div., Ankara, Türkiye	Senior Design Engineer
1994 Sept. – 1997 Nov.	TÜBİTAK-SAGE, Guidance and Control Div., Ankara, Türkiye	Senior Researcher Researcher

MILITARY SERVICE:

Year	Place	Enrollment
1999 Apr. – 1998 Apr.	1. HİBM K.lığı, Hyd. And Pneu. Systems Technical Support Div., Eskişehir, Türkiye	1st Lieutenant 2nd Lieutenant

FOREIGN LANGUAGES:

Advanced English

Basic German

PUBLICATIONS:

INTERNATIONAL JOURNAL ARTICLE

1. Ateşoğlu, Ö., Özgören, M.K., "*High-alpha Flight Maneuverability Enhancement of a Fighter Aircraft Using Thrust-Vectoring Control*", Journal of Guidance, Control and Dynamics, accepted for publication on February 12, 2007, in press.

INTERNATIONAL CONFERENCE PAPERS

1. Ateşoğlu, Ö., Özgören, M.K., "Autopilot Design for a Trajectory Tracking *Missile Using Optimal Control with Prescribed Degree of Stability*", International Aerospace Conference and Symposia 96, Ankara, Turkey, October 1996.

2. Ateşoğlu, Ö., "*Fuzzy Guidance and Control Inference Design for a Non-Linear Air to Surface Missile Model*", Nordic MATLAB Conference 2001, Oslo, Norway, October 2001.

3. Ateşoğlu, Ö., "*Fuzzy Guidance and Control Design for a Non-Linear Missile Model*", Artificial Intelligence and Neural Network Conference 2002, Istanbul, Turkey, June 2002.

4. Ateşoğlu, Ö., "*Guidance and Control Design and 6 DoF Simulations for a Target Drone*", UAV Systems, 18th Bristol Int. Conference, Bristol, UK, March 2003.

5. Semerci, E.A., Ateşoğlu, Ö., "*Nonlinear Modeling and PWM Integrated Controller Design for a Pneumatic Actuator*", 24th IASTED Int. Conference on Modeling, Identification and Control, IASTED MIC 2005, Innsbruck, Austria, February, 2005.

6. Ateşoğlu, Ö., "*IMU Data Generation From The Defined Motion Using the NDI Controller Design Technique*", IEEE & ION Position Location And Navigation Symposium, PLANS 2006, San Diego, CA, April 2006.

7. Eren, M., Ateşoğlu, Ö., Güner, L., "*Tarsus, A New Generation State Of The Art Tactical Artillery Survey and Gun Laying System*", IEEE & ION Position Location And Navigation Symposium, PLANS 2006, San Diego, CA, April 2006.

8. Eren, M., Ateşoğlu, Ö., Güner, L., "*Tarsus-A New Generation State Of The Art Tactical Artillery Survey System Utilizing GPS/VMS Aided Inertial Navigation Technology*", European Navigation Conference, ENC 2006, Manchester, UK, May 2006.

9. Ateşoğlu, Ö., Özgören, M.K., "*High-Alpha Flight Maneuverability Enhancement of a Twin Engine Fighter-Bomber Aircraft for Air Combat Superiority Using Thrust-Vectoring Control*", AIAA-2006-6056, AIAA Guidance, Navigation and Control Conference, Keystone, CO, August, 2006.

10. Ateşoğlu, Ö., "*Nearly Time-Optimal Point to Point Navigation Control Design for Power Wheelchair Dynamics*", IEEE Conference on Control

Applications, 2006 CCA, CACSD and ISIC, Munich, Germany, October 2006.

11. Eren, M., Ateşoğlu, Ö, Güner, L.,"*A Novel Tactical Artillery Surveying and Gun Laying System Family, Tarsus*", to appear in NATO RTO Symposium on Military Capabilities Enabled by Advances in Navigation Sensors, Antalya, Turkey, October, 2007.

NATIONAL CONFERENCE PAPERS

1. Ateşoğlu, Ö., "*Simulation Based Computer Applications on Strapdown System Algorithms for Inertially Guided Missile Position Computations*", (in Turkish), Kayseri 1. Havacılık Sempozyumu, Kayseri, Turkey, May 1996.

2. Ateşoğlu, Ö., "*Autopilot and Guidance Design for a Target Drone*", (in Turkish), Kayseri 3. Havacılık Sempozyumu, Kayseri, Turkey, May 2000.

3. Ateşoğlu, Ö., Nalbantoğlu, V, Akçayırlı, Y.İ., "*Grammian Based Observer Design and Calibration Maneuver Analysis for Land Navigation*", (in Turkish), Otomatik Kontrol Ulusal Toplantısı, TOK 2002, Ankara, Turkey, September 2002.

4. Ateşoğlu, Ö., Özgören, M.K., "*Missile Autopilot Design Based on Nonlinear Inverse Dynamics and Time Scale Separation*", (in Turkish), Otomatik Kontrol Ulusal Toplantısı, TOK 2005, Istanbul, Turkey, June 2005.

5. Eren, M., Ateşoğlu, Ö., Güner, L., "*Tarsus-Integrated GPS/VMS Aided Inertial Navigation Technology Based Artillery Surveying System*", (in Turkish), SAVTEK 2006, 3. Savunma Teknolojileri Kongresi, Ankara, Turkey, June 2006.

6. Ateşoğlu, Ö., Özgören, M.K., "*Dynamical Analysis of a Parallel Manipulator Used for Stabilization Control*", (in Turkish), 13. Ulusal Makina Teorisi Semp., UMTS 2007, Sivas, Turkey, June 2007.

7. Ateşoğlu, Ö., Özgören, M.K., "*Robust Nonlinear Inverse Dynamics Controller Design for the Automatic and Piloted Control of an UAV*", (in Turkish), to appear in Otomatik Kontrol Ulusal Toplantısı, TOK 2007, Istanbul, Turkey, September 2007.

MS THESIS

1. Ateşoğlu, Ö., Different Autopilot Designs and Their Performance Comparison for Guided Missiles, M.Sc. Thesis, Aeronautical Eng. Dep., METU, December 1996.